Per Grove Thomsen
Hans True
Editors

Non-smooth Problems in Vehicle Systems Dynamics

Proceedings of the Euromech Colloquium

Springer

Non-smooth Problems in Vehicle Systems Dynamics

Per Grove Thomsen · Hans True
Editors

Non-smooth Problems in Vehicle Systems Dynamics

Proceedings of the Euromech 500 Colloquium

Springer

Editors
Prof. Per Grove Thomsen
Technical Univ. of Denmark
DTU Informatics
Richard Petersen Plads 321
DK-2800 Kgs. Lyngby
Denmark
pgt@imm.dtu.dk

em. Univ. Prof. Dr. Hans True
Technical Univ. of Denmark
DTU Informatics
Richard Petersen Plads 321
DK-2800 Kgs. Lyngby
Denmark
ht@imm.dtu.dk

ISBN 978-3-642-01355-3 e-ISBN 978-3-642-01356-0
DOI 10.1007/978-3-642-01356-0
Springer Heidelberg Dordrecht London New York

Library of Congress Control Number: 2009927025

Cover design: eStudio Calamar S.L.

Printed on acid-free paper

Springer is part of Springer Science+Business Media (www.springer.com)

Contents

Part I Problems in Vehicle Dynamics

Typical Non-smooth Elements in Vehicle Systems 3
Hans True

Application of Nonlinear Stability Analysis in Railway Vehicle Industry . . 15
Oldrich Polach

Closed-Form Analysis of Vehicle Suspension Ride and Handling Performance 29
Mehdi Ahmadian

Limit Wheel Profile for Hunting Instability of Railway Vehicles 41
Laura Mazzola, Stefano Alfi, F. Braghin, and S. Bruni

Low-Cost Maintenance Operation for Avoiding Hunting Instability in a Metro Vehicle 53
F. Braghin, Stefano Alfi, S. Bruni, and A. Collina

Acoustic Optimization of Wheel Sets 67
Michael Beitelschmidt, Volker Quarz, and Dieter Stüwing

Measurement, Modelling and Simulation of Curve Squealing of Trains . . 73
Christoph Glocker, Eric Cataldi-Spinola, Rossano Stefanelli, and Jürg Dual

Selected Problems of Non-linear (Non-smooth) Dynamics of Rail Vehicles in a Curved Track 87
Krzysztof Zboiński

On Tangential Friction Induced Vibrations in Brake Systems 101
Georg Peter Ostermeyer

Dry Friction Element with Logical Switch for Numerical Simulation of Vehicle Dynamics and Its Application 113
Anna Orlova

Damper Modelling and Its Implementation in Railway Simulation Program 123
Asier Alonso and J.G. Giménez

Suppression of Bumpstop Instabilities in a Quarter-Car Model 137
Fredrik Svahn, Jenny Jerrelind, and Harry Dankowicz

Experimental Modal Analysis of Towed Elastic Tyres During Rolling 149
Dénes Takács and Gábor Stépán

Modelling and Simulation of Longitudinal Tyre Behaviour 161
Jaap P. Meijaard

Part II Dynamics of Non-smooth Problems

Bifurcations in Non-smooth Models of Mechanical Systems 173
Piotr Kowalczyk and Arne Nordmark

Vibrational Displacement Determined by Constructive and Force Asymmetry of System 187
Iliya I. Blekhman

Smoothing Dry Friction by Medium Frequency Dither and Its Influence on Ride Dynamics of Freight Wagons 189
Jerzy Piotrowski

Simulation of Gear Hammering With a Fully Elastic Model 195
Pascal Ziegler and Peter Eberhard

Part III Numerical Analysis of Non-smooth Problems

Discontinuities in ODEs: Systems with Change of State 211
Per Grove Thomsen

Towards Improved Error Estimates for Higher Order Time Integration of ODEs with Non-Smooth Right Hand Side 227
Martin Arnold

Sensitivity Analysis of Discontinuous Multidisciplinary Models: Two Examples 239
Andreas Pfeiffer and Martin Arnold

Smoothing Discontinuities in the Jacobian Matrix by Global Derivatives 253
Georg Rill

Index 263

Contributors

Mehdi Ahmadian, Ph.D. Railway Technologies Laboratory (RTL), Center for Vehicle Systems & Safety (CVeSS),Virginia Tech, MC-0901, Blacksburg, VA 24061, USA, ahmadian@vt.edu

Stefano Alfi Politecnico di Milano, Department of Mechanical Engineering, Via G. La Masa, 1, I-20156 Milano, Italy, stefano.alfi@polimi.it

Asier Alonso CEIT and TECNUN (University of Navarra), Paseo M. Lardizabal 13, E-20018 San Sebastian (Guipúzcoa), Spain, aalonso@ceit.es

Martin Arnold Martin Luther University Halle-Wittenberg, NWF III – Institute of Mathematics, D-06099 Halle (Saale), Germany, martin.arnold@mathematik.uni-halle.de

Michael Beitelschmidt Institut für Bahnfahrzeuge und Bahntechnik, Technische Universität Dresden, Hettnerstraße 3, D-01062 Dresden, Germany, michael.beitelschmidt@tu-dresden.de

Iliya I. Blekhman Institute of Problems of Mechanical Engineering, Academy of Sciences of Russia and Mekhanobr, Tekhnika Corporation, St. Petersburg, Russia, blekhman@vibro.ipme.ru

F. Braghin Politecnico di Milano, Department of Mechanical Engineering, Via G. La Masa, 1, I-20156 Milano, Italy

S. Bruni Politecnico di Milano, Department of Mechanical Engineering, Via G. La Masa, 1, I-20156 Milano, Italy, stefano.bruni@polimi.it

Eric Cataldi-Spinola SBB Cargo, Officine Bellinzona, Bellinzona, Switzerland

Harry Dankowicz Department of Mechanical Science and Engineering, University of Illinois at Urbana Champaign, Urbana, 61801, Illinois, USA, danko@illinois.edu

Jürg Dual IMES – Center of Mechanics, ETH Zurich, Switzerland

Peter Eberhard Institute of Engineering and Computational Mechanics, University of Stuttgart, Pfaffenwaldring 9, D-70569 Stuttgart, Germany, eberhard@itm.uni-stuttgart.de

J.G. Giménez CAF and TECNUN (University of Navarra), Sebastian (Guipúzcoa), Spain, ggimenez@cat.net

Christoph Glocker IMES – Center of Mechanics, ETH Zurich, Switzerland, glocker@imes.mavt.ethz.ch

Jenny Jerrelind KTH Vehicle Dynamics, Centre for ECO2 Vehicle Design, Royal Institute of Technology, SE-10044 Stockholm, Sweden, jennyj@kth.se

Piotr Kowalczyk School of Mathematics, Alan Turing building, The University of Manchester, Oxford road, Manchester, M13 9PL, UK, piotr.kowalczyk@manchester.ac.uk

Laura Mazzola Politecnico di Milano, Department of Mechanical Engineering, Via G. La Masa, 1, I-20156 Milano, Italy, laura.mazzola@polimi.it

Jaap P. Meijaard Laboratory of Mechanical Automation and Mechatronics, Faculty of Engineering Technology, University of Twente, Enschede, The Netherlands, J.P.Meijaard@utwente.nl

Arne Nordmark Dept of Mechanics, KTH, SE-100 44 Stockholm, Sweden, nordmark@mech.kth.se

Anna Orlova NVC "Vagony", Moskovskiy prospect, 9, St. Petersburg, 190031 Russia, a-orlova@yandex.ru

Georg Peter Ostermeyer Institute of Dynamics and Vibrations, Technical University of Braunschweig, Schleinitzstr. 20, D – 38106 Braunschweig, Germany, gp.ostermeyer@tu-bs.de

Andreas Pfeiffer DLR Oberpfaffenhofen, Institute of Robotics and Mechatronics, D-82230 Wessling, Germany, Andreas.Pfeiffer@dlr.de

Jerzy Piotrowski Institute of Vehicles, Warsaw University of Technology, Narbutta 84, PL-02-524, Warsaw, Poland, jpt@simr.pw.edu.pl

Oldrich Polach Bombardier Transportation, Winterthur, Switzerland, oldrich.polach@ch.transport.bombardier.com

Volker Quarz Institut für Bahnfahrzeuge und Bahntechnik, Technische Universität Dresden, Hettnerstraße 3, D-01062 Dresden, Germany, volker.quarz@tu-dresden.de

Georg Rill University of Applied Sciences Regensburg, Galgenbergstr. 30, D-93053 Regensburg, Germany, georg.rill@maschinenbau.fh-regensburg.de

Rossano Stefanelli Kistler Instrumente AG, Winterthur, Switzerland

Gábor Stépán Department of Applied Mechanics, Budapest University of Technology and Economics, Budapest, Hungary; Hungarian Academy of Sciences, Research Group on Dynamics of Vehicles and Machines, Budapest, Hungary, stepan@mm.bme.hu

Dieter Stüwing Institut für Bahnfahrzeuge und Bahntechnik, Technische Universität Dresden, Hettnerstraße 3, D-01062 Dresden, Germany, dieter.stuwing@tu-dresden.de

Fredrik Svahn KTH Vehicle Dynamics, Royal Institute of Technology, SE-100 44 Stockholm, Sweden, fsvahn@kth.se

Dénes Takács Department of Applied Mechanics, Budapest University of Technology and Economics, Budapest, Hungary; Hungarian Academy of Sciences, Research Group on Dynamics of Vehicles and Machines, Budapest, Hungary, takacs@mm.bme.hu

Per Grove Thomsen DTU Informatics, The Technical University of Denmark, Kgs. Lyngby, Denmark, pgt@imm.dtu.dk

Hans True DTU Informatics, The Technical University of Denmark, Kgs. Lyngby, Denmark, ht@imm.dtu.dk

Krzysztof Zboiński Faculty of Transport, Warsaw University of Technology, Koszykowa 75, PL-00-662 Warsaw, Poland, kzb@it.pw.edu.pl

Pascal Ziegler Institute of Engineering and Computational Mechanics, University of Stuttgart, Pfaffenwaldring 9, D-70569 Stuttgart, Germany, ziegler@itm.uni-stuttgart.de

Part I
Problems in Vehicle Dynamics

Typical Non-smooth Elements in Vehicle Systems

Hans True

Abstract The vehicle systems are modelled mathematically as parameter dependent multi-body systems. The connections between the elements are formulated either as dynamical equations or algebraic, or transcendental or tabulated constraint relations. The connections can rarely be modelled by analytic functions, and the missing analyticity can arise from non-uniqueness or discontinuities in the functions themselves or in their derivatives of any order. In vehicle systems the contact between the vehicle and its support (road or rail) is an important source of missing analyticity. The suspension systems of the vehicles consist of passive and active elements such as springs, dampers and actuators, and their characteristics are only analytic functions within certain intervals of operation. Unilateral contacts in the suspension systems may give rise to changes of the degrees of freedom of the system during operation, and cause impacts or sliding contact during the operation.

1 General Vehicle Model

Figure 1 shows a typical 4-axle railway passenger car. The car body rests on two 2-axle carriages called bogies (bo^{u}gies) or in USA trucks. The entire suspension system is built into the bogies.

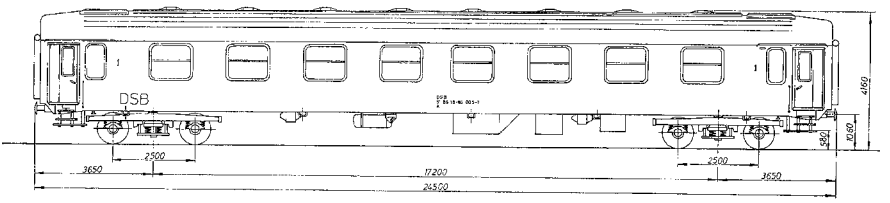

Fig. 1 A railway passenger car with a car body on two bogies

H. True (✉)
DTU Informatics, The Technical University of Denmark, Kgs.Lyngby, Denmark
e-mail: ht@imm.dtu.dk

P.G. Thomsen, H. True (eds.), *Non-smooth Problems in Vehicle Systems Dynamics*,
DOI 10.1007/978-3-642-01356-0_1,

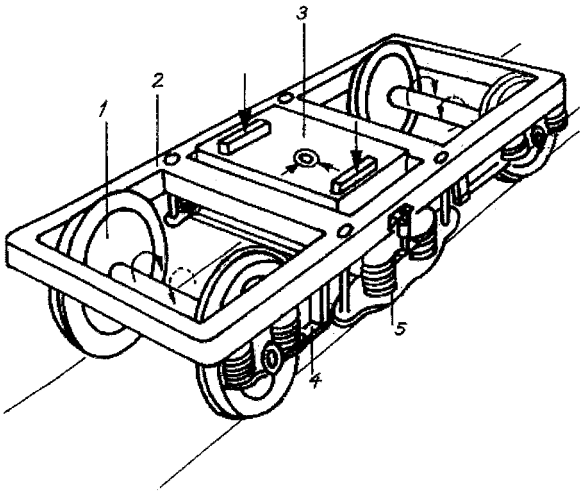

Fig. 2 Railway bogie. *1* Wheel set, *2* Bogie frame, *3* Bolster with pivot and side supports, *4* Wheel set guidance and primary suspension, *5* Secondary suspension in the bolster

Figure 2 shows an older bogie for a passenger car. The car body rests on the bolster (3) side supports and partly on the pivot, which gives the bolster three angular degrees of freedom with respect to the car body. The upper part of the bolster is supported on its lower part by two groups of springs and dampers (5). They comprise the secondary suspension. The lower part of the bolster is suspended in the bogie frame (2) by pendulums, so the upper part of the bolster has six degrees of freedom with respect to the bogie frame. The bogie frame rests on the axle boxes of the wheel sets (1) by means of four groups of springs and possibly dampers. They comprise the primary suspension, which gives the bogie frame six degrees of freedom with respect to each wheel set. For safety reasons the motions of the bogie frame and the car body must be restrained relatively to each other and to the wheel sets. These motion limiters create "non-smoothnesses". They are integral parts of all vehicles – also road and off-road vehicles.

Only railway passenger vehicles have both primary and secondary suspensions. Railway freight wagons have in general only one set of suspensions. In the next chapters we illustrate wagons without a bolster with a suspension between the car body and the wheel sets, which is common in Western, and Central Europe, and 4-axle freight wagons with the American 3-piece-freight truck, which has the suspension built into the bolster. Road and off-road vehicles generally have only one suspension system between the car body and the wheels since the rubber tires of the vehicles also act as effective springs and dampers in contrast to the rigid rail/wheel contact on the railways. Many trucks and most off-road vehicles have an effective suspension in the driver's seat for comfort and health protection.

Due to the greater complexity of the railway vehicle suspension systems we shall describe them in this article, but many of the elements or elements with similar functions are used in the automobile industry.

2 Rail/Wheel Contact

The rail/wheel rigid contact is a characteristic of railways. In order to provide a certain self-steering effect the wheels are generally rigidly connected with a rigid axle and are turned with a profile, which is tapered towards the field-side i.e., away from the track centre line. In order to prevent derailments the wheels have a flange on the other – the gauge-side. The rail profile is a rounded convex curve. The profiles of the new wheels and rails are well defined in international standards – either algebraically or in tables – but they change shapes through wear during their use. Figure 3 shows a typical set of new wheel and rail profiles.

The wheel/rail contact geometry is a very important parameter in railway vehicle dynamics since it determines the ideal point of attack of the rail forces on the wheel – *the contact point* – and the direction of their normal and tangent components in the contact point(s). The directions are defined through *the contact angle*, which is the common angle between the wheel set centre line and the wheel and rail profiles in the contact point. If multiple contact points exist, we handle each of them separately. Figure 4 shows the calculated lateral position of the contact point on the wheels and the corresponding contact angles versus the lateral displacement of the wheel set relative to the rail. It is interesting to see that these fundamental kinematic properties of rail/wheel interaction are *non-smooth functions*. Discontinuities of the functions or their derivatives of lower orders are seen.

The wheels and rails are, however, not ideally rigid bodies. They are flexible and deform under the load of the vehicle. Therefore the contact between the wheel and the rail is in reality spread out over a small *contact surface* and the non-smoothnesses may thereby be smoothened to some extent. They cannot, however,

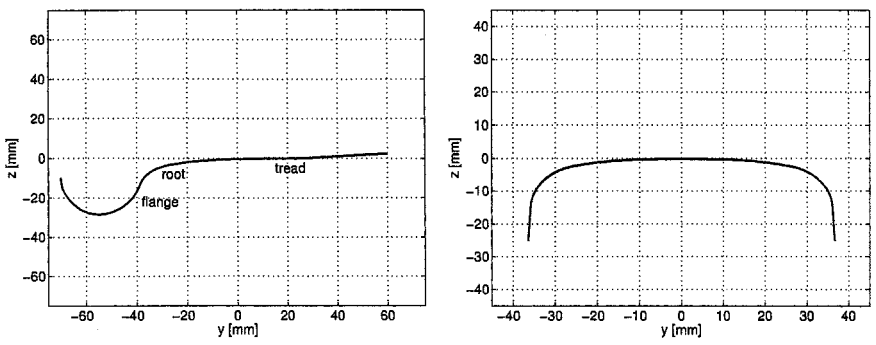

Fig. 3 S-1002 wheel profile (*left*) and UIC60 rail profile (*right*)

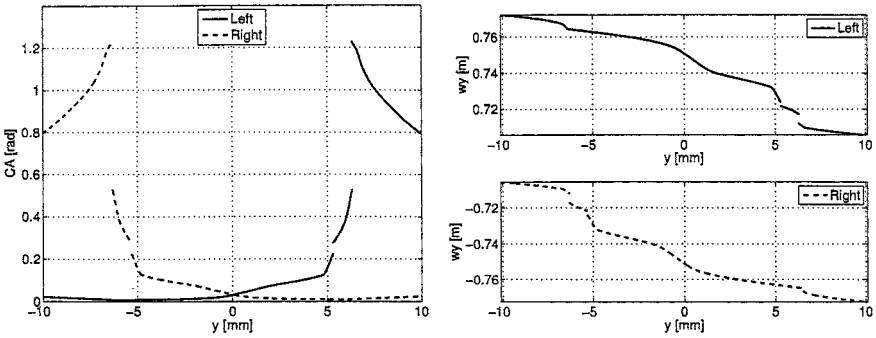

Fig. 4 The contact angle (*left*) and the lateral position of the contact point on the wheel (*right*) versus the relative lateral displacement of the wheel set for the profiles in Fig. 3

be neglected. Slivsgaard [3] found that when a certain laterally oscillating wheel set crossed a point of discontinuity in the curvature of the rail profile a small interval of speeds with chaotic motion developed due to the non-smoothness.

The shear force relation between the wheel and the rail has been treated in several papers. The most acknowledged relation was formulated by Kalker [1]. Due to the dry friction between the wheel and the rail, the two bodies stick to each other in a part of the contact surface and slide against each other in the other part. The resulting local deformations and the local sliding sums up to a finite sliding between the wheel and the rail, which is denoted *the creep*, and the resulting shear force, which is the sum of the shear stresses, is denoted *the creep force*. The creep-creep force relation has a discontinuity in the second derivative at zero creep.

3 Non-smooth Suspension Elements

In this chapter we show examples of common suspension elements with non-smooth characteristics. Figure 5 shows a coil spring with an additional stiff rubber spring inside to prevent the coil spring from collapsing under large loads. The characteristic of these combined springs is linear under small deformations. When the rubber spring is activated by a sufficiently large deformation of the coil spring, the characteristic of the assembly has a discontinuity in the first derivative, and the characteristic becomes nonlinearly concave for larger deformations. The characteristics of the hydraulic dampers that are used in automobiles and in almost all railway passenger vehicles have discontinuities in the second order derivative.

Dry friction damping dominates the freight wagon designs and we now show some examples.

Figure 6 shows an example of the most common freight wagon bogies used in Western and Central Europe. Note, please, that the bogie has only a primary

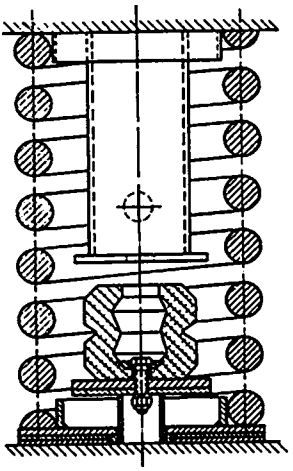

Fig. 5 A two-stage vertical spring consisting of a steel coil spring and a harder rubber spring

suspension system consisting of springs and so-called Lenoir dampers. The Lenoir dampers act on one side of the axle box of each wheel, and they are situated as shown on Fig. 7. The springs between the bogie frame and the car body shown on Fig. 7 is a simple secondary suspension that mainly serves to reduce the rolling motion of the car body.

The action of the Lenoir damper is illustrated on Fig. 8. When the spring is loaded, the link directs a part of the load in a horizontal direction, thereby forcing the "hat" above it to press against the small piston, which acts on a vertical friction surface on the axle box. The two dimensional dry friction with stick/slip provides the damping of the lateral and vertical motion between the axle box and the bogie frame.

The American 3-piece-freight truck and its variants are commonly used all over the world except in Western and Central Europe, where they are very rare. Figure 9 illustrates the simple design of the American 3-piece-freight truck, which is also called "the Barber truck".

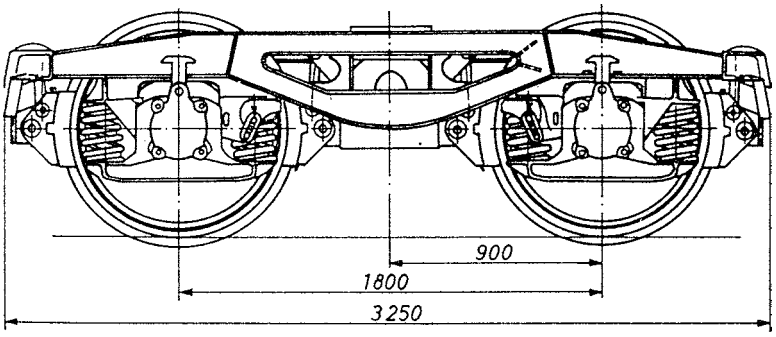

Fig. 6 Y25c freight wagon bogie

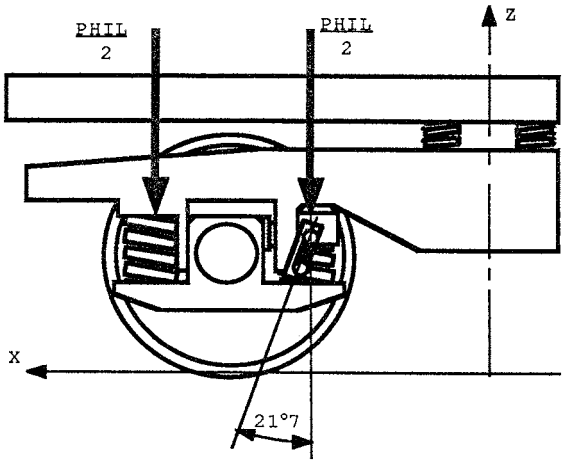

Fig. 7 The position of the Lenoir damper on the *left wheel* shown on Fig. 6. The inclined link is bolted to the bogie frame at its lower end

The three pieces of the bogie are the bolster and the two side frames. The car body rests on the bolster on a centre plate. The bolster has two side supports to limit the roll motion between the car body and the bolster, see Fig. 10.

The bolster is supported on each side frame by a group of springs, which can deflect in the horizontal plane as well as in the vertical direction. Spring loaded friction wedges are inserted between the bolster and the side frame to damp the

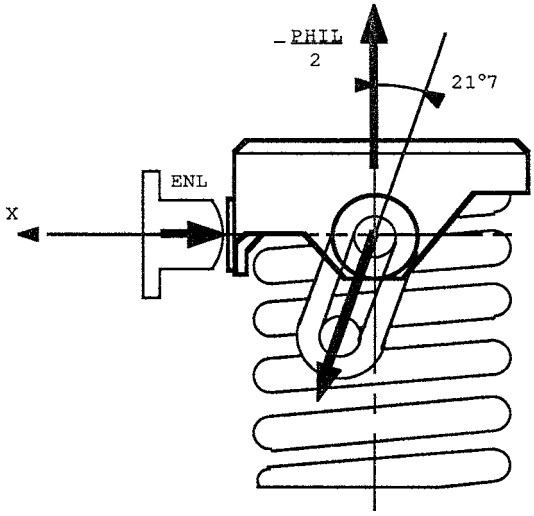

Fig. 8 The Lenoir damper. The piston touches the axle box so the dry friction force in the contact surface creates a load dependent damping of the relative vertical and lateral motion between the axle box and the bogie frame

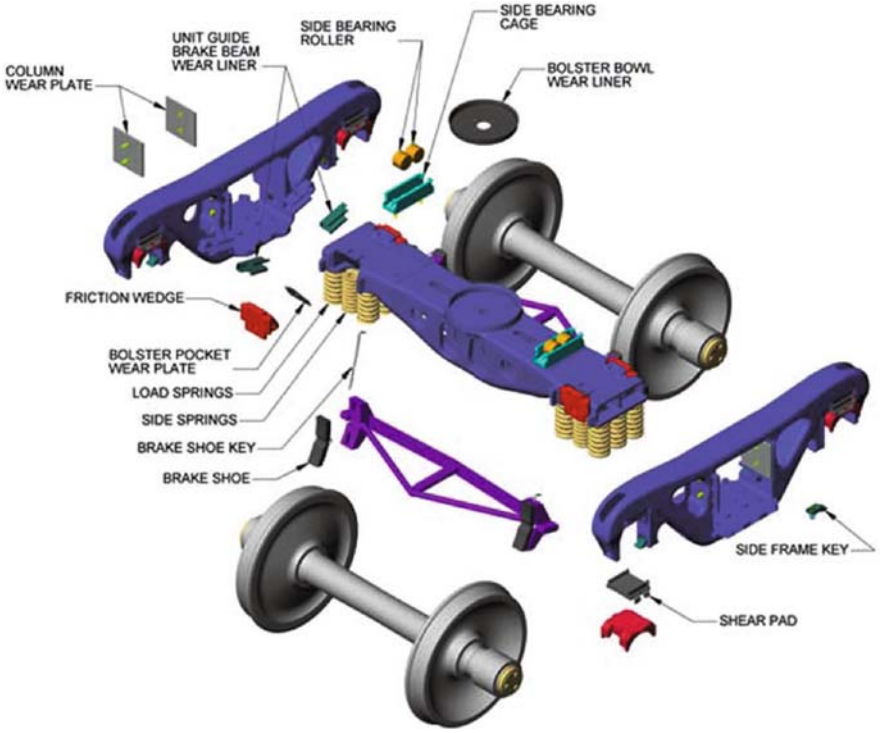

Fig. 9 An American 3-piece-freight truck (bogie)

relative lateral and vertical motion between the bolster and the side frame through dry friction with stick/slip see Fig. 11.

The side frames are supported on the axle boxes by adapters, which can move longitudinally on the side frame in order to provide the wheel sets with a yaw degree of freedom, which is damped by dry friction, see Fig. 12.

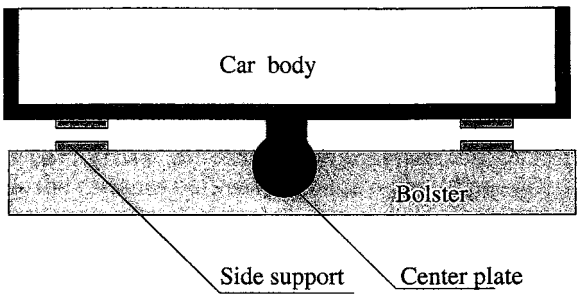

Fig. 10 The connection between the car body and the bolster. The contact surfaces are dry friction surfaces

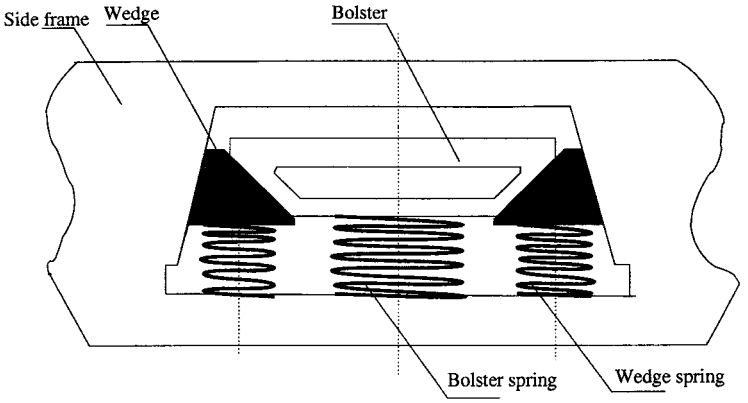

Fig. 11 Detail of the suspension with vertical and lateral dry friction damping between the wedges and the bolster and the side frame

All the damping in the American 3-piece-freight truck is thus dry friction damping between plane metal surfaces with stick/slip. The maximum "stick force" varies from a few percent of and above the sliding force between the elements, to around 50%. The percentage depends on pollution, weather and wear of the surfaces.

The last example of non-smooth suspension systems is of a UIC link suspension, which is the standard suspension on European 2-axle railway freight wagons. See Fig. 13.

The car body (1) is supported by the leaf spring (5) on which it is suspended by a pendular double link suspension (2) (3). The leaf spring rests on the axle box (6), which can move freely within narrow limits bounded by the wheel set guidance (4).

The free motion of the wheel set in the horizontal direction is shown in detail and explained on Fig. 14. The possible impacts between the axle box and the guidance introduce non-smoothnesses in the dynamical model.

On modern freight wagons the leaf spring is most often substituted by a parabolic leaf spring shown on Fig. 15. Under deflection of the spring the dry friction contact forces between the leaves provide the desired damping of the motion.

A cycle of loading and unloading therefore creates a hysteresis loop in the plot of the restoring force versus the deflection. It means that the curve of the loading characteristics is not uniquely determined as a function of the deflection. When the

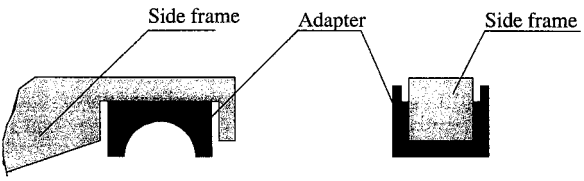

Fig. 12 The dry friction contact between the adapters and the side frames with longitudinal end stops

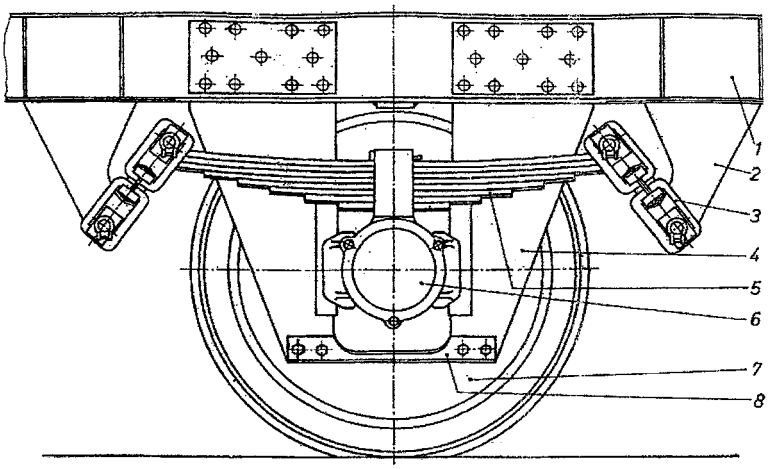

Fig. 13 The UIC standard suspension of a two-axle freight wagon. *1* Car body, *2* Suspension Bracket, *3* UIC links, *4* Wheel set guidance, *5* Leaf spring, *6* Axle box, *7* Wheel set, *8* Connecting bar

deflection of the spring is sufficiently large, the extra leaf in the spring becomes active and increases the stiffness of the spring. Thereby a jump of the first derivative of the characteristics is introduced.

The double link shown on Fig. 16 is a complicated element, which is designed to provide restoring forces through the pendular action in as well the longitudinal as the lateral direction together with damping of these motions through dry friction contact forces in the bearings of the pendulums.

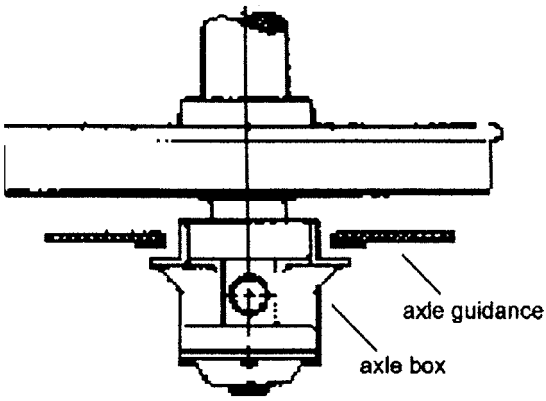

Fig. 14 Top view of the axle guidance with the gap between the axle box and the guidance. Under impact in the lateral direction the guidance act as a spring, in the longitudinal direction the guidance acts as a rigid body

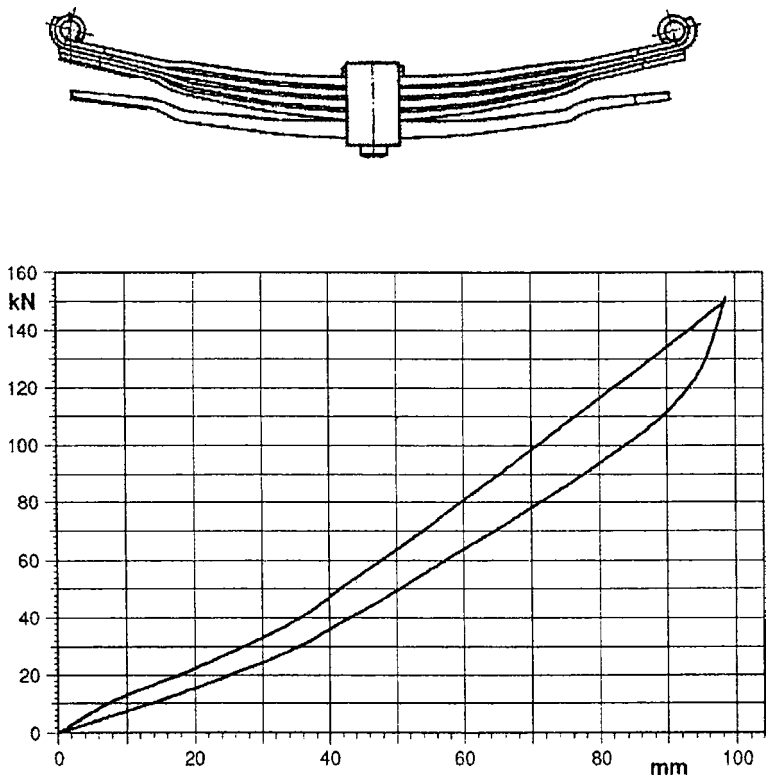

Fig. 15 Two-stage parabolic leaf spring with an example of the loading characteristics with hysteresis and the increase in stiffness when the lower leaf becomes active

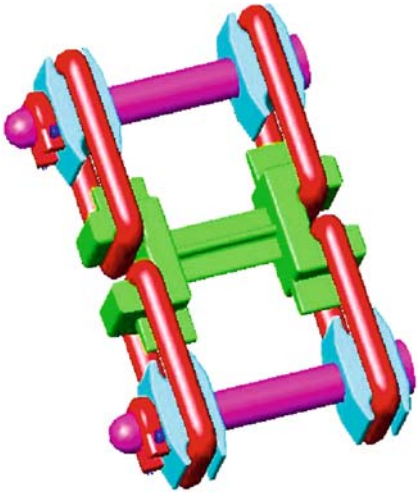

Fig. 16 UIC double link suspension. The double links move together around the *upper and lower bolts* in the longitudinal direction and separately around the eight hinge joints in the lateral direction

Under longitudinal loading the double links will move together and turn around the upper and lower bolts. Under lateral loading the double links are supposed to move together. If the deflection becomes sufficiently large, the lower link will hit the suspension bracket (2) in Fig. 13, whereby the length of the pendulum is halved, and the restoring force of the link is doubled. The actual motion of the links depends on the friction forces in the curved contact surfaces. These friction forces depend strongly on the mechanical properties of the contact surfaces, whether they are new or worn or polluted by humidity (water or oil or dust). Like in the case with the leaf spring, hysteresis effects and non-smoothnesses are introduced. The modelling of the action of the double link is therefore very complicated. A useful mathematical model of the action of the UIC standard link suspension was formulated by Piotrowski [2]. The parameters that are used must be measured in the laboratory.

4 Motorized Vehicles

Motorized vehicles have transmissions that connect the motor with the driven axle(s). Transmissions with mechanical gears are very common in road vehicles as well as in railway vehicles. Tooth backlash clearances in the gears introduce discontinuities in the mathematical model of the transmissions. The phenomenon is only mentioned here for the sake of completeness since it is the topic of the chapter by Ziegler and Eberhard in this book.

5 Discussion

The non-smoothnesses in vehicle constructions must of course be taken into account and be carefully modelled in the dynamical systems of vehicle dynamics. The non-smoothnesses in the dynamical systems are sources of bifurcations that do not exist in smooth systems – a grazing bifurcation is an example – or they may modify the structure of the classical bifurcations in smooth systems, True [4]. Slivsgaard [3] presents an example. The new bifurcations may change the dynamics of a vehicle quite drastically in certain parameter intervals.

The numerical solver must be chosen with respect to the non-smooth character of the dynamical problem in order to ensure reliability and robustness of the results of the numerical calculations. Special attention must be paid to the parameters of the solver such as time steps and error bounds, because the default values do not guarantee reliable results. The time integration must often be split up in intervals in which the dynamical problem is sufficiently smooth, or other measures must be specially introduced in order to obtain accurate results.

The following chapters in this book are devoted to the particular dynamical and numerical problems that arise in non-smooth dynamical systems and how to handle these problems in order to achieve reliable theoretical results.

References

1. J. J. Kalker. Wheel-rail rolling contact theory, pages 243–261. Mechanics and Fatigue in Wheel/Rail Contact, Proceedings of the Third International Conference on Contact Mechanics and Wear of Rail/Wheel Systems. Elsevier, Amsterdam, New York, Oxford, Tokyo, 1991.
2. J. Piotrowski. Model of the UIC link Suspension for Freight Wagons. *Archive of Applied Mechanics*, 73: 517–532, 2003.
3. E. C. Slivsgaard. Bifurkationer og Kaos i en ikke-lineær model af et enkelt jernbanehjulsæt (in Danish). Masters Thesis, LAMF, The Technical University of Denmark, 1992.
4. H. True. On a new phenomenon in bifurcations of periodic orbits, pages 327–331. Dynamics, Bifurcation and Symmetry, New Trends and New Tools. NATO ASI Series. Kluwer Academic Publishers, P.O. Box 322, NL-3300 AH Dordrecht, The Netherlands, 1994.

Application of Nonlinear Stability Analysis in Railway Vehicle Industry

Oldrich Polach

Abstract This paper deals with the use of nonlinear calculations and bifurcation analysis when investigating running stability during vehicle design and development in the rolling stock industry. Typical methods used for stability analysis in industrial applications are introduced, computation of bifurcation diagram presented and the influence of nonlinearities of the vehicle/track system on the type of Hopf bifurcation investigated. The relationship between the bifurcation diagram and the assessment of safety risk and the dynamic behaviour is discussed.

1 Introduction

A self-excited, sustained oscillation of wheelsets with conventional solid axles is a classic problem of railway vehicle dynamics. It is called hunting or instability by railway engineers. The frequency of such waving motion of wheelsets and bogies is related to the wheel/rail contact geometry. Equivalent conicity is applied as a simplified parameter in order to describe the wheel/rail contact geometry in railway practice. The equivalent conicity can vary to a large degree and therefore plays a significant role in the stability assessment of railway vehicles.

If the wheel/rail contact conditions lead to a bogie motion with a low frequency, approaching the vehicle carbody natural frequency, the possibility of considerable interaction may arise, leading to a limit cycle oscillation during which the amplitude of the car body is large relative to that of the wheelsets. In this case we refer to carbody instability (primary instability) or carbody hunting. If only the wheelsets and bogies or running gears are involved in the limit cycle oscillation, we refer to bogie instability (secondary instability) or bogie hunting. In modern vehicles carbody instability leads to a deterioration of lateral running behaviour, as well as ride comfort degradation without exceeding the safety criteria. A wheel/rail contact geometry characterized by high conicity typically limits the maximum permissible speed with respect to bogie hunting, i.e., running safety.

O. Polach (✉)
Bombardier Transportation, Winterthur, Switzerland
e-mail: oldrich.polach@ch.transport.bombardier.com

P.G. Thomsen, H. True (eds.), *Non-smooth Problems in Vehicle Systems Dynamics*,
DOI 10.1007/978-3-642-01356-0_2,

The necessity of stability investigations was only slowly recognized during the mid-twentieth century. A theoretical comprehension of railway vehicle stability came into being as a result of studies on linearised models; see e.g., [1] for details. At a later date, nonlinearities of the wheel/rail combination were also taken into consideration, see [2, 3] for further references.

The publications dealing with nonlinear stability assessment of railway vehicles often apply simplified models, conical or theoretical wheel profiles and theoretical rail profiles. No systematic study about the influence of nonlinearities on the stability and bifurcation behaviour of large vehicle models has been published yet. Considering complex systems of the vehicle/track and a large variation of wheel/rail contact geometries and friction conditions in railway service, the question appears how far are the conclusions from the published investigations valid for the industrial applications?

This article deals with use of nonlinear calculations and bifurcation analysis when investigating running stability during vehicle design and development in the rolling stock industry. It is organised as follows. Methods typically used for stability analysis in industrial application are introduced in Chap. 2. In Chap. 3, the bifurcation analysis is presented and the impact of the nonlinearities of the vehicle/track system on the bifurcation diagram explained. Chapter 4 discusses the relationship between the bifurcation diagram and the assessment of safety risk and the vehicle's dynamic behaviour.

2 Assessment of the Running Stability in Railway Industry

Stability analysis constitutes the most diversified part of vehicle dynamics due to the various possible methods, the wide range of input conditions and different assessment criteria. In spite of the vehicle/track system being always nonlinear, both nonlinear as well as linear calculations are applied for the stability assessment. In the linearized stability assessment, the contact of the wheelset and track is linearized differently to the other coupling elements. The quasi-linearization of wheel/rail contact, in which linearized wheel/rail parameters are computed for the specified wheelset lateral movement amplitude, is the standard method implemented in simulation tools used in railway vehicle engineering. Comparison of linearized and nonlinear stability assessment has been presented by the author in [4].

The nonlinear methods of stability assessment using computer simulations have been compared and discussed by the author in [3]. These can be classified depending on the track alignment used of:

- ideal track (no irregularity)
- real track with track irregularity (measured irregularities)
- combination of track disturbance followed by a section of ideal track, whereby the track disturbance can be represented by
  - single lateral disturbance
  - track section with irregularity.

Another classification can be introduced in relation to the assessment criteria of:

- decay of oscillations
- limit values specified for testing for the acceptance of running characteristics of railway vehicles in EN 14363 [5].

A lateral displacement of wheelsets is usually used to prove the decay of self-excited oscillations of a railway vehicle. Displacements of other bodies (bogie frame, carbody) can gain additional information to distinguish between the hunting of bogie or carbody.

The criteria used during the testing of vehicles for the acceptance of running characteristics are:

- forces between wheelset and track (sliding rms-value of sum of guiding forces) as specified for normal measuring method according to EN 14363 [5]
- lateral acceleration on the bogie frame (sliding rms-value) as specified for simplified measuring method according to EN 14363 [5].

There are pros and cons for all methods mentioned. The three most used methods are illustrated by examples of safety assessment, considering wheel/rail friction coefficient of 0.4 and a high equivalent conicity of 0.6 for the wheelset amplitude of 3 mm.

Method 1: Figure 1 shows the wheelsets lateral displacement as a result of simulation on ideal track, starting from a limit cycle at high speed and reducing the speed slowly. The speed at which the oscillation disappears is then the nonlinear critical speed [6].

Method 2: Figure 2 shows simulations of the reaction to a single lateral disturbance with amplitude of 8 mm and a span of 10 m, followed by an ideal track, for the variation of vehicle speed.

Method 3: Figure 3 presents simulations of a run on track with measured irregularities and analyses of the criteria according to EN 14363 for wheel/rail contact geometry A.

While the first method allows an unambiguous assessment of critical speed, it is rather rarely used as it requires a long simulation time. The second method is often

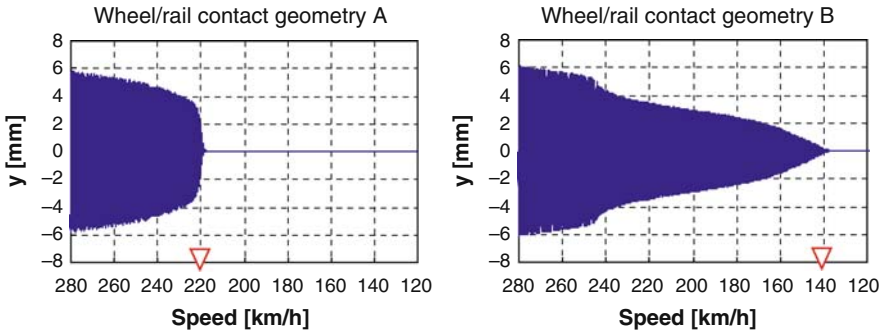

Fig. 1 Simulations of run on ideal track with speed decreasing by 4 km/h during one second

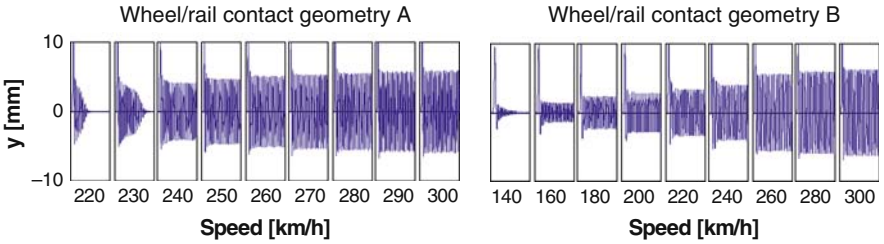

Fig. 2 Simulations of wheelset reaction on a single lateral excitation on ideal track

used because of simple handling and short simulation times. Likewise, the third method is often applied because of the easy possibility of comparison with vehicle test results.

The examples in Fig. 1 demonstrate different critical speeds and different behaviour for the same vehicle with the same equivalent conicity for the wheelset amplitude of 3 mm as specified for vehicle acceptance tests [5]. There is abrupt wheelset stabilization in the first example, whereas in the second example the amplitude of the limit cycle slowly reduces with decreasing speed.

Differing behaviour can be observed also in the examples in Fig. 2. The differences result from the nonlinearities of the investigated system. A prominent feature of nonlinear dynamical systems is the possible dependence of their long-time behaviour on the initial conditions, leading to the existence of multiple solutions.

The methods discussed so far can however only identify one solution. Furthermore, differing procedures and criteria for the stability assessment in railway applications can lead to different conclusions, because a limit cycle oscillation with a rather small amplitude will not necessarily lead to exceedance of the stability limit during vehicle testing. This can be seen in Fig. 4 on the analysis of the vehicle behaviour on an ideal smooth track behind a single disturbance. An assessment of nonlinear dynamical systems with respect to the influence of one or more system parameters on existence of multiple solutions can be carried out by bifurcation analysis, which will be discussed in the next chapter.

3 Bifurcation Analysis of the System Vehicle/Track

The usual way to present the bifurcation phenomenon is a bifurcation diagram [2]. When analysing the stability of railway vehicles, the bifurcation diagram displays the amplitude of the limit cycle (typically lateral wheelset displacement) as a function of speed. For some systems, the bifurcation diagram can be very complex including quasi-periodic or chaotic motion. Considering the main shape of the diagram, we can distinguish between the subcritical and supercritical Hopf bifurcation; see Fig. 5 [2, 3]. In case of subcritical bifurcation there is a speed range at which the solution can “jump” between a stable damped movement and a limit cycle depending on the excitation amplitude.

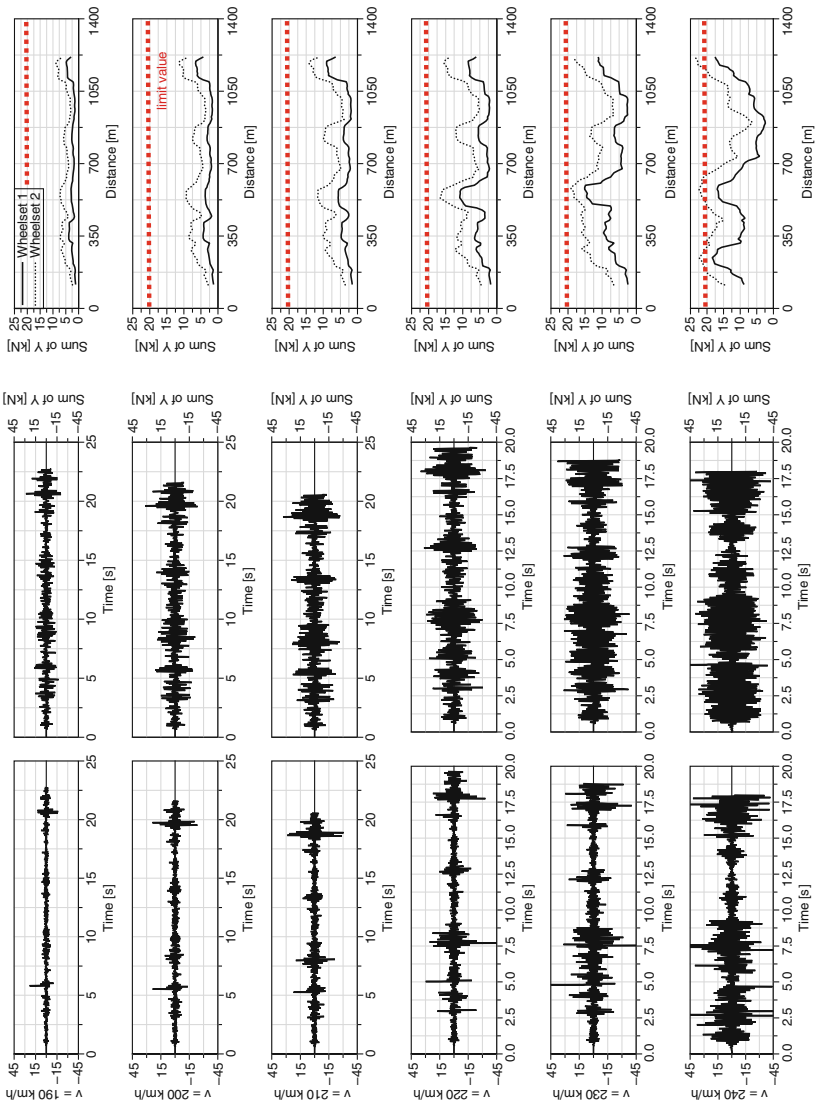

Fig. 3 Stability assessment based on simulations of vehicle acceptance tests

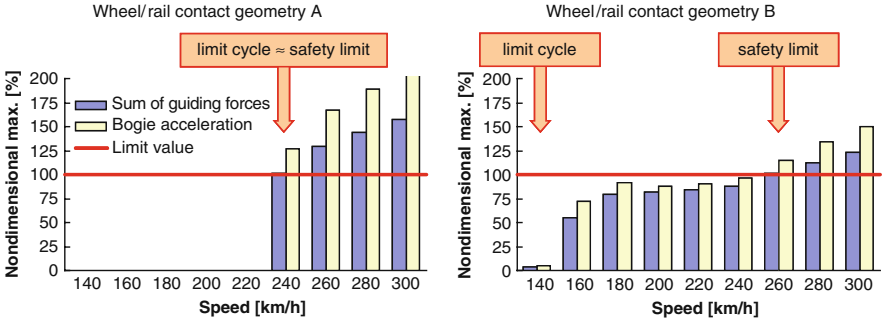

Fig. 4 Comparison of stability assessment based on the occurrence of a limit cycle and the assessment according to the safety limits specified for measurements in EN 14363 [5]

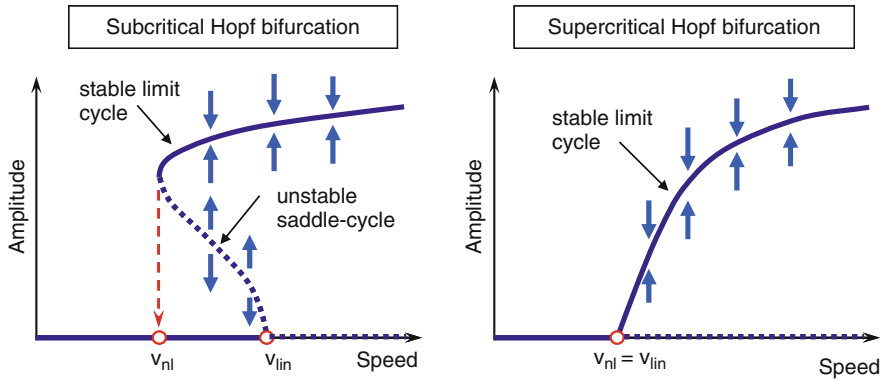

Fig. 5 Bifurcation diagram with subcritical and supercritical Hopf bifurcation; rows show the feedback of the nonlinear system

The calculation of the bifurcation diagram can proceed by a path following method (continuation) or by a set of numerical simulations. A software tool PATH for the continuation-based bifurcation analysis has been developed at the Technical University of Denmark [7]. It uses a mixture of integration in time and Newton iteration to find the periodic solutions. The code starts with the trivial solution that is known to be asymptotically stable at sufficiently low speed. The speed is then increased in small steps and the solution is followed for each value of the speed. When a bifurcation point is reached, the path to be followed is chosen in the phase-parameter space.

The integration of the software tool PATH with commercial MBS-software SIMPACK has been developed and described by Schupp [8]. However, this tool is not commercially available as a part of SIMPACK software package yet. Furthermore, the method is not straight forward. As stated in [8], external time integration is required to generate an initial estimation, because it is not possible to continue the unstable periodic solutions branching off from the Hopf bifurcation of the first branch.

Stichel [9] uses a rather straight forward method applying numerical simulation. A run over an initial lateral disturbance is simulated at a rather high speed. The simulation continues on undisturbed track until the oscillation of the vehicle has reached constant amplitude. The vehicle speed is reduced and a new simulation started with initial values from the previous simulation. This is repeated until the oscillating solution disappears.

A set of numerical simulations is also applied in the investigations presented in this article. A run over a single lateral disturbance with a span of 10 m is simulated and the amplitude of the limit cycle after a few seconds, behind the transition process, taken in the bifurcation diagram. This is repeated for a set of speeds including those leading to limit cycle oscillations. As first, a large disturbance with an amplitude of 8 mm was used to identify nonlinear critical speed. Then, a set of simulations with speed variation is repeated applying a small disturbance with 0.5 mm amplitude. If the solution without oscillations appears for speeds higher than the nonlinear critical speed, a set of simulations with amplitude variation is started, to identify the amplitude for which the stable solution without oscillation changes to a limit cycle. This value is then taken as a point of the unstable branch for the considered speed in the bifurcation diagram.

To study the impact of the nonlinearities and non-smoothness of the system vehicle/track, we will distinguish between:

- nonlinearity and non-smoothness of wheel-rail contact
- nonlinearity and non-smoothness of vehicle model itself.

The effects of these two groups of nonlinearities on the shape of bifurcation diagram will be investigated in the following subchapters.

3.1 Wheel-Rail Contact Nonlinearity

The influence of wheel/rail contact nonlinearity on railway vehicle behaviour at the stability limit can be seen in Fig. 6. The simulations were carried out with a multi-body model of a four-car articulated vehicle in simulation tool SIMPACK. The model consists of 124 bodies and possesses 201 degrees of freedom (DOF). The diagrams display the results of the second wheelset of the leading bogie, where the limit cycle was first observed.

From the presented example as well as from the author's other studies, it can be observed, that the influence of the wheel/rail contact nonlinearity can be assessed with the help of the contact geometry functions used for the linearization of wheel/rail contact:

- Difference of rolling radii Δr of the left and right wheel in function of the wheelset lateral displacement
- Equivalent conicity λ in function of wheelset displacement amplitude.

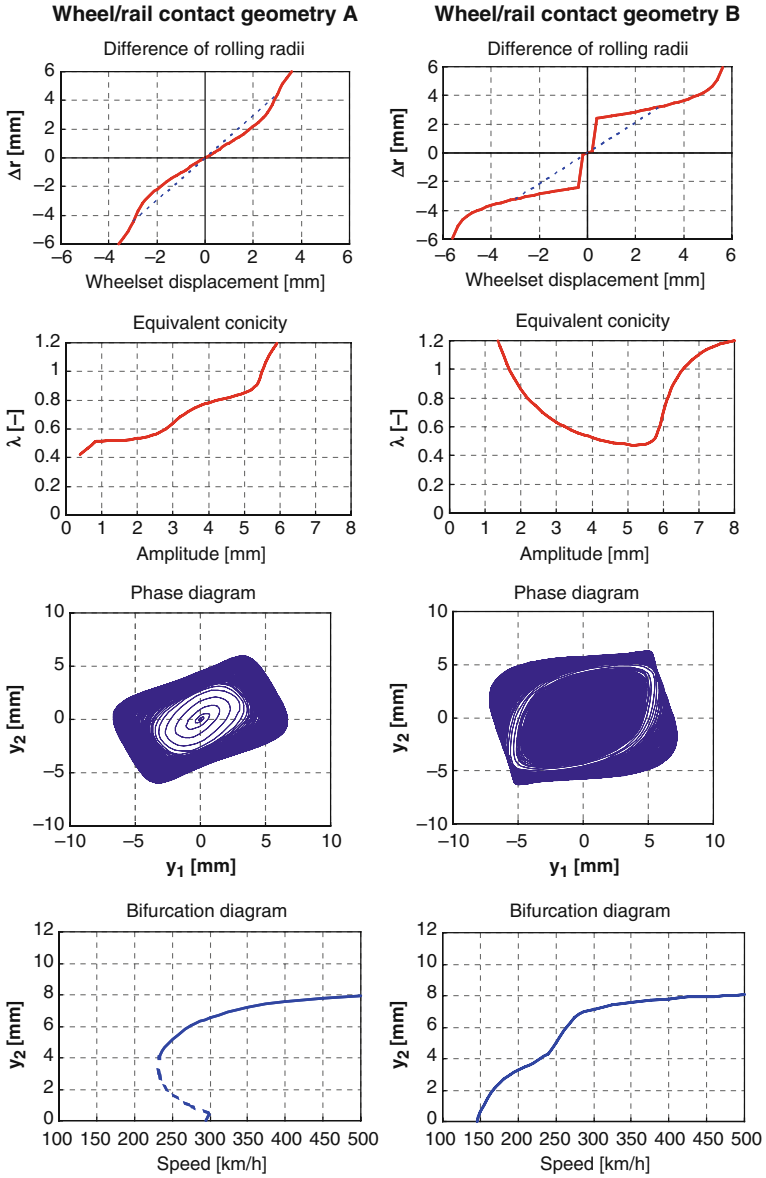

Fig. 6 Influence of wheel/rail contact nonlinearity on the behaviour of a railway vehicle at the stability limit on the example of two contact geometries with the same equivalent conicity for the wheelset amplitude of 3 mm

Both examples in Fig. 6 represent the same equivalent conicity for the amplitude of 3 mm. For the contact geometry A, there is a progressive increase of rolling radii difference in function of wheelset displacement and progressive equivalent conicity in function of wheelset amplitude. Abrupt limit cycle decay can be observed on the phase diagram of displacements of wheelset 1 and 2. There is a subcritical Hopf bifurcation in the bifurcation diagram of the wheelset 2. In contrast, for the contact geometry B there is strongly declining function of rolling radii difference and also strongly declining equivalent conicity function for amplitudes up to 4 mm (i.e., in the tread area away from flange contact) due to large movement of the contact area for the wheelset displacement between 0 and 1 mm. A slow decrease of oscillations and a supercritical Hopf bifurcation can be observed for this wheel/rail contact geometry.

The different behaviour of railway vehicles on the contact geometry with the equivalent conicity function of "Type A" and "Type B" has been described for the first time in [10] and outlined more in detail in [3]. The nonlinearity of the contact geometry often determines the type of the Hopf bifurcation of railway vehicles. It contradicts the repeatedly presented statement that the bifurcation analysis of a railway vehicle always or mostly leads to the subcritical Hopf bifurcation, with the nonlinear critical speed lower than linear critical speed. In fact, the supercritical Hopf bifurcation can also occur with railway vehicles, and probably more frequently than supposed until now. This is because the contact geometry of "Type A" is related to a conical wheel profile which is the profile mostly used in theoretical studies. The change of the contact geometry due to wheel wear often leads to more conformal tread contact characterized by contact geometry of "Type B", leading to the supercritical Hopf bifurcation with the nonlinear critical speed equal to the linear critical speed.

The nonlinear critical speed increases with reduction of wheel/rail friction coefficient, whereby the linear critical speed remains the same [3]. The subcritical Hopf bifurcation is less pronounced and can change to supercritical Hopf bifurcation for very low friction coefficients.

The described effects of wheel/rail contact conditions on bifurcation behaviour can be summarized as follows. The equivalent conicity value for the 3 mm amplitude characterizes the conicity level; a higher conicity leads to lower linear critical speed and vice versa. The slope of the equivalent conicity as a function of wheelset amplitude influences the type of Hopf bifurcation; a strongly decreasing conicity function for small amplitudes encourages supercritical Hopf bifurcation and vice versa. Similarly, the slope of creep force function influences linear critical speed, whereas the wheel/rail friction coefficient influences the form of Hopf bifurcation.

3.2 Nonlinearities of Vehicle Model

The nonlinearity of a vehicle model can supersede the effect of wheel/rail contact and change the type of Hopf bifurcation. Figure 7 shows as example the influence

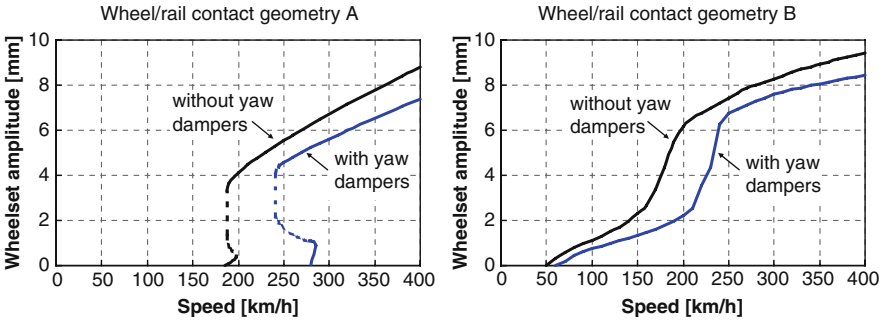

Fig. 7 Bifurcation diagrams of a double-decker coach for two different wheel/rail contact geometries with the same equivalent conicity for the wheelset amplitude of 3 mm

of nonlinear characteristic of yaw dampers on the bifurcation diagram of a double-decker coach with 39 bodies and 73 DOF, build in simulation tool SIMPACK. The nonlinearity of wheel/rail contact is still dominant, however, the implementation of yaw dampers with nonlinear characteristics leads to a change of the Hopf bifurcation for the wheel/rail contact geometry "Type A" in the left diagram. In contrast, on the right diagram (contact geometry "Type B") there is always a supercritical Hopf bifurcation. Introducing the yaw dampers, oscillations with large amplitudes are suppressed into higher speeds, whereas small amplitudes below 2 mm remain present already for low speed.

Figure 8 shows as example the influence of nonlinear, non-smooth characteristic of yaw dampers on the bifurcation diagram of the same vehicle and the wheel/rail contact geometry A. The damping force of yaw dampers is nonlinear due to a strong slope reduction at the blow-off force. The yaw damper characteristic No. 3 in Fig. 8 assumes a negligible force for a very small piston velocity, caused e.g., by a piston leakage. The variation of the blow-off force and the non-smooth characteristic of yaw damper, results to a change of Hopf bifurcation and to the variation of critical speed between 200 and 280 km/h.

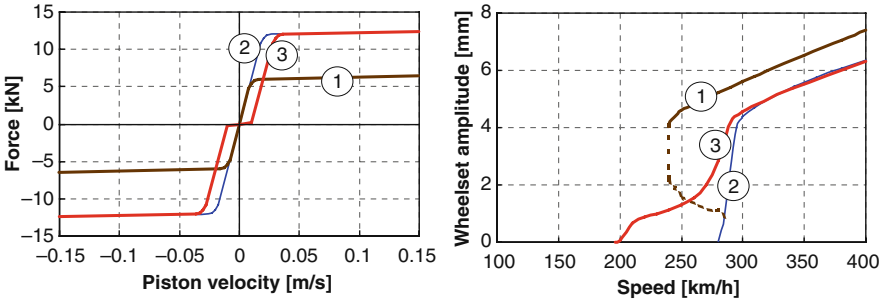

Fig. 8 Influence of yaw damper characteristic (*left diagram*) on the bifurcation (*right diagram*)

4 Discussion

The presented results demonstrate that the bifurcation analysis of a railway vehicle can lead to subcritical as well as supercritical Hopf bifurcation; the type of Hopf bifurcation is determined by the nonlinearities in the vehicle/track system, whereby the wheel/rail contact geometry has a significant influence on the vehicle behaviour at the stability limit. Can the bifurcation analysis enhance the nonlinear stability assessment in railway vehicle industry?

A detailed analysis of the bifurcation diagram for speeds far over the nonlinear critical speed can be very interesting from the theoretical point of view, however less important for industrial applications. Wheelset oscillation with a very small amplitude, say less than 1 mm would probably be overlooked during the tests due to real track irregularities, unless this oscillation is coupled with larger movements of other bodies. A very small variation in periodicity leading to a quasi-periodic or chaotic motion observed as a result of nonlinear investigations can often be more related to a particular modeling of wheel/rail contact than to real behaviour observed in service. The nonlinearity or non-smoothness is often "smoothed" in the reality as described by Piotrowski [11] on example of friction element. Detailed studies about very small deviations at particular conditions will therefore hardly enhance the stability assessment in railway industry.

For the assessment of running stability in the rolling stock industry, the main properties at various realistic conditions are of interest. From this point of view, significant differences can be observed between a system demonstrating the subcritical Hopf bifurcation and a system showing the supercritical one. What is the relationship between the bifurcation diagram and the vehicle behaviour at the stability limit? This relation is shown in Fig. 9. A vehicle/track systems showing a subcritical Hopf bifurcation usually reaches the nonlinear critical speed and the safety limits at the

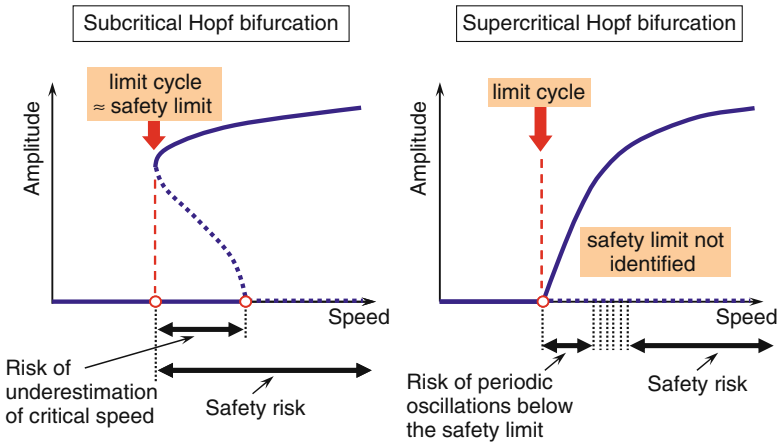

Fig. 9 Bifurcation diagram and assessment of safety and oscillation behaviour

same or similar speed. The stability assessment of such system can, however, lead to an underestimation of both criteria if the stability has been assessed by simulation applying too small disturbance or too small track irregularities. The system showing a supercritical bifurcation possesses nonlinear critical speed which is lower than the speed at which the safety limits are reached. The assessment of such system applying bifurcation analysis can deliver low critical speeds with criteria below the safety limits specified for vehicle acceptance. For a safety assessment of such system, other methods than bifurcation diagram of wheelset displacement are required, e.g., simulation of run on measured track irregularities. An exploitation of speeds higher than the nonlinear critical speed would however lead to sustaining oscillation. Even if the amplitude of this oscillation would be small, it could lead to fatigue damage and comfort deterioration.

The range of speeds between the nonlinear critical speed and the speed at which the safety limits are achieved should therefore be assessed using other kind of analysis regarding the fatigue and passenger comfort.

The bifurcation analysis allows assessing the influence of the level of track disturbance on the stability assessment and gaining a valuable output regarding the vehicle behaviour at the stability limit. It is, however, time consuming and rarely used in railway applications. Because of large variation of service conditions and parameters, a large set of investigations for different conditions is required during vehicle design in the rolling stock industry. The industry would require a robust procedure, which could be less exact, but allow a fast computation of bifurcation diagrams using a complex, realistic multi-body vehicle models for a set of different conditions wheelset/track and vehicle parameters, i.e., which allows a “rough and robust” assessment for a large set of input parameters.

5 Summary and Conclusion

The paper presents typical methods used for stability analysis in the railway vehicle industry and shows that they can lead to differing critical speeds because of: deviating computation procedures, wide possible range of input conditions, and differing assessment criteria.

The bifurcation diagram computation is explained and the influence of nonlinearities of the wheel/rail contact and of the vehicle model on the type of Hopf bifurcation shown. The presented examples demonstrate in contradiction to several other publications that the bifurcation analysis of a railway vehicle can lead not only to subcritical but also to supercritical Hopf bifurcation.

The stability assessment can overestimate the critical speed of a vehicle/track system, demonstrating subcritical Hopf bifurcation if the applied disturbance is too low. Contrary, it can deliver critical speeds below the safety limits for a vehicle/track system showing supercritical Hopf bifurcation.

An application of bifurcation analysis in vehicle design and development could enhance the nonlinear stability assessment of railway vehicles. However, an efficient

use of bifurcation analysis in industry is not possible today. Fast and robust algorithms or procedures applicable with commercial simulation tools would be required to allow an introduction of this method to rolling stock design and development.

References

1. Wickens A H (2006) A history of railway vehicle dynamics. In: Iwnicki S (ed) Handbook of railway vehicle dynamics. CRC Taylor&Francis, Boca Raton, London, New York, pp. 5–38
2. True H (1999) On the theory of nonlinear dynamics and its application in vehicle systems dynamics. Vehicle System Dynamics 31:393–421
3. Polach O (2006) On non-linear methods of bogie stability assessment using computer simulations. Proceedings of the Institution of Mechanical Engineers, Part F, Journal of Rail and Rapid Transit 220:13–27
4. Polach O (2006) Comparability of the non-linear and linearized stability assessment during railway vehicle design. Vehicle System Dynamics Supplement 44:129–138
5. N.N. (2005) EN 14363 Railway applications – Testing for the acceptance of running characteristics of railway vehicles – Testing of running behaviour and stationary tests. CEN, Brussels
6. True H (1994) Does a critical speed for railroad vehicle exist? Proceedings of the 1994 ASME/IEEE Joint Railroad Conference, Chicago, Illinois, March 22–24, 1994, pp. 125–131
7. Kaas-Petersen CH (1986) Chaos in a railway bogie. Acta Mechanica 61:89–107
8. Schupp G (2006) Bifurcation analysis of railway vehicles. Multibody System Dynamics 15:25–50
9. Stichel S (2002) Limit cycle behaviour and chaotic motions of two-axle freight wagons with friction damping. Multibody System Dynamics 8:243–255
10. Polach O, Vetter A (2004) Methods for running stability prediction and their sensitivity to wheel/rail contact geometry. Extended abstracts of the 6th International Conference on Railway Bogies and Running Gears, Budapest, 13–16 Sept., 2004, pp. 62–64
11. Piotrowski J (2009) Smoothing dry friction by medium frequency dither and its influence on ride dynamics of freight wagons. In: P.G. Thomsen, H. True (eds.), Non-smooth problems in vehicle system dynamics. Springer-Verlag Berlin Heidelberg, pp. 187–191

Closed-Form Analysis of Vehicle Suspension Ride and Handling Performance

Mehdi Ahmadian

Abstract A closed-form, analytical study that evaluates the response characteristics of a two-degree-of freedom quarter-car model using passive and semi-active dampers is provided as an extension to the results published in past studies for active suspensions. The semiactive methods that are considered include skyhook, groundhook, and hybrid control. The relationships between vibration isolation, suspension deflection, and road-holding are studied using the model. The performance indices that are used include vertical acceleration of the sprung mass, deflection of the suspension (rattle space), and deflection of the tire. The results indicate that hybrid semiactive control yields better comfort than passive suspension and the other semiactive control methods that are considered, without reducing the road-holding quality or requiring larger suspension rattle space for typical passenger cars.

1 Introduction and Background

In early 1980's Chalasani provided a non-dimensional analysis of active suspensions, employing a quarter car model and compared the results with passive suspensions, using metrics that are commonly used to evaluate vehicle ride and handling in simulation studies [1]. He extended his results to a full-vehicle model with seven degrees of freedom, and used the same ride and handling metrics to draw a comparison with passive suspensions [2]. This study intends to extend the results offered by Chalasani in [1] for semiactive suspensions that have received increased attention in the recent years.

Among the large number of semiactive control methods that have been extensively studied in the past, we select skyhook, groundhook, and hybrid control – depicted in Fig. 1 – because of their popularity and documented effectiveness in controlling suspension dynamics [3]. The semiactive control methods can be

M. Ahmadian (✉)
Railway Technologies Laboratory (RTL), Center for Vehicle Systems & Safety (CVeSS), Virginia Tech, MC-0901, Blacksburg, VA 24061, USA
e-mail: ahmadian@vt.edu

P.G. Thomsen, H. True (eds.), *Non-smooth Problems in Vehicle Systems Dynamics*,
DOI 10.1007/978-3-642-01356-0_3,

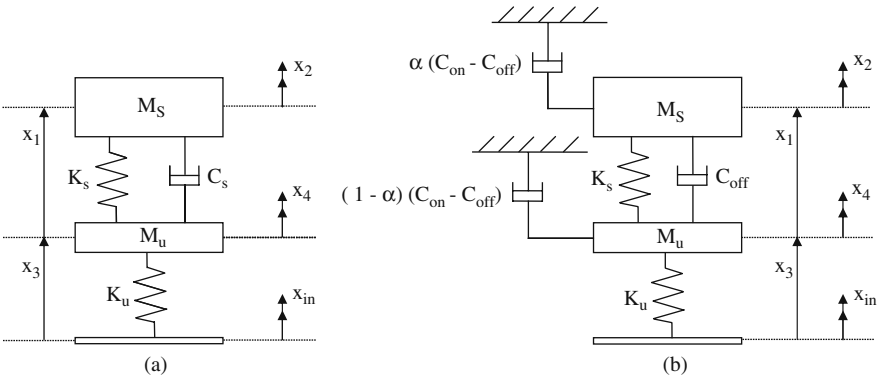

Fig. 1 Quarter-car suspension system: (**a**) Passive configuration; (**b**) Semiactive configuration

described by the following Eq. (1), where σ_{sky} and σ_{gnd} are the skyhook and groundhook components of the damping force, and G is a constant gain. The variable α is the relative ratio between the skyhook and groundhook control. When α is 1, the control policy reduces to pure skyhook, whereas when α is 0, the control is purely groundhook.

$$\left\{\begin{array}{ll} v_2(v_2 - v_1) \geq 0 & \sigma_{sky} = G\, v_2 \\ v_2(v_2 - v_1) < 0 & \sigma_{sky} = 0 \end{array}\right\}$$

$$\left\{F_{sa} = \alpha\, \sigma_{sky} + (1 - \alpha)\, \sigma_{gnd}\right\} \tag{1}$$

$$\left\{\begin{array}{ll} -v_1(v_2 - v_1) \geq 0 & \sigma_{gnd} = G\, v_1 \\ -v_1(v_2 - v_1) < 0 & \sigma_{gnd} = 0 \end{array}\right\}$$

With the skyhook configuration [4, 5], the tradeoff between resonance control and high-frequency isolation, common in passive suspensions, is eliminated [6]. The skyhook configuration excels at isolating the sprung mass from base excitations, at the expense of increased unsprung mass motion [7]. The groundhook configuration focuses on the unsprung mass. The hybrid configuration has been shown to take advantage of the benefits of both skyhook and groundhook control [3]. The hybrid configuration will use $\alpha = 0.5$.

2 Model Formulation

The passive representation of semiactive dampers controlled by the hybrid policy appears as shown in Fig. 1b. The off-state damping C_{off} is a small portion of the on-state damping C_{on}. For the ideal skyhook, groundhook and hybrid configura-

tions, we would have $C_{off} = 0$. It is not, however, possible to completely eliminate any amount of damping in the suspension, and it can even be undesirable [8]. The model of the quarter-car suspension system used in this analysis is an extension of the passive suspension model used in [1] to semiactive suspensions. The states of the model are the deflection of the suspension (x_1), the velocity of the sprung mass (x_2), the deflection of the tire (x_3), and the velocity of the unsprung mass (x_4). Road measurements have shown that an integrated white-noise input is a good approximation of the vertical displacement of the road surface, except at very low frequencies [1]. In this analysis, the velocity input v_{in} will therefore be modeled as a white noise input. The results obtained in [1] for passive suspensions can be re-derived by taking the results obtained for the semiactive model and replacing C_{off} by C_S and C_{on} by C_S (then $C_{on} - C_{off}$ is replaced by 0).

The mean square response of a motion variable y to a white noise input can be computed using the expression

$$E[y^2] = S_0 \int_{-\infty}^{\infty} \left|H_y(\omega)\right|^2 d\omega \tag{2}$$

where $H_y(\omega)$ is the transfer function describing the response of the motion variable y to the white-noise input [1], and S_0 is the spectral density of the white-noise input [1].

The motion variables of interest in this analysis are the same as in [1]: the sprung mass vertical acceleration $\dot{x}_2$, the suspension deflection x_1, and the tire deflection x_3. The following expressions will therefore be computed:

- $E[\dot{x}_2{}^2] = S_0 \int_{-\infty}^{\infty} |H_{\dot{x}_2}(\omega)|^2 d\omega$, used as a measure of the vibration level
- $E[x_1{}^2] = S_0 \int_{-\infty}^{\infty} |H_{x_1}(\omega)|^2 d\omega$, used as a measure of the rattle space requirement
- $E[x_3{}^2] = S_0 \int_{-\infty}^{\infty} |H_{x_3}(\omega)|^2 d\omega$, used as a measure of the road-holding quality

The measure of the vibration level can be used as a comfort index for the driver and the passengers since the human body is mostly affected by the acceleration to which it is subjected [9]. The lower the vibration level is, the more comfortable the ride would be.

The system can be fully described with the four equations of motion shown below:

$$\dot{x}_1 = x_2 - x_4 \tag{3}$$

$$\dot{x}_2 = -\frac{K_S}{M_S} x_1 - \frac{C_{off}}{M_S}(x_2 - x_4) - \frac{\alpha(C_{on} - C_{off})}{M_S} x_2 \tag{4}$$

$$\dot{x}_3 = x_4 - v_{in} \tag{5}$$

$$\dot{x}_4 = \frac{K_S}{M_U} x_1 + \frac{C_{off}}{M_U}(x_2 - x_4) - \frac{K_U}{M_U} x_3 - \frac{(1-\alpha)(C_{on} - C_{off})}{M_U} x_4 \tag{6}$$

Using a Matrix form, it can be rewritten as:

$$\begin{bmatrix} \dot{x}_1 \\ \dot{x}_2 \\ \dot{x}_3 \\ \dot{x}_4 \end{bmatrix} = M_{44} \begin{bmatrix} x_1 \\ x_2 \\ x_3 \\ x_4 \end{bmatrix} + \begin{bmatrix} 0 \\ 0 \\ -1 \\ 0 \end{bmatrix} v_{in} \tag{7}$$

where

$$M_{44} = \begin{bmatrix} 0 & 1 & 0 & -1 \\ -\frac{K_S}{M_S} & -\frac{C_{off}+\alpha(C_{on}-C_{off})}{M_S} & 0 & \frac{C_{off}}{M_S} \\ 0 & 0 & 0 & 1 \\ \frac{K_S}{M_U} & \frac{C_{off}}{M_U} & -\frac{K_U}{M_U} & -\frac{(1-\alpha)(C_{on}-C_{off})+C_{off}}{M_U} \end{bmatrix}$$

In the Laplace domain, Eq. (7) becomes:

$$M_{L44} \begin{bmatrix} x_1 & x_2 & x_3 & x_4 \end{bmatrix}^T = \begin{bmatrix} 0 & 0 & -1 & 0 \end{bmatrix}^T v_{in} \tag{8}$$

where

$$M_{L44} = \begin{bmatrix} s & -1 & 0 & 1 \\ \frac{K_S}{M_S} & s + \frac{C_{off}+\alpha(C_{on}-C_{off})}{M_s} & 0 & -\frac{C_{off}}{M_s} \\ 0 & 0 & s & -1 \\ -\frac{K_S}{M_U} & -\frac{C_{off}}{M_U} & \frac{K_U}{M_U} & s + \frac{(1-\alpha)(C_{on}-C_{off})+C_{off}}{M_U} \end{bmatrix}$$

The three transfer functions of interest

$$H_{x_1}(s) = \frac{x_1}{v_{in}}(s),\ H_{\dot{x}_2}(s) = \frac{\dot{x}_2}{v_{in}}(s),\ \text{and } H_{x_3}(s) = \frac{x_3}{v_{in}}(s)$$

can be derived from Eq. (8). The transfer function of the sprung mass vertical acceleration is:

$$H_{\dot{x}_2}(s) = \frac{s\, K_U(K_S + C_{off}\, s)}{D_{SA}(s)} \tag{9}$$

where

$$D_{SA}(s) = d_{sa4}\, s^4 + d_{sa3}\, s^3 + d_{sa2}\, s^2 + d_{sa1}\, s + d_{sa0}$$

with

$$\begin{aligned} d_{sa4} &= M_S\, M_U \\ d_{sa3} &= M_S(C_{off} + (1-\alpha)(C_{on}-C_{off})) \\ &\quad + M_U(C_{off} + \alpha(C_{on}-C_{off})) \end{aligned}$$

$$
\begin{aligned}
d_{sa2} &= K_S(M_S + M_U) + K_U\, M_S \\
&\quad + C_{off}(C_{on} - C_{off}) + \alpha(1-\alpha)(C_{on} - C_{off})^2 \\
d_{sa1} &= K_S(C_{on} - C_{off}) + K_U(C_{off} + \alpha(C_{on} - C_{off})) \\
d_{sa0} &= K_S\, K_U
\end{aligned}
$$

The transfer function of the suspension deflection is:

$$
H_{x_1}(s) = \frac{-K_U(M_S s + \alpha(C_{on} - C_{off}))}{D_{SA}(s)} \tag{10}
$$

The transfer function of the tire deflection is:

$$
H_{x_3}(s) = \frac{-h_{x3,3}\, s^3 - h_{x3,2}\, s^2 - h_{x3,1}\, s - h_{x3,0}}{D_{SA}\ (s)} \tag{11}
$$

where

$$
\begin{aligned}
h_{x3,3} &= M_S\, M_U \\
h_{x3,2} &= M_S(1-\alpha)(C_{on} - C_{off}) + M_U\ \alpha(C_{on} - C_{off}) \\
&\quad + C_{off}(M_S + M_U) \\
h_{x3,1} &= K_S(M_S + M_U) + C_{off}(\ C_{on} - C_{off}) \\
&\quad + \alpha(1-\alpha)(C_{on} - C_{off})^2 \\
h_{x3,0} &= (C_{on} - C_{off})K_S
\end{aligned}
$$

Replacing s by jω in Eqs. (9), (10), and (11) yields the transfer functions in the frequency domain. Using the formula shown in (12), the three expressions for the mean square responses of interest can be derived from the three transfer functions shown in Eqs. (9), (10), and (11). The formula shown in (12) is obtained using the H_2 optimization procedure explained in [10], which uses the techniques explained in [11].

$$
\int_{-\infty}^{\infty} \left| \frac{a_3\, s^3 + a_2\, s^2 + a_1\, s + a_0}{b_4\, s^4 + b_3\, s^3 + b_2\, s^2 + b_1\, s + b_0} \right|^2 ds =
$$

$$
\int_{-\infty}^{\infty} \left| \frac{-a_3\, j\omega^3 - a_2\, \omega^2 + a_1\, j\omega + a_0}{b_4\, \omega^4 - b_3\, j\omega^3 - b_2\, \omega^2 + b_1\, j\omega + b_0} \right|^2 d\omega =
$$

$$
\pi \frac{{a_3}^2\, b_0(-b_1\, b_2 + b_0\, b_3) + 2a_1\, a_3\, b_0\, b_1\, b_4}{b_0\, b_4(-b_1\, b_2\, b_3 + b_0\, {b_3}^2 + {b_1}^2\, b_4)} +
$$

$$
\pi \frac{b_4(-{a_2}^2\, b_0\, b_1 - {a_1}^2\, b_0\, b_3 + 2a_0\, a_2\, b_0\, b_3 - {a_0}^2\, b_2\, b_3 + {a_0}^2\, b_1\, b_4)}{b_0\, b_4(-b_1\, b_2\, b_3 + b_0\, {b_3}^2 + {b_1}^2 b_4)} \tag{12}
$$

The three mean square responses of interest can be expressed as:

$$E[\dot{x}_2{}^2] = f_{13}(M_S, M_U, K_S, K_U, C_{on}, C_{off}, \alpha) \tag{13}$$

$$E[x_1{}^2] = f_{14}(M_S, M_U, K_S, K_U, C_{on}, C_{off}, \alpha) \tag{14}$$

$$E[x_3{}^2] = f_{15}(M_S, M_U, K_S, K_U, C_{on}, C_{off}, \alpha) \tag{15}$$

These three large expressions are shown in detail in [10]. Dimensionless parameters can provide better insight into how the three mean square responses are influenced by the vehicle model parameters. The dimensionless parameters below will therefore be used to illustrate the effects of the parameters on the response of the quarter car. These parameters are:

- The Mass Ratio:

$$r_m = \frac{M_U}{M_S} \tag{16}$$

- The Stiffness Ratio:

$$r_k = \frac{K_U}{K_S} \tag{17}$$

- The Off-State Damping Ratio of the Sprung Mass:

$$\zeta_{off} = \frac{C_{off}}{2\sqrt{K_S M_S}} \tag{18}$$

- The On-State Damping Ratio of the Sprung Mass:

$$\zeta_{on} = \frac{C_{on}}{2\sqrt{K_S M_S}} \tag{19}$$

- The approximal Natural Frequency of the Unsprung Mass:

$$\omega_u = \sqrt{\frac{K_U}{M_U}} \tag{20}$$

Using the parameters shown above, the dimensionless expressions for the rms vertical acceleration of the sprung mass, the rms deflection of the suspension, and the rms deflection of the tire can be derived and expressed as

$$\left(\frac{E[\dot{x}_2{}^2]}{\pi S_0\ \omega_u{}^3}\right)^{1/2} = f_{21}(r_m, r_k, \zeta_{off}, \zeta_{on},\ \alpha) \tag{21}$$

$$\left(\frac{E[x_1{}^2]}{\pi S_0}\omega_u\right)^{1/2} = f_{22}(r_m, r_k, \zeta_{off}, \zeta_{on},\ \alpha) \tag{22}$$

$$\left(\frac{E[x_3{}^2]}{\pi S_0}\omega_u\right)^{1/2} = f_{23}(r_m, r_k, \zeta_{off}, \zeta_{on},\ \alpha) \tag{23}$$

These three large expressions are also expressed in detail in [10].

3 Modeling Results

Plotting the frequency responses of the different transmissibility ratios will prove to be useful in order to explain the relationship between the mean square responses quantities. Figures 2, 3, and 4 show the effects of varying the damping coefficients on the sprung mass acceleration response, the suspension deflection, and the tire

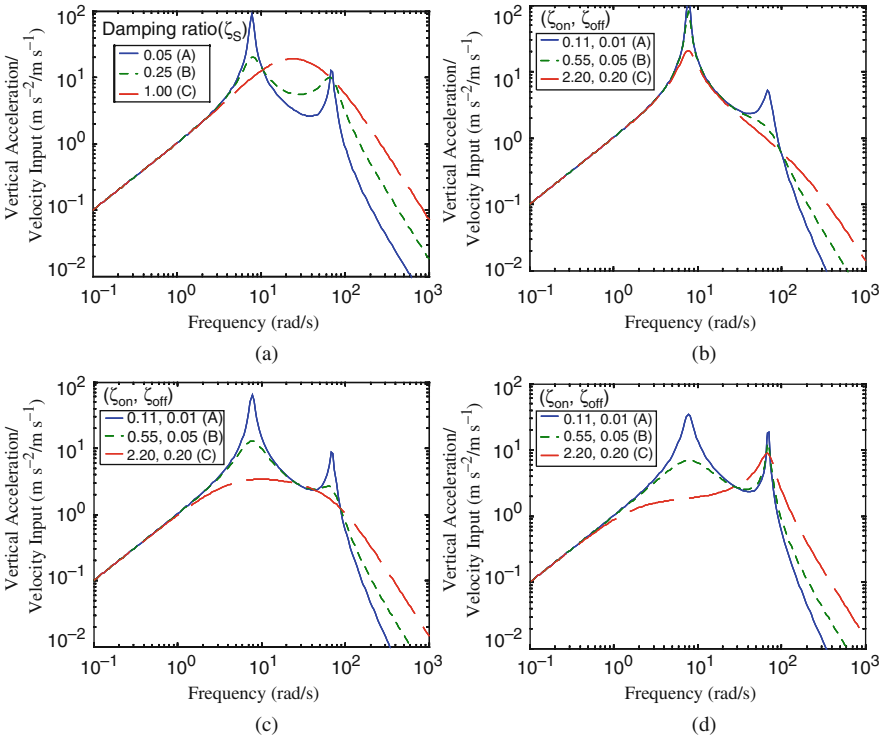

Fig. 2 Effect of damping on the vertical acceleration response: (**a**) Passive; (**b**) Groundhook; (**c**) Hybrid; (**d**) Skyhook

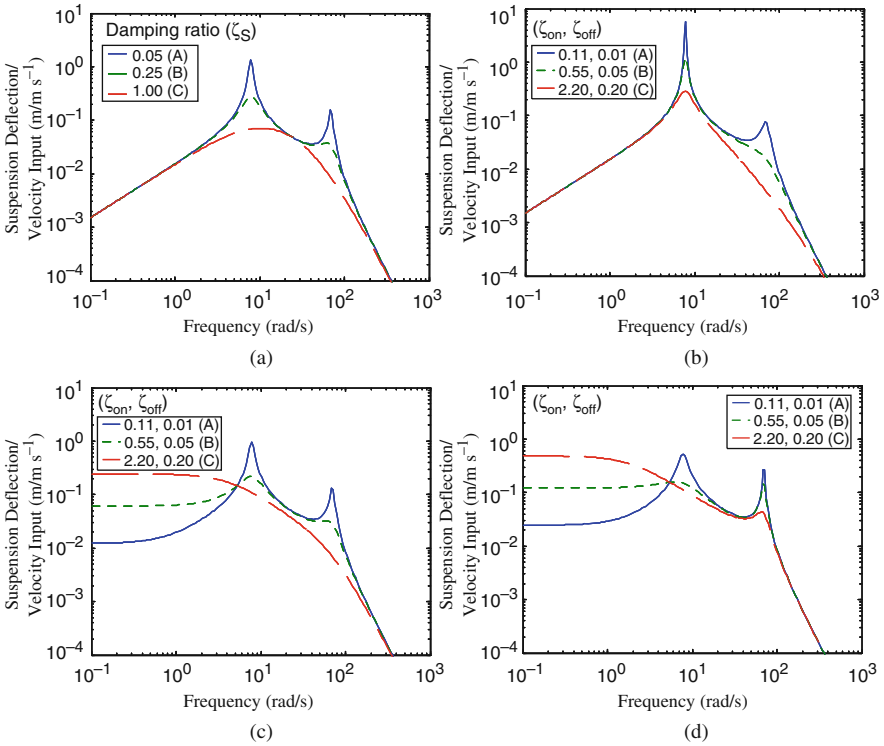

Fig. 3 Effect of damping on suspension deflection response: (**a**) Passive; (**b**) Groundhook; (**c**) Hybrid; (**d**) Skyhook

deflection respectively. Each figure shows the effect of the varying the damping coefficients for four configurations: passive, groundhook, hybrid (with $\alpha = 0.5$) and skyhook. The same masses and springs will be used for every configuration. Their numerical values are shown in Table 1.

The sprung mass natural frequency is $\omega_S = \sqrt{\frac{K_S}{M_S}} = 8.165\,\text{rad/s}$ (or 1.3 Hz)

The approximal unsprung mass natural frequency is $\omega_u = \sqrt{\frac{K_U}{M_U}} = 66.666\,\text{rad/s}$ (or 10.6 Hz)

No damping values are shown in Table 1 because the passive configuration involves a different suspension system than the groundhook, hybrid, and skyhook configurations. Also, several damping level will be used for each configuration.

For the passive case, the three figures will each be obtained for three different values of damping:

- $C_S = 196\,\text{N} \cdot \text{s/m}$: the corresponding damping ratio is $\zeta_s = 0.050$, which means the suspension is lightly damped
- $C_S = 980\,\text{N} \cdot \text{s/m}$: the corresponding damping ratio is $\zeta_s = 0.250$, which is a typical value for passenger cars
- $C_S = 3920\,\text{N} \cdot \text{s/m}$: the corresponding ratio is $\zeta_s = 1.000$, which means the suspension is heavily damped

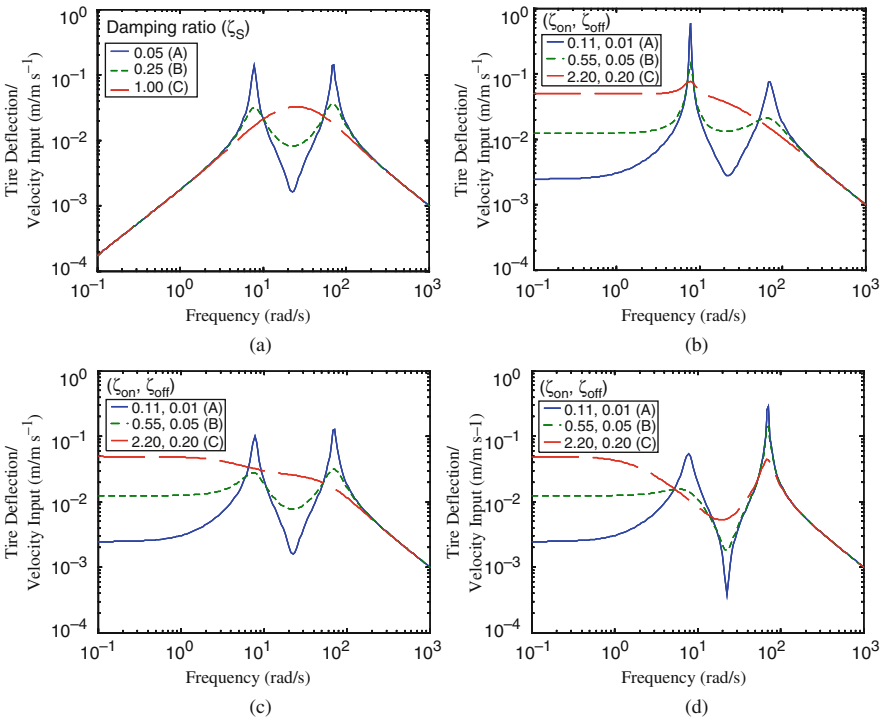

Fig. 4 Effect of damping on tire deflection response: (**a**) Passive; (**b**) Groundhook; (**c**) Hybrid; (**d**) Skyhook

Typical semiactive damping coefficients are chosen using the two relationships $C_{on} = 2.2\,C_S$ and $C_{off} = 0.2\,C_S$. These relationships also yield $(C_{on} - C_{off}) = 2\,C_S$.

For the groundhook, hybrid, and skyhook configurations, the pairs of damping coefficients used for plotting the frequency responses will therefore be:

- $C_{on} = 431.2\,\text{N}\cdot\text{s/m},\ C_{off} = 39.2\,\text{N}\cdot\text{s/m}$ (i.e., $\zeta_{on} = 0.110$ and $\zeta_{off} = 0.010$)
- $C_{on} = 2156\,\text{N}\cdot\text{s/m},\ C_{off} = 196\,\text{N}\cdot\text{s/m}$ (i.e., $\zeta_{on} = 0.550$ and $\zeta_{off} = 0.050$)
- $C_{on} = 8624\,\text{N}\cdot\text{s/m},\ C_{off} = 784\,\text{N}\cdot\text{s/m}$ (i.e., $\zeta_{on} = 2.200$ and $\zeta_{off} = 0.200$)

Having $\zeta_S = 0.050$ for the passive suspension or $(\zeta_{on}, \zeta_{off}) = (0.110, 0.010)$ for the semiactive suspension will correspond to the curves or to the points denoted as

Table 1 Model parameters

Parameter	Value
Sprung body weight (M_S)	240 Kg
Unsprung body weight (M_u)	36 Kg
Suspension stiffness (K_S)	16000 N/m
Tire stiffness (K_U)	160000 N/m

"A" in this chapter. Similarly, "B" will denote either $\zeta_S = 0.250$ or $(\zeta_{on}, \zeta_{off}) = (0.550, 0.050)$ and "C" will denote either $\zeta_S = 1.000$ or $(\zeta_{on}, \zeta_{off}) = (2.200, 0.200)$.

Figure 2 shows that increasing damping reduces the value of the vertical acceleration at the sprung mass natural frequency ω_S, which is the peak value for every configuration (passive, groundhook, hybrid and skyhook) unless the damping is too high. It also reduces the value of the vertical acceleration at the unsprung mass natural frequency ω_u. However, the area under the curve does not necessarily decrease with a reduced peak value of the acceleration. It means that the measure of the vibration level $E[\dot{x}_2{}^2]$ cannot be deducted from the peak value of the acceleration. It can be noted that the skyhook configuration is the one that needs to be chosen in order to minimize the vertical acceleration at the sprung mass natural frequency. However, the skyhook control policy may not be the best one for minimizing $E[\dot{x}_2{}^2]$.

Figure 3 shows that increasing damping reduces the value of the suspension displacement at the sprung mass natural frequency ω_S, which is the peak value for every configuration (passive, groundhook, hybrid and skyhook) unless the damping is too high. It also reduces the value of the suspension displacement at the unsprung mass natural frequency ω_u. However, the area under the curve does not necessarily decrease with a reduced peak value of the suspension displacement for the skyhook and the hybrid configuration. It means that the measure of the rattle space requirement $E[x_1{}^2]$ cannot be deducted from the peak value of the suspension displacement. It can be noted that the skyhook configuration is the one that needs to be chosen in order to minimize the suspension displacement at the sprung mass natural frequency. However, the skyhook control policy may not be the best one for minimizing $E[x_1{}^2]$.

4 Concluding Remarks

Figures 2, 3, and 4 show that hybrid control yields better performance than skyhook, groundhook, and passive configurations, as related to the vertical acceleration of the sprung mass, tire deflection, and suspension travel. Figure 5 compares the results

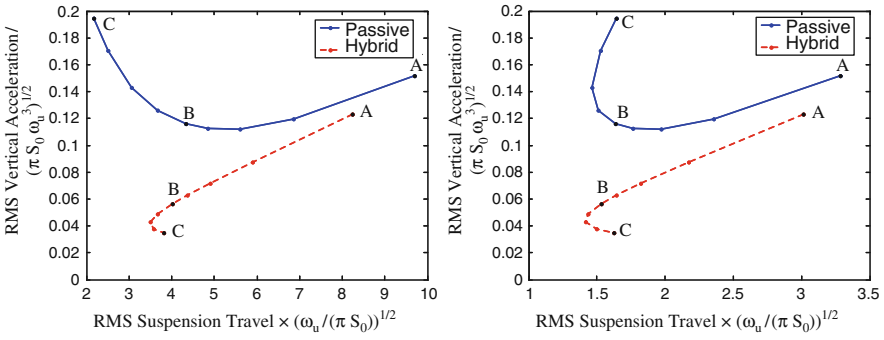

Fig. 5 Comparison between the performances of a passive suspension and a hybrid semiactive suspension (Mass ratio: 0.15; Stiffness ratio: 10)

obtained for hybrid semiactive suspension with the results obtained for passive suspension, for the stiffness ratio $r_k = 10$, which is a typical value for passenger cars. The mass ratio is still $r_m = 0.15$.

For the configuration B, corresponding to a typical damping for passengers cars, the hybrid configuration ($\alpha = 0.5$) reduces the rms acceleration of the sprung mass by half, and also reduces the rms suspension travel and the rms tire displacements in smaller proportions. This is for a typical mass ratio ($r_m = 0.15$) and a typical stiffness ratio ($r_k = 10$) for passenger cars. Therefore, using semiactive suspensions with the hybrid configuration yields a much better comfort than a passive suspension, without reducing the road-holding quality or increasing the suspension displacement for most passenger cars.

References

1. Chalasani, R.M., 1986, "Ride Performance Potential of Active Suspension Systems – Part I: Simplified Analysis Based on a Quarter-Car Model," *ASME Symposium on Simulation and Control of Ground Vehicles and Transportation Systems*, AMD-Vol. 80, DSC-Vol. 2, pp. 187–204.
2. Chalasani, R.M., 1986, "Ride Performance Potential of Active Suspension Systems-Part II: Comprehensive Analysis Based on a Full-Car Model," *ASME Symposium on Simulation and Control of Ground Vehicles and Transportation Systems*, AMD-Vol. 80, DSC-Vol. 2, pp. 205–234.
3. Ahmadian, M., 1997, "A Hybrid Semiactive Control for Secondary Suspension Applications," *Proceedings of the Sixth ASME Symposium on Advanced Automotive Technologies*, 1997 ASME International Congress and Exposition.
4. Crosby, M.J., Karnopp, D.C., 1973, "The Active Damper," The Shock and Vibrations Bulletin 43, Naval Research Laboratory, Washington, DC.
5. Karnopp, D.C., Crosby, M.J., "System for Controlling the Transmission of Energy Between Spaced Members," U.S. Patent 3,807,678.
6. Miller, L.R., 1986, "An Introduction to Semiactive Suspension Systems," Lord Library of Technical Articles, Document LL-1204.
7. Karnopp, D., 1995, "Active and Semiactive Vibration Isolation," ASME Journal of Vibration and Acoustics, 117(3B), pp. 177–185.
8. Ahmadian, M., 1999, "On the Isolation Properties of Semiactive Dampers" Journal of Vibration and Control, 5, pp. 217–232.
9. Griffin, M.J., 1996, *Handbook of Human Vibrations*, Academic Press, New York.
10. Blanchard, E.D., 2003, "On the Control Aspects of Semiactive Suspensions for Automobile Applications", M.S. thesis, Virginia Polytechnic Institute and State University, Blacksburg, VA.
11. Asami, T., Nishihara, O., 2002, "H_2 Optimization of the Three-Element Type Dynamic Vibration Absorbers," ASME Journal of Vibration and Acoustics, 124(4), pp. 583–592.

Further Reading

Kalker, J.J., 1991, *Wheel-rail rolling contact theory*, pages 243–261. Mechanics and Fatigue in Wheel/Rail Contact, Proceedings of the Third International Conference on Contact Mechanics and Wear of Rail/Wheel Systems. Elsevier, Amsterdam, New York, Oxford, Tokyo.

Piotrowski, J., 2003, “Model of the UIC link Suspension for Freight Wagons,” Archive of Applied Mechanics, 73, pp. 517–532.

Slivsgaard, E.C., 1992, *Bifurkationer og Kaos i en ikke-lineær model af et enkelt jernbanehjulsæt* (in Danish). Masters Thesis, LAMF, The Technical University of Denmark.

True, H., 1994, *On a new Phenomenon in Bifurcations of Periodic Orbits*, pages 327–331. Dynamics, Bifurcation and Symmetry, New Trends and New Tools. NATO ASI Series. Kluwer Academic Publishers, P.O. Box 322, NL-3300 AH Dordrecht, The Netherlands.

Limit Wheel Profile for Hunting Instability of Railway Vehicles

Laura Mazzola, Stefano Alfi, F. Braghin, and S. Bruni

Abstract Given a railway vehicle and a track, is it possible to define a wheel limit profile that allows the vehicle to run at a given speed without the occurrence of unsafe hunting motion? Nowadays some railway operators and maintenance staff identify the maximum admissible wear on the profiles comparing the rail equivalent conicity with a limit curve obtained on the basis of experimental evidence. The present paper analyses the relationship between equivalent conicity and the dynamic behaviour of the vehicle in tangent track. This can be used to implement condition – based rail reprofiling strategies.

1 Introduction

Wheel-rail contact geometry plays a key role in defining the dynamic behaviour of a railway vehicle running on the track: therefore, profile changes produced by the process of wear profoundly affect vehicle performances and ride safety, then excessive modifications of the original profile need to be periodically corrected by re-profiling the wheels to their original profile.

In particular, as far as high-speed rail vehicles are concerned, the main effect produced by the wearing of wheel profiles is the increase of the self-centring effect caused by the variation of rolling radius with lateral wheelset displacement, the so-called "conicity" of the wheel: although this effect is responsible for the inherent self-guidance property of railway wheelsets with solid axle, at high speed it favours the onset of a self-sustained combined lateral and yaw vibration of the bogie known as "hunting" which may be so large to become relevant to ride safety and passengers' comfort.

Unfortunately, the costs associated with wheel re-profiling represent a considerable share of the overall maintenance costs of rail vehicles: railway operators are therefore concerned with optimising their wheel re-profiling strategy, with the aim

L. Mazzola (✉)
Politecnico di Milano, Department of Mechanical Engineering, Via G. La Masa, 1, I-20156 Milano, Italy
e-mail: laura.mazzola@polimi.it

P.G. Thomsen, H. True (eds.), *Non-smooth Problems in Vehicle Systems Dynamics*,
DOI 10.1007/978-3-642-01356-0_4,

of maximising the distance run by the wheels before being turned, though ensuring appropriate levels of ride safety and performance.

Aim of this paper is to relate wheel wear with the critical speed of a high-speed rail vehicle, investigating the possibility to define a limit profile for the worn wheel, representing the maximum degree of wear compatible with the vehicle achieving its maximum service speed without experiencing hunting oscillations. The relevance of this limit profile in view of maintenance optimisation is clear, since it could be used to take decisions concerning wheel re-profiling based on an objective approach rather than on experience and qualitative judgement. Furthermore, the calculation of the limit profile can be tailored on each vehicle type in a fleet, considering its peculiar running properties, possibly also incorporating the effect of non-nominal vehicle condition, e.g. degraded behaviour of suspension components.

On account of the non-linearities introduced by wheel-rail contact forces, the problem addressed in this paper falls in the field of non-linear dynamics [1, 2]. Furthermore, the problem is of non-smooth nature, due to the discontinuities appearing in the relationship between the wheel/rail contact parameters and the lateral shift of the wheelset, which are caused by jumps of the contact point on the wheel and rail surfaces, and/or by the formation of multiple contact points. Previous investigations [1, 3], have demonstrated that for such type of non-linear and non-smooth dynamic problem a solution based on a linearised stability calculation is not appropriate, since this approach may neglect the existence of self-excited stationary solutions for the hunting oscillation of the bogie at speeds lower than the "linear" critical speed provided by the linearised approach. For this reason, the problem is studied here using a non-linear approach based on the simulation of vehicle dynamics under the random excitation provided by track irregularity (see Sect. 3), as proposed in [4] and used in [3, 5].

The method proposed in this paper, to establish a relationship between wheel wear and the critical speed of the vehicle, is based on the use of the "equivalent conicity" diagram: the equivalent conicity is a measure of the variation of the rolling radius difference between the two wheels of a wheelset produced by a lateral shift of the wheelset on the rails. The name corresponds to the fact that for a wheelset having conical wheels resting on sharp-edged rails (bicone) the rolling radius difference would be proportional to the lateral shift, the coefficient of proportionality being the angle of the cone. For real wheel profiles, and especially for worn ones, the rolling radius difference shows a strongly non-linear variation with the lateral shift of the wheelset, so that the equivalent conicity depends on the amplitude of the lateral oscillation of the wheelset over the track, leading to equivalent conicity, diagram as described in detail in Sect. 2 of this paper.

2 The Equivalent Conicity Concept

As described in the introduction, the equivalent conicity diagram is a geometric description of the wheel – rail couple in absence of any wheelset angle of attack. Except the very special case of conical wheel profiles resting on sharp-edged rails,

the rolling radius difference varies non-linearly with the shift of the wheelset. To linearize this curve, the equivalent conicity concept is used:

$$\Delta R = 2\gamma y + \eta \tag{1}$$

where ΔR is the difference of the rolling radii between right and left wheels, y is the relative lateral wheel-rail displacement, γ is the equivalent conicity and η is a constant offset value. Note that the equivalent conicity is not the analytical linearization of wheel and rail profiles around the centered wheelset position but an engineering approximation that accounts for an "average slope" of the rolling radius difference $\Delta R(y)$ diagram over a finite range lateral wheel-rail displacement. Several different methods for the practical calculation of the equivalent conicity exist. Among them in particular in this paper three are considered for the identification of the equivalent conicity diagram: UIC 519 method, Trapezoidal integration method, Harmonic quasi-linearization method.

2.1 UIC 519 Method

The UIC 519 method [6] is based on the kinematic movement (i.e. neglecting the effect of inertial forces) of a free wheelset running along a tangent track.

To determine the equivalent conicity the equation of wheelset oscillation, depending on the non linear $\Delta R(y)$ function is integrated numerically, determining the trajectory $y = y(x)$ of the wheelset (where x and y are the longitudinal and lateral positions of the wheelset on the track).

From the trajectory, the wavelength λ is extracted and the equivalent conicity determined as the value of the bicone angle that would produce the same wavelength of kinematic oscillation according to Klingel's formula [7].

$$\gamma_{UIC519} = \frac{2\pi^2 e r_0}{\lambda} \tag{2}$$

2.2 Trapezoidal Integration Method

The trapezoidal integration method determines the equivalent conicity by averaging over an interval $-\Delta y + \Delta y$ of the wheelset displacement the conicity value expressed by formula (1). Computing the integral of the $\Delta R\ (y)$ curve over a given wheelset lateral displacement interval Δy and by dividing such integral by the four times the considered interval:

$$\gamma_{TI} = \frac{1}{4\Delta y^2} \int_{-\Delta y}^{\Delta y} \Delta R dy \tag{3}$$

The interval over which the average is taken is centered on the position corresponding to zero value of $\Delta R(y)$ so that the offset value η is set to zero.

2.3 Harmonic Quasi-Linearization Method

The harmonic quasi-linearization method is based on the assumption that the wheelsets describe a sinusoidal movement in space.

The equivalent conicity is computed by averaging, the rolling radius variation over one wavelength of wheelset motion

$$\gamma_{HQL} = \frac{\int_0^{2\pi} \Delta R \sin \tau \, d\tau}{2\pi a} \tag{4}$$

The main difference with respect to the trapezoidal integration method is that here ΔR values are weighted by a sine wave function, so that values far from the centred wheelset position are weighted with larger weight.

The Fig. 1 compares the equivalent conicity diagrams obtained according to the three methods for a worn ORES1002 profile.

UIC 519 and harmonic quasi-linearization methods are in very good agreement with each other, whereas the differences between the trapezoidal integration method and the other two are larger, especially for small values of Δy. In the following calculation, the harmonic quasi-linearization method is applied.

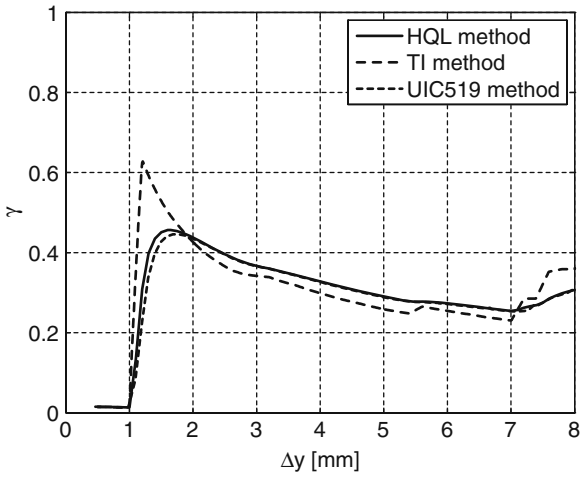

Fig. 1 Equivalent conicity diagram: Calculation method comparison

3 Numerical Evaluation of the Critical Speed

The reliable estimation of the critical speed for a railway vehicle requires to be addressed by fully considering the nonlinear and non-smooth nature of the problem. In this paper, a method for the numerical evaluation of the vehicle critical speed calculation is used, based on the simulation of the vehicle non-linear running behaviour in tangent track, subject to the random excitation produced by track irregularity.

The method is inspired by the European standard EN14363, according to this standard, the critical speed is identified from line tests as the threshold speed above which the rms value of either the track shift forces or the lateral acceleration of the bogie frame exceed a given limit value. More precisely, the standard differentiates a so-called "normal measuring method", which should be used for the homologation of a new vehicle, and a "simplified measuring method", which can be used to extend the homologation of an existing vehicle. In the normal measuring method, the track shift forces ΣY (sum of the guiding forces on the two wheels of the same axle) are measured applying a low-pass filter at 20 Hz and the rms value $s\Sigma Y$ of this measured quantity is computed. The vehicle is considered to be unstable if this quantity exceeds the limit value $(s\Sigma Y)_{\text{lim}}$ defined as:

$$(s\Sigma Y)_{\text{lim}} = {}^{1}\!/_{2}\left(10 + \frac{2Q_0}{3}\right) \tag{5}$$

where Q_0 is the static vertical wheel load and both Q_0 and $(s\Sigma Y)_{\text{lim}}$ are expressed in kN. In the simplified measuring method, the lateral bogie acceleration over the axle box is measured applying a band-pass filter with amplitude ± 2 Hz centred on the frequency f_0 corresponding to the maximum spectrum amplitude. The rms. value of the filtered lateral bogie acceleration $s\ddot{y}^{+}$ is computed, and vehicle instability is associated with the overcoming of the limit value $\left(s\ddot{y}^{+}\right)_{\text{lim}}$ defined as:

$$\left(s\ddot{y}^{+}\right)_{\text{lim}} = \frac{1}{2}\left(12 - \frac{m_b}{5}\right) \tag{6}$$

where m_b is the bogie mass expressed in thousands of kg and $\left(s\ddot{y}^{+}\right)_{\text{lim}}$ is expressed in m/s^2.

The approach used in this paper to derive a numerical estimate of the vehicle critical speed is to use nonlinear numerical simulation to reproduce vehicle dynamics under the excitation of random track irregularity, as may occur along a test run, increasing vehicle speed stepwise until any of the instability thresholds prescribed by EN14363 is exceeded. The procedure is exemplified by the results of a critical speed calculation case reported in Fig. 2, in which for conciseness only the results obtained for the leading bogie are displayed: simulations are performed starting from the lowest speed value of 240 km/h, which is increased by 5 km/h from one simulation to the next one. For each speed value, the rms. of the lateral acceleration (pass-band filtered as explained above) and the rms. of the track shift forces (low pass filtered at 20 Hz) are computed and the process is iterated until one of the rms.

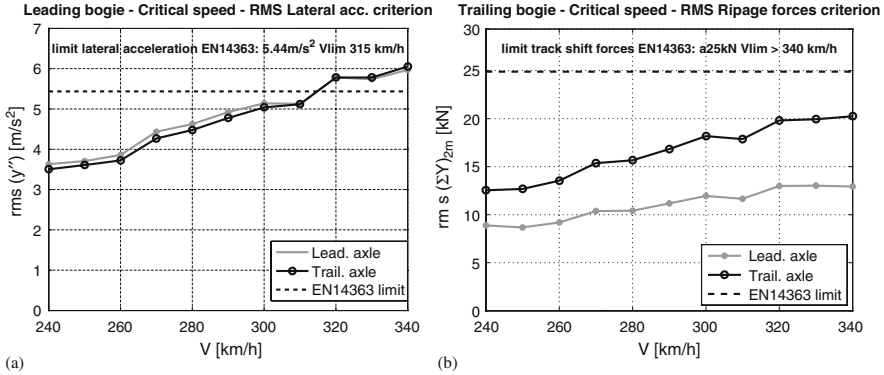

Fig. 2 Numerical estimation of the critical speed (**a**) simplified method (**b**) normal method

values exceeds its limit as stated by formulae (5) or (6). The critical speed value is then obtained by linear interpolation between the two speed values falling across the limit condition.

In the example shown in Fig. 2, the result of this procedure applied on the lateral acceleration of the bogie frame (simplified method, left subfigure) provides a critical speed of 315 km/h, whereas considering the track shift forces (normal method, right subfigure) the critical speed estimate falls above the maximum considered vehicle speed. It is observed that the critical speed defined based on the lateral bogie acceleration is much lower than the one defined on the basis of the track shift forces. An explanation for this behaviour is described in [5]. In any case, the lowest of the two values (in this case 315 km/h) is taken as the estimate of the critical speed.

3.1 Multi-Body Model of the Railway Vehicle

The numerical model of the vehicle used for the critical speed estimation was defined using ADTreS, an in-house code for the numerical simulation in time domain of the non-stationary dynamic behaviour of rail vehicles travelling on a flexible track developed at the Politecnico di Milano, Department of Mechanical Engineering [8, 9].

In this work a weak interaction is assumed among the vehicles in the train set, and therefore the mathematical model is confined to one single vehicle, considering a trailer car of a concentrated power high speed train. For the carbody and the bogies, a rigid body motion with constant forward speed is assumed, and hence five degrees of freedom per body are introduced (vertical and lateral displacement, yaw, pitch and roll rotation). For the wheel sets, besides the rigid motion coordinates, an additional degree of freedom is introduce to consider the torsional flexibility of the axle. The simplifying assumption of rigid track is considered in all calculations.

3.2 Wheel Rail Contact Model

Wheel-rail contact represents the main source of non-linearity and non-smoothness in the problem considered here. Indeed, wheel-rail contact parameters like the rolling radius variation, the contact angle and the curvature of wheel and rail profiles depend nonlinearly on the position of the wheel relative to the track. Furthermore, the type of non-linearity involved is of non-smooth nature since it is associated with the formation of multiple contacts between the same wheel/rail couple and/or to "jumps" of the contact point across the wheel and rail profiles. As an example, Fig. 3 shows, for one of the worn wheel/worn rail couple considered in the stability analyses, the variation of the rolling radius as function of the lateral wheelset position respective to the track: the effect of contact jumps is clearly visible.

Whereas other modelling techniques introduce an artificial smoothing of wheel-rail contact non-linearities by the use of an "elastic contact" simplifying assumptions [10], in the modelling approach presented here non-smooth effects are dealt with using a multi-Hertzian contact model, which fully accounts for the non-smooth transition of wheel-rail contact forces among multiple contacts active on the wheel and rail surface.

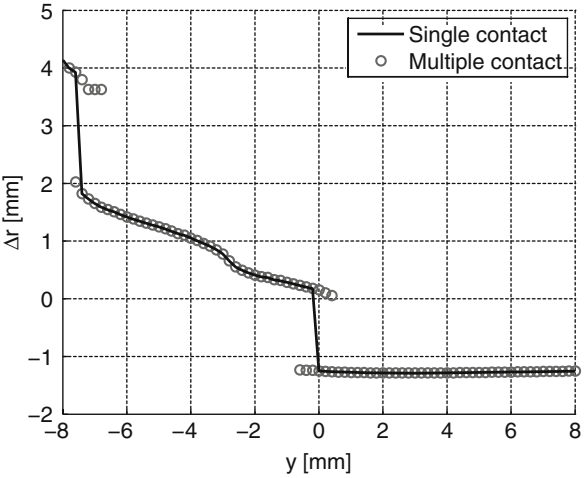

Fig. 3 Rolling radius variation diagram with non-smoothness produced by the jumps of the contact point

4 Equivalent Conicity as a Mean to Relate Hunting Motion and Wheel Rail Profiles

Experimental and operational evidence shows that the critical speed of a railway vehicle is strongly affected by the geometry of wheel-rail contact, and a usual measure which is taken to quantify this effect is represented by the equivalent conicity

diagram, see e.g. the comment by Dr. J. Evans reported in [4]. Accordingly, railway operators and maintenance managers try to define limit values for the $\gamma(\Delta y)$ diagrams to detect the maximum allowable wear-induced modification of the wheel profile which is compatible with the vehicle running in service below the critical speed.

An example of this approach is represented in Fig. 4, where a limit curve proposed by a maintenance manager is reported, together with some conicity diagrams obtained for different wheel profiles[1] measured on serviced wheel sets. The conicity diagrams in the figure are divided in two sets: the ones plotted in solid lines correspond to wheel sets for which an instability warning was recorded while running at the maximum service speed (300 km/h), whereas the diagrams plotted in dashed line correspond to a degree of wheel profile wear for which no instability warning occurred. As can be seen, the proposed limit curve separates well the two sets of data, and hence the empirically based criterion can be considered to work well in this case.

However, a number of limitations exist on this empirical approach: besides lacking a physical interpretation of the phenomenon, it does not provide any mean to implement a "predictive" approach, in the sense that the limit curve can only be determined based on the processing of on-board condition monitoring signals, whereas it would be impossible to define a limit curve for a different type of rolling stock or for a different service profile. Furthermore, when the conicity diagram falls within the "admissible zone", no information is provided about the further mileage the wheelset will be able to run before requiring re-profiling. Aim of this work is hence to understand how this type of approach can be supported and improved by

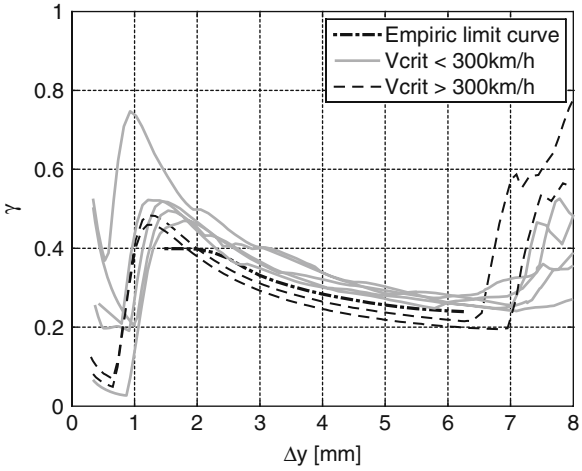

Fig. 4 Empiric limit curve

[1] The conicity diagrams reported are obtained coupling the measured wheel profiles with the theoretical UIC60 profile with 1435 mm gauge and 1:20 inclination.

mathematical modelling and numerical simulation, with the two aims of understanding on a wider basis the relationship between the conicity diagram and the onset of vehicle hunting and, to provide a numerical procedure to define the limit curve for a given vehicle and service scenario.

An analysis of all in-service worn ORES1002 wheel profiles available to the authors showed that the conicity diagrams can be filed in two main categories: in the first one the conicity is very high for low values of the wheelset lateral shift, becomes lower for intermediate values of Δy and then increases again, see Fig. 5.

In the second case, the conicity is almost constant at relatively low values for low Δy, shows a sort of step increase for intermediate Δy values and reaches high values when the contact is displaced on the wheel flange, see Fig. 6.

It is interesting to observe that exactly the same two conicity patterns were identified by Polach in [3], where it was shown that the two patterns correspond to different ways by which the hunting motion onsets above the critical speed. The two patterns are labelled in that paper with "B" and "A" letters respectively, and hence will be named hereafter as "Type B" (the one showed in Fig. 5) and "Type A" (the one in Fig. 6).

In Figs. 5 and 6, the conicity diagrams shown are divided in two groups, those for which the critical speed falls below 300 km/h (considering the same high-speed vehicle as in Fig. 4) are plotted in solid line, whereas those for which the critical speed falls above 300 km/h are plotted in dashed line. The critical speed is in this case determined by the use of the numerical procedure described in Sect. 3, and not from service measurements: for Type B profiles, the results compare well with those coming from service data, since the same limit curve of Fig. 4 again separates the profiles with critical speed above 300 km/h from the others. When Type A profiles are considered, for which no service data is available for the type of vehicle considered here, the empirical limit curve introduced in Fig. 4, clearly can no longer be

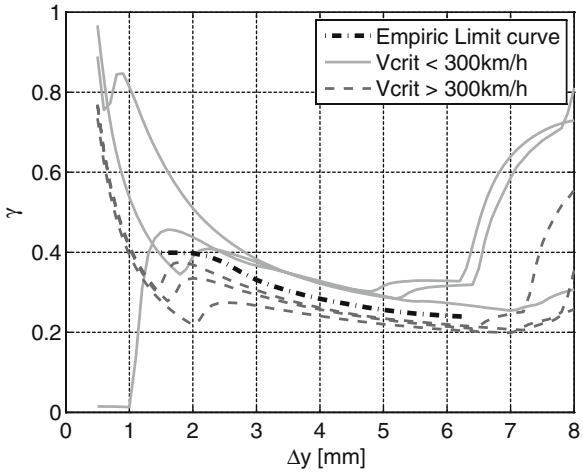

Fig. 5 Equivalent conicity diagram: Type B shape

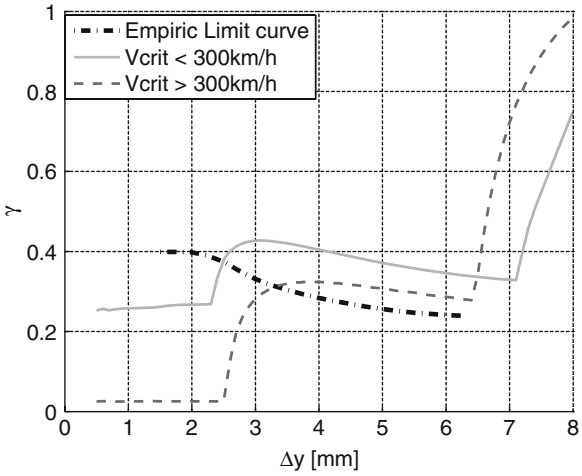

Fig. 6 Equivalent conicity diagram: Type A shape

accepted: it appears that a Type A profile with critical speed above 300 km/h may reach a higher value of conicity than a Type B profile in the 4.1–4.3 mm range of Δy. This is due to the fact that clearly on account of the equivalent conicity of this type of profile is much lower than for type B profiles for smaller lateral displacements of the wheels.

Based on the results presented in Figs. 5 and 6, it can be concluded that a single limit curve valid for any wheel wear pattern which might possibly occur in service cannot be defined, not even when the analysis is confined to one single initial wheel profile shape (the ORES1002 one in this case). Instead, the results suggest that limit curves can be defined more effectively when these are applied to groups of conicity diagrams showing homogeneous trends, like Type A and Type B in this section.

Unfortunately, this approach leaves open the question how to manage a situation where a conicity diagram cannot be clearly recognised to belong to one or the other "type" and, more fundamentally, still suffers from not being based on a physical interpretation of the relationship between conicity and hunting motion.

As a first attempt to overcome these limitations, it was observed that the integral curve obtained from the equivalent conicity diagram might be better suited than conicity itself to allow the definition of a limit curve, valid for all types of profiles. Indeed, the integral of the conicity is directly related with the energy introduced by wheel-rail contact forces in the hunting vibration of the wheelset, so that a higher integral value of the conicity shall be related to a lower critical speed of the vehicle.

Figure 7 compares the results of the calculation of the integral curve of the conicity diagram according to the formula:

$$\Gamma(\Delta y) = \int_{\Delta y_{\min}}^{\Delta y} \gamma(\Delta y)\, d\Delta y \tag{7}$$

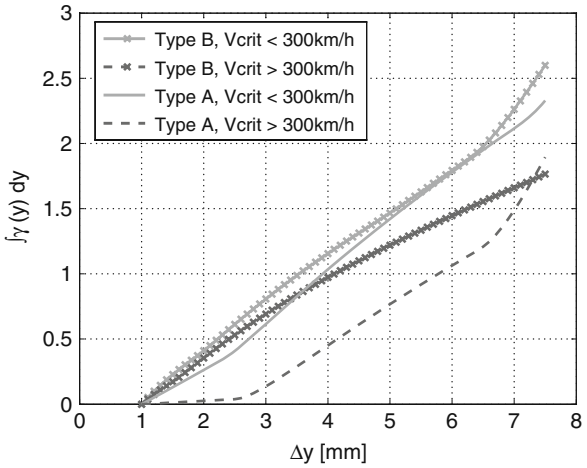

Fig. 7 Comparison of the integral curves obtained from Type A and Type B conicity diagrams

The integral is computed starting from $\Delta y_{min} = 1$ mm, to avoid the effect of abrupt variations of the conicity value which may occur for very low values of the lateral shift.

Four different cases are compared in Fig. 7:

- Type A conicity diagram corresponding to a critical speed below 300 km/h
- Type A conicity diagram corresponding to a critical speed above 300 km/h
- Type B conicity diagram corresponding to a critical speed below 300 km/h
- Type B conicity diagram corresponding to a critical speed above 300 km/h

as can be observed in Fig. 7, in the Δy range from 4 to 7 mm, the curves obtained from profiles having critical speed below 300 km/h are well separated from the other two. The same result was obtained using different examples of Type B profiles, whereas no generalisation is possible for Type A profiles, on account of the very limited number of profiles of this type available. Still the results shown in the figure suggest that a more reliable and general way to relate wheel wear and the onset of hunting motion could be provided based on an appropriate post-processing of the conicity diagram, rather than on the conicity diagram itself. As to the best post-processing option and the corresponding "universal" limit curve, the problem remains open at this point of the research.

5 Conclusion

The present paper proposed first results of a research aiming at the definition of quantitative relationships between wheel wear and the vehicle critical speed. Starting from the common empirical approach based on defining a limit curve for the

equivalent conicity diagram, the work investigated the relationship between equivalent conicity and the critical speed.

To this end, a method to define the vehicle critical speed was applied, based on the numerical simulation of the non-linear dynamic behaviour of the vehicle running in tangent track under the random excitation produced by track irregularity. The numerical simulation hence fully accounts for the non-linear and non-smooth effects related to wheel-rail contact geometry.

The results presented show that a simple limit curve cannot be defined for the equivalent conicity diagram, because different types of worn wheel profiles (e.g. Type A and Type B introduced in Sect. 4) require different limit curves.

The use of the integral of conicity instead of conicity itself appears to be in a more univocal relationship with the critical speed of the vehicle. Moreover no conclusive statement can be formulated at this point of the research and further work is required to fully explain the results presented here on a physical basis.

References

1. True H., On the theory of nonlinear dynamics and its application in vehicle systems dynamics. Vehicle System Dynamics, Vol. 31 (1999), pp. 393–421
2. Moelle D. and Gasch R., Nonlinear bogie hunting. Proceeding of the 7th IAVSD Symposium (1982), pp. 455–467
3. Polach O., On non-linear methods of bogie stability assessment using computer simulations. Proceedings of the Institution of Mechanical Engineers, Vol. 220, Part F: Journal of Rail and Rapid Transit (2006), pp. 13–27
4. Goodall R. M. and Iwnicki S. D., Non Linear Dynamic Techniques vs. Equivalent Conicity Methods for Rail Vehicle Stability Assessments, Vehicle System Dynamics, Supplement Vol. 41 (2004), pp. 791–799
5. Alfi S., Bruni S., and Mazzola L., Effect of motor connection on the critical speed of high speed railway vehicles, Vehicle System Dynamics, Supplement Vol. 46 (2008), pp. 201–214
6. UIC code 519, Method for determining the equivalent conicity, 1st edition, UIC, December 2004
7. Wickens A. H., Fundamentals of Rail Vehicle Dynamics: Guidance and Stability, Swets and Zeitlinger Publisher (2003)
8. Bruni S., Diana G., Collina A., and Vanolo P., Lateral Dynamics of a Railway Vehicle in Tangent Track and Curve: Tests and Simulations Vehicle System Dynamics Supplement Vol. 31 (2000), pp. 791–799
9. Braghin F., Bruni S., and Diana G., Experimental and numerical investigation on the derailment of a railway wheelset with solid axle, Vehicle System Dynamics, Vol. 44, No. 4 (April 2006), pp. 305–325
10. Netter H., Schupp G., Rulka W., and Shroeder K., New aspects of contact modelling and validation within multibody system simulation of railway vehicles, Vehicle System Dynamics, Supplement Vol. 28 (1998), pp. 246–269

Low-Cost Maintenance Operation for Avoiding Hunting Instability in a Metro Vehicle

F. Braghin, Stefano Alfi, S. Bruni, and A. Collina

Abstract Due to the relevant costs of rail re-profiling in underground metro lines, stake holders are available to consider alternative solutions. In the present research, a low-cost maintenance operation for avoiding hunting instability occurring on a section of a metro line has been proposed and experimentally verified.

1 Introduction

Hunting instability is a very important topic for railway vehicles since it involves both the safety and the ride comfort. In case of occurrence, the vehicle's operating speed has to be reduced and countermeasures have to be undertaken.

Hunting motion is usually considered a problem typical of high speed trains. However, hunting instability can also affect metro vehicles, whose maximum speed is significantly lower than high speed trains, in case some very particular circumstances occur such as absence of yaw dampers and/or high wear of wheel and rail profiles. Unfortunately, the introduction of yaw dampers (when absent) or their substitution (when ineffective) has a very high impact on maintenance costs and therefore stake holders usually judge such solution economically unfeasible. Instead, in presence of highly worn wheel and/or rail profiles, wheel and/or rail re-profiling has to be undertaken. While wheel re-profiling can be carried out by taking the vehicle temporarily out-of-service, rail re-profiling requires that the line is provisionally closed. Therefore, stake holders do prefer the first solution even though it may turn out that wheel re-profiling has to be frequently repeated. Thus, in the last years, stake holders are available to take into account alternative solutions that allow to reduce maintenance costs.

In the present paper, a low-cost maintenance operation for suppressing hunting instability occurring on some sections of Milan's metro line is described and exper-

F. Braghin (✉)
Politecnico di Milano, Department of Mechanical Engineering, Via G. La Masa, 1, I-20156, Milano, Italy
e-mail: francesco.braghin@polimi.it

P.G. Thomsen, H. True (eds.), *Non-smooth Problems in Vehicle Systems Dynamics*,
DOI 10.1007/978-3-642-01356-0_5,

imentally tested. On the considered track, metro trains were suffering from hunting instability already at the relatively low speed of 60 km/h, thus preventing them to reach their maximum operating speed of 85 km/h and requiring wheel re-profiling after approximately 25000 km. The cause of such unstable motion was identified in the absence of yaw dampers and in the worn rail profiles that determined a highly conformal contact with wheel profiles. The level of conformity of wheel-rail profiles led to equivalent conicity values (calculated according to [1]) in some cases higher than 0.8. Hunting instability was solved by changing rail inclination and thus modifying contact conditions between wheels and rails. Numerical simulations showed that a zero inclination angle would have allowed to gain the highest increase in the vehicle's stability. Nevertheless the stakeholder decided to reduce the original rail inclination instead of suppressing it. Although not optimal, this maintenance operation still allowed the avoidance of hunting motion up to the vehicle's maximum speed. Experimental results, before and after the maintenance operation, are presented and compared to numerical simulations obtained with a nonlinear vehicle – track interaction model ([2]).

2 Experimental Assessment of Hunting Instability

As already described in the introduction, Metro Milan Line 2 underground vehicles (Fig. 1) were suffering from hunting instability at relatively low speed (60 km/h) on some sections of the line.

A test campaign was carried out to precisely identify the speed at which hunting instability occurred and at which locations along the line. To assess vehicle stability, different methods can be used ([3, 4]). However, the one based on EN14363 standard allows to assess the vehicle's critical speed under realistic working conditions, i.e. in presence of track as well as wheel irregularity. Note that, in fact, EN14363 stan-

Fig. 1 Metro Milan line 2 underground vehicle

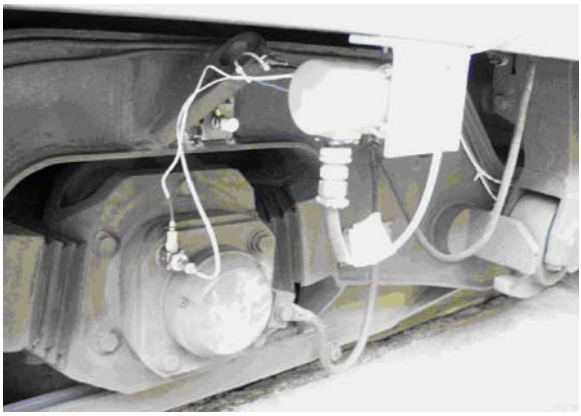

Fig. 2 Instrumented bogie and axlebox for instability detection

dard prescribes two different "instability indicators", one based on the lateral bogie acceleration measured above the leading and trailing axleboxes and one based on the sum of the guiding forces on the leading and trailing bogie axles. It has been shown ([5]) that these two "instability indicators" lead to quite different results in terms of critical speed and that the most conservative one is that based on bogie accelerations. It was therefore decided to instrument the underground vehicle with accelerometers measuring both the vertical and lateral accelerations at axlebox level and at bogie level above the axlebox of both the first two wheelsets (Fig. 2). Also vehicle speed and bogie – carbody relative rotation for curve detection were acquired.

Table 1 sums up the results of the tests carried out on the critical sections at various vehicle speeds (from 55 km/h to 85 km/h with steps of 10 km/h). Axlebox acceleration signals were post-elaborated according to EN14363 standard to assess vehicle stability and the bandwidth of 4–8 Hz was taken into account. This frequency range is of particular interest being the typical hunting instability frequency around 5–6 Hz.

It can be seen that above 55 km/h the RMS value of the lateral axlebox acceleration of the first wheelset is higher than 2 m/s^2.

The cause of such high RMS values was identified in the absence of yaw dampers and in the worn rail profiles that determined a highly conformal contact with wheel profiles as shown by the high values of the equivalent conicity obtained from the measured wheel and rail profiles.

Table 1 Filtered RMS values of the bogie lateral acceleration above the axlebox of the leading wheelset on the Gorgonzola – Cascina Antonietta track

Vehicle speed (km/h)	RMS value (m/s^2)
55	1.52
65	2.19
75	2.78
85	3.13

2.1 The Equivalent Conicity

As well known, the equivalent conicity diagram is a geometric description of the wheel – rail couple in absence of any wheelset angle of attack. It is based on the variation of the rolling radius difference as a function of the wheel-rail relative lateral displacement. Except for the very special case of conical wheel profiles resting on sharp-edged rails, the rolling radius difference varies non-linearly with the shift of the wheelset. To linearise this curve, the equivalent conicity concept is used:

$$\Delta R = 2\gamma y + \eta \tag{1}$$

where ΔR is the difference of the rolling radii between right and left wheels, y is the wheel-rail relative lateral displacement, γ is the equivalent conicity and η is a constant offset value. Note that the equivalent conicity is not the analytical linearization of wheel and rail profiles around the centered wheelset position but an engineering approximation of real wheel and rail profiles that accounts for much wider wheel-rail relative lateral displacements. Thus, several different methods for the practical calculation of the equivalent conicity exist such as the UIC 519 method, the trapezoidal integration method, the harmonic quasi-linearisation method, the SNCF method and the BR method. In the following, the UIC 519 method will be used.

For the wheel-rail couple under investigation, the equivalent conicity diagram is shown in Fig. 3. It can be seen that the equivalent conicity assumes values higher than 1 for wheel-rail relative lateral displacements smaller than 2 mm and reaches a minimum equal to approx. 0.8 for wheel-rail relative lateral displacements equal to 3 mm. These high values of equivalent conicity are due to the conformity of the

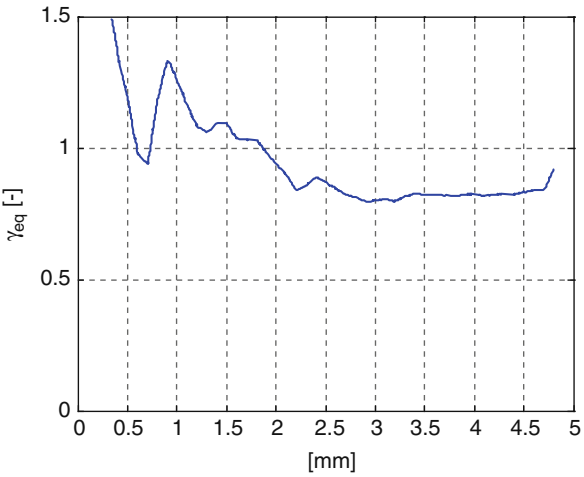

Fig. 3 Equivalent conicity determined according to UIC 519 method of the measured wheel and rail profiles (rail inclination equal to 1/20)

contacting profiles. Since the equivalent conicity can be considered as a reference parameter for the definition of the vehicle stability and its maximum allowable speed, a high value means low critical speed.

3 Numerical Investigation of a Feasible and Low-Cost Solution

Once the causes of the low speed hunting instability have been identified, feasible and low-cost solutions were searched for. Since the introduction of yaw dampers would have required a re-design of the bogies and thus high costs, the solution was identified in the reduction of the equivalent conicity values.

To obtain a quantitative analysis of the running behaviour of the metro vehicles and to have a tool to asses the effectiveness of the possible solutions to reduce the hunting motion of the vehicles, a complete model of the metro-track interaction was implemented in the numerical code ADTreS formerly developed by the Mechanical Engineering Department of Politecnico di Milano ([2]). The model of train-track interaction implemented in ADTreS is defined in the time domain and it is based on a mixed flexible/rigid body schematisation of the vehicle and a finite element representation of the track. The equations of motion of these two subsystems are coupled by the wheel-rail contact forces that are a function of both the vehicle and track coordinates. The equations are integrated using a time-step algorithm based on Newmark's method.

3.1 The Vehicle Model

The metro vehicle is a one coach, two bogies and four wheelsets vehicle. The multibody model is based on a rigid body schematisation of the carbody and bogie frames whereas the wheelsets are introduced through a modal superposition approach taking into account both the rigid and the flexible modes. Each rigid body has five degrees of freedom being the forward speed assigned. The equations of motion of the bodies are written with respect to a local reference system moving along the ideal track centreline. The vehicle's equations of motion take the form:

$$\mathbf{M}_v\ddot{\mathbf{x}}_v + \mathbf{R}_v\dot{\mathbf{x}}_v + \mathbf{K}_v\mathbf{x}_v = \mathbf{F}_{in}\,(V, t) + \mathbf{F}_{nl}\,(\mathbf{x}_v, \dot{\mathbf{x}}_v) + \mathbf{F}_{cv}\,(\mathbf{x}_v, \dot{\mathbf{x}}_v, \mathbf{x}_t, \dot{\mathbf{x}}_t, t) \quad (2)$$

where $\mathbf{M}_{\mathrm{v}}$, $\mathbf{R}_{\mathrm{v}}$, $\mathbf{K}_{\mathrm{v}}$ are the mass, the damping and the stiffness matrices of the vehicle respectively, $\mathbf{x}_{\mathrm{v}}$ is the vector of the vehicle's degrees of freedom, $\mathbf{x}_{\mathrm{t}}$ is the vector of the track's degrees of freedom, $\mathbf{F}_{\mathrm{in}}$ is the vector of the inertial forces associated to the motion of the local reference, $\mathbf{F}_{\mathrm{nl}}$ is the vector of the forces associated to non-linear suspension elements (e.g. bumpstops) and $\mathbf{F}_{\mathrm{cv}}$ is the vector of the contact forces.

3.2 The Track Model

The track is a typical ballasted track with concrete sleepers connected to the rails through direct fastenings. The sleepers are supported by a ballast bed having width equal to 25–30 cm. A finite element schematisation is adopted for reproducing rails, sleepers and subgrade. In particular, rails are represented through Euler-Bernoulli beam elements whereas sleepers are schematized as rigid bodies. The fasteners are schematised as linear lumped parameter visco-elastic elements and the ballast is represented through a layer of linear visco-elastic distributed elements. The equation of motion of the track subsystem is given by:

$$\mathbf{M}_t \ddot{\mathbf{x}}_t + \mathbf{R}_t \dot{\mathbf{x}}_t + \mathbf{K}_t \mathbf{x}_t = \mathbf{F}_{ct} \left(\mathbf{x}_v, \dot{\mathbf{x}}_v, \mathbf{x}_t, \dot{\mathbf{x}}_t, t \right) \tag{3}$$

where $\mathbf{M}_t$, $\mathbf{R}_t$, $\mathbf{K}_t$ are the mass, the damping and the stiffness matrices of the track respectively and $\mathbf{F}_{ct}$ is the vector of the contact forces.

3.3 The Contact Model

The coupling term between the two sets of Eqs. (2) and (3) is given by the contact forces that are calculated according to the following procedure.

Preliminary to the simulation of train – track interaction, a geometric analysis of the wheel and rail coupled profiles is carried out in order to pre-compute contact parameters, to be stored in tabular form, as a function of wheel-rail lateral displacement and angle of attack. This geometrical analysis is carried out considering the motion of a rigid wheelset with respect to rigid rail profile. The so obtained contact tables are interpolated at each simulation step thus allowing to determine the contact forces on each potential contact point. This is done in two subsequent steps: at first the normal contact problem is solved using Hertz theory; then the tangential contact forces are determined according to the Shen, Hedrick & Elkins formulation.

3.4 Simulation of Train-Track Interaction

Once the numerical model of train-track interaction was setup, a comparison between numerical and experimental results has been carried out. Figures 4 and 5 show the measured and simulated bogie lateral acceleration above left axlebox of the front wheelset with original wheel-rail profiles at a speed of 85 km/h. It can be seen that there is a very good agreement between the measured lateral bogie acceleration and the simulated one.

Using the vehicle numerical model, feasible and low-cost solutions to the low-speed hunting instability were therefore searched for. As already said, since the installation of anti-yaw dampers was considered economically unfeasible, two different solutions aiming at reducing the equivalent conicity values were investigated:

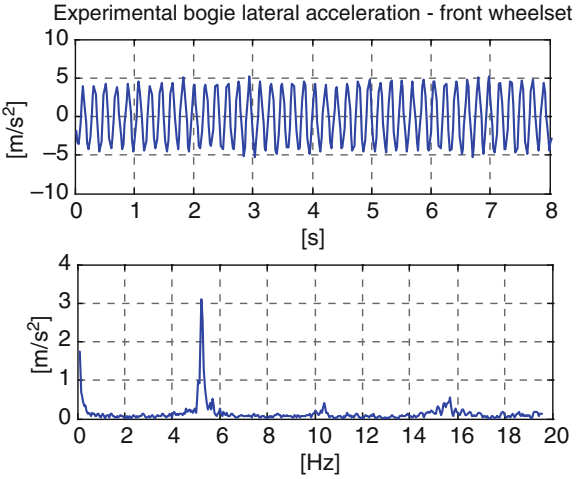

Fig. 4 Measured bogie lateral acceleration above left axlebox of front wheelset due to measured original wheel – rail couple (rail inclination equal to 1/20)

rail re-profiling and the variation of rail inclination. Even though rail re-profiling leads to the lowest values of equivalent conicity (Fig. 6), it was considered too expensive by the operator. Thus, numerical simulations were performed to asses the effect of a reduction of the rail inclination on hunting instability.

Two rail inclination values were considered: a 1/40 reduction and a 1/20 reduction with respect to the nominal value (the latter corresponding to the complete removal of the rail inclination). Figures 7 and 8 show the effects of a 1/40 reduction of rail inclination both in terms of equivalent conicity (purely geometrical analysis)

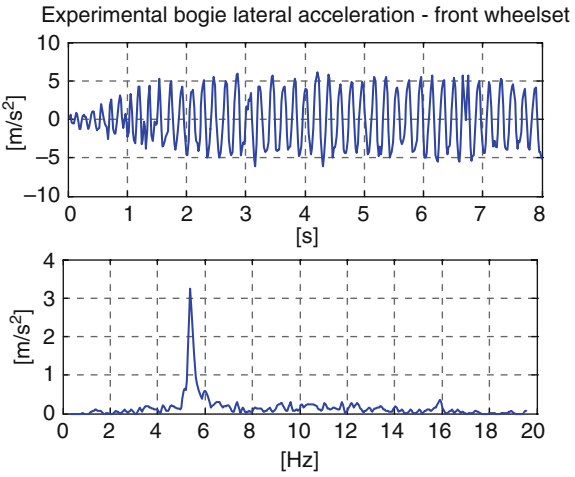

Fig. 5 Simulated bogie lateral acceleration above left axlebox of front wheelset due to measured original wheel – rail couple (rail inclination equal to 1/20)

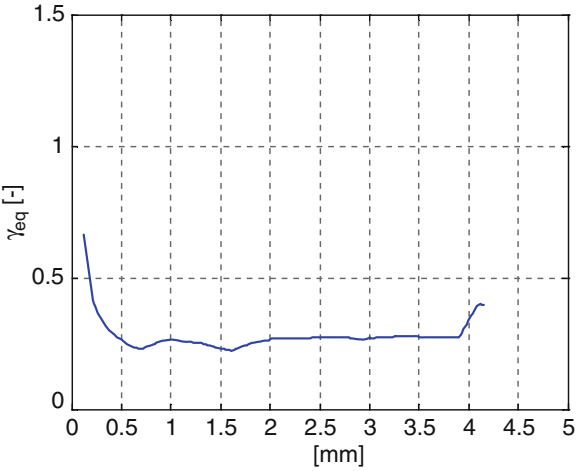

Fig. 6 Equivalent conicity determined according to UIC 519 method of the measured wheel and new (re-profiled) rail profiles (rail inclination equal to 1/20)

and lateral bogie frame acceleration above the axlebox of the leading wheelset (both in terms of time history and spectrum) when the vehicle is running at 85 km/h along a straight track. It can be seen that the acceleration peak is almost half that of the original case and that the equivalent conicity reaches a value of 0.5 at 3 mm of wheel-rail relative lateral displacement.

If the rail inclination is completely removed (Figs. 9 and 10), the amplitude of the oscillations, that could be observed in the bogie lateral acceleration signal, is significantly smaller than that of the original case and the peak value in the acceleration spectrum disappears. Also the equivalent conicity is further reduced and reaches a

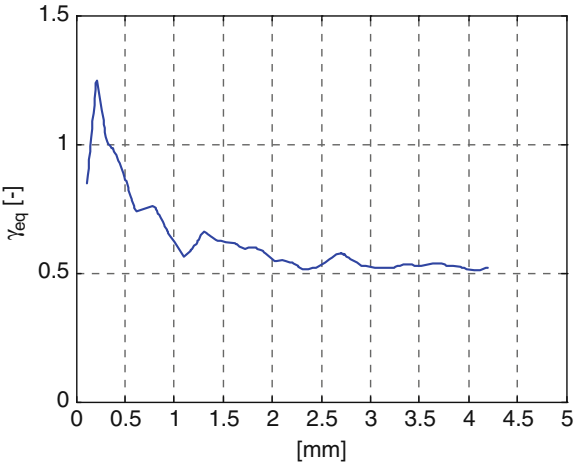

Fig. 7 Equivalent conicity of wheel – rail couple once rail inclination is reduced to 1/40

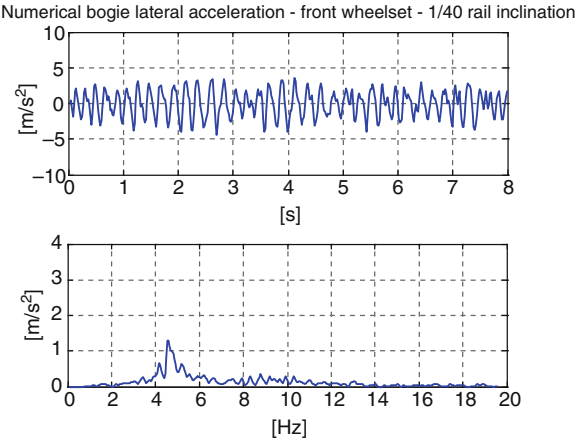

Fig. 8 Simulated bogie lateral acceleration above left axlebox of front wheelset due to wheel – rail couple once rail inclination is reduced to 1/40

value of 0.3 at 3 mm of wheel-rail relative lateral displacement. This proves that there is a good correlation between the equivalent conicity and the hunting instability. It should however be pointed out that no limit value for the equivalent conicity can be set out since equivalent conicity only accounts for the geometry of the contacting bodies while the stability limit is also a function of the suspensions, yaw dampers, track deformability, etc.

Table 2 shows the RMS values of the simulated bogie lateral acceleration filtered according to EN14363 for the different rail inclinations considered at two different vehicle speeds, i.e. at 75 km/h and at 85 km/h. It can be observed that the removal of the rail inclination is a very effective mean to reduce (of about 70%) the bogie

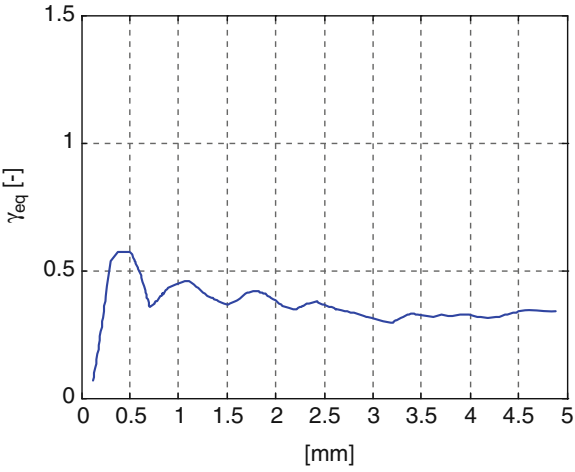

Fig. 9 Equivalent conicity of wheel – rail couple once rail inclination is reduced to 0

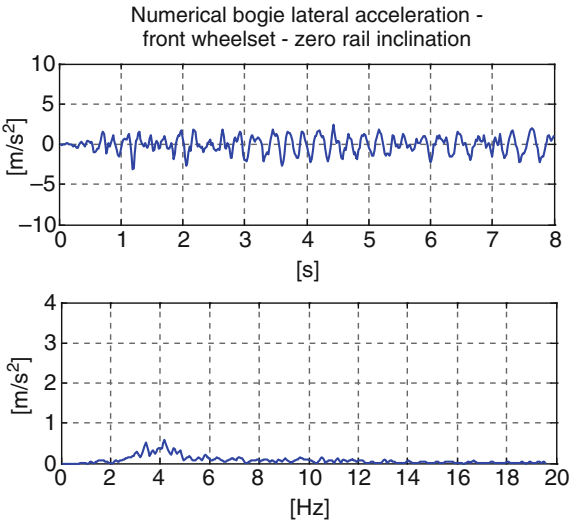

Fig. 10 Simulated bogie lateral acceleration above left axlebox of front wheelset due to wheel – rail couple once rail inclination is reduced to 0

Table 2 Filtered RMS values of the bogie lateral acceleration above the axlebox of the leading wheelset obtained from numerical train-track simulations

	Rail inclination		
Vehicle speed (km/h)	1/20 (original) (m/s^2)	$1/40(m/s^2)$	$0(m/s^2)$
75	3.25	1.54	0.97
85	3.49	2.08	1.17

lateral acceleration. An inclination of 1/40, although not optimal, allows to reduce the RMS value of the simulated bogie lateral acceleration of about 40–50%.

4 Low-Cost Solution

Based on the conclusions drawn from the multibody simulations, the stakeholder decided to reduce the rail inclination in one of the most critical locations along the track to 1/40 thus allowing to experimentally verify the proposed low-cost solution. The same measuring setup as described in paragraph 2 was adopted.

Figure 11 shows the measured bogie lateral acceleration above the left axlebox of the front wheelset on one track section with original rail inclination and a following track section where the rail inclination was reduced to 1/40. Figure 12 shows the corresponding vehicle speed. Although the vehicle speed is almost equal on the two sections, the bogie lateral acceleration becomes almost a half on the track section with reduced rail inclination (track irregularity was not measured but can

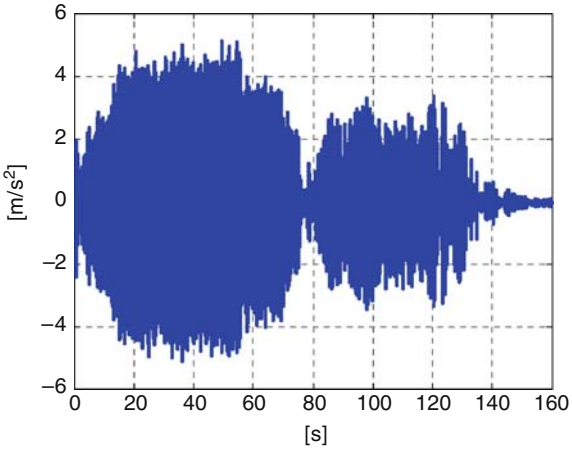

Fig. 11 Measured bogie lateral acceleration above left axlebox of front wheelset on original and modified track sections

be assumed as being equal on the two sections). The effectiveness of the proposed low-cost solution for increasing the critical vehicle speed (speed at which hunting instability occurs) has therefore been proven.

Figures 13 and 14 show the bogie lateral acceleration spectrum obtained form the measured signals. Again, the amplitude of the resonance peak at 5 Hz is significantly smaller in case of reduced rail inclination thus showing that the no hunting instability occurred.

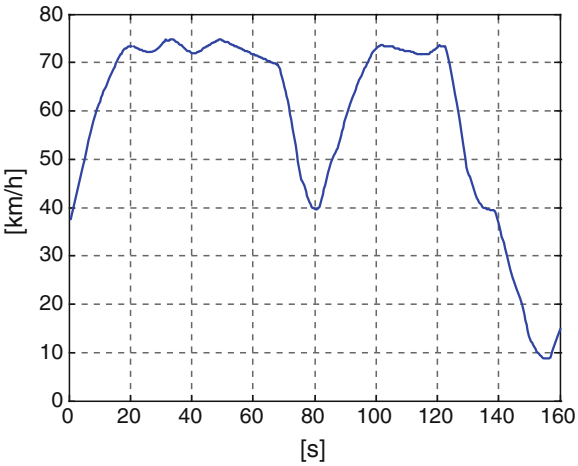

Fig. 12 Measured test vehicle speed on original and modified track sections

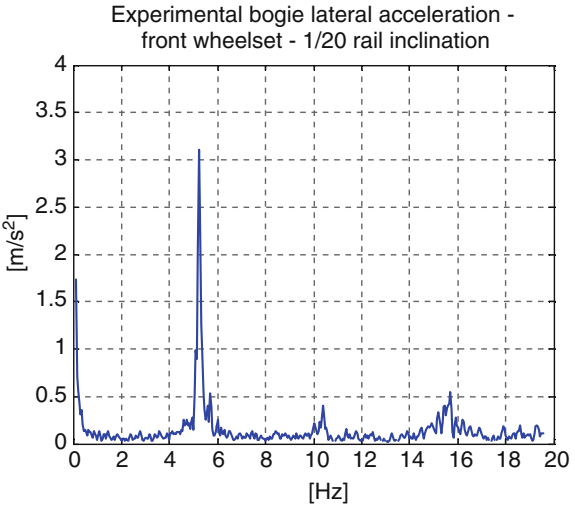

Fig. 13 Measured spectrum of bogie lateral acceleration above left axlebox of front wheelset on original track

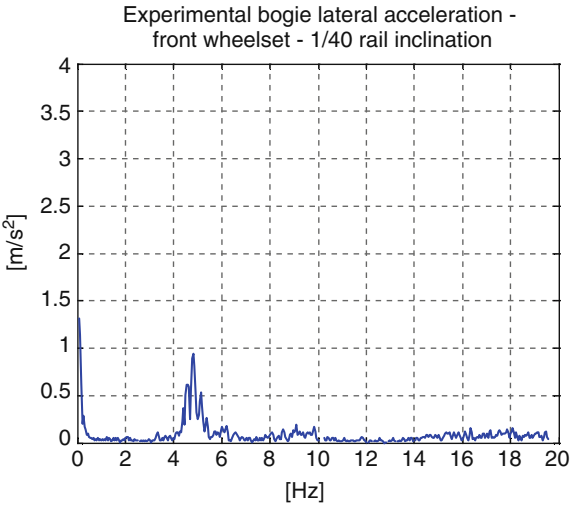

Fig. 14 Measured spectrum of bogie lateral acceleration above left axlebox of front wheelset on modified track

5 Conclusions

In the presented paper, a low-cost maintenance operation for suppressing hunting instability occurring on a section of a metro line is described and experimentally tested. On the considered track, metro trains were suffering from hunting instability already at the relatively low speed of 60 km/h, thus preventing them to reach

their maximum operating speed of 85 km/h and requiring wheel re-profiling after approximately 25000 km. The cause of such unstable motion was identified in the highly worn rail profiles that determined a highly conformal contact with wheel profiles. The level of conformity of wheel-rail profiles led to equivalent conicity values (calculated according to [1]) in some cases higher than 0.8. The main cause was found to be the very low damping of the bogie suspensions.

Since the installation of anti yaw dampers on all vehicles was judged economically unfeasible, the problem was solved by changing rail inclination and thus modifying contact conditions between wheel and rail. Numerical simulations showed that a zero inclination angle would have allowed to gain the highest increase in the vehicle's stability and that there is a clear dependence between the high equivalent conicity and the vehicle's critical speed. Nevertheless the stakeholder decided to reduce the original rail inclination instead of removing it. Although not optimal, this maintenance operation still allowed the avoidance of hunting motion up to the vehicle's maximum speed. Experimental results, before and after the maintenance operation, are presented and compared to numerical simulations obtained with a nonlinear vehicle – track interaction model ([2]).

References

1. UIC code 519, Method for determining the equivalent conicity, 1st edition, UIC, December 2004
2. Bruni S., Collina A., Diana G., and Vanolo P., Lateral dynamics of a railway vehicle in tangent track and curve: tests and simulation. Vehicle System Dynamics, Vol. 33, Supplement, pp. 464–477, 1999
3. Polach O., On non-linear methods of bogie stability assessment using computer simulations, Proceedings of the Institution of Mechanical Engineers, Vol 220 Part F: J. of Rail and Rapid Transit, pp.13–27, 2006
4. Braghin F. and Bruni S., Critical Velocity of Railway Vehicles, Proceedings of the 10th MINI Conference on Vehicle System Dynamics, Identification and Anomalies 2006
5. Alfi S., Bruni S., and Mazzola L., Effect of motor connection on the critical speed of high speed railway vehicles, Vehicle System Dynamics, Vol. 46, Supplement, pp. 201–214, 2008

Acoustic Optimization of Wheel Sets

Michael Beitelschmidt, Volker Quarz, and Dieter Stüwing

1 Introduction

In recent years, railway noise has become a high profile issue and the industry has come under pressure to reduce operating noise because legislative rules concerning noise emission will be tightened in the near future. Especially for freight traffic there is a need to improve, i.e. to reduce, the noise generation of rolling stock.

It is well-known that the major noise source of a rail vehicle is the wheel-rail contact, so the research has been directed primarily at this area. On freight vehicles the use of tread brakes directly influences the wheel-rail noise as this brake type cannot only be noisy in itself, but also lead to noise producing irregularities in the wheel surface. The replacement of conventional cast iron brake blocs with composite blocks is one major research result to achieve smoother wheel surfaces, thus reducing the vibrational excitation of both wheel and rail, in turn leading to lower noise.

The part nearest to the contact zone is obviously the wheel set, hence it is directly excited by the dynamic contact forces and structure born sound is emitted as the wheel disc is forced to vibrate. A second way to reduce wheel rail noise therefore is to reduce the sensitivity of bogie parts to the excitation, i.e. to improve the structural vibration behaviour.

While research projects, such as Silent Freight or Low Noise Train, focus on damping vibrations by applying absorbers, here the idea is to reduce the modal density of the wheel set in the frequency band of excitations caused by the surface irregularities of wheel and rail.

M. Beitelschmidt (✉)
Institut für Bahnfahrzeuge und Bahntechnik, Technische Universität Dresden, Hettnerstraße 3, D-01062 Dresden, Germany
e-mail: michael.beitelschmidt@tu-dresden.de

P.G. Thomsen, H. True (eds.), *Non-smooth Problems in Vehicle Systems Dynamics*,
DOI 10.1007/978-3-642-01356-0_6,

2 The Optimization Method

The sound level of noise, emitted by the wheel disc, results from a process, which is mainly characterized by the following three stages [cf. 1]:

1. The force excitation in the rolling contact. Its amplitude may be reduced e.g. by rail grinding.
2. The occurrence of wheel structure-borne sound, due to the force excitation. Applying dampers or acoustically optimizing the wheel shape allow to significantly reduce this structure-borne sound.
3. The sound radiation, which depends on the level of efficiency, describing the transformation of structure vibrations into emitted sound. This radiation efficiency may not be significantly influenced in the frequency band of interest.

The most promising way to reduce rolling noise is obviously to consider the wheel structure-borne sound, as the other two stages are hard to be influenced by the wheel manufacturer or the rolling stock operator.

The optimization approach is therefore based on a numerical modal analysis of the wheel resp. wheel set, using a FEM-package. The so gained distribution of eigenmodes in the frequency band of interest may then be compared to the frequency band of excitations.

As the frequency dependent characteristics of the excitations are known, e.g. typical wavelengths of rail corrugation, the frequency band of excitations can be determined as a function of the vehicles' velocity range.

The aim of acoustic optimization is to shift the acoustically relevant eigenmodes out of this frequency band, i.e. to reduce the modal density. This is achieved by modifying the wheel shape in an appropriate manner – which is not a trivial task as constructive restrictions have to be considered so that the parameter space for optimization is limited.

3 On the Modal Behaviour of the Wheel Set

The wheel set's modal behaviour is characterized by coupled bending, torsional and longitudinal vibrations. The axle shows all three vibration types, while the wheels vibrate in axial and radial direction. The wheel vibrations may be divided into umbrella oscillations with circumferential knot lines and "blower oscillations" with radial knot lines or combinations of both.

Here, eigenmodes are distinguished by their dominant deformation and the number of radial and circumferential knot lines. So, the abbreviation "A,1,2" denotes an axially dominated eigenmode with one circumferential knot line and two radial knot lines, and "R,0,2" is dominated by a radial oscillation with two radial knot lines. The latter is of interest here, because it is coupled with significant axial amplitudes.

Eigenmodes with axial plate oscillations of the wheel discs and one radial knot line are always coupled with bending oscillations of the axle, while umbrella oscillations of wheel discs are coupled with longitudinal oscillations of the axle.

"Blower oscillations" or coupled modes with two or more radial knot lines do not affect the axle. These are only weakly damped.

The most important eigenmodes for acoustic optimization are axially dominated oscillations with circumferential knot line in the tyre as the above mentioned "A,1,2", because the oscillating wheel disc surface causes a significant sound radiation. Also, bending oscillations of the axle coupled with axial wheel oscillations, as "B,2 +A,0,1", are of importance.

4 Optimization Examples

Applying the above described optimization approach, a first wheel prototype has been developed for operating speeds up to 240 km/h [2]. The wheel was manufactured by an industrial partner and tested under real conditions in comparison to conventional wheels (Fig. 1).

The wheel showed the expected noise reduction, but this design concept is not further developed, because it is relatively pricy to manufacture – due to its complex shape. Furthermore it could not completely satisfy requirements for block brakes.

Instead, another wheel type – the so called BA 004 – has been chosen to develop a second version for freight traffic. The BA 004 shows good thermal behaviour; a promising starting point to get an optimized shape, which will not cause problems concerning the thermal load capacity.

In this second step, not only the wheel but the whole wheel set has been optimized, to take into account the acoustically relevant eigenmodes with axle bending.

To identify eigenmodes of interest for acoustic optimization, a resonance plot is generated. Therein, eigenfrequencies over excitation frequency are plotted. Straight

Fig. 1 Prototype of the first optimized wheel

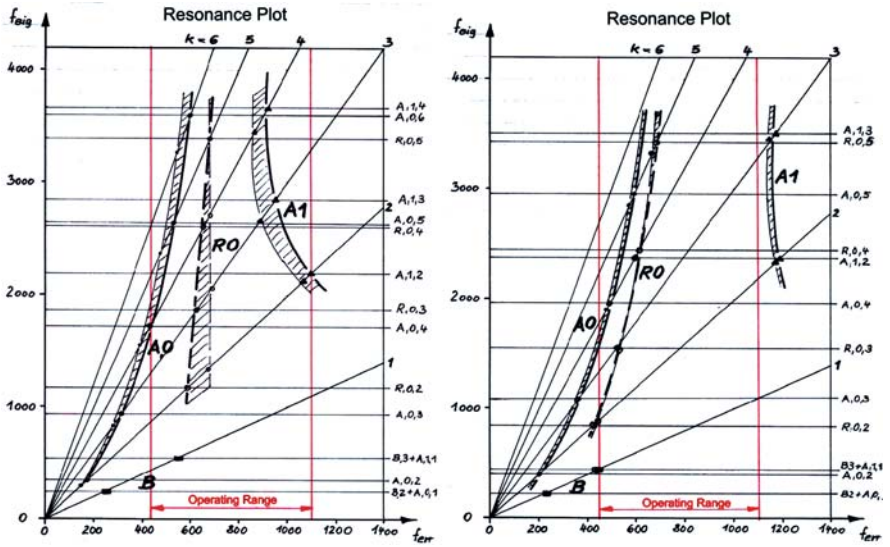

Fig. 2 Resonance plot of reference wheel set (BA 004 – *left*) and optimized wheel set (*right*)

lines with constant gradient, starting at the origin, represent harmonic orders of excitation (Fig. 2).

The resonance plot (Fig. 2, left) shows that three eigenmodes are affected in the frequency band of excitations. These are "R,0,2", "A,1,2" and "B,3 + A,1,1".

To avoid resonances with these eigenmodes, the wheel set has to be optimized, such that "R,0,2" is shifted under 880 Hz and "A,1,2" above 1200 Hz. The eigenmode "B,3 + A,1,1" with axle bending has to be shifted under 440 Hz.

In order to optimize the wheel shape, the wheel disc's cross section between tyre and hub has been parameterized. Several optimization algorithms have then been

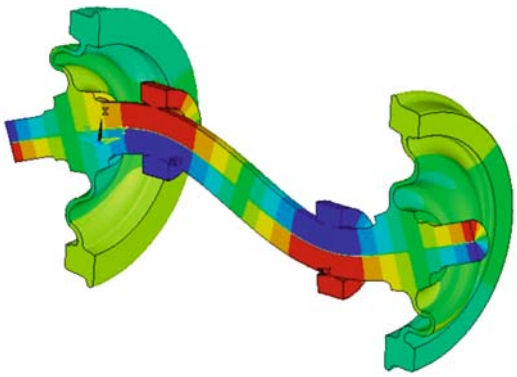

Fig. 3 Acoustically optimized wheel set for freight traffic. Visualization of a bending mode

applied to modify the wheel shape. One important boundary condition has been an upper wheel mass limit of 380 kg.

The optimization result is shown in (Fig. 2) on the right: additional masses on the axle help to shift the bending mode **down** to the operating ranges lower bound. The axially dominated mode is increased at about 200 Hz, while the radially dominated is decreased at about 330 Hz. Eigenmodes remaining in the operating frequency range are of less influence. The FE-model of the optimized wheel set is shown in (Fig. 3).

The new wheel set promises even better acoustic behaviour than the first version, being at the same time less cost intensive to produce.

References

1. F. G. Kollmann. Maschinenakustik: Grundlagen, messtechnik, Be-rechnung, Beeinflussung. 2. neubearb. Aufl., Springer, Berlin, 2000.
2. D. Stüwing, Schalltechnische Strukturoptimierung eines Vollrades für Reisezugwagen mit Fahrgeschwindigkeit bis v = 240 km/h, internal report, TU Dresden, 2001.

Measurement, Modelling and Simulation of Curve Squealing of Trains

Christoph Glocker, Eric Cataldi-Spinola, Rossano Stefanelli, and Jürg Dual

Abstract Curve squealing of railway wheels occurs erratically in tight curves with a frequency of about 4 kHz. Squealing is caused by a self-excited stick-slip oscillation in the wheel-rail contact. The mechanism which activates squeal is still unexplained and will be analyzed in the paper at hand. By starting with a modal model of the elastic wheel equipped with a three-dimensional hard Coulomb contact, a stability analysis of the stationary run through a curve is performed for the four wheels of the investigated bogie. The results show that in particular the front inner wheel tends to squeal. A numerical simulation performed on the unstable states shows the existence of a self-excited stick-slip oscillation with a frequency that compares well with the ones measured at squeal.

1 Introduction

Curve squealing occasionally arises when railway vehicles run through tight curves at low speed. It is characterized by a narrow-banded noise emission in the range of 4000 Hz, which normally occurs for some seconds. Curve squealing belongs to the class of self-induced vibrations. In contrast to external and parametric excitation, self-induced vibrations require the system to be nonlinear. The source of squeal has to be attributed to the wheel-rail contact: Creep between wheel and rail, which always occurs because of the kinematic design of the curve in combination with the wheel sets, induces frictional vibrations in the contacts which manifest themselves as structural oscillations in the range of micrometers of the wheels and rails.

Swiss Federal Railways (SBB) in the person of Roland Müller have been started cooperating with the Center of Mechanics at ETH Zurich. Within this cooperation, two doctoral theses [1, 2] have contemporaneously been written. Together, they provide a rather complete analysis of curve squealing, from the mechanism of self-excitation up to the emission of noise, and may establish a basis for systematic development of remedial actions. The work [2] has focused more on the

C. Glocker (✉)
IMES - Center of Mechanics, ETH Zurich, Switzerland
e-mail: glocker@imes.mavt.ethz.ch

P.G. Thomsen, H. True (eds.), *Non-smooth Problems in Vehicle Systems Dynamics*,
DOI 10.1007/978-3-642-01356-0_7,

experimental characterization of the squeal phenomenon, in which on-site measurement of the noise and the parameters responsible for it takes the center stage. A mechanical model of the mechanism of self-excitation has been developed in [1], for which the data from [2] have been used as inputs. The paper at hand reports on the results obtained for the numerical-experimental analysis of the mechanism of self-excitation. They are mainly taken from [1] but supplemented with measurements from [2].

Experience of many years in non-smooth dynamics have led to the strong belief that analyzing mechanisms of friction-induced vibrations requires utmost carefulness in both, the modeling of the mechanical system and the selection of the numerical schemes. Therefore, the following strategy has been chosen: The degrees of freedom to be taken into account in the squeal model are extracted from a FE-computation and succeeding modal reduction of an elastic wheel which is shown in Sect. 3. In order to properly apply the contact forces on this model, the stationary run of a driving trailer through a curve is studied in Sect. 4 with a commercial multi-body code. As results, the stationary state of all wheels, and in particular the location of the contact points, the inclination of the contact plane, the direction and magnitude of the creep and the contact forces are then known. In Sect. 5, data from Sects. 3 and 4 are combined to set up the mechanical model for curve squealing. Special attention is paid for the model of the wheel-rail contact, for which a hard unilateral constraint has been used in the normal direction, and a Coulomb friction element in the two tangential directions. Based on this model, curve squealing is numerically analyzed with the institute's research code in Sects. 6 and 7.

2 Measurements

In this section, some results of the field measurements performed in [2] are summarized. They will serve as a basis for developing the squeal model. Measurements have been taken during regular train service in three phases in a relatively tight curve (radius 200 m, gauge 1450 mm, cant 110 mm, rail inclination 1:40, rail type UIC54E) on track 303 near the station Bern-Ausserholligen, in which trains are running at low speed and squeal has frequently reported to occur. The vehicles singled out for the measurements are particular regional trains of SBB (series 560) composed of a rail car, a driving trailer (type Bt 29-30) and some intermediate cars, which periodically run on this track. As shown in [2], the squealing wheel has been found in many cases to be the leading inner wheel of the leading bogie of this driving trailer, and squealing has been around 4100 Hz. Because of this, the driving trailer has been chosen as the vehicle subjected to closer investigation (Sect. 4), and its utmost front inner wheel as the one of central interest.

Both sides of the track have been equipped with a free-field electret condenser microphone to record the noise generated by the squeal. The recorded signals have been processed by a short-time FFT and displayed as color-coded frequency-time diagrams, in which the time instances of the wheel axles passing the microphones

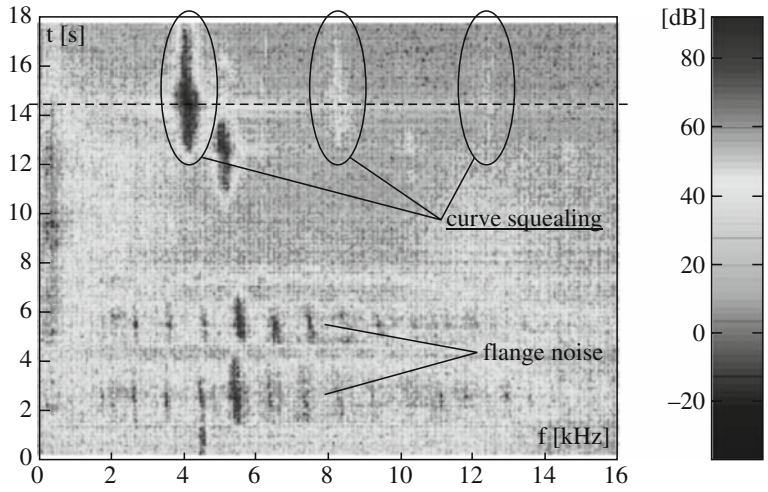

Fig. 1 Frequency spectrum of the noise recorded at one microphone. Recording is initiated when the first wheel set passes the microphone. The squealing wheel set is marked by a dashed line

have additionally been marked (Fig. 1). In order to measure the vibrations of the rails, triaxial acceleration sensors have been installed at the bottom of both rails.

The velocity of the axles passing by has initially been determined by axle counters, but has later been replaced by a couple of laser distance sensors on each rail. In this way, the lateral displacements and the angles of attack of the wheels relative to the rail could have been accessed from the distances measured to the wheel rims.

Figure 1 shows the frequency spectrum of the noise of a train passing by, which has been recorded by one of the microphones. Squeal can be observed between 12 and 18 s. In addition to the fundamental frequency of about 4 kHz, distinct superharmonics at 8 and 12 kHz are clearly seen in the diagram, which points at the strong nonlinear character of squeal. Furthermore, one observes a slight shift of about 150 Hz in the fundamental frequency, which occurs at the very instance at which the squealing wheel passes the microphone. This shift has also been found in the signals of the acceleration sensors and can be ascribed to the Doppler effect [2], indicating that the noise is mainly emitted from the wheel but not from the rail. Because of this, only the wheel is modeled in Sect. 3 as an elastic body, whereas the rail is considered as rigid for the entire analysis. Flange noise can also be observed in Fig. 1. It occurs between 2 and 6 seconds and can clearly be distinguished from curve squealing, as it is characterized by a wide-band frequency spectrum caused by the front outer wheel of the associated bogie.

3 Elastic FE Model of the Wheel

For the FE-analysis of the elastic wheel (elasticity modulus $2.068 \cdot 10^{11}\,\mathrm{N/m^2}$, Poisson ratio 0.29, density $7820\,\mathrm{kg/m^3}$) commercial software has been used. The middle diagram in Fig. 2 shows a cross-section of the mesh which has been mod-

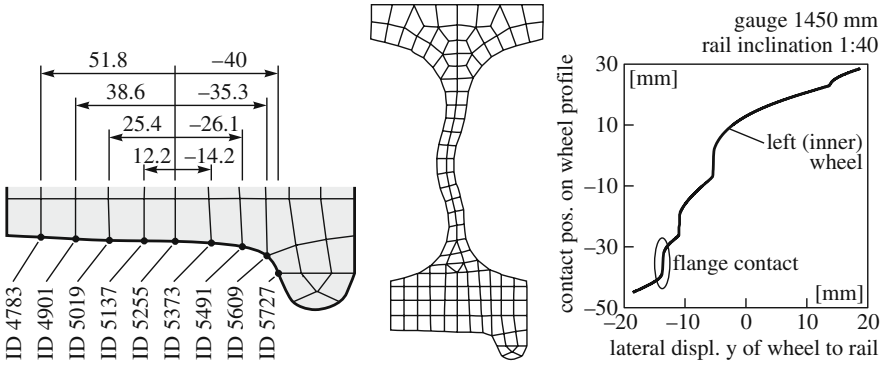

Fig. 2 *Left two diagrams*: Cross-section of the mesh and identification of the FE-nodes on the tread (wheel diameter 820 mm). – *Right diagram*: Profil pairing for wheel S1002 and rail UIC54E

eled by 8-node linear solid elements and proven to be reliable up to frequencies of about 6000 Hz. The mesh is designed at the wheel rim such that changes in the wheel diameter can easily be adjusted. Such changes occur during the lifetime of a wheel due to reprofiling of the tread as a maintenance procedure, which reduces the wheel diameter step by step from 820 mm for a new to 760 mm for a worn wheel. The cross-section of the mesh in Fig. 2 consists of 122 elements, which results in a total of 12720 elements and 48960 degrees of freedom for the wheel. The left diagram shows the position of the FE-nodes on the tread of the wheel and is later used to determine the node on which the contact force acts. All calculations are performed with a mesh that is fixed on the wheel. The rotation of the wheel relative to the mesh and the wandering of the contact force along the circumference are neglected.

The FE-model of the wheel has been validated by experimental modal analysis with a laser scanning vibrometer for two different situations, i.e. for a free wheel at ETH and a wheel mounted on the driving trailer at SBB works in Zurich. The wheels are excited up to 10 kHz on their rims in axial direction by a piezo element with a periodic chirp signal. Figure 3 shows the results of this comparison. In the left column, computed eigenforms are displayed for the two boundary conditions that the wheel is either freely floating or inertially fixed at its center nodes to take into account the connection to the axle as it is for a mounted wheel. All measurements and calculations for the free wheel have been conducted for diameters of 820 and 760 mm. In all cases, the computed eigenfrequencies deviate for less than 5% over the entire frequency spectrum of up to 6 kHz from those having been measured. Interestingly, the wheel-rail contact, which has not been considered in the FE-calculations but is present in the measurements of the mounted wheel, seems to have only minor influence on the results: If possible, the eigenforms align themselves at the wheel such that one of their nodal points agrees with the wheel-rail contact point. In other words, the dynamics of the mounted wheel under contact with the rail seems to be adequately represented by the eigenforms for the wheel

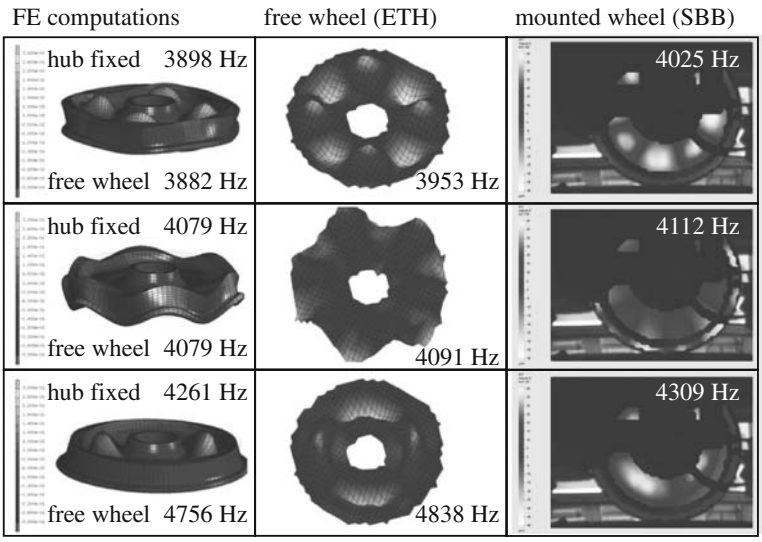

Fig. 3 Calculations versus measurements of selected eigenforms under different boundary conditions for a wheel with a diameter of 820 mm

with only the center nodes fixed. This set of eigenforms will therefore be used for setting up the squeal model by modal reduction in Sect. 5.

4 Multibody Simulation of the Stationary Run

For the simulation of stationary runs through curves of the driving trailer, type Bt 29–30, a commercial multibody simulation program has been used. The model of the driving trailer is schematically depicted in Fig. 4. It consists of the car body, the two bogie frames and the four wheel sets, which are connected to the bogies by axle guides. All bodies are modeled as rigid. The catch, the primary and secondary suspensions which use the Krettek-Grajnert air spring model [3], the anti-roll bar, the vertical primary damper as well as the lateral dampers are represented as force elements. All data are as much as possible extracted from the technical documentation of the vehicle or have been chosen in close cooperation with railway experts. The track in Ausserholligen is modeled as three sections: A straight track of 15 m length, followed by a 15 m long transition curve in which the cant of 110 mm and the curvature is uniformly established, followed finally by the curve with constant radius of 200 m. The complete track is modeled with an inclination of 1:40, a gauge of 1450 mm and the standard rail profile UIC54E. Flexibility of the rail and supporting underground as well as all sorts of irregularities are not considered. All calculations are conducted with the standard wheel profile S1002 and the wheel-rail contact model of Polach [4] which has been available in the multibody code.

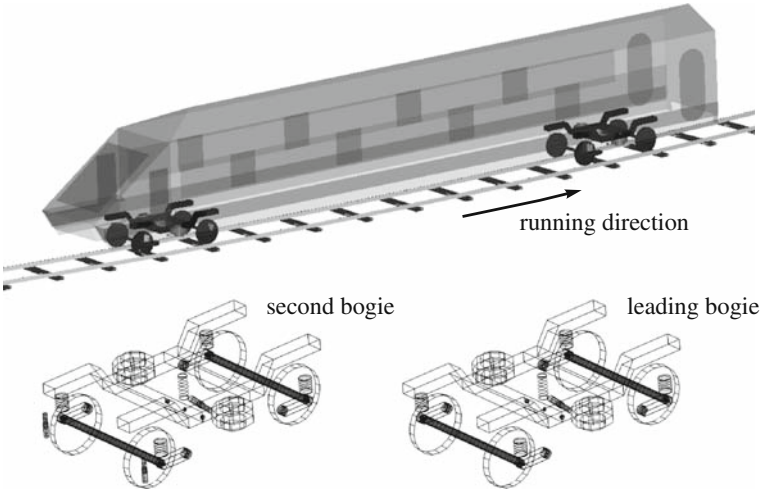

Fig. 4 Multibody model of the driving trailer and of its two bogies

Figure 5 depicts the coordinates which are necessary for the interpretation of the simulation results. They are shown exemplary for the curve inner wheels of each wheel set. For each wheel, a reference system $(\mathbf{e}_x^R, \mathbf{e}_y^R, \mathbf{e}_z^R)$ is defined, of which the $\mathbf{e}_x^R$ axis lies in the horizontal plane and is tangential to the rail in the contact point. The $\mathbf{e}_y^R$ axis is inclined with respect to the horizontal plane by the cant angle. Further, a contact system $(-\mathbf{n}, \mathbf{t}_1, \mathbf{t}_2)$ is introduced for each wheel, of which the orientation is determined by the simulation results. This contact system follows from the angle of attack β around the $\mathbf{e}_z^R$-axis, and, subsequently, from the contact angle α around the new $\mathbf{e}_x^R$-axis. Herein, the vectors $\mathbf{t}_1$ and $\mathbf{t}_2$ span the contact plane, $\mathbf{n}$ is the contact normal, and $\mathbf{t}_1$ lies in the plane of the wheel. Except for the contact angle α, all angles are assumed to be small. It therefore does not play a role in which order

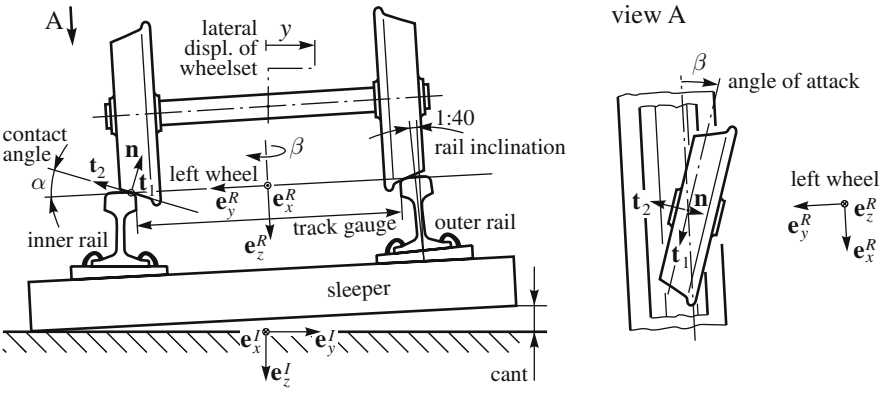

Fig. 5 Kinematic model of the wheel sets and definition of the associated coordinates

Table 1 Results from the multi body simulation for the front inner wheel of the leading bogie Units: f_i in kN, χ_{Tk} in $\frac{\text{mm}}{\text{s}}$, α in deg, β in mrad, y in mm

μ	f_x	f_y	f_z	χ_{T1}	χ_{T2}	α	β		y		node ID
0.1	−0.04	−6.02	−50.62	0.4	−64.9	1.17	15.77	wet	11.60	wet	5019
0.2	−1.41	−11.02	−50.12	8.1	−61.3	1.38	14.92		13.49		5019
0.3	−3.61	−15.63	−49.90	13.4	−58.3	1.40	14.19	∼ 15	13.62	∼ 10.5	5019
0.4	−6.30	−20.01	−49.76	17.6	−57.0	1.40	13.87		13.64		5019
0.5	−9.28	−24.25	−49.74	20.4	−55.8	1.40	13.59		13.66		5019
0.6	−11.76	−28.70	−49.77	21.6	−54.9	1.41	13.38	dry	13.67	dry	5019

the various angles are applied to finally arrive at the contact angle. Furthermore, it does not matter in which approximate radial directions the likewise small lateral displacements y of the wheel sets are interpreted.

The aim of the simulations is to predict the stationary motion of the driving trailer on the curved track for a chosen constant driving velocity and friction coefficients. The nominal values of the resulting loads and contact-kinematical parameters of each wheel have to be extracted from these simulation results. Table 1 shows the illustrative results for the leading curve-inner wheel of the leading bogie, which have been calculated for a driving velocity of 4.1 m/s, being typical for curve squealing, and for various friction coefficients. The triple (f_x, f_y, f_z) denotes the components of the contact force acting on the wheel displayed in the reference system $(\mathbf{e}_x^R, \mathbf{e}_y^R, \mathbf{e}_z^R)$, (χ_{T1}, χ_{T2}) are the creep velocities of the wheel relative to the rail in the directions $(\mathbf{t}_1, \mathbf{t}_2)$ at the contact point, β and α are the resulting angle of attack and the contact angle, and y is the lateral displacement of the wheel set as defined in Fig. 5. From the latter, the position of the contact point on the tread can be determined by the wheel-rail profile pairing diagram in Fig. 2. Subsequently, the FE node closest to the contact point is identified from the left diagram in Fig. 2 which approximately determines the point at which the contact force acts. In addition, the angle of attack β and the lateral displacement y have been measured by using a pair of laser distance sensors being attached to the rails on each side of the track, where various friction coefficient have been realized by artificial wetting of the rail surface.

5 Design of the Squeal Model

Sections 3 and 4 provide all the data that are necessary to set up the squeal model illustrated in Fig. 6. In the model it is assumed that the center nodes of the wheel are fixed to the inertial frame, whereas the rail is moving relative to the center of the wheel with the (now negative) creep velocities from Table 1. The overall creep velocities are therefore the superposition of those for stationary motion from Table 1 and those stemming from elastic vibrations. The elastic model of the wheel uses the mass and stiffness matrices from the finite element calculation for a wheel with fixed center nodes. Furthermore, the node C on which the contact force acts, as well as the orientation of the contact system $(-\mathbf{n}, \mathbf{t}_1, \mathbf{t}_2)$ are already determined by Sect. 4. This allows us to incorporate into the system the contact forces $(\lambda_N, \lambda_{T1}, \lambda_{T2})$ acting

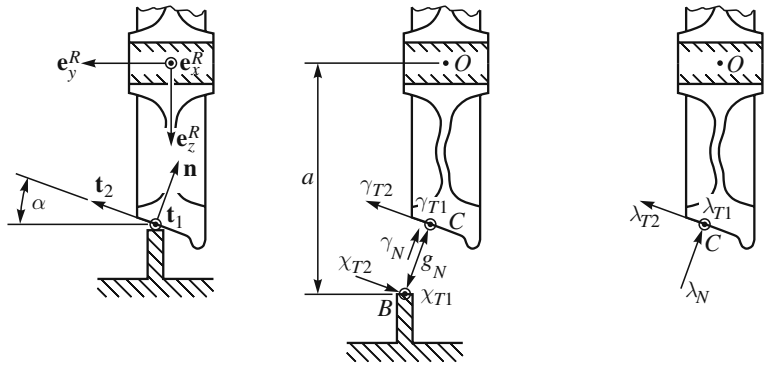

Fig. 6 The squeal model, consisting of the elastic wheel and the rigid rail. *Left diagram*: Orientation of the inertial and the contact frame. – *Middle diagram*: Definition of the contact kinematical entities. – *Right diagram*: Point of action and directions of the contact forces

at the contact node C in the directions $(\mathbf{n}, \mathbf{t}_1, \mathbf{t}_2)$. The middle diagram in Fig. 6 shows the entities necessary to describe the kinematics of the contact. These are the contact gap g_N in normal direction which can directly be calculated from the nodal displacements of point C, and the relative velocities $(\gamma_N, \gamma_{T1}, \gamma_{T2})$ of point C with respect to point B on the rail. The normal relative velocity γ_N is obtained directly by projecting the nodal velocities on the normal $\mathbf{n}$, whereas the tangential velocities γ_{Ti} consist of the differences in nodal velocities in the tangential directions and the creep velocities χ_{Ti}, which enter the model as kinematic excitation.

The contact is modeled as a hard unilateral constraint with spatial Coulomb friction and constant friction coefficient μ. The contact law in normal direction implies for a closed contact that the contact gap vanishes ($g_N = 0$) and the contact force acts as a compressive force ($\lambda_N > 0$). In tangential directions, the Coulomb friction law is employed which makes a clear distinction between stiction and sliding: If the magnitude of the tangential force $(\lambda_{T1}, \lambda_{T2})$ is smaller than $\mu\lambda_N$, then the contact is in stiction and we have $\gamma_{T1} = \gamma_{T2} = 0$. When the magnitude of the tangential friction force equals $\mu\lambda_N$, then the contact is allowed to slide, accompanied by a friction force $(\lambda_{T1}, \lambda_{T2})$ opposing the relative velocity $(\gamma_{T1}, \gamma_{T2})$. Drilling friction (pivoting friction) is not considered, as it is not essential for the squeal mechanism. The numerical code [5] is based on a complete mathematical description of these contact laws [6] which also allow for detachment and impulsive forces due to collisions.

The squeal model, which previously has been formulated in nodal displacements with already the contact forces contained, is subsequently reduced to the first 61 eigenforms from Sect. 3. This sufficiently approximates the system up to 6 kHz. In addition, the modal damping values of these 61 eigenforms have experimentally been determined in a laboratory setup [1] and taken into account in the equations of motion. The equations of motion expressed in the 61 modal amplitudes are therefore composed of the constant and symmetrical mass, damping and stiffness matrix, as well as of three constant generalized force directions for the contact forces

$(\lambda_N, \lambda_{T1}, \lambda_{T2})$, and of the contact force laws in normal and tangential directions. The gap function g_N depends now in principle on all the 61 modal amplitudes which serve as the generalized coordinates. Similarly, the relative velocities $(\gamma_N, \gamma_{T1}, \gamma_{T2})$ are dependent on the 61 modal velocities. In a last step, the distance a (Fig. 6) between the wheel center and the rail is adjusted such that the resulting normal contact force λ_N in the reduced (temporarily frictionless) model agrees with the associated component of the contact forces (f_x, f_y, f_z) obtained from the multibody simulation.

6 Stability Analysis of the Stationary Run

In this section, the stability of the stationary run through a curve is analyzed. By considering the equilibrium of the equations of motion for a given driving velocity, the 61 constant modal amplitudes for stationary sliding are determined for the constant creep velocities (χ_{T1}, χ_{T2}). The equations of motion are linearized around this equilibrium position. The only nonlinearity in the system stems from the direction of the friction force for sliding which is determined by the direction of the relative velocity in the contact point. The linearization of this nonlinear term contributes to both the stiffness and damping matrix, which destroys their symmetry and opens the possibility for dynamic instabilities. The (linear) stability is determined by the eigenvalues of this linearized system. For the particular case of curve squealing, this approach follows the theory in [7], in which general theorems on the stability of motion of systems with hard Coulomb contact are presented.

Figure 7 shows the results of this stability analysis for all four wheels of the leading bogie, which have been computed with the eigenmodes of an 800 mm wheel with fixed center nodes. The radial direction in the stability charts corresponds to the chosen friction coefficient, whereas the azimut angle addresses the numerically varied creep directions (χ_{T1}, χ_{T2}). Points in the stability charts, which correspond to the states calculated from the multibody simulation, are marked by black stars. For the leading inner wheel, these points correspond to the friction coefficient and creep velocities in Table 1. Points for which the real part of one of the eigenvalues is strictly positive are marked in dark grey and correspond to unstable stationary driving states. The points in light grey indicate asymptotically stable states. We infer from the upper left stability chart in Fig. 7 that the leading inner wheel is prone to instability, as the actual calculated states from the multibody simulation enter the unstable region already for small friction coefficients. Contrary, the inner second wheel is safely within the stability region. The results for the leading outer wheel are doubtful, because the flanging in the simulation is only modeled as a single but not as a more realistic double contact. The results of the outer second wheel indicate that the stationary motion is stable, at least in theory. However, uncertainties in the model and irregularities in the real system make this result questionable as the distance to the stability border is not big enough to ensure stability in praxis. These theoretical results agree with the measurements of Sect. 2.

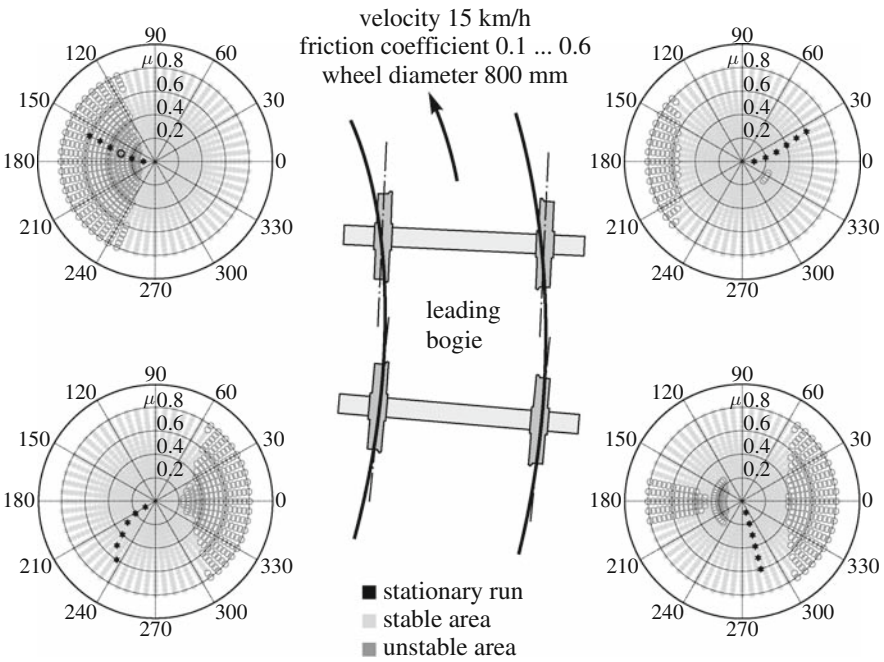

Fig. 7 Stability charts for the four wheels of the leading bogie

7 Numerical Simulation of Self-Excitation

In the linear stability analysis of Sect. 6 it has been shown that, in particular, the stationary run of the inner leading wheel can become unstable. However, it is still unknown whether this instability leads to a bounded oscillatory motion and how this oscillatory motion would look like. To this end, the nonlinear differential inclusions of the reduced model described in Sect. 5 are numerically simulated. The simulations have been conducted with a research code dedicated to mechanical systems with impact and friction. The time integration is performed with an half-implicit index-2-solver and the inequalities are solved with nonlinear projections [5].

The results of the simulations will exemplarily be shown for the leading inner wheel with the initial condition corresponding to the black circle in the upper left stability chart of Fig. 7. Hence, we consider the run of a wheel with a diameter of 800 mm, a friction coefficient of 0.3 and the associated data which follow from Table 1. Figure 8 shows the results of these simulations after the motion of the wheel has reached a periodic state and the initial transients have decayed. The upper diagram on the left-hand side of Fig. 8 shows the response of the friction force $(\lambda_{T1}^2 + \lambda_{T2}^2)^{1/2}$ (dotted line) which in stiction phases reduces to values much smaller than the stiction threshold $\mu\lambda_N$ (solid line). Both the longitudinal and lateral relative velocities γ_{T1} and γ_{T2} vanish during these stiction phases as is shown in the lower left diagram. The phase planes of the longitudinal and lateral contact displacements

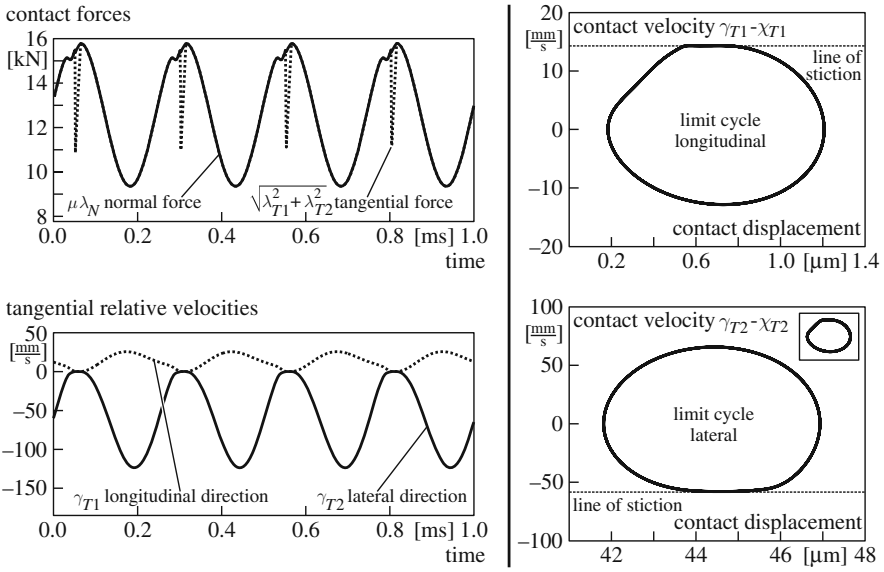

Fig. 8 Numerical simulation of the friction-induced self-excited oscillations at the leading inner wheel of the leading bogie

are depicted on the right hand side of Fig. 8 and reveal a limit cycle behavior. Note that the contact displacements are shown on the horizontal axes, whereas the contact velocities, being their time derivatives, are shown on the vertical axes. The latter equal the differences $\gamma_{Ti} - \chi_{Ti}$ of the relative velocities γ_{Ti} and the stationary creep velocities χ_{Ti}. Stiction ($\gamma_{Ti} = 0$) occurs in the phase planes when the contact velocities reach the lines of stiction indicated in the figures. The phase plane for the longitudinal direction clearly shows a corner in the limit cycle at the transition from sliding to stiction, i.e. when the line of stiction is hit, which is typical for stick-slip oscillations. This non-smooth effect is also present in lateral direction but hardly visible. The motion in lateral direction is much larger than the one in longitudinal direction as can be seen from the comparative inset in the lower diagram. We emphasize that each calculation has been conducted with one and only one friction coefficient, being independent of velocity and time, which serves at the same time as static and dynamic friction coefficient. The friction-induced limit cycle shown in Fig. 8 has a frequency of about 3.99 kHz.

A qualitative comparison of simulations and measurements is depicted in Fig. 9. The left diagram shows the frequency content of the measured squeal noise, corresponding to the dashed line in Fig. 1, and the FFT of the lateral contact velocity. In the right diagram, the measured frequency content of an acceleration sensor, being attached to the foot of the rail, is compared to the calculated lateral contact acceleration. This comparison, which is of only qualitative nature, reveals that the relative intensity of the superharmonic resonances in the measurements and simulations agree quite well.

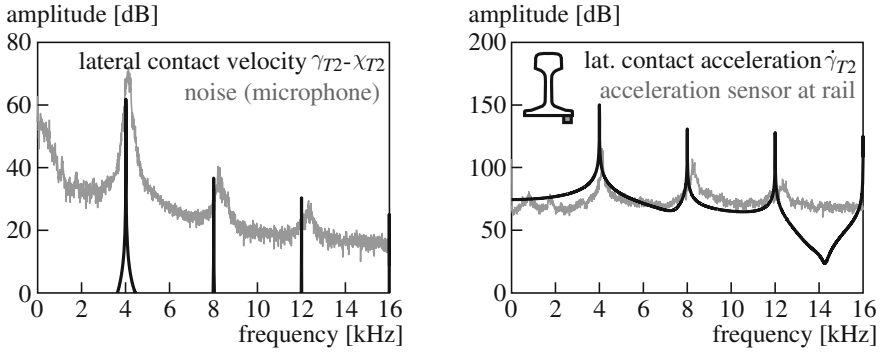

Fig. 9 Qualitative comparison of the frequency spectra at squeal obtained from numerical simulation and measurements

8 Conclusion

The proposed approach enables ones to completely describe the squeal phenomenon of railway vehicles. All phenomena related to squeal, which have occurred in the measurements or have been discussed with railway experts, can be explained by the results of the numerical calculations. Important parameters for the curve squeal phenomenon are the contact kinematical entities. Of equal importance is the geometry of the wheel which determines its eigenforms and frequencies, and of course the friction coefficient. The particular form of the friction curve, which is normally regarded to be of prime importance, plays in fact only a minor role. At present, three modes of the free wheel with fixed center nodes can be identified to be essential for the squeal mechanism. These three modes have to occur at similar frequencies, one for which the wheel oscillates in lateral direction at its rim, and two radial modes which allow for a variation of the normal force. Each calculation step presented in the paper opens the way to test arbitrary wheel designs and railway profiles on their vulnerability for squeal, in order to propose targeted changes in their design. From the theoretical point of view, a detailed bifurcation analysis of the system has still to be conducted. Furthermore, it still needs to be clarified how the choice of the eigenmodes in the system reduction influences the results, and whether the squeal phenomenon might finally be reduced to only two relevant modes.

References

1. Cataldi-Spinola, E.: Curve Squealing Mechanism of Railway Vehicles. Diss. ETH No. 17453, ETH Zürich (2007)
2. Stefanelli, R.: Kurvenkreischen: Untersuchung der Rahmenbedingungen, die zu Kreischen führen, und akustische Modellierung der kreischenden Räder. Diss. ETH No. 16686, ETH Zürich (2006)
3. Grajnert, J., Krettek, O.: Zur Phänomenologie und Ersatzmodellbildung von Luftfedern. ZEV+DET Glasers Ann. **115** (7/8), 218–223 (1991)

4. Polach, O.: Rad-Schiene-Modelle in der Simulation der Fahrzeug- und Antriebsdynamik. Elektrische Bahnen **99** (5), 219–230 (2001)
5. Studer, Ch.: Augmented Time-Stepping Integration of Non-Smooth Dynamical Systems. Diss. ETH No. 17597, ETH Zürich (2008)
6. Glocker, Ch.: Set-Valued Force Laws. Lecture Notes in Applied Mechanics Vol. 1, Springer, Berlin-Heidelberg (2001)
7. Martins, J.A.C., Barbarin, S., Raous, M., Pinto da Costa, A.: Dynamic Stability of Finite Dimensional Linearly Elastic Systems with Unilateral Contact and Coulomb Friction. Comput. Methods Appl. Mech. Engrg. **177**, 289–328 (1999)

Selected Problems of Non-linear (Non-smooth) Dynamics of Rail Vehicles in a Curved Track

Krzysztof Zboiński

Abstract The contribution presents four problems connected with the Colloquium topics. They are of theoretical nature in the wider aspect but all refer to the results of practical simulations of rail vehicle motion in a curved track. The first two can be counted to typical non-smooth problems in rail vehicle dynamics. They refer to two-point contact modelling and vehicle stability in curves, respectively. The third problem is closely related to the second one. It refers to railway vehicle dynamics above critical velocity in transition curves. The forth one can also be recognized as the non-smooth problem but not so typical one. It refers to modelling the kinematics in a curved track. All the problems reveal that one needs to be very careful when studying rail vehicle dynamics and trying to simplify its non-linearities at the same time. Non-smooth functions can influence results of numerical analysis strongly, being the features of the physical and modelling nature.

1 Introduction

As stated above four different problems are discussed in this work, related to non-smooth rail vehicle dynamics. The author faced them in numerical studies of the dynamics in a curved track Both circular and transition curves are of interest, here.

General aim of the paper is to present: the variety of problems of non-smooth character; the strength of influence of non-smooth functions on results of numerical analysis; and the nature of these functions, which arises from the system's physical features and the modelling techniques as well. Broad subject-matter of the present contribution causes that most space must be given to presentation of the simulation results revealing the essence of each problem. As a consequence, explanations of these problems represent in most the general ideas. Their details are presented in the highest volume possible, however their serious reductions influencing profoundness and ease of the understanding were unavoidable.

K. Zboiński (✉)
Faculty of Transport, Warsaw University of Technology, Koszykowa 75, 00-662 Warsaw, Poland
e-mail: kzb@it.pw.edu.pl

P.G. Thomsen, H. True (eds.), *Non-smooth Problems in Vehicle Systems Dynamics*,
DOI 10.1007/978-3-642-01356-0_8,

Modelling method, models and the objects were subject to analysis in many earlier works by the present author. That is why we represent them briefly, now.

2 Objects of the Analyses and Their Models

Simulation results presented concern three objects. These are hsfv1 freight car, bogie of MKIII coach, and 25TN freight car bogie. Kinematical structure of the first two objects is the same (Fig. 1a). The structure of the third object differs in two constraints ($\psi_l = \psi_b,\ \psi_t = \psi_b$). They describe no yaw rotations (ψ) of wheelsets ($l,\ t$) relative to bogie frame (b). Vehicle models are supplemented with laterally (Fig. 1b) and vertically (Fig. 1c) flexible track models. Depending on the object, vehicle-track system has got 18 or 16 DOF, respectively. Anyone interested in values of the system parameters should refer to [11–13].

Geometry in wheel/rail contact, tangential contact forces, calculated with use of the FASTSIM programme, and MBS kinematics constitute the non-linearities in the system. Linear suspension elements are adopted at the same time.

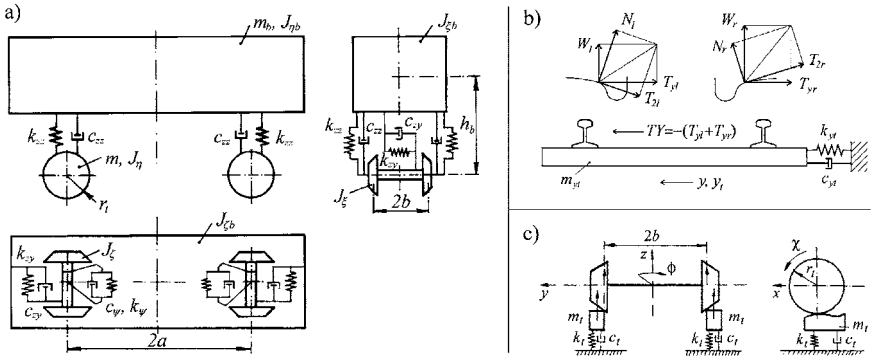

Fig. 1 Vehicle-track model's structure

3 Two-Point Contact Modelling, a Cause for Non-smooth Vehicle Model Properties

The problem treated here is related to modelling of two-point contact during curving, as well as contact parameters being tabulated at the same time (Fig. 2). Both above factors alone introduce non-smooth functions into the system. Here, their simultaneous impact on the results of simulation is shown.

Successive table columns in Fig. 2 define: n_p – number of contact points; y_{rel} – wheel/rail lateral relative shift; ϕ – wheelset's roll angle, $\delta r_l,\ \delta r_r$ – left and right wheels' rolling radii increments; $\gamma_l,\ \gamma_r$ – left and right wheels' contact angles; $P_l,\ P_r$ – left and right wheels' contact areas; $(a/b)_l,\ (a/b)_r$ – left and right contact

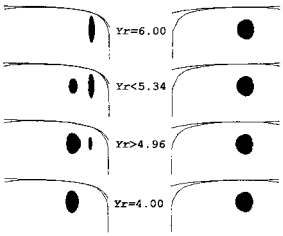

WHEEL/RAIL CONTACT PARAMETERS: Wheel BR-P10, Rt=920mm, Yaw=0, Track UIC60, Load=96.14kN

1	6.50	11.86	-.16	1.15	66.75	.46	49.59	77.05	6.915	1.342	.341	.728
1	6.40	10.10	-.15	.84	59.77	.47	45.29	77.72	2.915	1.311	.275	.740
1	6.30	5.23	-.15	.69	30.31	.48	70.94	77.67	1.547	1.293	.630	.740
1	6.00	4.31	-.15	.57	22.79	.48	40.29	79.24	4.102	1.264	.204	.764
2	5.34	3.35	-.14	.39	16.40	.48	36.90	81.50	4.580	1.190	.170	.800
2	4.96	1.26	-.14	.33	7.13	.48	67.90	82.70	1.680	1.160	.580	.820
1	4.00	1.09	-.13	.25	6.12	.48	65.88	86.14	1.778	1.060	.550	.875
1	2.00	.68	-.09	.11	4.51	.76	74.38	96.83	1.352	.830	.690	1.036
1	0.00	-0.00	.00	-0.00	1.35	1.35	128.00	127.95	.447	.447	1.414	1.414
1	-2.00	-.09	.68	-.11	.76	4.52	96.80	74.78	.830	1.367	1.036	.690
1	-4.00	-.13	1.09	-.25	.48	6.13	86.13	65.88	1.061	1.778	.875	.550
2	-4.96	-.14	1.26	-.33	.48	7.13	82.70	67.90	1.190	1.680	.820	.580
2	-5.34	-.14	3.35	-.39	.48	16.40	81.50	36.90	1.190	4.580	.800	.170
1	-6.00	-.15	4.31	-.57	.48	22.81	79.23	39.74	1.264	4.138	.764	.204
1	-6.30	-.15	5.23	-.69	.48	30.31	77.67	70.94	1.293	1.547	.740	.630
1	-6.40	-.15	10.10	-.84	.47	59.77	77.72	45.29	1.311	2.915	.740	.275
1	-6.50	-.16	11.90	-1.16	.46	66.89	77.04	49.62	1.342	6.847	.728	.341

Fig. 2 Graphical representation of 2-point contact and the corresponding contact parameter table

ellipses' semi-axes ratios; ρ_l, ρ_r – left and right functions of curvatures in contact. Each pair of neighbouring rows with n_p=2 defines terminal points of 2-point contact range.

In order to realize what may be the consequences of improper modelling these factors let us compare two methods. In the first (original) method no change of the parameters within 2-point contact range happened. The parameters were frozen for both contact points and did not change as a function of y_{rel}. Note, that no significant displacements of the patches are observed in Fig. 2. The only parameters being changed were contact patch areas. Their values were not directly interpolated basing on the terminal values but calculated as an effect of change in vertical load distribution between the terminal points of 2-point contact. That distribution was based on the linear interpolation with the factors (Fig. 3b) dependent of y_{rel} value.

In the second (modified) method extrapolation of the parameters as a function of y_{rel} within 2-point contact range was introduced. The function was used based on the ellipse shape (Fig. 3a) that allows for limited change. Actually, limited displacements of the patches can be observed from contact geometry programme (Fig. 2). Besides, this function exploits well known fact that in instance of 1-point contact linear interpolation works well. This explains why tangency of linear and non-linear factors in point K (Fig. 3a) was provided. Analytical form of this function is $SFACT = b\sqrt{1-(x-1)^2/a^2} - y_k$. Its values are fixed by $0 \le SFACT \le w$. The maximum value is limited by parameter w. In practise, the method works well for values close to $w = 0.15$. Again, contact patch areas are not interpolated directly but change as an effect of the vertical load distribution between the terminal points

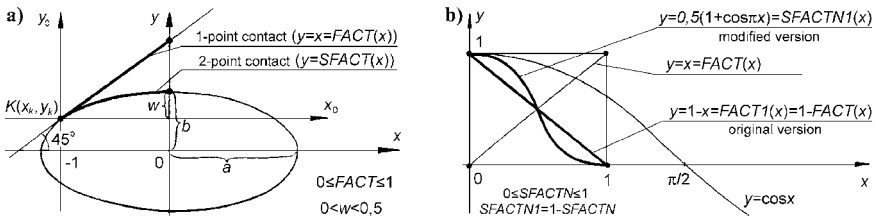

Fig. 3 Graphical representation for patches in 2-point contact of change in: **a)** interpolation and extrapolation factors for contact parameters, **b)** interpolation factors for vertical load distribution

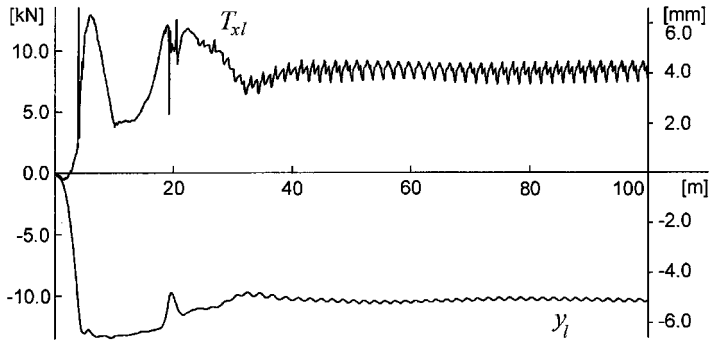

Fig. 4 Leading wheelset longitudinal contact force and lateral displacement before modification

of 2-point contact. This distribution is calculated using the non-linear (cosine based) interpolation, however (Fig. 3b).

Simulation results in present section concern leading bogie of MKIII coach. It runs (after short transition curve TC) along circular curve CC of radius R=450 m with velocity v=20 m/s. Such values guarantied 2-point contact for outer wheel of the leading wheelset. Longitudinal contact force T_{xl} for this wheel, influencing co-ordinates of vehicle lateral dynamics, is shown for both methods in Figs. 4 and 5, respectively. Additionally, leading wheelset lateral co-ordinate y_l is represented. It can be seen that unphysical oscillations observed in the standard case of tabulated data interpolation are entirely removed through the measures undertaken in the modified method.

The detailed analysis shown that the most important contact parameters in discussed context are rolling radii increments (this way rolling radii themselves). Change in their method of interpolation was the absolute necessity. Smooth vertical load distribution between the contact patches of 2-point contact is recommended although it appeared that the distribution on the linear basis is enough in some cases. The experience gathered while investigating the case presented is recently used by the author [19] in modelling tram/track interactions in tight curves.

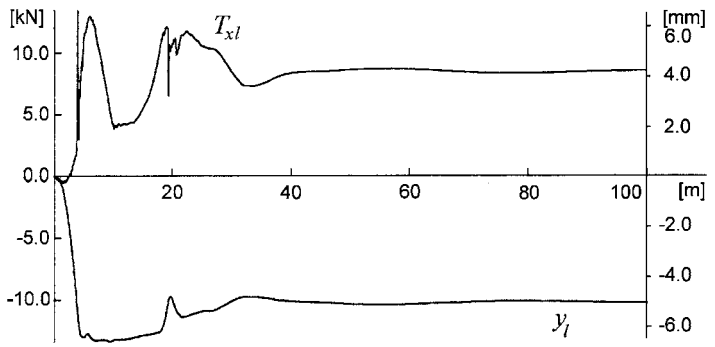

Fig. 5 Leading wheelset longitudinal contact force and lateral displacement after modification

4 Non-smooth Properties While Studying Stability in Curves

The second treated problem is connected with rail vehicle stability in a (circularly) curved track. Here, non-smooth properties of the system are of interest, which result from bifurcation(s) of the solution. Leading wheelset lateral displacement y_l is of interest in this context. Vehicle velocity v is the bifurcation parameter. Exceeding its critical value (critical velocity v_n – Fig. 6a, b) causes for vehicle model jump of the solution from stable stationary one to stable periodic one. Analogous behaviour of the real objects is also reported. In case of simple vehicle models, e.g. with non-linearities in wheel/rail geometry and forces as the major ones and with no non-linearities in the suspension, just described features of the system can be easily explained on the basis of self-exciting vibrations and bifurcation theories. So, in principle in the same way as for a straight track. The key elements here are sub-critical Hopf and saddle-node bifurcations that correspond to velocities v_c and v_n, respectively (Fig. 6a, b). Velocity v_s refers to unbounded growth of oscillations and the corresponding stop of calculations.

The results presented are limited direct contribution into development of general non-linear dynamics methods and theories, as they refer to the earlier methods known for a straight track, e.g. [4, 9]. However, the originality and importance of these results for the railway vehicle dynamics seem to be of high value indeed. It is author's contribution to the question of stability in curves and breaking down

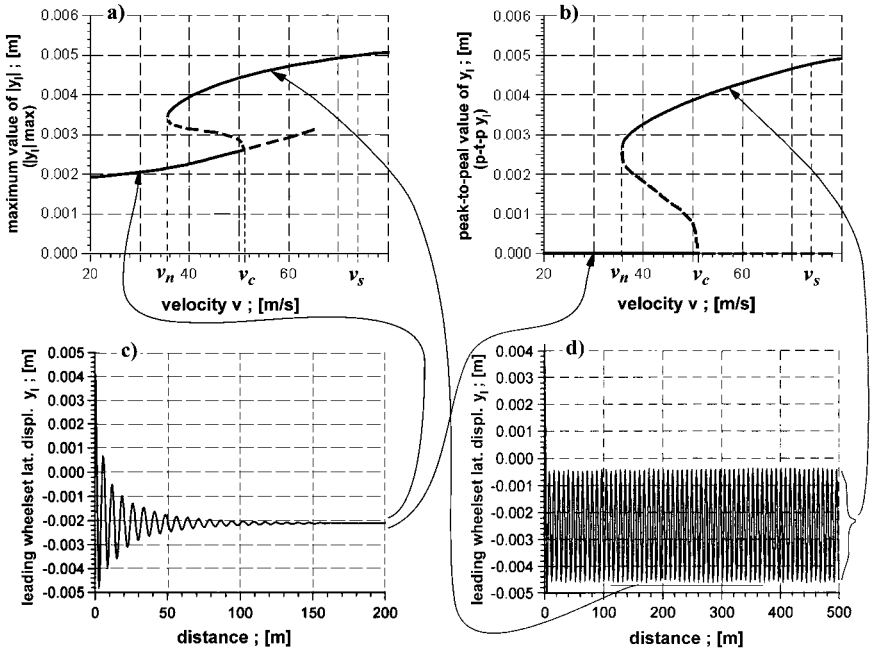

Fig. 6 View of bifurcation plots and idea of their creation in curved track stability analysis

the traditional approach that restrains to stability in straight track and exceptionally discusses stability in curved track. In spite of putting the problem explicitly [11] and later explicit studies by the author [15–18] and others [1–3, 5–8, 10, 20], a group of researchers and railway practitioners exists considering the hunting motion either to be absent in a curved track or to be unworthy of interest (consequently the stability). They advocate traditional opinion that periodic vibrations of constant amplitude (limit cycles) above critical velocity appear for straight track only, whereas in circular curves the motion is of quasi-static nature.

The curved track analysis is based on bifurcation plots, as it is for a straight track. The differences in bifurcation plots comparing to that case are: stable stationary solutions are not zero ones any more (Fig. 6a, c); a pair of bifurcation plots instead of one is necessary in order to take account of limit cycles non-symmetry in a curved track (Fig. 6a, b); each curve radius R calls for its own pair of bifurcation plots; combining the plots for different R into single diagram one can obtain stability map representing the model stability in whole range of R.

Consequently, practical results are presented in form of the stability maps composed of graph pairs (Figs. 7, 8, and 9). First graph in the pair represents ($|y_l|$ max), i.e. change in maximum of the lateral displacement absolute value $|y_l|$ versus v. The second one represents (p-t-p y_l), i.e. peak-to-peak value of y_l versus v, and enables to take account of limit cycles non-symmetry in curves. Both graphs include the lines matching circular track sections of different R (from small ones to straight track ST, where $R = \infty$). Each line is built following a series of single simulations for different v and the same R. Note that comparing to theoretical plots (Fig. 6a, b) the maps (Figs. 7, 8, and 9) do not represent unstable solutions (thick broken lines in Figs. 6a, b) and v_c, the critical velocity of linear system. They are of lower practical significance and their omission speeds up the calculations vastly.

Comparison of the maps corresponding to different vehicles or to the same vehicle with different values of its parameters enables to perform analysis of stability properties of such objects. Influence of various factors on the stability can be estimated this way, too. Some factors already studied are [1, 15, 17, 18]: way of regard to angle of attack, suspension parameters, track superelevation, wheel and rail

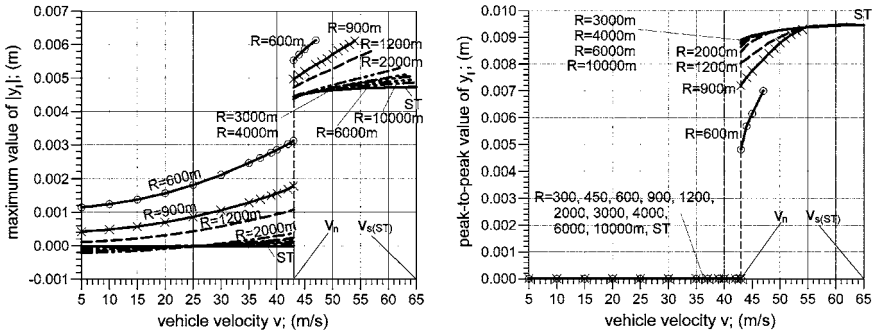

Fig. 7 Stability map for unworn S1002/UIC60 wheel/rail pair and 1:40 rail inclination; see [17]

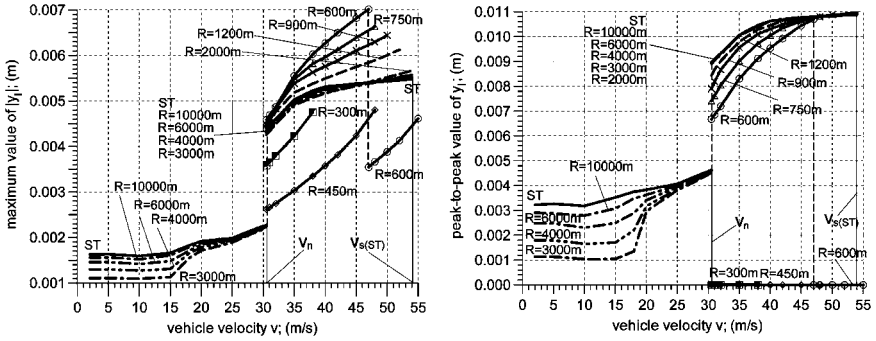

Fig. 8 Stability map for worn s1002/uic60 wheel/rail pair and 1:40 rail inclination; based on [17]

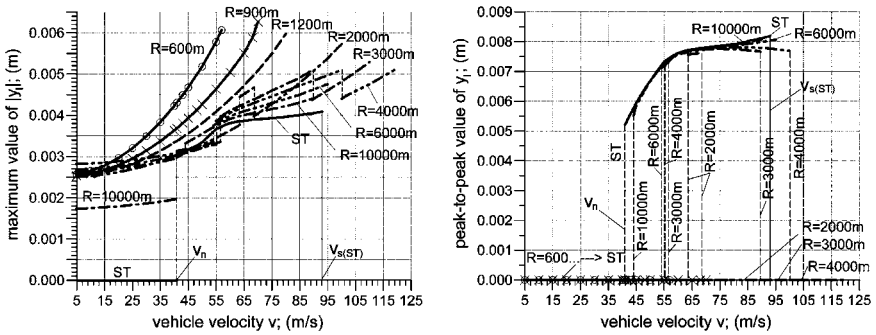

Fig. 9 Stability map for unworn wheel/rail pair S1002/UIC60 and 1:20 rail inclination; see [18]

nominal profiles, wear of wheel and rail profiles, vehicle type, inclination of rails, and way of mean rolling radius r_t determination. Critical velocity v_n, maximum displacements $|y_l|$ max, peak-to-peak values p-t-p y_l, and values of velocity v_s, are those the analysis is interested in.

Example for such analysis are Figs. 7, 8, and 9 that concern hsfv1 freight car model. The main feature of the map in Fig. 7 is uniform results for all radii R and straight track as well. Velocity v_n is the same for them (v_n=43.5 m/s) and separates areas of stable stationary and stable periodic solutions in the same way. Important differences in Fig. 8, comparing to Fig. 7, are: limit cycles below v_n for large radii (R=3000, 4000, 6000, 10000 m and ∞); quasi-statics above v_n for small radii (R=300 and 450 m); jump from limit cycle to quasi-statics for R=600 m; significant drop in v_n to 30.5 m/s; drop in v_s; and observable increase of $|y_l|$ max and p-t-p y_l. Comparing to Fig. 7, important differences in Fig. 9 are: quasi-statics above v_n for small radii (R=600, 900, 1200 m); jump from limit cycle to quasi-statics for R=2000, 3000, 4000 m; different values of v_n for R=2000, 3000, 4000, 6000, 10000 m and ST; and dramatic increase in v_s.

It is seen that both the wear of wheel and rail profiles (Fig. 8) and the change in rail inclination (Fig. 9) ruins very well-ordered picture of the model stability

properties for nominal profiles and inclination (Fig 7). It can be expected that severe non-linearities in vehicle suspension would ruin that picture as well.

5 Non-linear Features of the System in Transition Curves

The third problem represented in this contribution refers to the previous one. Discussing that, the author is going to share his experience about the railway vehicle dynamics above critical velocity v_n in transition curves. The limit cycles shall not be expected, as here curve radius R and superelevation H change continuously.

Example simulations (Figs. 10, 11, 12, and 13) are considered for compound routes consisted of straight ST, transition TC, and circular CC track sections. Lateral y, vertical z, roll ϕ, and yaw ψ co-ordinates are shown. Indices b, l and t denote body (or bogie frame), leading-, and trailing wheelsets, respectively. Despite for small R some of the v values can be questionable in terms of real objects' possible derailment, the selected examples are still interesting from the research point of view.

Three general behaviour groups can be recognised in TC. First, often logical behaviour in TC takes place as direct outcome of features for ST and CC. Then fluent passage from behaviour in ST to that in CC exists (Figs. 10 and 11). Despite this, both the increase (Fig. 10) and decrease (Fig. 11) of the oscillation amplitudes in TC can take place. Second, many times in TC behaviour happens unpredictable from features for ST and CC (Fig. 12). In this group one can observe: drop and tendency of oscillations to disappear in TC with their vast rise in CC; drop and almost disappearance of oscillations at the and of TC and then almost no oscillations in CC; sudden and complete disappearance of oscillations in TC with their moderate renewal in CC (Fig. 12); and rise of oscillations in TC above levels for ST and CC. Third, sometimes unexpected behaviour appears in TC resulting in change of

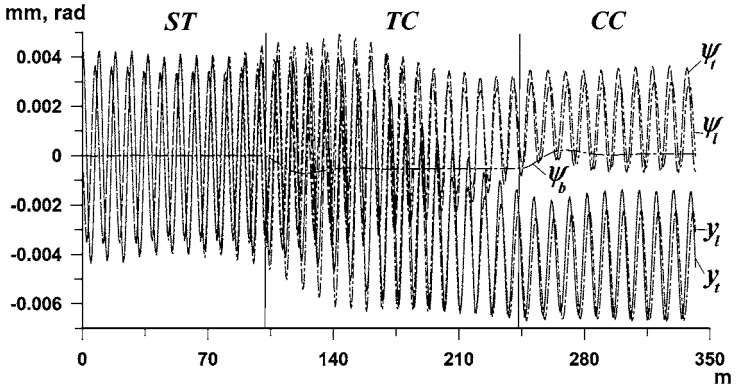

Fig. 10 Limit cycles of 2-axle freight car model on compound route ST, TC and CC; $v = 45.3\,\mathrm{m/s}$, $R = 600\,\mathrm{m}$, $H = 0.16\,\mathrm{m}$

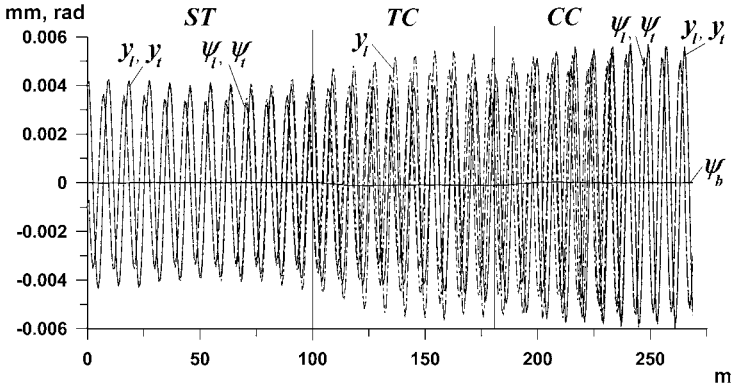

Fig. 11 Limit cycles of 2-axle freight car model on compound route ST, TC and CC; $v = 45.3\,\mathrm{m/s}$, $R = 6000\,\mathrm{m}$, $H = 0.077\,\mathrm{m}$

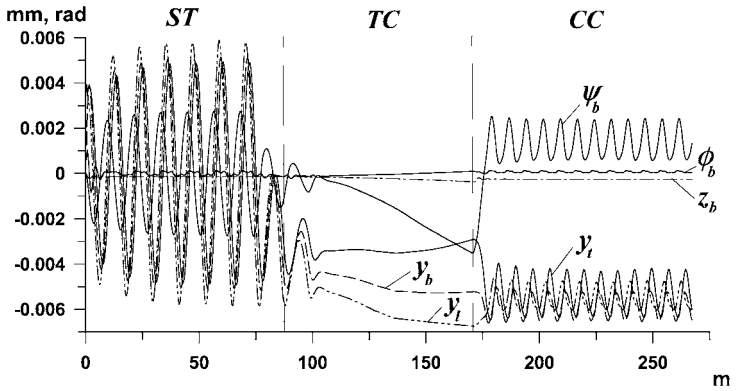

Fig. 12 Limit cycles of 2-axle 25TN bogie's model of freight car on compound route ST, TC and CC; $v = 29.5\,\mathrm{m/s}$, $R = 300\,\mathrm{m}$, $H = 0.15\,\mathrm{m}$

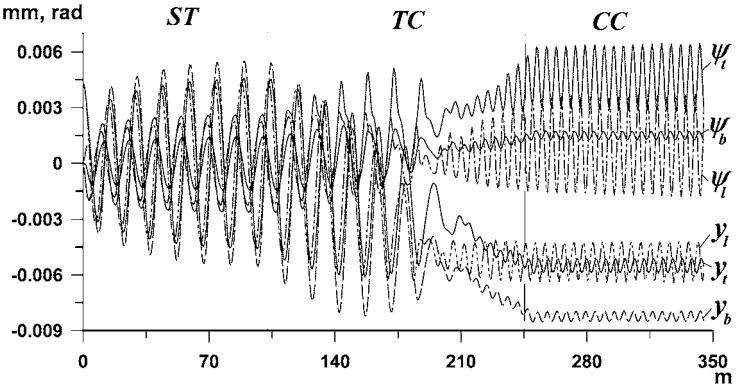

Fig. 13 Limit cycles of 2-axle bogie model of MKIII coach on compound route ST, TC and CC with increased values of track stiffness and damping; $v = 54\,\mathrm{m/s}$, $R = 600\,\mathrm{m}$, $H = 0.16\,\mathrm{m}$

solution for CC (Fig. 13). The switch to oscillations of different character happens in TC (bifurcation probable of the limit cycle to another one in CC).

Variety of the behaviours in TC manifests the rail vehicle-track system's non-linear nature with the particularly good result. Studies by present author reveal that even in case of well recognized stability properties in ST and CC (even for whole range of R represented on stability maps), correct prediction of behaviour of rail vehicle on TC for velocities above v_n is impossible (at least difficult). One could state that a lot of factors influence this behaviour. Some still seem to be not recognized. The studies done so far indicate superelevation H and vehicle model (e.g. constraints and parameters' values) as the factors influencing that behaviour.

6 Description of Kinematics, a Cause of Non-smooth Functions Within the System

The forth problem may surprise some readers. This problem reveals that even kinematics can introduce non-smooth functions into the system in certain conditions. It arises from the description of rail vehicle dynamics in track based moving coordinate systems (in type of A' in Fig. 14). Such description makes inertia terms dependent on the transportation (the motion of A' system) appear in the equations of motion. These terms are called imaginary forces and torques (e.g. centrifugal forces and gyroscopic torques) [11–14]. They are actually a cause for non-smooth functions being of interest, here.

In order to understand this fact better two types of measures were undertaken. Firstly, basing on results of [12], the most important imaginary forces and torques were selected. Next they were numerically generated for the routes composed in succession of ST, TC and CC (e.g. Figs. 15a and 16a). Simulation programme for vehicle dynamics was used. This way courses of the non-smooth functions caused by the equations of motion terms were obtained. Secondly, basing on analytical form of imaginary forces and torques [12–14], and in particular on the form of

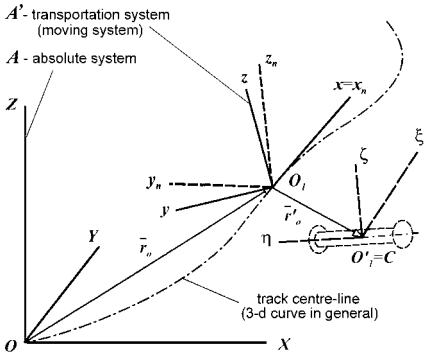

Fig. 14 The reference systems adopted

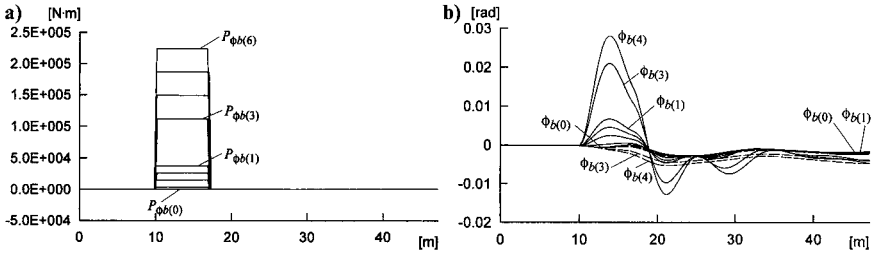

Fig. 15 a) Roll (*longitudinal*) imaginary torque of vehicle body; **b)** Influence of the body roll imaginary torque's omission on the body roll angle ϕ_b. Both figures for several accelerations

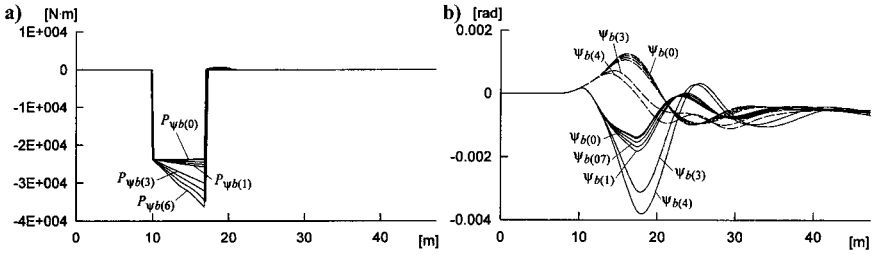

Fig. 16 a) Yaw (*vertical*) imaginary torque of vehicle body; **b)** Influence of the body yaw imaginary torque's omission on the body yaw angle ψ_b. Both figures for several accelerations

components of linear and angular velocities and accelerations of the transportation [13, 14], as well as on the courses of the obtained functions the physical quantity responsible for non-smoothness was identified. Here, owing to limited volume of this contribution, just discussion of the first type of measures is possible.

Often some or all terms of the imaginary forces and torques are neglected in the equations as common conviction spread of their negligible importance. To evaluate the real importance, in view of the terms omission, simulation tests were done on the same routes as above. Results from complete and incomplete (with selected imaginary terms omitted) models were compared (e.g. Figs. 15b and 16b).

Example Figs. 15 and 16 included here refer to motion of 2-axle hsfv1 car model. Lengths of track sections equal 10, 7 and 30 m for ST, TC and CC, respectively. Unnaturally short TC was selected for the research purposes. The real lengths were also studied. The curve radius $R = 300$ m. Simulations concern motion with constant and variable velocity v ($v = 15$ m/s at the beginning of TC). Variation of v is defined by different values of the acceleration a (specified in the figures in m/s^2 within the brackets). In Figs. 15b and 16b, solid line represents co-ordinates for the complete model, while dashed line represents those for the incomplete one.

The general conclusions coming out from the figures as well as the entire study are as follows. The terms of imaginary torques dependent on ε, the angular acceleration of the transportation, are responsible for the non-smooth effects. These appear exactly when passing between different track sections (ST–TC, TC–CC, and vice

versa) and lead sometimes to unexpected problems with the equations integration. The last happens despite the integration method is used intended for stiff differential equations (Gear method). The same terms result in the differences in solutions for complete and incomplete models. Summing these terms up, the body roll $P_{\phi b}$ and yaw $P_{\psi b}$ imaginary torques appear most important. Their importance rise with rise of acceleration (speeding up) and deceleration (braking). The roll torque is the leader in terms of influence on co-ordinates absolute values. Even so, it disappears entirely for constant velocity ($a = 0$; Fig. 15), what is not the case for the yaw torque (Fig. 16). General omission of imaginary torques is not justified.

7 Conclusion

The problems discussed confirm that one needs to be very careful while studying rail vehicle dynamics and simplifying the non-linearities at the same time. It is demonstrated that non-smooth functions can influence results of numerical analysis radically. Such functions are the result of system's physical features but of the modelling techniques as well. Except non-smooth functions present within vehicle model that can be improved by the better modelling, the entirely physical non-smooth nature of rail vehicle stability exists that cannot be improved in this way.

References

1. Dusza, M.: Simulation studies of railway vehicle motion stability in curves with regard to influence of changes of the system chosen parameters. PhD thesis, Warsaw Technical University, Faculty of Transport, Warsaw (2005) – in Polish
2. Hoffmann, M.: Dynamics of European two-axle freight wagons. PhD thesis, Technical University of Denmark, Informatics and Mathematical Modelling, Lyngby (2006)
3. Hoffmann, M., True, H.: The dynamics of European two-axle railway freight wagons with UIC standard suspension. Proc. 20th IAVSD Symp., Veh. Syst. Dyn. **46**(S1), 225–236 (2008)
4. Knothe, K., Bohm, F.: History of stability of railway and road vehicles. Veh. Syst. Dyn. **31**(5–6), 283–323 (1999)
5. Lee, S.Y., Cheng, Y.C.: Nonlinear hunting stability analysis of high-speed railway vehicles on curved tracks. Heavy Veh. Syst. **10**(4), 344–361 (2003)
6. Lee, S.Y., Cheng, Y.C.: Nonlinear analysis on hunting stability for high-speed railway vehicle truck on curved tracks. J. Vib. Acoust. – Trans. ASME **127**(4), 324–332 (2005)
7. Lee, S.Y., Cheng, Y.C.: Influences of the vertical and roll motions of frames on the hunting stability of trucks moving on curved tracks. J. Sound Vib. **294**(3), 441–453 (2006)
8. True, H., Birkedal Nielsen, J.: On the Dynamics of steady curving of railway vehicles. Proc. 6th Mini Conf. on Vehicle System Dynamics, Identification and Anomalies, Budapest, Nov. 9–11, 1998, pp. 73–81. Technical University of Budapest, Budapest (1999)
9. True, H., Jensem, J.Ch.: Parameter study of hunting and chaos in railway vehicle dynamics. Proc. of 13th IAVSD Symposium. Veh. Syst. Dyn. **23**(suppl.), 508–521 (1994)
10. True, H., Hansen, T. G., Lundell, H.: On the quasi-stationary curving dynamics of a railroad truck. ASME/IEEE Joint Rail Conference, Pueblo, Col., March 16–18, 2005. RTD-Vol. **29**, pp. 131–138, ASME (2005)
11. Zboiński, K.: Dynamical investigation of railway vehicles on a curved track, European J. Mech., Part A Solids **17**(6), 1001–1020 (1998)

12. Zboiński, K.: Importance of imaginary forces and kinematic type non-linearities for description of railway vehicle dynamics. Proc. Inst. Mech. Eng., Part F, J. Rail Rapid Transit **213**(F3), 199–210 (1999)
13. Zboiński, K.: The methodology of modelling of rail vehicle dynamics with regard to a given transportation and its applications. D.Sc. thesis. Sci. Work. – Transp. **43**. Publishing House of the Warsaw University of Technology, Warsaw (2001) – in Polish
14. Zboiński, K.: Numerical and traditional modelling of dynamics of multi-body system in type of a railway vehicle. Arch. Transp. **16**(3), 81–106 (2004)
15. Zboiński, K., Dusza, M.: Analysis and method of the analysis of non-linear lateral stability of railway vehicles in curved track. Proc. 18th IAVSD Symposium. Veh. Syst. Dyn. **41**(suppl.), 222–231 (2004)
16. Zboiński, K., Dusza, M.: On the problems with determination of railway vehicle lateral stability in curves by means of numerical simulation. Proc. 9th Mini Conf. VSDIA, pp. 163–170, Budapest University of Technology and Economics, Budapest (2004)
17. Zboiński, K., Dusza, M.: Development of the method and analysis for non-linear lateral stability of railway vehicles in curved track. Proc. 19th IAVSD Symposium. Veh. Syst. Dyn. **44**(S1), 147–157 (2005)
18. Zboinski, K., Dusza, M.: Bifurcation approach in studying the influence of rolling radius modelling and rail inclination on the stability of railway vehicles in a curved track. Proc. 20th IAVSD Symposium, Veh. Syst. Dyn. **46**(S1), 1023–1037 (2008)
19. Zboiński, K., Kleban, H.: The model of rail vehicle dynamics in a curve of small radius and its simulation tests. Inst. of Veh. Pap. **64**(1), 175–182, Warsaw University of Technology, Warsaw (2007) – in Polish
20. Zeng, J., Wu, P.: Stability analysis of high-speed railway vehicles, JSME Int. J. Series C, Mech. Syst., Mach. Elem. and Manuf. **47**(2) (special issue), 464–470 (2004)

On Tangential Friction Induced Vibrations in Brake Systems

Georg Peter Ostermeyer

Abstract The basis for the analysis of friction in brake systems is the brake pad's tribological interface. An investigation of this interface reveals friction intensive surface structures. These so-called "patches" are extremely hard and carry the main part of the friction power. By complex interaction processes of wear and heat these patches are generated permanently but leave the system after a certain period of time. So there is an equilibrium of flow of contact patches in the brake pad interface, with the outcome being a dynamic macroscopic friction coefficient, whose "inertia" can be well described by differential equations in the form of special balance equations. Systematic expansions of these balance equations even allow, for the first time, a simulation of different test cycles of the AK-Master test for friction materials with high accuracy. These friction force variations are generated by the dynamics of the local surface geometry and can explain physically effects of measurements, which were up to now described by control theoretic approximations [7, 8].

Beside these effects the dynamics of friction is influenced by lateral vibrational dynamics of these patches on a very fast timescale. This timescale is so fast that processes of patch growth and destruction are negligible. Beyond that, the vibration frequencies of the patches, as well as the actual local friction power on each of these surface structures, vary over a wide range of values, which is the result of a great variety of patch sizes and heights in the interface. Generally, one would expect a smoothing of these local and stochastically distributed vibration effects. It can however be shown, that the oscillations of the patches are subject to synchronization processes, with the result being in-phase patch vibrations on macroscopic areas of the brake pad of significant size. Thereby, self-excited vibrations of the patches can lead to lateral oscillations of the pad's friction force on a macroscopic scale. These are able to excite the whole system of brake pad and disk.

G.P. Ostermeyer (✉)
Institute of Dynamics and Vibrations, Technical University of Braunschweig, Schleinitzstr. 20, D – 38106 Braunschweig, Germany
e-mail: gp.ostermeyer@tu-bs.de

P.G. Thomsen, H. True (eds.), *Non-smooth Problems in Vehicle Systems Dynamics*,
DOI 10.1007/978-3-642-01356-0_9,

1 Introduction

Nearly everybody has used once sandpaper to modify wooden surfaces by hand. And surely everybody has observed agglutinations on the sandpaper at the grinding process. At least this is to be observed when you are grinding the finish (Fig. 1).

During grinding the swarf is moving between wood and sandpaper. At some parts of the sandpaper thin and hard patches are growing up, formed by heat and wood powder. With your fingers you feel hot spots through the sandpaper at exactly these patches. At these patches the friction power produces heat but nearly no wear any more. When there are to many patches the sandpaper gets unusable.

In technical applications for high wear rates the production of such patches has to be avoided. This can be done by the modification of the form of abrasive grain -this controls the density and the form of wear particles- and by introducing elastic belts, which controls the stability of the patch growing process. This will be described elsewhere.

In technical applications for high friction forces but low wear rates these surface patch structures are essential. A typical technical system with these properties are brake systems [1, 2]. Here one can observe these hard surface structures, the so called patches [3, 4]. These patches carry the main part of friction power of the system and their dynamics influences the dynamics of global friction [5, 6].

These patches control and determine in a fundamental way the friction and wear properties of the brake system. The basic structure of a brake pad consists of a comparative supple matrix, with embedded small and hard structures or particles. An example for an ancient brake material with such properties is wood (e.g. used to slow down windmills at forthcoming storms). Modern brake materials in automotive engineering consist of a soft polymeric matrix with embedded SiO_2-particles, iron swarfs or similar materials.

By pressing the brake pad material onto the brake disk, wear debris is produced. At the starting point the main part of the debris is generated from the polymeric

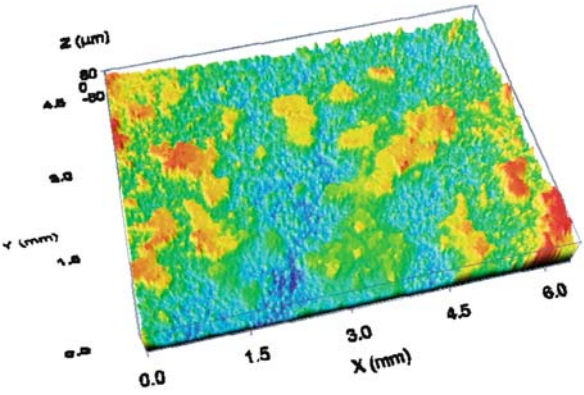

Fig. 1 Confocal microscope picture of grinding paper

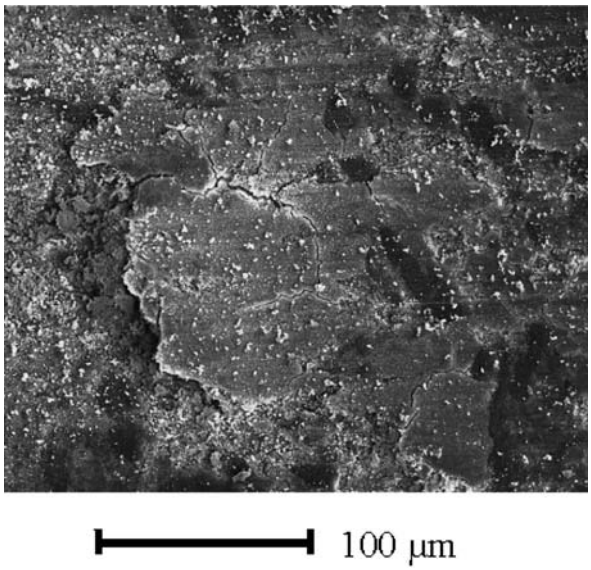

Fig. 2 Patch structures on a brake pad (REM – picture)

matrix. This debris is similar to the wear of friction produced by using a rubber on a sheet of paper (Fig. 2).

The wear particles move through the contact zone. When reaching the rim of the contact zone, a fraction of the wear particles sticks at the brake disk and moves again into the contact zone after one rotation of the disk. Another part is emitted to the environment.

Two important things will happen when, caused by the wear of the polymeric matrix, a SiO_2-particle or an iron swarf reaches the surface of the brake pad, see Fig. 3. First, due to the higher wear rate of the polymeric matrix compared with the hard particle, the particle is getting pressed into the polymeric matrix. Secondly

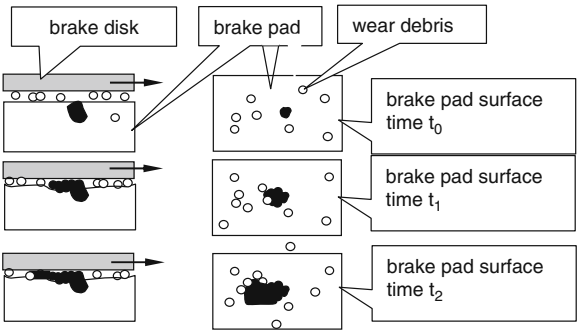

Fig. 3 Section of the brake system at different moments $t_0 < t_1 < t_2$, growth of a patch. On the *left* a side view, on the *right* a *top* view on the pad surface section

the wear particle flow in the boundary layer is disturbed. As a result of the increasing local normal and tangential stress in the surrounding area of the particle, the local temperature will also increase. For technical brake systems the stress and the temperature may increase until alloying processes between the hard particle and the wear particle flow will occur (some analysis indicates even the possibility of creating ceramic structures). This leads to an accretion of hard and thin contact patches on the braking material contrary to the wear particle flow.

Hereby the hardness of the patches is in the range of those for the inhomogeneities.

With this generation of contact patches, the brake material surface can be divided into two different contact zones, see Fig. 4. The contact zone of type I is defined by the contact of the polymeric matrix and the contact zone of type II is defined by the hard patches. The main energetic conversion is produced at the contact zones of type II. So the major part of the breaking power is dissipated in this contact zone of type II. That leads to very high temperatures of the contact patches that even the integral temperature of the brake pad surface will reach about 300°C.

The wear around the contact patches, the heat generation and mechanical stress are leading to crack growth in the hard contact patches. Furthermore the asperity structure of the break disk enforces local movements/vibrations of the contact patches on the soft polymeric structure and leads also to a crack propagation. These effects results in a destruction of contact patches after a certain time (see Figs. 5 and 2)

The boundary layer on the brake material is characterized by the growth and the destruction of contact zones of type II on the surface of the soft polymeric matrix. The main part of the incoming energy is dissipated by these contact patches [5, 6]. Therefore the friction is defined by a dynamic equilibrium of processes that generate and destruct these patches. The current friction is not a stationary function of e.g. normal force or velocity but is determined by the history of the load and the wear. Whether it is well known, that friction, heat and wear are intimately connected, usually friction laws are formulated without heat and wear. An argument for this is

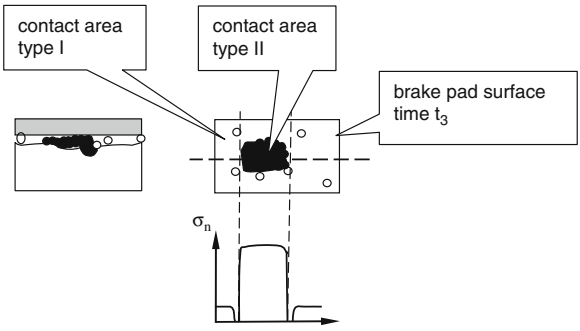

Fig. 4 Section of the brake system, different contact zones (type I and type II) and in principle the normal load distribution along the *dashed line*. On the *left* a side view, on the *right* a *top* view on the pad surface section

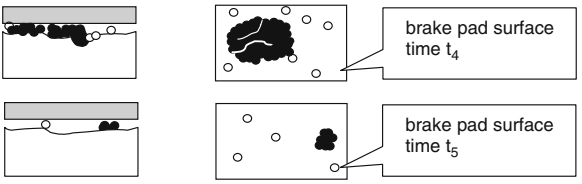

Fig. 5 Section of the brake system at different moments $t_3 < t_4 < t_5$, destruction of a patch. On the *left* a side view, on the *right* a *top* view on the pad surface section

the assumption of different timescales, the phenomena are living on. Heat is often taken into account only via the temperature dependent material datas only.

2 Dynamics of Friction Caused by Heat and Wear

The frictional resistance is significantly determined by the contact areas of type II. These contact patches are depending from wear and heat generation, which depend from frictional resistance by themselves. Figure 6 illustrates the interconnectedness

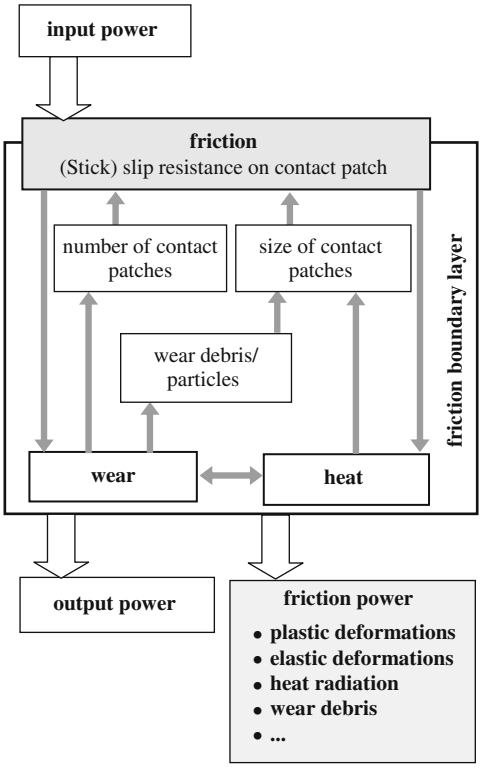

Fig. 6 Friction in technical brake systems

of the above described effects. The illustration therefore shows a closed loop dependency of friction, heat and wear [6]. This shows that friction depends on the wear history. Wear has to be taken into account in a friction law, too, when friction has to be described for shot time intervals.

The dependence on temperature here is given by the growth of patches. The process generates heat, which has to be described by a friction law. This temperature has to be taken into account, when temperature dependent elastic moduli or other temperature dependencies of material data are essential. This last effect has to be included when concrete material behaviour is taken into account, for instance the dynamic behaviour of the patches on the elastic pad. This will be done in the next chapter.

The dynamic equilibrium of accretion and destruction of contact patches is a substantial property of contact area A_{II} and a fundamental consequence of wear.

With respect to Coulomb's ideas the friction coefficient μ is described by the magnitude of the friction force R divided by the magnitude of the normal force N:

$$\mu = \frac{R}{N}$$

Expanding this fraction by the norm v of the tangential velocity vector between the two contacting bodies, one receives

$$\mu = \frac{Rv}{Nv}, \qquad Nv = \left\| \vec{N} \right\| \, \| \vec{v} \|$$

This formulation gives another interpretation of the friction coefficient μ. It is now a dimensionless measure of the total friction power Rv in units of a characteristic system power, given by the product of the magnitudes of the vectors of normal force and tangential velocity. This characteristic system power is actually an idle power (because the vectors of normal force and tangential velocity are perpendicular to each other) but very handy for the following description of the dynamic friction law. It is a fundamental input parameter for the tribological processes in the brake.

For simplicity it is assumed that the friction power is proportional to the total area A_P of contact patches. In this simple analysis the energy flowing in all other contact regions will be neglected. The total patch area A_P on the pad is determined by an equilibrium of flow caused by the growth and destruction of single contact patches. This equilibrium of flow is a fundamental consequence of the closed loop interaction of friction and wear schemed in Fig. 6. Since the friction power is described by μ, the total patch area A_P itself and especially the dynamics of A_P are correlated with μ and its temporal change. So the equilibrium of flow of friction power must be given by a balance equation of μ [6].

This means that the above delineated processes do not affect μ itself but only its derivation with respect to time. So the friction in general becomes a dynamic process. The approach of the equilibrium of flow for μ leads to general balance equations.

Models of the coefficient of kinetic friction usually use the sum of all asperity interactions in the contact area and assume a negligible wear for short time intervals.

The model presented above shows, that because of the dependency of the current size and quantity of contact patches from the history of wear, the wear has to be taken into account even for short time intervals. Therefore the defining equation for μ has to be an balance equation instead of an algebraic equation:

$$\begin{aligned}
\dot{\mu} &= f_1(\mu, a_1, a_2, \ldots) - f_2(\mu, a_1, a_2, \ldots) \\
\dot{a}_1 &= g_1(\mu, a_1, a_2, \ldots) \\
\dot{a}_2 &= g_2(\mu, a_1, a_2, \ldots) \\
&\ldots .
\end{aligned} \tag{1}$$

The accretion of the contact patches is described by the function f_1 and the function f_2 covers the effects that lead to the destruction of the patches. The a_i are further state variables as heat, wear and so on, each of this variables is result of a balance equation too. To fill this law, in a first attempt the variables temperature and wear are taken into account in a rather simple manner: the wear is usually in literature approximately given by the friction power, so wear is given by the product μNv. The heat can be treated in the usual way, where the source is given again by the friction power. These functions can be build up in detail, see [6, 12]. A fourth order equation for μ is given in [9], where even parts of the well known AK-Master test are predictable described by this friction law.

Using a cellular automaton, we reproduced this interaction [10–12] and as a result we obtained precisely the well known surface structures of a break pad, see Fig. 7 showing a section of size 1.5 mm × 1.5 mm. In addition the Automaton computes the topography of the brake pad and the wear particle density.

For very slow variations of the normal force and the velocity and short application times one can use approximately the stationary solution μ_{stat} of the dynamic friction laws. This stationary solution has the well known shape of a Stribeck curve.

The stationary solution μ_{stat} can be written in the following form,

$$\mu_{stat}(N, v) = \frac{\varepsilon}{\varepsilon + x}\Delta\mu + \mu_\infty \tag{2a}$$

Classical measurements of friction acquire always such a stationary solution of the friction coefficient. With these measurement data, one can determine the constants ε, $\Delta\mu$ and μ_∞. The load parameter x is given by

$$x = Nv \tag{2b}$$

When normal load and velocity are changing faster, they affect the topography dynamics described above resulting in non steady state behavior of the friction coefficient itself. The characteristic time scales of these surface dynamics varies from about 0.01 s up to the application time of the brake (Fig. 8).

On very fast timescales, where the effect of geometry changes in the friction surface by the grow and destruction of the patches are negligible the dynamics of friction is influenced by lateral vibrational dynamics of these patches on a very fast

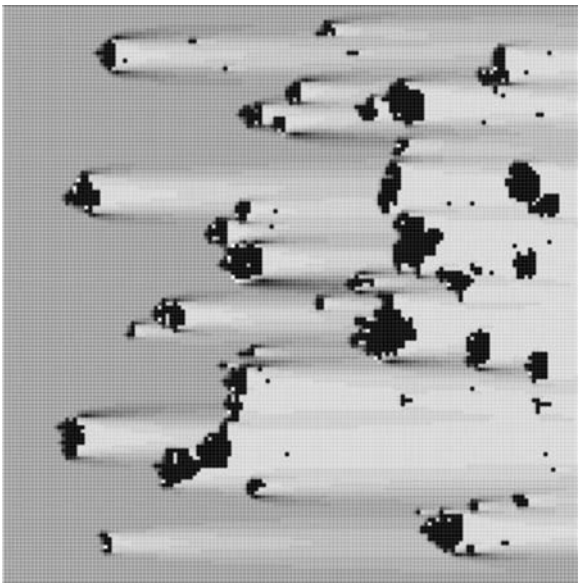

Fig. 7 The friction surface of the pad during braking with patches (*black*) and wear debris (concentration correlated with *gray scale*) computed with a Cellular Automaton

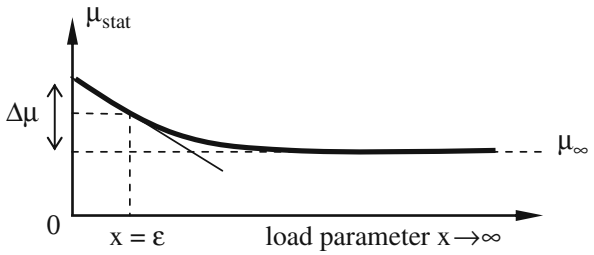

Fig. 8 The stationary behaviour of the friction coefficient depending on the parameters $\Delta\mu$, μ_∞, ε

timescale. The lateral vibration frequency of a single patch can be estimated to cover a range of about 0.5–20 kHz. This timescale is so fast that processes of patch growth and destruction are negligible. On each patch the stationary solution (2) describes the friction force evolution again.

3 On Tangential Vibrations in the Brake System

Due to the fact that the main part of the friction power is carried by the contacts between patch and disk, only these contacts will be considered in the following. The permanent changes in size and number of the contact patches shall be neglected for

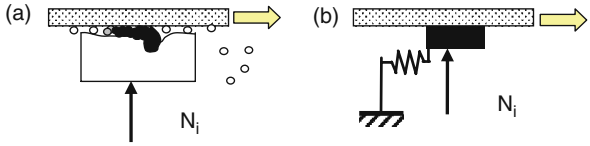

Fig. 9 Lateral patch vibrations (**a**) described by a 1 dof friction oscillator (**b**)

the following examinations, since these changes live on a rather slow time scale with respect to the patch vibrations. Beyond that, only the lateral dynamics are of interest in this chapter. Therefore, the patches appear as classical stick-slip oscillators on a permanently moving surface, which is the brake disk. They are coupled among one another via the polymeric matrix. Each of these stick-slip oscillators is subject to an individual normal force N_i, since patch size and normal force are correlated. Moreover, the patch size controls its elastic connection to the under layer and the vicinity of neighbored patches determines the visco-elastic coupling (Fig. 9).

For the dependency of friction versus sliding velocity, the function (2) is utilized. The equation of motion for this individual patch, decoupled from all other patches, has the simple form:

$$m\,\ddot{x} + cx = \mu(v_{rel}) \cdot N - b\,\dot{x}, \quad v_{rel} = v - \dot{x} \tag{3}$$

Therein, v is the brake disk's tangential sliding velocity. As is known, such a system is subject to self-induced vibrations. For the case of a sufficiently high friction force, compared to the damping force, a stationary vibration along a given limit cycle is the consequence,

Usually one would expect that due to the wide range of the oscillating masses and the respective stiffnesses (and thereby the frequencies), the oscillation of the patches is not synchronizised and stochastic or chaotic. This type of phasing, which is schemed by the different colours in Fig. 10a, leads to a rather temporally homogeneous load transmission into the disk overloaded by a wideband noise. In case of constant velocity and normal load this mechanism would transport the local friction behavior on each patch to the macroscopic pad.

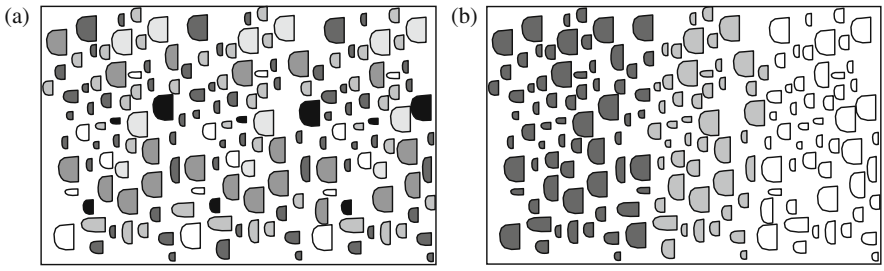

Fig. 10 The phase of the patch oscillators, (**a**) unsynchronized state, (**b**) synchronized state

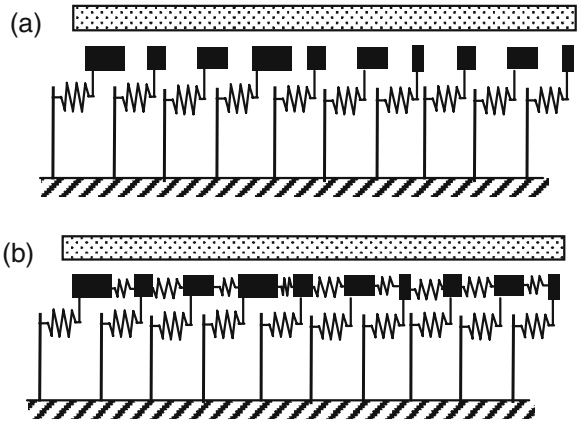

Fig. 11 (**a**) 10 decoupled stick-slip-oscillators (**b**) 10 coupled stick-slip-oscillators

By the vicinity of the patches the oscillators are weakly coupled. The question is whether there can occur a synchronization (see Fig. 10b) of these patch oscillations under special circumstances, so that macroscopically the load transmission has a periodic character. In this case that phenomenon leads to a lateral excitation of the disk-pad-system and can cause noise problems. This fundamental mechanism will be illustrated by the systems in Fig. 11.

As a major consequence of the coupling, all patches run through the friction curve in-phase. The friction curve has in general a falling characteristic in brake systems. On the macroscopic scale, this results in significant oscillations of the global friction force along the whole pad surface rather than in only small stochastic variations of the friction force versus time, as would be the case in an unsynchronized system, Fig. 12 (a). Simple estimations indicate that the vibration frequencies of the patches

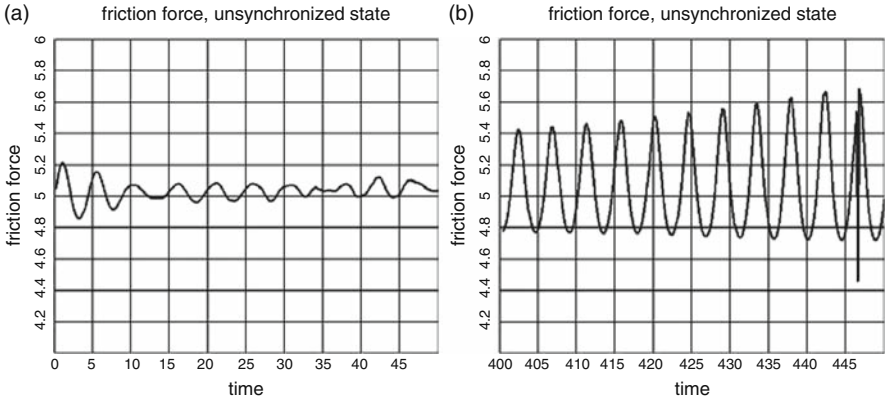

Fig. 12 Resulting friction force of ten stick-slip oscillators in the (**a**) unsynchronized state, (**b**) synchronized state

can be expected in a range between 1 and 10 kHz. The high-frequency stick-slip oscillations can excite vibrations of the whole system of brake pad and disk.

4 Conclusions

The investigations on lateral dynamics in brake systems, discussed in this paper, revealed the existence of macroscopic stick-slip oscillations in the high-frequency range. These can be fundamental for the explanation of generally known phenomena, such as the squealing. The effect of excitation caused by the synchronization can be even more significant using the real number of oscillating patches, which is magnitudes of order larger than in the system with ten patches shown in this paper.

References

1. Severin, D., Musiol, F. “Der Reibprozess in trocken laufenden mechanischen Bremsen und Kupplungen” Konstruktion 47 (1995), 59–68
2. Severin, D., Dörsch, St. “Friction mechanism in industrial brakes” WEAR 249 (2001), 771–779
3. Bergman, F., Eriksson, M., Jacobson, S. “Influence of disc topography on generation of brake squeal” WEAR 225–229 (1999) 621–628
4. Eriksson, M. “Friction and contact phenomena of disc brakes related to squeal”, Comprehensive summaries of Uppsala dissertations from the faculty of science and technology, Uppsala (2000)
5. Ostermeyer, G.-P. “Arbeits- und Ergebnisbericht 1998–2 – 1999 – 2000 – 2001/1 zum Sonderforschungsbereich 605 Elementarreibereignisse – Teilprojekt C4” Berlin (2001)
6. Ostermeyer, G.-P. “On the dynamics of the friction coefficient” WEAR 254 (2003), 852–858
7. Stelter, P. Nichtlineare Schwingungen reibungserregter Strukturen. VDI Reihe 11, Nr. 137 (1990)
8. Kröger, M., Lindner M., Popp K. “Modellierung instationärer Reibkräfte”, Proc. Appl. Math. Mech. 2 (2003), 140–141
9. Ostermeyer, G.-P., Bode, K. On Dynamic Friction Phenomena in Brake Systems, to appear in Proc. of the Int. Symposium on Friction, Wear and Wear Protection (DGM), WILEY-VCH (2008)
10. Ostermeyer, G.P., Müller, M. “New developments of friction models in brake systems”, Proceedings of the 23rd SAE Brake Colloquium and Exhibition, Orlando (2005), 187–200, also in SAE 2005 Transactions Journal of Passenger Cars – Mechanical Systems
11. Ostermeyer, G.-P., Mueller, M. “Dynamic interaction of friction and surface topography in brake systems”, Tribol. Int. 39(1) (2006), 370–380
12. Ostermeyer, G.-P., Müller, M., Abendroth, H., Wernitz, B. “Surface topography and wear dynamics of brake pads”, Proceedings of the 24th SAE Brake Colloquium and Exhibition, Grapevine (2006)

Dry Friction Element with Logical Switch for Numerical Simulation of Vehicle Dynamics and Its Application

Anna Orlova

Abstract When modeling dry friction in mechanical elements various models are used to deal with the switch between stick and slip condition. When the standard numerical integration methods come to abrupt change in the system's state, they start cutting down the integration step to locate the event that increases the required processor time. The paper proposes to deal with that by developing the dry friction element model in parallel with modification of numerical integration method.

1 Mechanical Model of the Friction Element

Mechanical model of the friction element (one dimensional) is presented in Fig. 1. The element consists of Coulomb friction part with coefficient ν_f in series with a spring c_f. Compression force to the friction element is applied through the spring

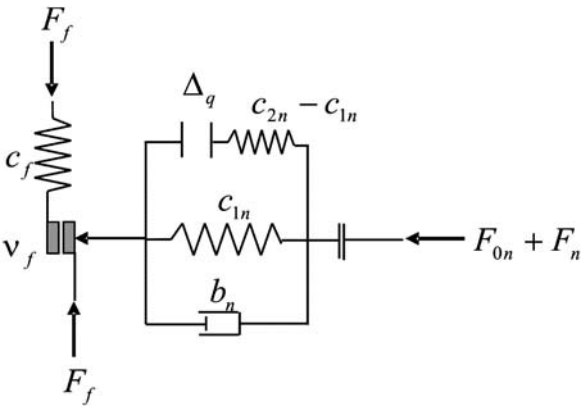

Fig. 1 Mechanical model of the friction element

A. Orlova (✉)
NVC "Vagony", Moskovskiy prospect, 9, St. Petersburg, 190031 Russia
e-mail: a-orlova@yandex.ru

P.G. Thomsen, H. True (eds.), *Non-smooth Problems in Vehicle Systems Dynamics*,
DOI 10.1007/978-3-642-01356-0_10,

c_{1n} and damper b_n in parallel. When the force in the compression element is zero, then the friction element does not work, turning of the compression force into zero is represented by unnoted gap element. The stroke of the elastic compression element is limited to Δ_q.

The spring in series with dry friction in many problems has physical meaning and is used not only to overcome the singularity in Coulomb friction element. Examples are presented in Fig. 2. Constant contact side bearings, [3], are often installed on three-piece bogies to provide elastic resistance to car body roll and friction torque when the bogie rotates under the car body in curves. The bearing consists of a cage that houses elastic supports (may be springs or rubber elements) and a cap that is in contact with the flat surfaces on the car body. The cap is pressed down by part of the weight of the car body and the elastic supports experience corresponding nominal compression. As the railcar moves, its oscillations lead to certain dynamic variation of the compression force. When the vehicle negotiates the curves, first the elastic support works in lateral direction and then, when the elastic force becomes bigger than the friction force, the plates on the car body start to slide over the side

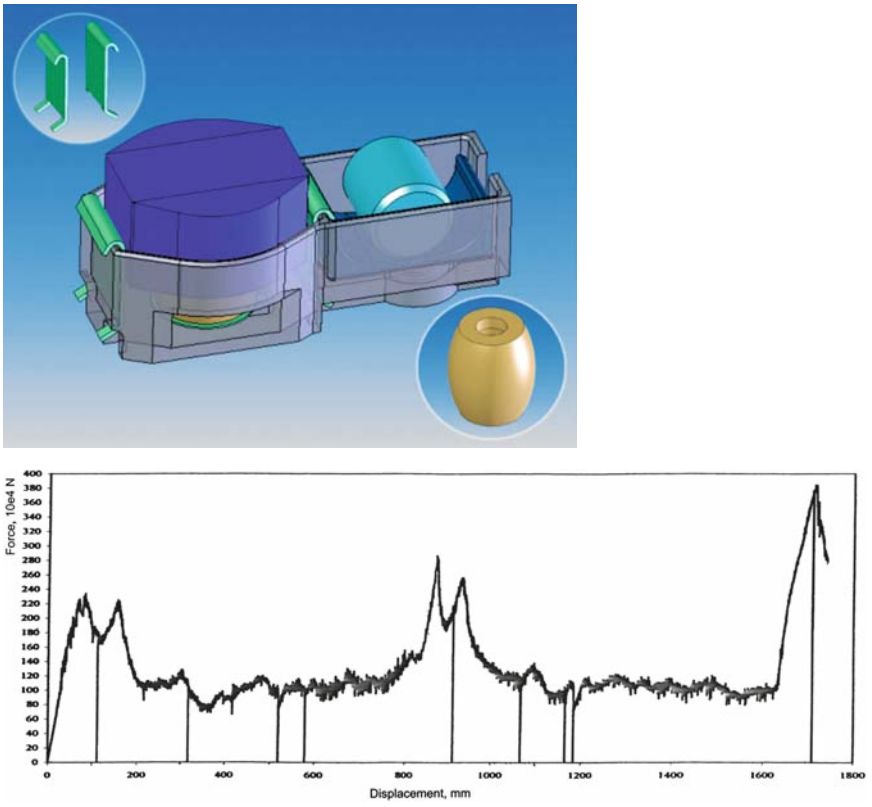

Fig. 2 Examples of modeled structures: (**a**) constant contact side bearing, (**b**) force-displacement history of elastic-plastic deformation of car body

bearing cap. The vertical compression of the elastic support is limited by the clearance between the cap and the cage.

The same model can as well be applied to constructions that experience first elastic and then plastic deformation. In this case the stiffness c_f that is in series with dry friction describes the construction elastic properties, whereas the former friction force $\nu_f\,(F_{0n} + F_n)$ can be interpreted as the force that causes plastic deformation, the pressure $(F_{0n} + F_n)$ being constant.

In mathematical description the dry friction force F_f included the logical switch that considered the stick and slip conditions with non zero compression force and absence of the force in other case:

$$F_f = \begin{cases} \nu_f(F_{0n} + F_n), & F_{0n} + F_n < 0, \quad slip \\ c_f q_f, & F_{0n} + F_n < 0, \quad stick \\ 0, & F_{0n} + F_n \geq 0, \quad off \end{cases} \tag{1}$$

where f is the subscript for the friction force, n is the subscript for the compression force, F_{0n} is the nominal value of the compression force, F_n is the dynamic component of the compression force, q_f is the dynamic deformation in direction of the friction force, c_f is the stiffness of the element in direction of the friction force, ν_f is the friction coefficient.

The compression force acting on the friction element was calculated in two stages. In the first stage initial elastic deformation under nominal force F_{0n} was determined

$$q_{0n} = \begin{cases} 0, & F_{0n} = 0 \\ F_{0n}/c_{1n}, & c_{1n}\Delta_q \leq F_{0n} < 0 \\ \Delta_q + \left(F_{0n} - c_{1n}\Delta_q\right)/c_{2n}, & F_{0n} < c_{1n}\Delta_q \end{cases} \tag{2}$$

where c_{1n} is the stiffness of the elastic element producing pressure on the friction element before it reaches the bump stop, c_{2n} is the stiffness of the elastic element producing pressure on the friction element after it reaches the bump stop, Δ_q is the displacement that corresponds to the bump stop.

Knowing the initial elastic deformation and dynamic deformation (that results from the generalized coordinates of the dynamic system) the total compression force was calculated as follows

$$F_{0n} + F_n = \begin{cases} 0, & q_n + q_{0n} \geq 0 \\ c_{1n}(q_n + q_{0n}) + b_n\dot{q}_n, & \Delta_q \leq q_n + q_{0n} < 0 \\ c_{1n}\Delta_q + c_{2n}\left(q_n + q_{0n} - \Delta_q\right) + b_n\dot{q}_n, & q_n + q_{0n} < \Delta_q \end{cases} \tag{3}$$

where b_n is the equivalent viscous damping coefficient in the element producing pressure on the friction element, $\dot{q}_n$ is the displacement rate in direction of compression force.

Formulation of switch conditions between stick and slip conditions in Eq. (1) was oriented towards application of numerical integration methods. Before taking the integration step it was assumed that the state of the system will not change at the end of it, the generalized coordinates were calculated using the state of the friction elements from the previous integration step. Conditions whether the system state changed within the integration step were checked at the end of it.

The condition for the friction element to change from stick (in step i) to slip (in step $i+1$) was formulated in terms of forces

$$\left|F_f^{(i+1)}\right| > \left|\nu_f \left(F_{0n} + F_n^{(i+1)}\right)\right| \tag{4}$$

i.e., the force F_f calculated assuming that the element is sticking is greater than the compression force multiplied by the friction coefficient.

The condition to change from slip (in step i) to stick (in step $i+1$) was formulated as velocity sign change:

$$\dot{q}_f^{(i)} \cdot \dot{q}_f^{(i+1)} < 0, \tag{5}$$

besides the condition $\left|F_f^{(i+1)}\right| < \left|\nu_f \left(F_{0n} + F_n^{(i+1)}\right)\right|$ should hold.

2 Modification of the Integration Method

The system of the equations of motion was assumed in normal form:

$$\dot{X} = F\{t, X\} \tag{6}$$

where X is the column of system's generalized coordinates, $F\{t, X\}$ is the functional of generalized forces (including the state of friction elements and switch conditions between them), t is time.

In numerical integration of Eq. (6) it was assumed that in each step the functional $F\{t, X\}$ does not change, that allows writing down, for example, the Runge-Kutta algorithm with constant step size, [2], in form:

$$\begin{aligned}
X^{(i+1)} &= X^{(i)} + \frac{h}{6}(k_1 + 2k_2 + 2k_3 + k_4) \\
k_1 &= F^{(i)}\left\{t^{(i)}, \quad X^{(i)}\right\} \\
k_2 &= F^{(i)}\left\{t^{(i)} + \frac{h}{2}, \quad X^{(i)} + k_1\frac{h}{2}\right\} \\
k_3 &= F^{(i)}\left\{t^{(i)} + \frac{h}{2}, \quad X^{(i)} + k_2\frac{h}{2}\right\} \\
k_4 &= F^{(i)}\left\{t^{(i)} + h, \quad X^{(i)} + k_3 h\right\}
\end{aligned} \tag{7}$$

where h is the integration time step, i is the number of the integration step, $t^{(i)}$ – time at the beginning of the integration step.

The switch in the elements was estimated in the end of the integration step. To determine the time instant within the integration step when stick-slip conditions changed, linear interpolation of generalized coordinates was assumed:

$$X = \frac{t^{(i+1)} - t}{h} X^{(i)} + \frac{t - t^{(i)}}{h} X^{(i+1)}, \qquad t^{(i)} \le t \le t^{(i+1)}, \tag{8}$$

that allowed locating the switch instant of the friction element from stick to slip condition by formula:

$$t^*_{toSlip} = t^{(i)} + h \frac{\left| v_f \left(F_{0n} + F_n^{(i+1)} \right) \right| - \left| F_f^{(i)} \right|}{F_f^{(i+1)} - F_f^{(i)}}, \tag{9}$$

or the switch instant from slip to stick condition by analogues formula:

$$t^*_{toStick} = t^{(i)} + h \frac{-q_f^{(i)}}{q_f^{(i+1)} - q_f^{(i)}}. \tag{10}$$

The following algorithm of switching the state variables of friction elements and choosing the time step length was applied.

In condition that at the end of the integration step there was no switches found, the integration step and the functional did not change, the initial conditions for the next step were calculated according to standard integration method (7), the functional in the right part of (6) did not change.

If at the end of the integration step there were obtained switches in several elements, then the element that switched first was found (switching time determined by (9) or (10)) and the integration step was cut down to that instant, $h^* = t^* - t^{(i)}$. The initial conditions for the next step were calculated using linear interpolation of generalized coordinates (8), the functional for the element that experienced the switch changed.

The drawback of the proposed method was found to be the case when there are multiple friction elements in the system and situation occurs when two of them have switch instants that are close to each other. Figure 3 demonstrates the situation when in the integration step between i and $i + 1$ there was obtained the switch instant S1 for one of the dry friction elements (procedure makes a return step 1 to S1) and in the next integration step (step forward denoted 2) the switch instant S2 was obtained (step back denoted 3) where S2 < S1. In the next step forward (denoted 4) the time instant S1 is obtained again and the procedure steps back 5. This leads to infinite loop of the integration method in vicinity of S1 and S2 that needs to be terminated by the procedure by determining multiple switch points in vicinity of the minimum time and switching several elements simultaneously.

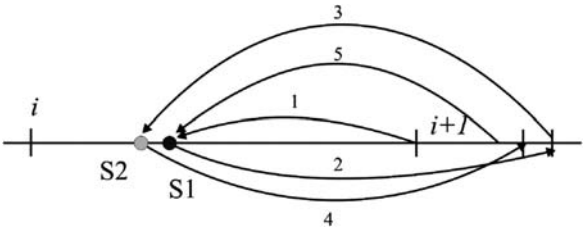

Fig. 3 Infinite loop situation in the proposed modification of integration method

3 Application of the Proposed Method to the Problem of a Train Bumping into an Obstacle

The application of proposed method is demonstrated on the problem of a train bumping into the obstacle, [1]. The coupler devices of the train (Fig. 4) are equipped with the draft gears that are operating in normal conditions and with crash elements that experience plastic deformation after the critical force, acting on the coupler, is exceeded. Rake mechanism does not allow the coupler crash elements to extend and switches the coupler out of force transition chain after its total stroke is realized.

After the coupler crash elements have exhausted their plastic deformation stroke, the nose part of the first car comes in contact with the obstacle, and tambour parts

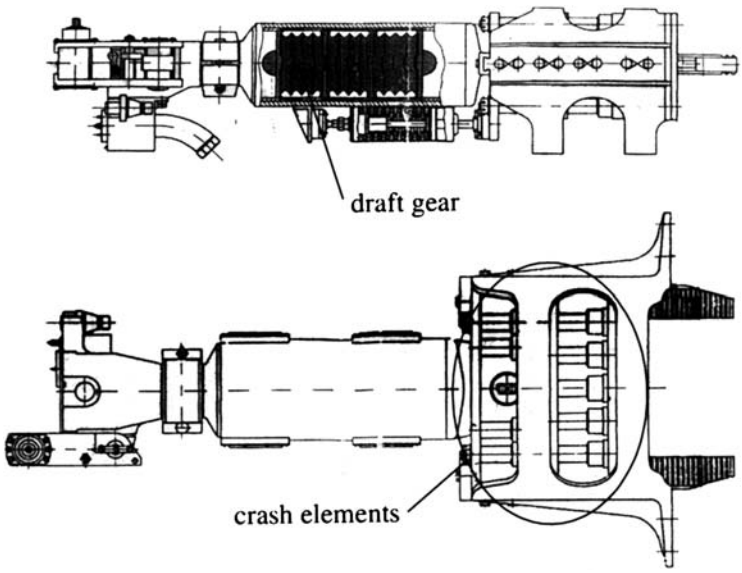

Fig. 4 Coupler device with crash elements

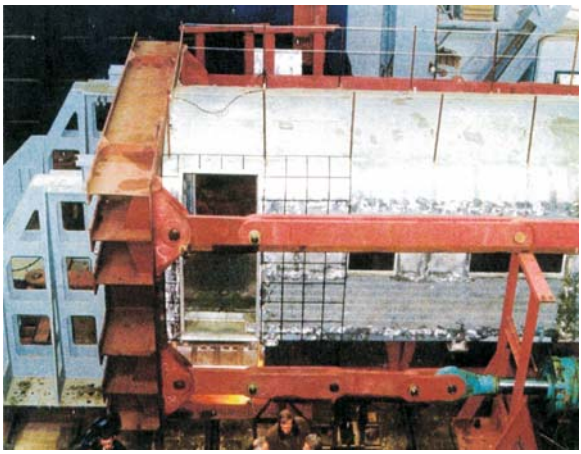

Fig. 5 Testing the car tambour parts to determine the longitudinal force that causes their plastic deformation

between the cars come into contact with each other. The tambour parts (Fig. 5) are designed to withstand much smaller longitudinal force than the rigid passenger compartment, and thus play the part of the plastic damper.

In the mathematical model the train was represented by a set of masses moving along the straight line and connected with each other by elements shown in Fig. 6. The model considered the coupler with crash elements and the possibility of tambours to undergo plastic deformation. At the initial condition the train moved with constant velocity and then bumped into the still obstacle.

Simulation results for one car crashing into the obstacle are presented in Fig. 7. Initial speed of 80 t vehicle was 50 km/h. Integration was done with 0.1 s integration

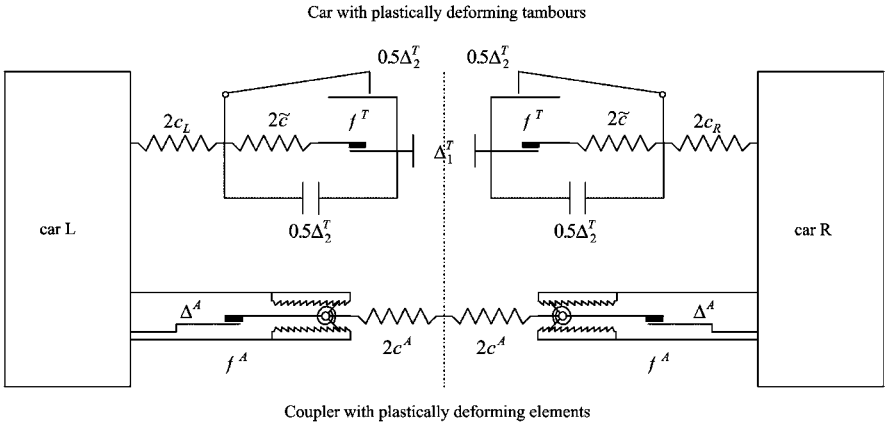

Fig. 6 Mechanical model of connection elements between the cars

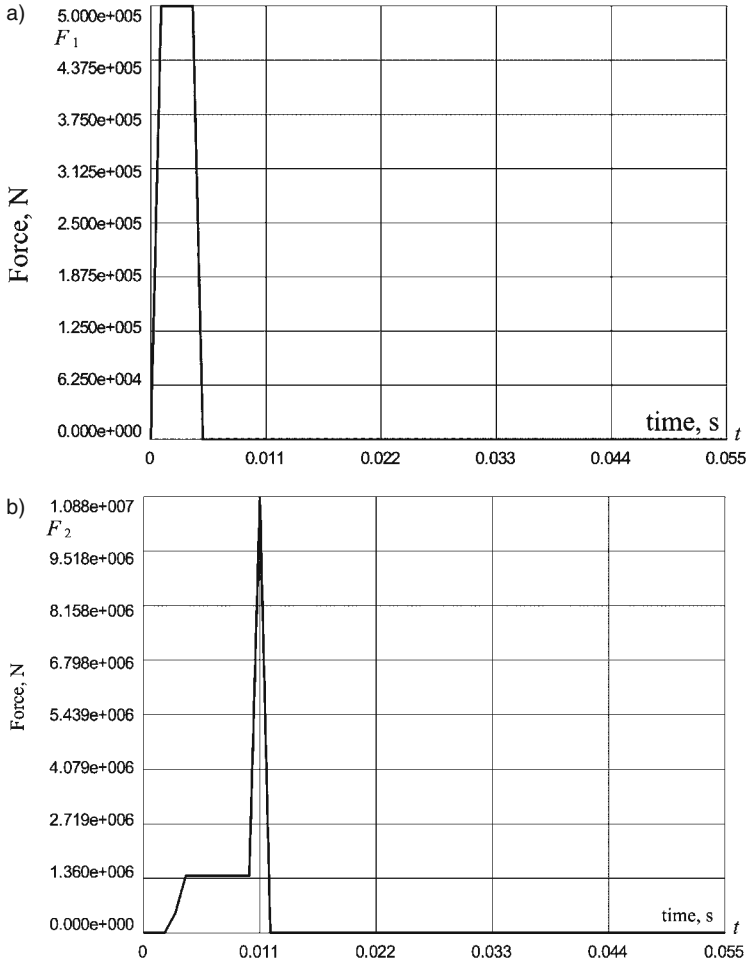

Fig. 7 Histories of forces in (**a**) the coupler with crash elements and (**b**) in the tambour (nose part of first car)

step. Bumping into the obstacle caused full plastic deformation of crash elements in the first coupler: three switch points obtained refer to transitions between elastic and plastic, plastic and elastic, elastic and off states. The nose part of the train also experienced full plastic deformation and 4 switch points were obtained: switching the element on, when the distance to the obstacle became zero, transition from elastic to plastic state, transition from plastic state to elastic deformation of the passenger compartment, zero force when the elasticity of the car body pushed the vehicle away from the obstacle.

Simulation results for 6 car train crashing into the obstacle are presented in Figs. 8 and 9. Initial speed of the train consisting of 48 t cars was 20 km/h. Integration

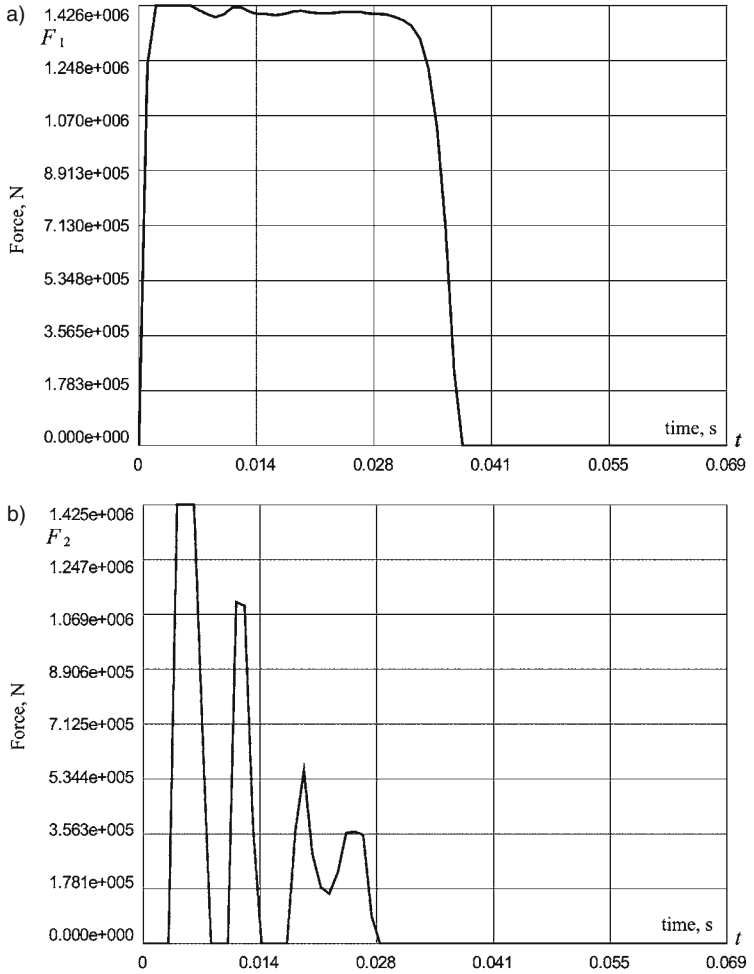

Fig. 8 Histories of forces in the coupler (**a**) and tambour (**b**) between the first car and the obstacle

was done with 0.1 s integration step. The algorithm efficiently obtained all the switch points between various states of the coupler crash elements and tambours.

4 Conclusions

Integration method was modified to deal with dry friction or plastic deformation by stick-slip (elastic-plastic) switch location using linear interpolation of generalized coordinates. Application to accidental collision of the train into the obstacle is shown.

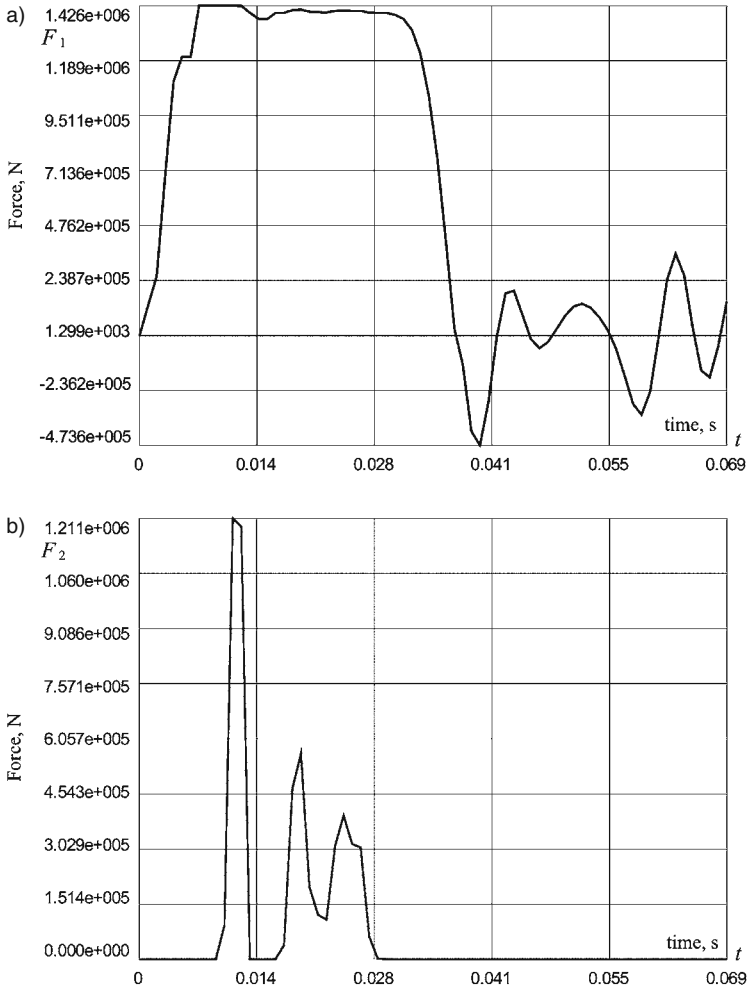

Fig. 9 Histories of forces in the couplers (**a**) and tambours (**b**) between the first and the second cars

References

1. Arsentyev A.S. Dynamic features of high speed train Sokol / Smirnov S.A., Dyatlov A.N., Boronenko Yu.P., Orlova A.M., Solovjev V.M. // 17th IAVSD Symposium Extended abstracts, Lyngby, August 2001, 3 p.
2. Garg, V.K., Dukkipati, M. Rolling stock dynamics. Moscow: Transport, 1998, 389 p.
3. Orlova, A., Boronenko, Yu. The anatomy of railway vehicle running gear // In: Handbook of railway vehicle dynamics. Ed. S. Iwnicki. ISBN-13: 978-0-8493-3321-7. – CRC Press, Taylor & Francis Group, 2006, pp. 39–84.

Damper Modelling and Its Implementation in Railway Simulation Program

Asier Alonso and J.G. Giménez

Abstract This chapter presents a mathematical model of a railway hydraulic damper. The objective is to develop a model suitable to be implemented in a railway simulation program. Computational cost should, therefore, be maintained low not to decrease the simulation speed (rate) to unacceptable values.

A model based mainly in physical characteristics (piston section, volume of the chambers, characteristics of the valves, etc.) is developed. In a first part of the chapter, the modelling of each part of the damper is discussed. Afterwards, the model of the complete damper is constructed and finally, model results are compared satisfactorily with experimental tests.

The chapter also includes a discussion on the numerical problems associated with the developed model and a new simplified version is proposed to overcome the majority of the difficulties presented in the original model.

1 Introduction

In order to obtain precise results when simulating the dynamic behaviour of a railway vehicle it is necessary to develop accurate models of all the elements that play an important part in the dynamics of the vehicle (wheel to rail contact, air springs, rubber elements, dampers, etc.). However, besides the accuracy requirements it is necessary that the developed models are simple enough to be implemented in dynamic simulation programs, as a too complex model of any component could increase the computational cost up to unacceptable levels.

The objective of this work is to obtain a mathematical model of railway hydraulic dampers that fulfil the above mentioned requirements. The idea is to develop a model based mainly in physical characteristics (piston section, volume of the chambers, characteristics of the valves, etc.). In this way, the model could be applied to

A. Alonso (✉)
CEIT and TECNUN (University of Navarra), Paseo M. Lardizabal 13, E-20018 San Sebastian (Guipúzcoa), Spain
e-mail: aalonso@ceit.es

P.G. Thomsen, H. True (eds.), *Non-smooth Problems in Vehicle Systems Dynamics*,
DOI 10.1007/978-3-642-01356-0_11,

different dampers just modifying the "geometrical" parameters and so the number of tests to adjust the model parameters can be reduced to the minimum. To achieve the objective, in a first step the operation of a typical railway damper is studied. Secondly, a complete model of the damper is developed. The results obtained with the model are compared with experimental results in order to determine its accuracy. Finally, a reduced model simple enough to be implemented in a dynamic simulation program will be developed.

2 General Description of a Railway Damper

Railway dampers are hydraulic devices generating damping forces mainly due to the resistance of a fluid when passing through valves and orifices.

Analysing the structure of a railway damper it can be seen that it is composed by three chambers: the compression chamber, the rebound chamber and an auxiliary one. The auxiliary chamber is not completely full of oil, having both oil and air inside it.

Analysing the design of the dampers it is clear that the volumes of both the rebound and the compression chambers change with the movement of the piston rod. It can also be seen that the section areas of both chambers are different due to the piston rod. These elements are usually designed in such a way that the section of the rebound chamber is half of the section of the compression chamber. This is done in order to obtain similar forces in the compression and the rebound stroke.

All the chambers are connected through three valves:

- The auxiliary chamber is connected to the compression chamber by a check valve that allows the oil flow only from the auxiliary chamber to the compression chamber.
- In a similar way, there is another check valve between the compression and the rebound chamber that allows the oil flow from the first to the second one.
- The last one is a damping valve and connects the rebound and the auxiliary chambers.

During the operation of the damper two different situation can be distinguished: the compression stroke and the rebound stroke (Fig. 1).

During the compression stroke the volume of the compression chamber is reduced (therefore, there is an increase of the pressure in this chamber). In the same way, the volume of the rebound chamber is increased producing a reduction of the pressure. Due to the difference of the pressures in both chambers the check valve situated in the piston rod opens, allowing the oil flow from the compression to the rebound chamber.

It can be clearly seen that if the piston goes in, the reduction of the volume of the compression chamber is larger than the increase of the volume of the rebound chamber. This produces an increment of the pressure at both chambers generating a flow through the damping valve from the rebound chamber to the auxiliary one.

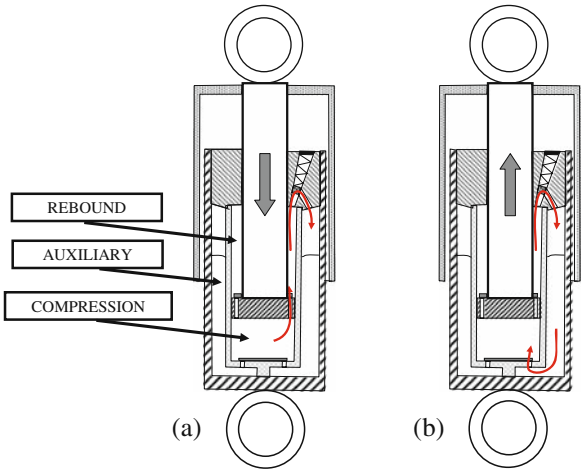

Fig. 1 Damper operation (**a**-compression stroke, **b**- rebound stroke)

Finally as the pressure of the compression chamber is larger than the pressure in the auxiliary one the check valve situated in the bottom remains closed.

During the rebound stroke the piston goes out. This movement produces an increase of the pressure in the rebound chamber and a flow through the damping valve. In the compression chamber there is an increase of the volume and a reduction of the pressure. This causes that the check valve situated in the piston rod remains closed and that the other check valve opens, obtaining a flow from the auxiliary chamber to the compression one.

As a conclusion of this analysis it can be seen that the oil always flow in the same direction in this type of dampers (see Fig. 1).

Also it can be conclude that, in order to develop an accurate model of the damper special attention must be put to the valves modelling and the relationship between flows, piston rod movement and the compressibility of the oil.

3 Modelling of the Main Components

3.1 Damping Valve

Figure 2 shows a schematic representation of a typical damping valve (in this scheme, point *A* belong to the rebound chamber and point *B* belongs to the auxiliary chamber). Operation of this element is as follows:

- If the force caused by the pressure difference between the rebound and the auxiliary chamber is lower than the preload of the coil spring, then the oil can only flow through the orifice (*Q1*).
- However if the pressure in the rebound chamber is high enough, then the force caused by the pressure can move the valve and the oil flows through the orifice and trough this gap (*Q1* and *Q2*).

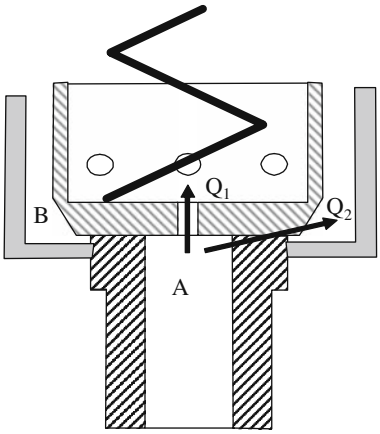

Fig. 2 Damping valve scheme

It is worth pointing out that in certain dampers there are many valves in parallel.

The design variables of this valve are the following ones: the diameter of the orifice (in certain valves the orifice does not exist), the spring constant, the preload of the coil spring and the number of valves.

In order to model this element the relationship between pressures and oil flow must be obtained. For that, the Bernoulli equation can be used:

$$Q = C_D A_{out}(P_{aux}, P_{rebound}, K_{spring}, F_{spring}, geom.\ characteristics) \times \sqrt{\frac{2(P_{rebound} - P_{aux})}{\rho}} \quad (1)$$

Where: Q is the oil flow, C_D is an nondimensional parameter (usually between 0.5 and 0.8), A_{out} is the passing area, $P_{rebound}$ is the pressure in the rebound chamber, P_{aux} is the pressure in the auxiliary chamber, K_{spring} is the stiffness of the coil spring, F_{spring} is the preload of the spring and ρ is the oil density.

As it can be seen, the passing area depends on the rebound chamber pressure. As this pressure increases the coil spring is compressed and the value of the passing area increases (see Fig. 3).

3.2 Check Valves

Figure 4 shows a schematic representation of a check valve. The main component is a thin disc that can be deformed under the action of a differential pressure. The opening of the valve is bounded by two stops.

- If the pressure at B is higher than the pressure at A then the disc remains undeformed and the oil flow is zero.

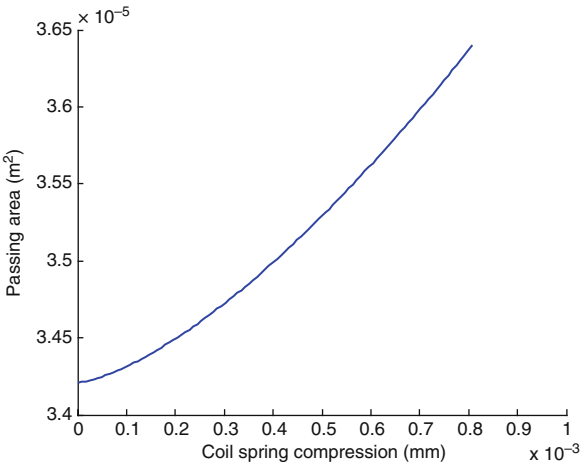

Fig. 3 Passing area as a function of the coil spring compression

Fig. 4 Check valve scheme

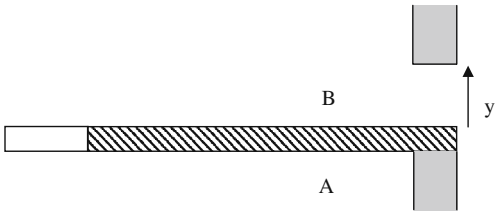

- However, if the pressure at A is higher than pressure at B there is a deformation in the disc and a passing area is generated, therefore generating an oil flow from A to B.

In order to model this element the opening of the valve as a function of the differential pressure must be obtained. For that, a finite element code has been used (Fig. 5). Figure 6 shows the obtained results.

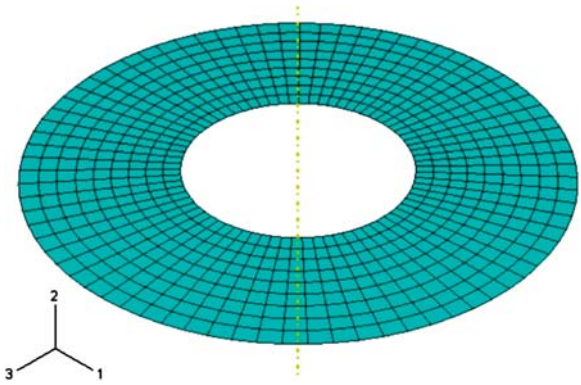

Fig. 5 FE model of the check valve

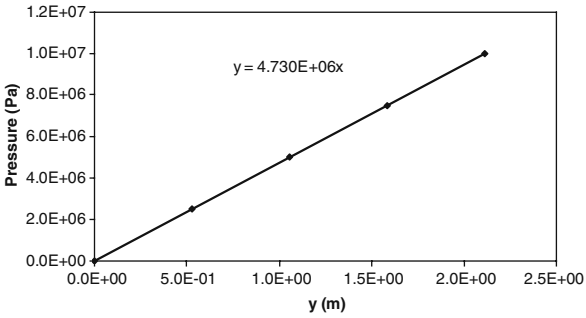

Fig. 6 Valve opening versus pressure difference

As it can be seen, the stiffness of the disc is very low: the opening of the valve is maximum (it reach the stop) at very small pressures. Therefore it can be concluded that the check valve can be modelled as an orifice that only allows the oil flow in one direction.

3.3 Chamber Equations

3.3.1 Rebound and Compression Chamber

In order to model the rebound and compression chamber the following phenomena must be taken into account:

- Piston rod displacement
- Oil flows through valves, orifices, etc.
- Oil compressibility

The equation that relates the above mentioned phenomena is the following one:

$$\sum Q_i + A_{pistion} \cdot V = \beta \cdot Vol \cdot \frac{dP}{dt} \tag{2}$$

Where β is the bulk modulus of the oil, V is the velocity of the piston rod, A_{piston} is the piston section and *Vol* is the volume of the chamber (see Fig. 7).

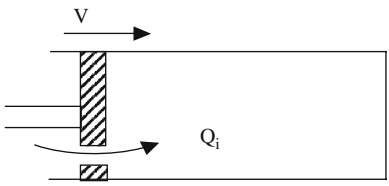

Fig. 7 Compression and rebound chamber scheme

3.3.2 Auxiliary Chamber

As it has previously been pointed out, the auxiliary chamber is partially filled with air. Obviously, the oil of this chamber can be considered as uncompressible compared with the air. If the air mass inside the auxiliary chamber is considered constant, then the following equation can be used to determine the pressure:

$$\frac{d(P_{aux} Vol_{aux})^{\gamma}}{dt} = 0 \tag{3}$$

Where: P_{aux} auxiliary chamber pressure, γ polytrophic constant and Vol_{aux} volume of the air.

The volume of the air can be calculated with the following formula:

$$V = V_0 - \int Q \, dt \tag{4}$$

Where V_0 initial volume of the oil and Q oil flow that enters to the chamber.

4 Model Results

Once the main elements of the railway damper have been studied, the mathematical model of the complete system can be constructed. It can be seen that the system have three non linear differential equations (one for each chamber) and that the equations are related by means of the oil flows between the chambers. In order to solve these equations MATLAB-SIMULINK® has been used.

In order to determine the accuracy of the model, a damper H04_1222 of KONI has been modelled and tested. The experimental results were obtained at the test bench shown in Fig. 8. It is worth pointing out that in order to measure the displacement of the damper an additional LVDT sensor has been installed in the cylinder on the damper. This has been done in order to eliminate the influence of the rubber elements that every damper has in their ends.

Figure 9 shows the results obtained for different test conditions. Figure 9a shows the force as a function of the piston rod position (frequency 3 Hz, amplitude 5 mm). Figure 9b shows the same information but the velocity has been used instead of the position. As it can be seen the experimental results are quite close to the theoretical ones.

Fig. 8 Test bench

Figure 9c–e show the behaviour of the damper in other cases (frequency 2 Hz, amplitude 2 mm), (frequency 2 Hz, amplitude 8 mm) and (frequency 1 Hz, amplitude 10 mm) respectively

Finally, Fig. 9f shows a case in which the preload of the damping valve has been modified. In the figure, the points in which the pressure in the rebound chamber is high enough to exceed the preload of the damping valve can be clearly seen. This produces a variation of the force velocity curve.

5 Simplified Model Suitable to Be Implemented in a Railway Simulation Program

The complete model of the damper is too complex to be implemented in a railway simulation program (since it includes several equations to model the pressures at the chambers, oil flows, etc.). Also it has been checked that due to the opening and closing of the check valves the behaviour is very non linear (as an example Fig. 10 represent the pressure evolution at the compression and rebound chambers during

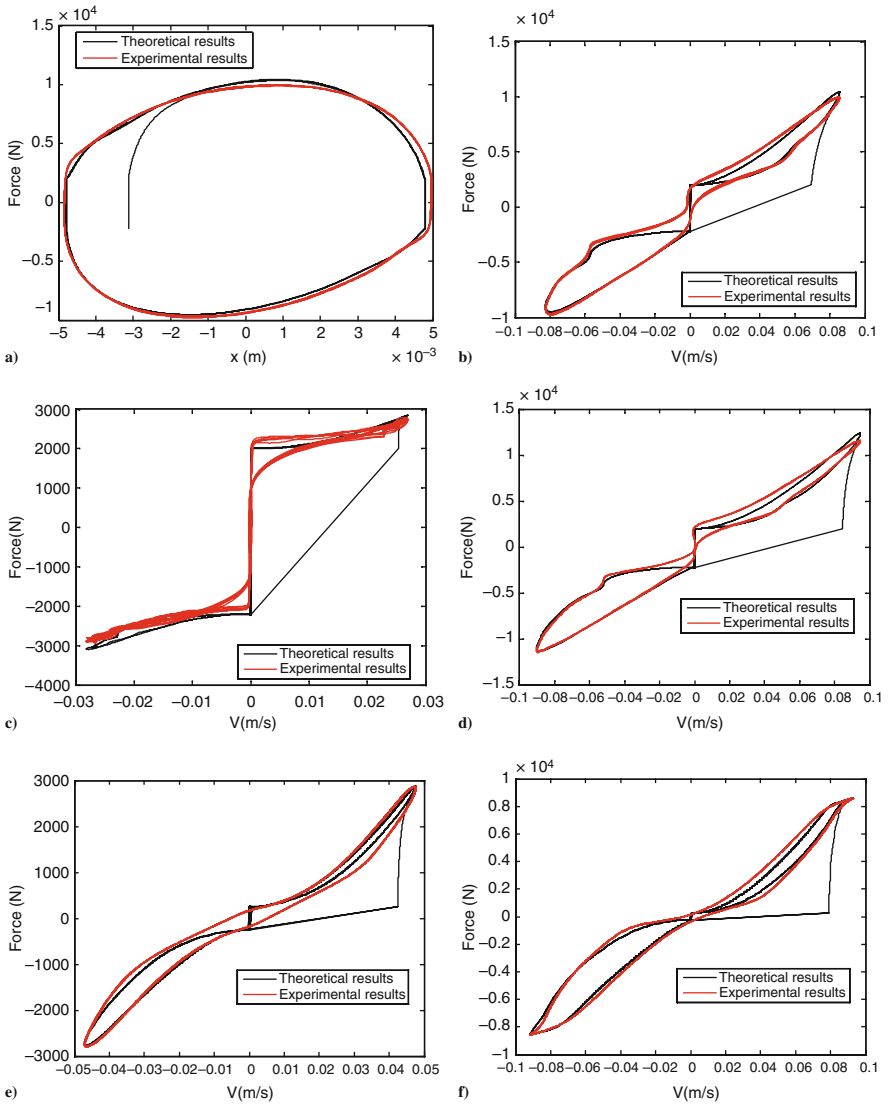

Fig. 9 (**a**) force vs. displacement (3 Hz, 5 mm), (**b**) force vs. speed (3 Hz, 5 mm), (**c**) force vs speed (2 Hz, 2 mm), (**d**) force vs speed (2 Hz, 8 mm), (**e**) force vs speed (1 Hz, 10 mm), (**f**) force vs speed (2 Hz, 8 mm spring preload modified)

the rebound stroke, it can be observed that in the opening (t = 0.26 s) and closing (t = 0.42 s) of the check valves situated in the bottom of the damper the behaviour is very non linear.

Due to that, it has been considered necessary to develop a simplified model suitable to simulation programs. To achieve this objective, a detailed analysis of the

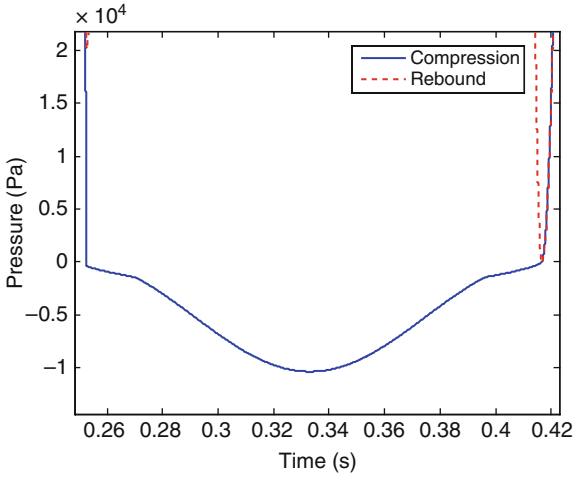

Fig. 10 Pressure evolution during the opening and closing of the check valves

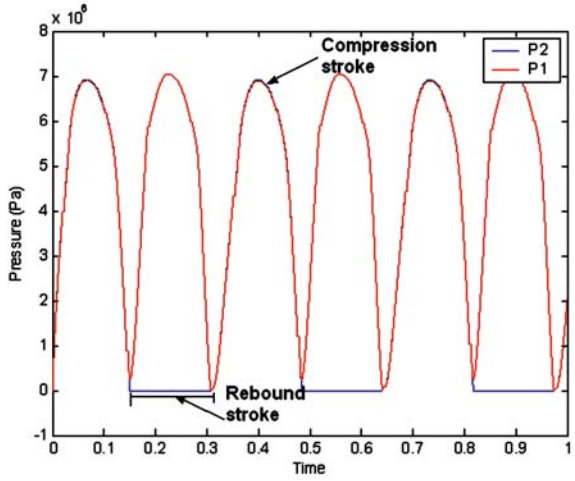

Fig. 11 Compression (P2) and rebound (P1) chamber pressures with respect to time

damper operation has been done. Figure 11 shows the evolution of the pressures at the rebound and compression chambers with respect to time:

5.1 Auxiliary Chamber

Figure 12 shows the pressure at the auxiliary chamber with respect to time in a certain case. It can be clearly seen that the pressure variation in this chamber is very small. Therefore to develop the simplified model, it is considered that the pressure at the auxiliary chamber is constant and equal to the atmospheric pressure.

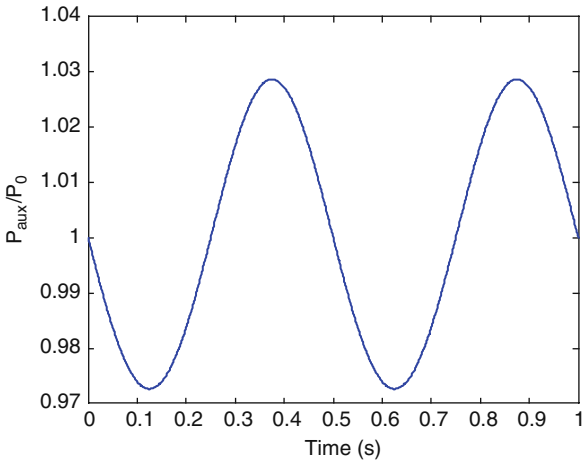

Fig. 12 Pressure at the auxiliary chamber with respect to time

5.2 Compression Stroke

During the compression stroke the following considerations can be done

- The check valve situated in the piston is open. Also the pressure difference between the compression chamber and the rebound chambers is very small (see Fig. 11). Therefore, in order to obtain a simplified model, it can be considered that the pressures at both chambers are the same.

$$Q_{Compression \rightarrow \text{Rebound}} \neq 0$$
$$P_{rebound} = P_{compression}$$

- The check valve situated in the bottom of the damper remains closed.

$$Q_{Auxiliary \rightarrow Compression} = 0$$

- There is an oil flow through the damping valve.

$$Q_{compression \rightarrow Auxiliary} \neq 0$$

Introducing these simplifications, the complete model can be reduced to a single differential equation during the rebound stroke:

$$Q_{compression \rightarrow Auxiliary} + (A_{rebound} - A_{compression}) \cdot V = \beta \cdot (Vol_{rebound}(x) + Vol_{compression}(x)) \frac{dP_{rebound}}{dt} \quad (5)$$

5.3 Rebound Stroke

In this case, the following considerations can be done:

- The check valve situated in the piston is open:

$$Q_{Compression \rightarrow \text{Rebound}} = 0$$

- The pressure in the compression chamber is very small (see Fig. 11):

$$P_{compression} = 0$$

Introducing these simplification, the following equation can be obtained for the rebound stroke.

$$Q_{31}(P_1, geom\ characteristics) - A_{rebound} \cdot V = \beta \cdot Vol_{rebound}(x)\frac{dP_1}{dt} \qquad (6)$$

Summarizing, it can be concluded that the whole model can be simplified into two differential equations: the first one for compression and the second one for extension. These equations have been programmed in order to compare the results provided by the simplified equations and the complete model. Figure 13 shows the results of such comparison. As it can be seen the results are very similar. Also it can be said that the computational cost of the method has been largely reduced.

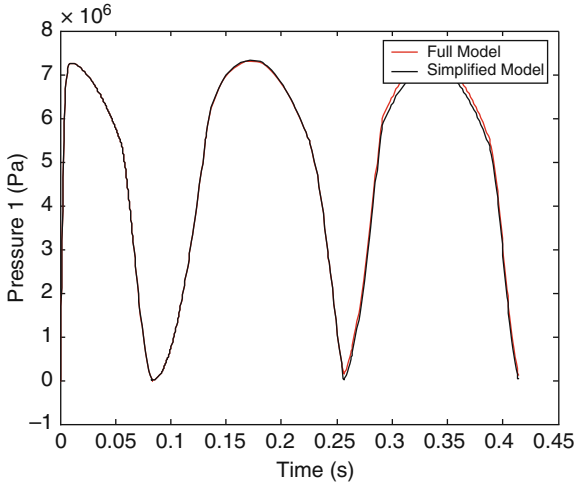

Fig. 13 Comparison of the results provided by the complete model and the simplified one

6 Conclusions

In order to finish the following asseverations can be done:

- A physical model of a railway damper has been developed.
- The results obtained with the model have been compared with experimental results. It has been checked that the correlation between them is good. However, it has also been checked that the computational cost of the full model is too high to be implemented in a railway simulation program.
- A simplified model fast enough to be implemented in a dynamic simulation program has been developed. It is worth pointing out that the results obtained with the simplified model are very similar to those provided by the complete model.

Suppression of Bumpstop Instabilities in a Quarter-Car Model

Fredrik Svahn, Jenny Jerrelind, and Harry Dankowicz

Abstract Vehicle manufacturers are constantly pushed to reduce the aerodynamic drag of vehicles, for example by constructing lower vehicles with less road clearance. This, however, reduces the available margin for oscillations within the suspension. If the oscillation amplitude exceeds a critical value, the suspension will impact a bumpstop. Under periodic excitation, the onset of low-velocity impacts is associated with a strong instability in favor of high-velocity impacts. Such impacts reduce comfort and could be damaging to the vehicle. Efforts should therefore be made to limit impact velocities with the bumpstop, for example by suppressing the instability associated with low-velocity impacts. This paper proposes a low-cost feedback-control strategy, based on making small adjustments to the position of the bumpstop, that serve to suppress the transition to high-velocity impacts with the bumpstop in the case of periodic excitation. The control law is derived from the theory of discontinuity maps. The results demonstrate that the feedback strategy works even when wheel-hop is present.

1 Introduction

The current climate debate is pushing vehicle manufacturers to develop more environmentally friendly solutions, the primary goal being to reduce fuel consumption. One way of achieving this is to make vehicles with less road clearance to reduce the aerodynamic drag. A lower road clearance, however, reduces the available margin for oscillations of the suspension (known as the *rattle space*). If the amplitude of the oscillation exceeds a critical value the suspension will impact a large rubber bushing, a bumpstop. High-velocity impacts with the bumpstop reduce passenger comfort and could be damaging to the vehicle, so the impact velocity needs to be kept at a minimum.

F. Svahn (✉)
KTH Vehicle Dynamics, Royal Institute of Technology, SE-100 44 Stockholm, Sweden
e-mail: fsvahn@kth.se

P.G. Thomsen, H. True (eds.), *Non-smooth Problems in Vehicle Systems Dynamics*,
DOI 10.1007/978-3-642-01356-0_12,

It is known from studies of mechanical vibro-impact oscillators that the onset of low-velocity impacting motion along a periodic steady-state motion may result in a dramatic and unanticipated transition to a motion involving high-velocity impacts. The objective of this paper is to consider this phenomenon in the context of vehicle suspensions.

One solution to avoid high-velocity impacts with the bumpstop is to fit the vehicle with an active suspension that would modify the relative motion between the sprung and unsprung mass through the addition of continuous actuation (cf. [5, 8, 13, 14]). The inclusion of an active suspension, however, leads to substantial increases in energy consumption. An alternative is to allow low-velocity impacts of the bumpstop [12] but employ a low-cost control strategy that would prevent transitions to high-velocity impacting motions.

This work considers a two-degree-of-freedom quarter-car model with bumpstops, with parameter values representative of a typical passenger car. Here, the method of discontinuity maps (originally developed by Nordmark in [10] and since then used and analyzed extensively; see e.g. [1, 4, 6, 11]) is used to investigate the correction to the non-impacting dynamics introduced subsequent to the onset of low-velocity impacts. Specifically, the discontinuity-map approach is used to distinguish between sub- and super-critical bifurcation scenarios associated with the existence of a periodic steady-state trajectory with zero impact velocity. Of the two scenarios the subcritical corresponds to the case where the steady-state behavior of the quarter-car model exhibits a discrete jump from the non-impacting motion to an impacting motion with high-velocity impacts. In contrast, in the super-critical case, impact velocities along the steady-state response vanish in the limit as the bifurcation point is approached.

In [2] Dankowicz and Jerrelind introduced a feedback-control strategy which, with suitably chosen control gains, guarantees a super-critical bifurcation scenario even when such would not occur in the absence of control. This is achieved by making small adjustments to the position of the bumpstop at opportune moments during the system oscillation. In [3] Dankowicz and Svahn presented a constructive proof of the method and applied it to one- and two-degree-of-freedom spring-mass-systems. In this paper, the control strategy is shown to be applicable to systems with additional discontinuities in the dynamics, including a bilinear suspension damping and wheel-hop.

Some notes on notation: Normal-faced letters, such as q and z, denote scalar-valued quantities. Bold-faced letters, such as $\mathbf{x}$ and $\mathbf{P}$, denote vector-valued quantities. Calligraphic letters, such as $\mathcal{P}$ and $\mathcal{C}$, denote surfaces in state space. Sub- and superscripts in conjunction with scalar or vector-valued quantities, such as $\mathbf{x}^*$ or $\mathbf{P}_0$, are used to distinguish different scalars or vectors. Matrix products are denoted with a centered dot as in $\mathbf{c} \cdot (\mathbf{x} - \mathbf{x}^*)$. Composition of maps is denoted by the $\circ$ symbol representing application from right to left. Finally, the symbols $\uparrow$ and $\downarrow$ followed by numerical values are used to denote changes in the quantity preceding the symbols that reach the numerical value from above or below, respectively.

2 The Quarter-Car Model

The simplest mechanical model of a vehicle used in studying vertical motion is the quarter-car model [7] (cf. Fig. 1 which also includes a bumpstop). This is widely employed for evaluating comfort criteria and for developing control methods for vehicle suspensions. As the model reduces the vehicle dynamics to the two vertical translational degrees of freedom of the chassis and the wheel set, it is unable to account for roll and pitch motions of the vehicle.

Three distinctly different conditions of motion are considered in this paper. Specifically, a condition of *contact* applies to the mechanism when the lower mass, representing the tyre and wheel set, is displaced relative to the ground by a distance smaller than the relaxed radial dimension of the tyre and there is a resultant positive normal reaction force on the tyre. In contrast, a condition of *free flight* applies to the mechanism when the lower mass is displaced from the ground by a distance greater than the relaxed radial dimensions of the tyre.

With the inclusion of damping in the tyre-ground interactions, it becomes necessary to consider a condition of *quasi-contact*. This corresponds to the case when the lower mass is displaced relative to the ground by a distance smaller than the relaxed radial dimension of the tyre, but the nominal reaction force is negative. In this case, the actual reaction force is assumed to equal zero until a subsequent event-triggered transition.

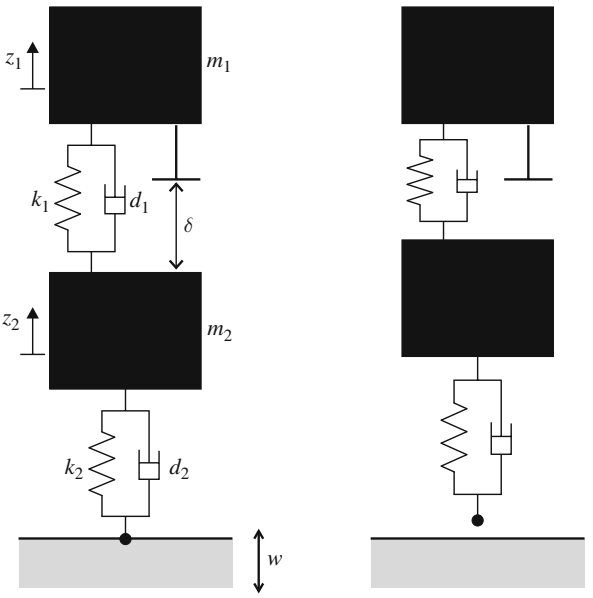

Fig. 1 A two-degree-of-freedom mechanical model of the vertical motion of a vehicle suspension in contact (*left panel*) and in free flight (*right panel*)

2.1 Vector Fields

With reference to Fig. 1, let z_1 and z_2 denote the deflections away from the loaded equilibrium position of the sprung (m_1) and unsprung (m_2) masses, respectively, in the absence of ground excitation. Assuming a periodically varying ground displacement with period $2\pi/\omega$, the system dynamics can be described in state-space form through the introduction of a state vector $\mathbf{x}=\left(q_1\ u_1\ q_2\ u_2\ \varphi\right)^T$, where $q_1=z_1-z_2$, $u_1=\dot{z}_1-\dot{z}_2$, $q_2=z_2$, $u_2=\dot{z}_2$, and $\varphi=\omega t \bmod 2\pi$ and an associated vector field

$$\mathbf{f}(\mathbf{x})=\begin{pmatrix} u_1 \\ -\left(\frac{1}{m_1}+\frac{1}{m_2}\right)(k_1q_1+d_1u_1)+\frac{1}{m_2}\left(k_2\left(q_2-w\right)+d_2\left(u_2-\dot{w}\right)\right) \\ u_2 \\ \frac{1}{m2}\left(k_1q_1+d_1u_1-d_2\left(u_2-\dot{w}\right)-k_2\left(q_2-w\right)\right) \\ \omega \end{pmatrix} \tag{1}$$

in the case of contact, and

$$\mathbf{f}(\mathbf{x})=\begin{pmatrix} u_1 \\ -\left(\frac{1}{m_1}+\frac{1}{m_2}\right)(k_1q_1+d_1u_1)+\frac{m_1+m_2}{m_2}g \\ u_2 \\ \frac{1}{m2}\left(k_1q_1+d_1u_1\right)-\frac{m_1+m_2}{m_2}g \\ \omega \end{pmatrix} \tag{2}$$

in the case of free flight and quasi-contact. Here, k_1 is the suspension stiffness, k_2 is the tyre stiffness, w is the ground displacement, d_1 is the suspension damping (of bilinear nature: one value in compression and one in expansion, d_2 is the tyre damping, and g is the acceleration of gravity).

2.2 Transitions

Transitions between the three distinct conditions of motion are triggered by discrete events including the onset and loss of contact as well as rigid impacts with the bumpstop.

Excluding, for a moment, impacts with the bumpstop, the motion of the mechanism may transition from a condition of free flight only through the onset of contact with the ground triggered by the event $q_2-(m_1+m_2)g/k_2-w\downarrow 0$. Similarly, the opposite event $q_2-(m_1+m_2)g/k_2-w\uparrow 0$ triggers the loss of contact associated with a transition from a condition of quasi-contact to one of free flight.

Continuing to ignore impacts with the bumpstop, the motion of the mechanism may transition from a condition of contact only through the vanishing of the tyre-ground interaction force associated with a transition to quasi-contact and triggered by the event $k_2\left(w-q_2\right)+d_2\left(\dot{w}-u_2\right)+(m_1+m_2)g\downarrow 0$. Similarly, the opposite

event $k_2(w-q_2)+d_2(\dot{w}-u_2)+(m_1+m_2)g \uparrow 0$ triggers the onset of contact associated with a transition from a condition of quasi-contact.

In addition to the transitions enumerated above, discrete events triggered by impacts with the bumpstop impose discrete changes both in the system state as well as, possibly, in the condition of motion. Specifically, impacts are here triggered by the event $q_1+\delta \downarrow 0$ and result in discrete changes in state given by

$$\mathbf{x} \mapsto \begin{pmatrix} q_1 \\ -eu_1 \\ q_2 \\ \frac{m_1}{m_1+m_2}(1+e)u_1+u_2 \\ \varphi \end{pmatrix}, \tag{3}$$

where e is a Newtonian coefficient of restitution.

In the discussion below, events are said to be *transversal* provided that they are associated with a non-vanishing first derivative of the corresponding trigger function, and *grazing* otherwise.

3 Dynamical Instabilities

For sufficiently small amplitude of oscillation of the ground displacement, the response of the quarter-car model remains in a condition of sustained contact without collisions with the bumpstop. Increased values of the ground-displacement oscillation amplitude may be associated either with the onset of transitions to distinct modes of motion or the onset of discrete jumps in system state associated with impacts. Such changes in the qualitative nature of the short-term time history are known to be associated with potentially dramatic changes in the steady-state response of the system. Examples include sudden changes in the number of coexisting steady-state responses, their stability properties, or their regularity.

As a special case, this paper focuses on the onset of impacts with the bumpstop associated with a periodic oscillation of period $2\pi/\omega$ of the mechanism that includes a zero-velocity contact with the bumpstop, i.e., a point $\mathbf{x}^*$ of *grazing* contact along the state-space trajectory where $q_1+\delta=u_1=0$ and $\dot{u}_1>0$. In this case, subsequent changes in ground-displacement oscillation amplitude are typically associated with a sudden transition to a distinct steady-state oscillation with high-velocity impacts with the bumpstop (a *sub-critical bifurcation*) or to a, possibly chaotic, steady-state oscillation with sustained low-velocity impacts (a *super-critical bifurcation*). The discussion below highlights the tools available to predict the nature of the transition and practical means for guaranteeing the super-critical case.

3.1 Discontinuity Maps

The effects on the system response of the onset of low-velocity impacts with the bumpstop can be reduced down to the correction to the state-space flow in the

vicinity of the grazing point in the absence of impacts. Known in the literature as the *discontinuity map*, this correction can generally not be found explicitly but can be expressed to arbitrary order of approximation as a series expansion in the deviation from the grazing point.

To this end, denote by $\mathcal{P}$ the set of points in state space for which $u_1{=}0$ and $\dot{u}_1{>}0$. In particular, $\mathbf{x}^* \in \mathcal{P}$ is a point of *transversal intersection* of the grazing state-space trajectory with $\mathcal{P}$. Provided that all other events along the grazing trajectory are transversal, it follows that there exists a smooth Poincaré map $\mathbf{P}_0$ that maps points near $\mathbf{x}^*$ on $\mathcal{P}$ to the subsequent point of intersection with $\mathcal{P}$ after a time $\approx 2\pi/\omega$ when impacts are disregarded.

As described in [2, 3], the inclusion of impacts is captured by the composite Poincaré map

$$\mathbf{P}{=}\mathbf{P}_0 \circ \mathbf{D} \tag{4}$$

that again maps points $\mathbf{x}^*$ on $\mathcal{P}$ to the subsequent point of intersection with $\mathcal{P}$ after a time $\approx 2\pi/\omega$. Here, $\mathbf{D}$ is the sought-after discontinuity map. Specifically,

$$\mathbf{D}(\mathbf{x}) = \begin{cases} \mathbf{x} & \text{if } q_1 + \delta \geq 0 \\ \mathbf{x}^* + \beta\sqrt{q_1^* - q_1} + \mathcal{O}(\mathbf{x} - \mathbf{x}^*) & \text{if } q_1 + \delta < 0 \end{cases} \tag{5}$$

where $\mathcal{O}(\mathbf{x} - \mathbf{x}^*)$ denotes terms of order linear or higher in $\mathbf{x} - \mathbf{x}^*$ and

$$\beta{=}-(1+e)\begin{pmatrix} 0 \\ 0 \\ u_2^* \\ \frac{m_1}{m_1+m_2}\dot{u}_1^* + \dot{u}_2^* \\ \omega \end{pmatrix}. \tag{6}$$

Thus, for an initial point $\mathbf{x} \approx \mathbf{x}^*$ on $\mathcal{P}$ with $q_1^* - q_1{>}0$, to lowest order the subsequent point of intersection with $\mathcal{P}$ deviates from $\mathbf{x}^*$ along the direction $\partial_{\mathbf{x}}\mathbf{P}_0(\mathbf{x}^*)\cdot\beta$ by an amount proportional to $\sqrt{q_1^* - q_1}$. For sufficiently large values of $q_1 - q_1^*$, the growth in the deviation associated with this square root is potentially balanced by the contracting nature of the smooth Poincaré map $\mathbf{P}_0$. In contrast, while the rate of contraction of $\mathbf{P}_0$ is finite for all small values of $\mathbf{x} - \mathbf{x}^*$, the growth rate associated with the square root grows beyond all bounds as $\mathbf{x} \to \mathbf{x}^*$. Its destabilizing influence must therefore be properly accounted for in order to establish the nature of the transition triggered by the onset of grazing contact with the bumpstop.

As argued in [6] a necessary condition for the super-critical bifurcation scenario is the positivity of the sequence

$$\xi_n{=}\begin{pmatrix} 1 & 0 & 0 & 0 & 0 \end{pmatrix}\cdot\left(\partial_{\mathbf{x}}\mathbf{P}_0(\mathbf{x}^*)\right)^n\cdot\beta, n{=}1,\ldots,\infty. \tag{7}$$

In this case, for an infinitesimal small perturbation away from $\mathbf{x}^*$ in a direction such that an impact occurs, the number of cycles until the next impact goes to infinity as the parameter value corresponding to grazing is approached.

3.2 Compositions

As suggested in the previous section, the only condition for the existence of the smooth Poincaré map $\mathbf{P}_0$ is the transversal nature of all events other than the grazing impact event. In practice, $\mathbf{P}_0$ may be obtained by the composition of distinct maps corresponding to transitions between successive events.

In the case of the quarter-car model, events include the transitions between distinct conditions of motion, discrete jumps in state space due to impacts as well as changes in the relative direction of motion of the upper and lower masses corresponding to a discrete change in the damping constant d_1. Since the vector field is smooth in between each such event and assuming transversality, Poincaré maps could then be derived between each such successive event by solving the suitable variational equations and applying the appropriate surface projection (cf [2]).

4 Feedback Stabilization

To suppress a sub-critical transition to steady-state oscillations of the vehicle model that exhibit high-velocity impacts with the bumpstop, a low-cost control method is proposed here, based on the ideas presented in [2, 3]. Specifically, a feedback strategy is formulated that makes small adjustments to the position of the bumpstop that control the destabilizing influence of the square-root terms in the discontinuity map.

4.1 Control Algorithm

The control strategy proposed here relies on a discrete adjustment to the value of δ at an opportune moment during the oscillatory motion of the quarter-car model at which no interference would result from such an adjustment. Specifically, denote by $\mathbf{x}^{**}$ a suitably chosen point along the grazing trajectory and let $\mathcal{C}$ be some state-space surface that is transversal to the grazing trajectory at $\mathbf{x}^{**}$. Feedback-induced changes in δ are then imposed at moments of intersection with $\mathcal{C}$ and expressed in terms of the deviation from $\mathbf{x}^{**}$. As an example, let $\mathbf{x}^{**}$ be a point with $u_1{=}0$ and $\dot{u}_1 < 0$ and define $\mathcal{C}$ as the collection of all such points. In this case, adjustments to the bumpstop position are imposed at moments of local maxima in the relative separation q_1 between the upper and lower masses.

Although a nonlinear feedback strategy could be formulated, the sub- or super-criticality of the bifurcation associated with the onset of grazing contact depends entirely on the linearization about the point $\mathbf{x}^{**}$. Specifically, consider the feedback strategy

$$\delta \mapsto \delta^* + \mathbf{c} \cdot \left(\mathbf{x} - \mathbf{x}^{**}\right) + c_0 \left(\delta - \delta^*\right), \tag{8}$$

where $\mathbf{c}$ and c_0 is a collection of control parameters and δ^* is the nominal value of δ. The objective of control design is therefore the selection of numerical values for the control parameters that achieve the desired outcome.

As shown in [2, 3], the success of the proposed control strategy can again be evaluated in terms of a suitably defined ξ sequence. In particular, the theoretical analysis relies on the inclusion of δ as a state variable and the augmentation of the vector fields, impact map, Poincaré maps, and β vector. Selection of numerical values for the control parameters can then either be achieved by a rigorous methodology (cf. [3], albeit a very selective and, for other reasons, not practical choice) or by trial-and-error-based evaluation of some large finite set of entries of the ξ sequence (as in [2]).

5 Simulation Results

Restrict attention to the case when $w(t)=a\cos\omega t$, where a is the ground-displacement oscillation amplitude. In the numerical results quoted below, $m_1=423$ kg, $m_2=13$ kg, $k_1=20000$ N/m, $k_2=200000$ N/m, $d_1=1200$ Ns/m in compression and 4000 Ns/m in expansion, $d_2=50$ Ns/m, and $e=0.9$ corresponding to a medium-sized passenger car. Moreover, with the inclusion of feedback-based adjustments to δ, the actual implemented value of δ is the value in the interval $[\delta^* - 0.04\,\text{m}, \delta^* + 0.04\,\text{m}]$ closest to that computed using Eq. (8).

Figure 2 (for which $a^*=0.041$ m, $\delta^*=0.086$ m, $\omega^*=8\pi$ rad/s, $c_0=0.8$, and $\mathbf{c}=\begin{pmatrix}0.35 & 0 & 0.1 & 0 & 0\end{pmatrix}$) shows the transitions in the steady-state system response following the grazing contact with the bumpstop of a periodic steady-state oscillation of the quarter-car model that remains in a condition of sustained contact. Here, the numerical values of the control parameters were chosen by trial-and-error, ensuring that a large, but finite number of entries in the corresponding ξ sequence are positive.

As clearly can be seen in Fig. 2, the steady-state response in the absence of control exhibits a finite jump in the impact velocity from zero at grazing to near 5 cm/s as a is increased beyond a^*. In contrast, the proposed control strategy guarantees a robust, super-critical bifurcation to what appears to be an irregular response with bumpstop impact velocities that approach zero as $a \downarrow a^*$.

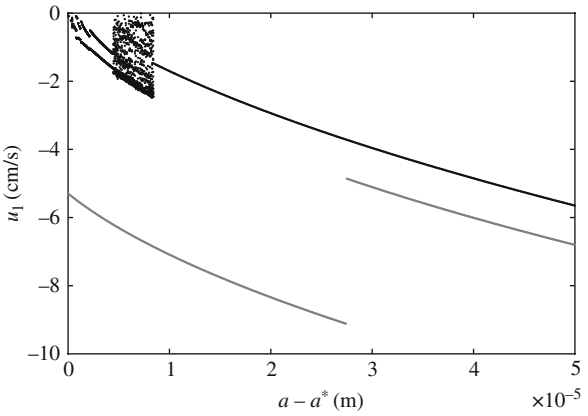

Fig. 2 Impact velocity as a function of increasing values of ground-displacement oscillation amplitude with (*dark gray*) and without (*light gray*) control

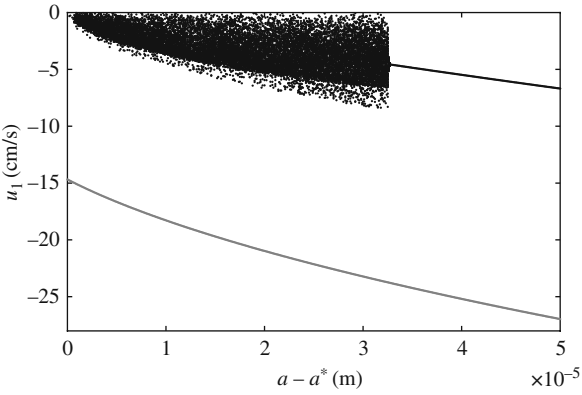

Fig. 3 Impact velocity as a function of increasing values of ground-displacement oscillation amplitude with (*dark gray*) and without (*light gray*) control

Similar results are shown in Fig. 3 (for which a^*=0.04 m, δ^*=0.118 m, ω^*=16π rad/s, c_0=0.9, and $\mathbf{c}=\begin{pmatrix}0.4 & 0 & -0.4 & 0 & 0\end{pmatrix}$) corresponding to the bifurcation scenario following grazing contact of a periodic steady-state oscillation that includes wheel-hop, i.e., a combination of conditions of contact, quasi-contact, and free flight.

Although the control strategy is derived solely with the intention of ensuring a super-critical bifurcation behavior, it is interesting to investigate its effectiveness in reducing impact velocities for larger, more realistic changes in ground-displacement oscillation amplitude. Figure 4, obtained using the same numerical values as Fig. 2, shows that some reduction in impact velocities remains even for values of $a - a^*$ on the order of centimeters.

Finally, we observe that the steady-state behavior to which the system response transitions in the case of a sub-critical bifurcation persists even as the ground-displacement oscillation amplitude is reduced below a^*. Figure 5 combines the data from Fig. 2 in which a is increased beyond a^* with that from a subsequent run in which a is decreased below a^*. As seen in the figure, no such *parameter hysteresis* is observed in the presence of control.

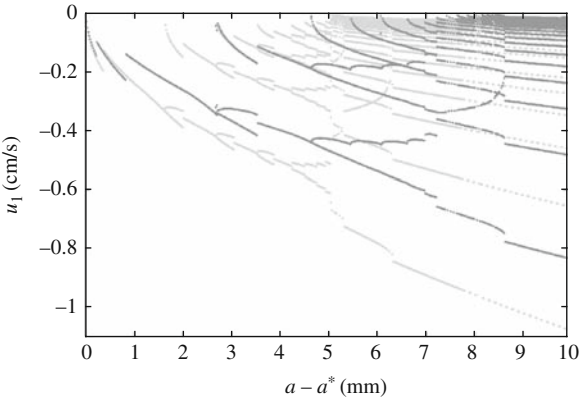

Fig. 4 Impact velocity as a function of increasing values of ground-displacement oscillation amplitude with (*dark gray*) and without (*light gray*) control

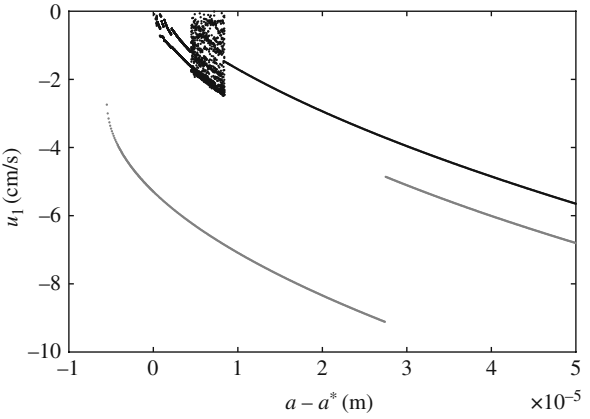

Fig. 5 Impact velocity as a function of increasing and decreasing values of ground-displacement oscillation amplitude with (*dark gray*) and without (*light gray*) control

6 Discussion

In this work a low-cost control strategy has been proposed in order to suppress instabilities associated with the onset of bumpstop impacts in a quarter-car model of a vehicle. The analysis has demonstrated that this can be achieved at least locally, for small increments of the excitation amplitude away from the grazing amplitude. It was also shown that the control law removes undesirable hysteresis effects present in the uncontrolled system. Additionally, a contribution of this work compared to the earlier publications on the control algorithm [2, 3], is that the proposed control strategy was shown to handle discontinuities in the system dynamics other than impacts, such as wheel-hop.

As the control method is based on linearizations, such that only local results are guaranteed, it would be desirable to extend it to a global control law. One alternative is a gain scheduling strategy [9] implying that different reference points are used and control parameters are varied based upon the present excitation of the system. Alternatively, the control map, Eq. (8), could be extended with nonlinear terms to achieve a global reduction of impact velocities.

Acknowledgments This material is based upon work supported by the National Science Foundation under Grant Nos. 0237370/0635469 and by the Swedish Science Council, Division of Engineering Mechanics, Grant Nos. 2003-3699 and 2004-6342.

References

1. Chin W, Ott E, Nusse HE et al. (1994) Grazing bifurcations in impact oscillators. Phys Rev E 50(6):4427–4444
2. Dankowicz H, Jerrelind J (2005) Control of near-grazing dynamics in impact oscillators. Proc R Soc A 461(2063):3365–3380
3. Dankowicz H, Svahn F (2007) On the stabilizability of near-grazing dynamics in impact oscillators. Int J Robust Nonlinear Control 17(15):1405–1429

4. Dankowicz H, Zhao X (2005) Local analysis of co-dimension-one and co-dimension-two grazing bifurcations in impact microactuators. Physica D: Nonlinear Phenom 202(3–4): 238–257
5. Esmailzadeh E, Bateni H (1992) Optimal active vehicle suspensions with full state feedback control. SAE Tech Pap Ser 41–52
6. Fredriksson MH, Nordmark AB (1997) Bifurcations caused by grazing incidence in many degrees of freedom impact oscillators. Proc R Soc A 453(1961):1261–1276
7. Gillespie TD (1992) Fundamentals of Vehicle Dynamics. SAE, Warrendale
8. Holen P (2006) On modally distributed damping in heavy vehicles. Doctoral Thesis,TRITA-AVE 2006:78, KTH Engineering Sciences, Stockholm
9. Khalil HK (2000) Nonlinear systems, 3rd edn. Prentice Hall, New Jersey
10. Nordmark AB (1991) Non-periodic motion caused by grazing incidence in an impact oscillator. J Sound and Vib 145(2):279–297
11. Piiroinen PT, Virgin LN, Champneys AR (2004) Chaos and period-adding: Experimental and numerical verification of the grazing bifurcation. J Nonlinear Sci 14(4):383–404
12. Stensson A, Asplund C, Karlsson L (1994) Nonlinear behaviour of a MacPherson strut wheel suspension. Veh Syst Dyn 23:85–106
13. Tan H-S, Bradshaw T (1997) Model identification of an automotive hydraulic active suspension system. Proc Am Control Conf 2920–2924
14. Verros G, Natsiavas S (2001) Dynamics of vehicles with semi-active suspensions exhibiting wheel hop. Veh Syst Dyn Suppl 35:135–148

Experimental Modal Analysis of Towed Elastic Tyres During Rolling

Dénes Takács and Gábor Stépán

Abstract The lateral vibration of towed wheels, the so-called shimmy, is one of the most intricate phenomena of vehicle system dynamics. In this paper, a simple mechanical model of shimmy is constructed from a towed elastic wheel with a perfectly rigid suspension system. The brief presentation of the mathematical model of the system is followed by the detailed experimental analysis. The physical parameters of a carefully designed experimental rig are determined in different experimental setups. The most relevant stability boundary of the straight-line stationary rolling is calculated theoretically and then validated by experiments. The vibration frequencies of the system in different parameter domains, with special attention to the stable regions, are investigated by the modal analysis of the towed tyre during rolling.

1 Introduction

The lateral vibration of towed wheels (so-called shimmy) is one of the most interesting phenomena in vehicle dynamics. In spite of the fact that shimmy has been studied for almost a century [2], the prediction and the elimination of shimmy are critical parts of landing gear and motorcycle design [1, 4, 8, 3].

This paper investigates a simple elastic tyre model with one rigid-body degree-of-freedom. The theoretical analysis of the so-called delayed tyre model in question was accomplished in previous studies [7], where the linear stability chart and the vibration frequencies at the stability boundaries were calculated.

To validate the theoretical results, an experimental rig was built corresponding to the simple mechanical model in question. The most relevant stability boundary of the theoretical stability chart was also checked experimentally. Quasi-periodic vibrations were also observed close to the theoretically predicted double Hopf point in [6].

D. Takács (✉)
Department of Applied Mechanics, Budapest University of Technology and Economics, Budapest, Hungary; Hungarian Academy of Sciences, Research Group on Dynamics of Vehicles and Machines, Budapest, Hungary
e-mail: takacs@mm.bme.hu

P.G. Thomsen, H. True (eds.), *Non-smooth Problems in Vehicle Systems Dynamics*,
DOI 10.1007/978-3-642-01356-0_13,

In this study, we briefly present a mechanical model extended by torsional spring and damper at the king pin. The stability chart is plotted for different system parameters. The identification methods of the physical parameters in different experimental setups are presented numerically. One of the stability boundaries is validated by experimental analysis in an appropriate band of the system parameters. The variations of vibration frequencies with respect to the towing speed are calculated by a convenient numerical method from the analytically determined characteristic equation of the system. These results are also confirmed by the experimental modal analysis of the towed wheel during rolling.

2 Mechanical Model

The model in question is investigated in [7] in details without torsional spring and damper at the king pin. The central element of the mechanical model in Fig. 1 is an elastic tyre that is in contact with the ground along a contact line of length $2a$. The wheel of elastic tyre is towed by a rigid caster of length l with constant velocity v. The system is described by the general coordinates, which are the caster angle $\psi(t)$ and the lateral deformation $q(x,t)$ of the tyre relative to the centre plane of the wheel. The deformation of the tyre outside the contact patch is defined by the exponentially decaying functions originated in the stretched string-like tyre model, see [5]:

$$q(x,t) = \begin{cases} q(-a,t)\mathrm{e}^{(x+a)/\sigma}, & \text{if} \quad x \in (-\infty, -a], \\ q(x,t), & \text{if} \quad x \in (-a, a), \\ q(a,t)\mathrm{e}^{-(x-a)/\sigma}, & \text{if} \quad x \in [a, \infty). \end{cases} \tag{1}$$

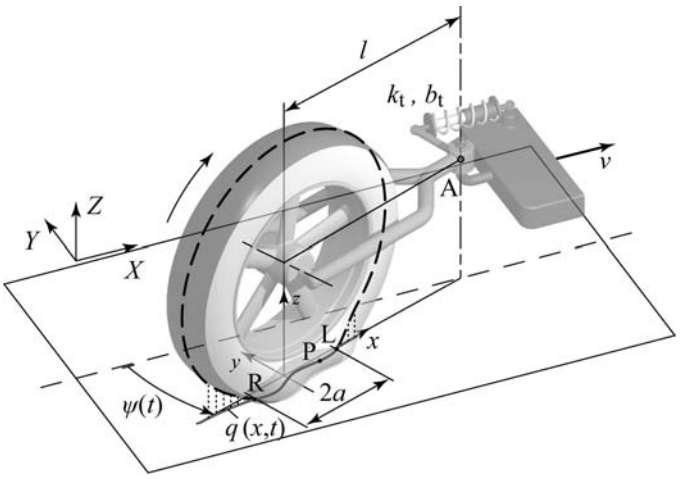

Fig. 1 The mechanical model of the towed tyre

Because the tyre contact points translate backwards relative to the caster, the element of the tyre located at a longitudinal position x will change in time. Consequently, $q(x,t)$ describes the lateral displacement of the tyre particle located at x instantaneously. The total derivative of $q(x,t)$ with respect to the time is

$$\frac{\mathrm{d}}{\mathrm{d}t}q(x,t) = \dot{q}(x,t) + q'(x,t)\dot{x}, \tag{2}$$

where dots and prime refer to partial differentiations with respect to time t and space variable x, respectively.

The equation of motion is given by the integro-differential equation (IDE):

$$\begin{aligned} J_{\mathrm{A}}\ddot{\psi}(t) = &- k\int_{-\infty}^{\infty}(l-x)q(x,t)\mathrm{d}x - b\int_{-\infty}^{\infty}(l-x)\frac{\mathrm{d}}{\mathrm{d}t}q(x,t)\mathrm{d}x \\ &- k_{\mathrm{t}}\psi(t) - b_{\mathrm{t}}\dot{\psi}(t), \end{aligned} \tag{3}$$

where J_{A} is the mass moment of inertia of the overall system with respect to the z axis at the king pin, k and b are the specific stiffness and damping factor of the tyre, respectively, while the parameters k_{t} and b_{t} are the stiffness and the damping factor of the torsional spring and the torsional damper at the king pin.

In case of rolling, the tyre contact points do not move, thus, the kinematical constraint is given by the partial differential equation (PDE):

$$\dot{q}(x,t) = v\sin\psi(t) + (l-x)\dot{\psi}(t) - q'(x,t)\dot{x}, \tag{4}$$

where $x \in [-a,a]$ and $t \in [t_0,\infty)$. The boundary condition $q'(a,t) = -q(a,t)\big/\sigma$ characterizes the lateral deformation at the leading edge L with the so-called relaxation length σ. The longitudinal translational rates of the tyre elements in the contact patch is

$$\dot{x} = -v\cos\psi(t) + q(x,t)\dot{\psi}(t). \tag{5}$$

3 Travelling Wave-Like Solution

In this study, we consider rolling, which means that the position of a tyre element is constant while the element is in contact with the ground. Thus, a time delay can be introduced to describe the time needed for a tyre element to travel backward from the leading point L to the actual position P characterized by x. This time delay can be obtained from

$$\begin{bmatrix} X(x,t) \\ Y(x,t) \end{bmatrix} = \begin{bmatrix} X(a,t-\tau(x)) \\ Y(a,t-\tau(x)) \end{bmatrix}. \tag{6}$$

If the system is linearized, this leads to

$$\tau(x) = (a - x)/v. \tag{7}$$

With the help of this time delay, the travelling wave-like solution of the linearized form of the kinematical constraint (4) is given by

$$q(x,t) = (l - x)\psi(t) - (l - a)\psi(t - \tau(x)) + q(a, t - \tau(x)). \tag{8}$$

4 Stability Analysis

Since the travelling wave-like solution of the linearized system is known, the coupled IDE-PDE system can be transformed into a delay differential equation (DDE). This long calculation can be found in [7]. In this paper, the characteristic equation of the linearized system is presented only:

$$\begin{aligned} D(\lambda) = {} & V^2\Sigma\lambda^3 + (2V^2 + 2\zeta V\Sigma)\lambda^2 + (\Sigma + 4\zeta V)\lambda - \frac{L - 1 - \Sigma}{L^2 + 1/3 + \Sigma(L^2 + 1 + \Sigma) + K} \times \\ & \times \left\{ \Sigma(\mathrm{e}^{-\lambda} - 1 + L(\mathrm{e}^{-\lambda} + 1) + \Sigma(\mathrm{e}^{-\lambda} - 1)) + \frac{2}{\lambda}\left(\left(L - 1 + \frac{2}{\lambda}\right) - \left(L + 1 + \frac{2}{\lambda}\right)\mathrm{e}^{-\lambda}\right)\right\} \\ & + 2 - \frac{4\zeta V L(\Sigma + 1)(\Sigma\lambda + 2)}{L^2 + 1/3 + \Sigma(L^2 + 1 + \Sigma) + B} - \frac{2\zeta V(L - 1 - \Sigma)}{L^2 + 1/3 + \Sigma(L^2 + 1 + \Sigma) + B} \times \\ & \times \left\{ \Sigma\lambda(\mathrm{e}^{-\lambda} - 1 + L(\mathrm{e}^{-\lambda} + 1) + \Sigma(\mathrm{e}^{-\lambda} - 1)) - 2(\mathrm{e}^{-\lambda} + 1 + L(\mathrm{e}^{-\lambda} - 1) + \Sigma(\mathrm{e}^{-\lambda} + 1))\right\}, \end{aligned} \tag{9}$$

where the dimensionless parameters are the dimensionless towing length, the dimensionless towing speed, the dimensionless tyre relaxation, the dimensionless torsional stiffness and torsional damping, defined as

$$L := \frac{l}{a}, \quad V := \frac{v}{2a\omega_\mathrm{n}}, \quad \Sigma := \frac{\sigma}{a}, \quad K := \frac{k_\mathrm{t}}{2a^3k}, \quad B : \frac{b_\mathrm{t}}{2a^3b}, \tag{10}$$

respectively. The natural angular frequency and the damping ratio of the steady system are

$$\omega_\mathrm{n} = \sqrt{\frac{2k}{J_\mathrm{A}}\left(a\left(l^2 + \frac{a^2}{3}\right) + \sigma(l^2 + a^2 + a\sigma)\right) + \frac{k_\mathrm{t}}{J_\mathrm{A}}} \tag{11}$$

and

$$\zeta = \frac{1}{2\omega_\mathrm{n}}\left(\frac{2b}{J_\mathrm{A}}\left(a\left(l^2 + \frac{a^2}{3}\right) + \sigma(l^2 + a^2 + a\sigma)\right) + \frac{b_\mathrm{t}}{J_\mathrm{A}}\right), \tag{12}$$

respectively.

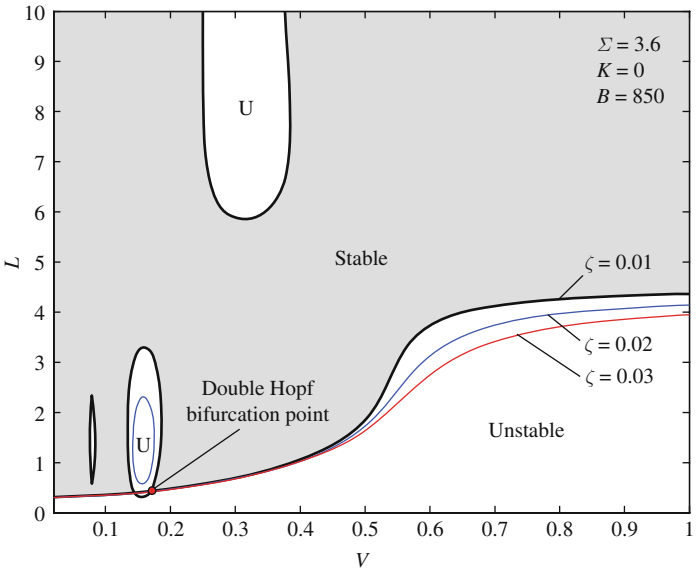

Fig. 2 Linear stability chart of the towed wheel for different values of the damping ratio

The stability boundaries of the system can be calculated with the help of the D-subdivision method. This means that after the substitution of the pure imaginary $\lambda = \mathrm{i}\omega$ into the characteristic equation, $\mathrm{D}(\mathrm{i}\omega)$ is separated to real and imaginary parts. On the stability boundary, both the real and the imaginary parts of the characteristic equation have to be zero. With the help of these criteria and using an appropriate numerical method, the typical stability boundaries can be determined for a specific range of the self-excited vibration frequency ω. A stability chart of the system is shown in Fig. 2 demonstrated in the (V, L) plane for different values of the damping ratio ζ. The dimensionless tyre relaxation, torsional stiffness and torsional damping are chosen according to the presented measurement results in Sect. 5.1.

5 Experiments

To validate the theoretical results, an experimental rig was designed and built (see Fig. 3). Despite the simple mechanical model that consists of a tyre and a caster, the system has large number of parameters, namely, the caster length l, the towing speed v, the specific stiffness k and damping b of the tyre, the tyre relaxation length σ, the torsional spring stiffness k_t and damping factor b_t, the half of the contact length a and the mass moment of inertia of the system J_A. First, the identification of these parameters was carried out.

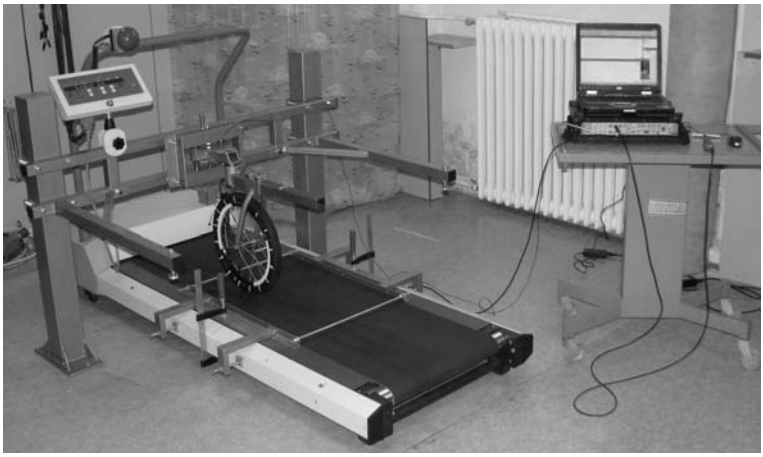

Fig. 3 The experimental rig with the vibration measuring system PULSE

5.1 Parameter Identification

The mass moments of inertia of the caster and the wheel were measured with the help of a simple pendulum experiment. The caster with the wheel was hanged in the vertical plane with different caster lengths, and the period of the swinging was measured. From the period, the mass moments of inertia were calculated. In the equations, the mass moment of inertia J_A of the overall system with respect to the z axis at the king pin depends also on the caster length – this gives a limitation for the use of the dimensionless form of the stability chart. The results of the measuring process give the formula:

$$J_A = 0.1561 + 2.539 \times (0.036 + l)^2 [\mathrm{kgm}^2] \tag{13}$$

In former studies, some parameters were measured in different experimental setups. For example, the specific stiffness k [N/m^2] and damping b [Ns/m^2] of the tyre were identified in a rigid frame [7]. The tyre was placed between two planes, and it was pulled in lateral direction with constant forces. From the lateral displacements of the tyre, the stiffness was calculated. Then the tyre was hit in lateral direction, and the lateral acceleration was measured. With the help of the logarithmic decrement, the damping was obtained. In [7], where the mechanical model was extended with the tyre relaxation, the relaxation parameter was also measured in the same rigid frame. The tyre was fixed between the two transparent plastic plates, and it was pulled in lateral direction again. Since the deformation of the tyre was visible outside the contact patch through the transparent plate, the relaxation length σ of the tyre was determined.

The stiffness, damping and tyre relaxation parameters were measured by the above methods, and these values were used in (11) and (12) with neglected torsional

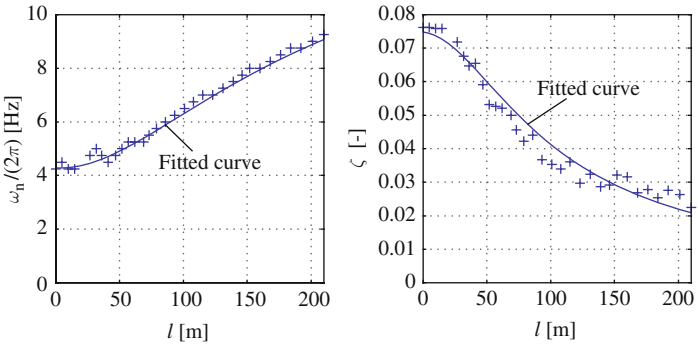

Fig. 4 The measured natural frequencies and damping ratios with the fitted curves

stiffness and damping to estimate the natural angular frequency and the damping ratio of the experimental rig. However, this gave large differences between the theoretically calculated and the measured data. On one hand, we recognized that the mechanical model has to be extended with torsional damping, since the torsional damping of the bearing at the king pin seemed to be not negligible.

On the other hand, to get more correct system parameters, the tyre with the whole suspension system were fitted on the conveyor belt. The length of the contact patch was tuned to a constant value $2a = 0.079\,[\mathrm{m}]$, and the natural angular frequency and the damping ratio of the system was measured at different caster lengths. To do this, a piezo-electric accelerometer was put on the end of the caster and its signal was connected to the measuring system PULSE. Since the mass moments of inertia, the contact length and the caster length were known, the parameters σ, k, b and b_t could be determined by fitting the theoretical curves to the measured data (see Fig. 4). In these experiments there was no torsional spring added at the king pin, that is, $k_t = 0\,[\mathrm{Nm/rad}]$. The identified values of parameters are $\sigma = 0.142\,[\mathrm{m}]$, $k = 57.7\left[\mathrm{kN/m^2}\right]$, $b = 6\left[\mathrm{Ns/m^2}\right]$ and $b_t = 0.63\,[\mathrm{Nms/rad}]$.

5.2 Validation of the Linear Stability Boundary

To simplify the validation of the theoretically calculated stability boundary, the dimensionless stability chart was transformed into dimensional form. Namely, all of the relationships of the system parameters are taken into account to realize the stability chart in the (v, l) plane. Therewith, the comparison and representation of the theoretical and experimental results are simple.

The linear stability of the towed wheel was investigated at different caster lengths. During rolling with different constant speeds, the caster was slightly perturbed, and the response of the system was observed. The dimensional form of the stability chart is shown in Fig. 5. The experimental and theoretical stability boundaries are qualitatively similar. The quantitative difference can be noticed in

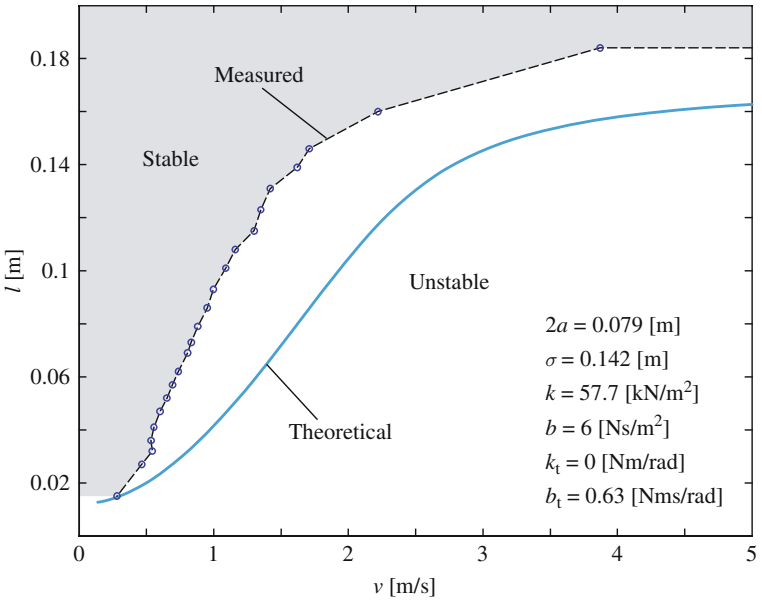

Fig. 5 The experimentally detected stability boundary compared to the theoretical one

the stability behaviour. In practice, the towed wheel become unstable at lower towing speed than it is predicted by the theory. The behaviour of the system indicates subcritical Hopf bifurcation at the stability boundary, which can be suspected as the reason of the identified differences.

5.3 Modal Analysis

One of the most important properties of the phenomenon shimmy is the quasi-periodic vibration. The stability analysis of the investigated single rigid-body degree-of-freedom mechanical model predicts two different frequencies at the intersection of two stability boundaries. In a former study [6], the vibration frequencies are investigated numerically and experimentally, but in the unstable domain only, where the vibration amplitudes are large, and the nonlinearity of the system can not be neglected.

To prove the theoretically calculated linear vibration frequencies experimentally, modal analysis of the towed wheel was carried out. The caster was hit during rolling with different constant speeds, and the response of the system was recorded. The vibration frequencies of the measured signals have to correlate to the imaginary parts of the numerically determined eigenvalues. The real parts of the eigenvalues show which frequencies are relevant at the actual towing speed. In Figs. 6, 7, and 8, the real and the imaginary parts of the theoretical eigenvalues and the measured vibration frequencies are shown versus the towing speed at the different

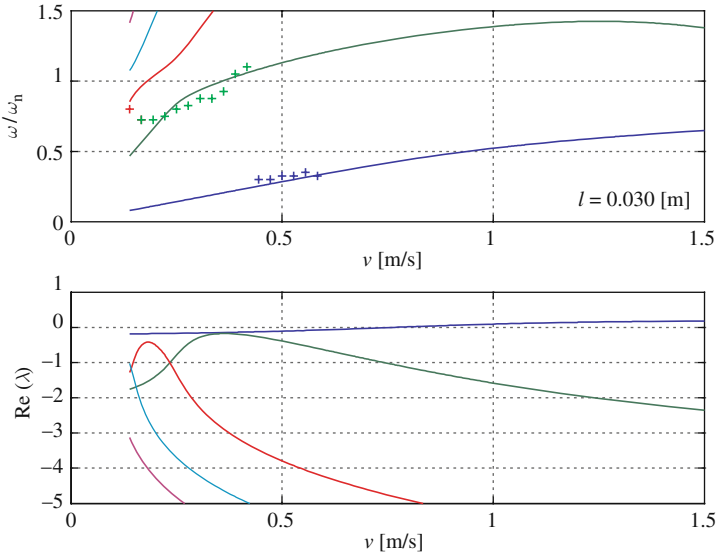

Fig. 6 Measured vibration frequencies and the numerically determined eigenvalues versus towing speed at $l = 0.030$ [m]

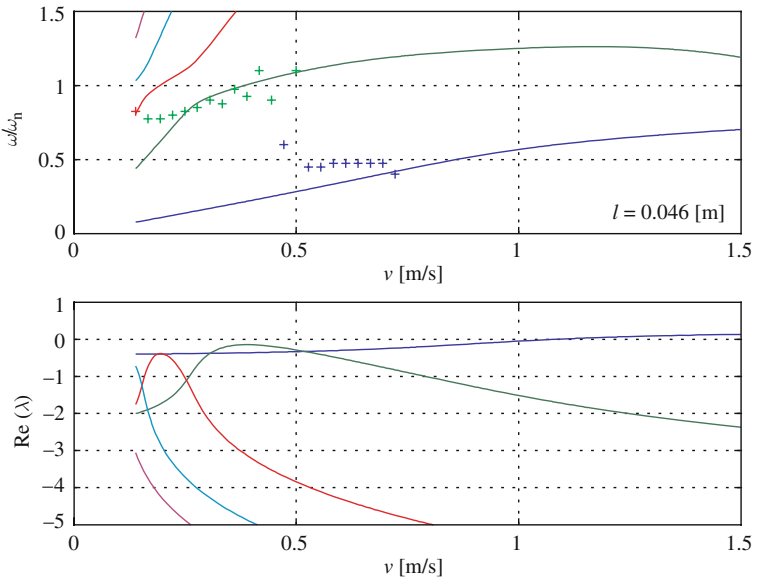

Fig. 7 Measured vibration frequencies and the numerically determined eigenvalues versus towing speed at $l = 0.046$ [m]

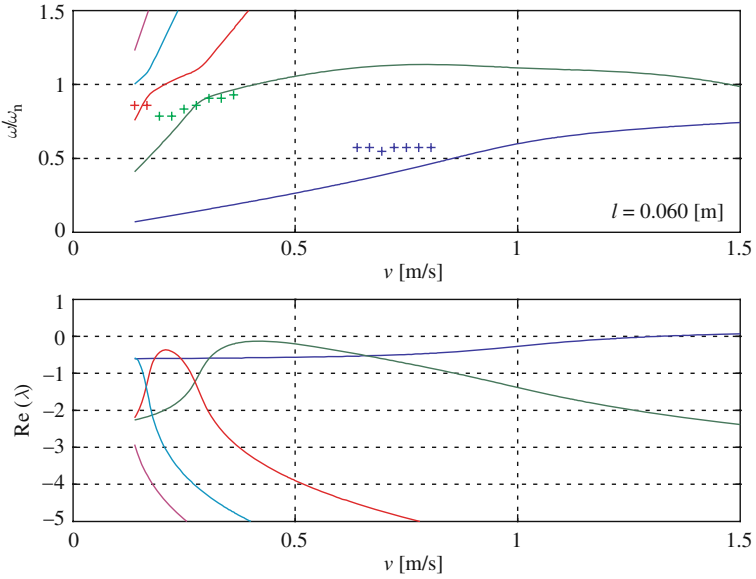

Fig. 8 Measured vibration frequencies and the numerically determined eigenvalues versus towing speed at $l = 0.060$ [m]

caster lengths. It can be observed, that the measured vibration frequencies have good agreement with the theoretically predicted frequencies.

If the real parts of two eigenvalues are close together, both vibration frequencies are relevant and both of them should appear in the oscillation signal. This can be shown in Fig. 6 at the towing speed 0.4 [m/s], and in Fig. 7 at 0.5 [m/s].

6 Conclusions

In this paper, a simple one rigid-body degree-of-freedom mechanical model is used for investigating shimmy. The mathematical model and its stability analysis are confirmed by detailed experiments.

The theoretical vibration frequencies of the linear model are also confirmed by the experimental modal analysis of the towed wheel. All the theoretically predicted frequencies can be found in the vibration signal in the stable domain of the stability chart.

The results confirm the relevance of the memory effect in tyre models during the investigation of rolling instabilities. Also, this approach offers new sets of parameters for tyre modelling.

Acknowledgments This research was supported by the Hungarian National Science Foundation under grant no. OTKA K68910.

References

1. Besselink I J M (2000) Shimmy of aircraft main landing gears. PhD Thesis. Delft University of Technology
2. Broulhiet G (1925) The suspension of the automobile steering mechanism: Shimmy and tramp. Bull Soc. Ing. Civ. Fr. 78:540–554
3. Catani G, Mancinelli N (2007) Motorcycle local stability analysis under acceleration and braking by model linearization and eigenproblem solution. IDECT/CIE-2007, Proceedings, Las Vegas
4. Coetzee E (2006) Shimmy in aircraft landing gear. Tech. rep. Problem presented by Airbus. http://www.smithinst.ac.uk/Projects/ESGI56/ESGI56-AirbusShimmy/Report. Accessed 5 September 2008.
5. Pacejka H B (2002) Tyre and vehicle dynamics. Elsevier-Butterworth-Heinemann, Oxford
6. Takács D, Stépán G (2007) Experiments on quasi-periodic wheel shimmy. IDETC/CIE-2007, Proceedings, Las Vegas
7. Takács D, Orosz G, Stépán G (2009) Delay effects in shimmy dynamics of wheels with stretched-string like tyres. Eur. J. Mech. Solid/A, 28:516–525.
8. Thota P, Krauskopf B, Lowenberg M (2008) Shimmy in a nonlinear model of an aircraft nose landing gear with non-zero rake angle. ENOC-2008, Proceedings, Saint Petersburg

Modelling and Simulation of Longitudinal Tyre Behaviour

Jaap P. Meijaard

Abstract A mechanical model of moderate complexity is presented for evaluating the normal and longitudinal contact force between a tyre of a vehicle and the road. The model consists of a stretched beam on an elastic foundation with elastic tread elements that can touch the road, through which the forces are transmitted. Three friction models are considered, with increasing complexity: the Coulomb model with different static and kinetic friction coefficient, a speed-dependent friction model, and a dynamic model with an internal state. Realistic steady-state tyre characteristics are found. For the more complex friction models, an alternation of regions with low sliding velocity and transition regions with high sliding velocity may be present.

1 Introduction

Accurate modelling of the forces generated between a pneumatic tyre and the road surface is important for predicting handling behaviour of road vehicles. For the design of control systems for the prevention of wheel lock during braking, spin during acceleration and excessive yaw rates, even more accurate models are needed, which have to be valid near the limits of the capabilities of the tyres and at higher frequencies.

Current tyre force models can be classified in three main groups. A first group consists of analytic models based on simplifying physical assumptions. Examples are brush models and string models. A second group consists of empirical models, which fit empirical data with tabular values and parameterized interpolation formulas. The choice of the form of these formulas is usually guided by results from models from the first group. The main examples are the magic formulas proposed by Pacejka and others [6]. A third group consists of detailed physical models. An example is the FTyre model [3]. A review of earlier physical tyre force models is given by Smiley [9]. More recent models can be found in [2] and the proceedings

J.P. Meijaard (✉)
Laboratory of Mechanical Automation and Mechatronics, Faculty of Engineering Technology, University of Twente, Enschede, The Netherlands
e-mail: J.P.Meijaard@utwente.nl

P.G. Thomsen, H. True (eds.), *Non-smooth Problems in Vehicle Systems Dynamics*,
DOI 10.1007/978-3-642-01356-0_14,

of the three tyre colloquia [5, 1, 4]. Pacejka [6] gives an overview of analytical physical and phenomenological models. Here, a physical model based on simplifying assumptions is proposed. It will appear that the force cannot be calculated in a closed form, but the numerical calculations remain limited. To limit the complexity of the model, only longitudinal behaviour is considered in this paper. Extensions to include lateral behaviour are feasible, however.

Several factors may influence the force generation of pneumatic tyres on a road surface. The natural interpretation is that these factors, such as the temperature, wetness, speed, tyre load and pressure, influence the coefficient of friction. Some other possible explanations for the influence of these factors on the force characteristics are considered here. Firstly, some fundamentals of rubber friction are discussed, with emphasis on the unimodal dependence of friction on the sliding velocity and the time–temperature equivalence. Secondly, a one-dimensional tyre model for longitudinal forces is proposed, in which the tyre belt is modelled as an elastic beam that is supported by an elastic foundation and is in contact with the road through elastic tread elements. This model is able to predict the normal force distribution for given tyre parameters. For an assumed friction characteristic, forward velocity and slip, the stationary longitudinal force can be calculated. This makes it possible to assess the influence of varying the tyre parameters on the longitudinal tyre force.

2 Tyre Force Model

2.1 Mechanical Model

The tyre model is schematically shown in Fig. 1. The belt is modelled as a pre-stressed beam on an elastic foundation. The centre line of the beam is inextensible, but the flexural rigidity is finite, but quite small. The foundation is a combination of a Winkler foundation with a force proportional to the lateral displacement and a Pasternak foundation with a force proportional to the second derivative of the lateral displacement, which is caused by a shearing of the tyre flanks. The pre-stress of the beam gives a contribution to the equations with the same form as the Pasternak foundation, so these two contributions can be taken together. Elastic tread elements are attached to the belt that can make contact with the road. The tread elements have

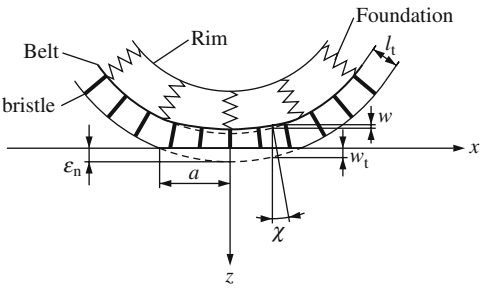

Fig. 1 Mechanical tyre model: beam on an elastic foundation with tread elements

decoupled normal and shear rigidities. Friction between the tread elements and the road is present. It is assumed that there is a continuous distribution of infinitesimal tread elements. The model is one-dimensional, as all properties over a transversal section are taken together in variables at the central, equatorial, plane of the wheel.

A position along the belt is indicated by a material coordinate x with a moving origin straight below the centre of the wheel. The length of the contact patch is $2a$, so contact occurs for $-a \leq x \leq a$. The belt has a nominal radius R_b and the tread elements have length l_t. The belt has no longitudinal displacement with respect to the wheel hub and a normal displacement w; the longitudinal and normal displacements for the tips of the tread elements are u_t and w_t. The masses of the belt and the tread elements are neglected. The flexural rigidity of the belt is EI and the stiffness parameters of the foundation are k_W and k_P for the Winkler and Pasternak parts, respectively. The tread elements have a normal stiffness $k_{\mathrm{t}z}$ and shear stiffness $k_{\mathrm{t}x}$ per unit of length. No damping besides the friction between tread elements and the road is included in the model. To keep the model manageable, the equations are linearized and the curvature of the belt is neglected, except in the contact patch for determining the contact forces.

2.2 Friction Models

The friction force for sliding between elastomers and a hard surface depends on the speed of sliding. This dependence can be approximated by a friction coefficient that is a Gaussian function of the logarithm of the sliding velocity [7],

$$\mu(v) = \mu_\mathrm{k} + (\mu_\mathrm{m} - \mu_\mathrm{k}) \exp\left[-\frac{h^2}{2} \ln^2 \frac{v}{v_\mathrm{m}}\right]. \tag{1}$$

Here, v is the sliding speed, μ_m is the maximal coefficient of friction at $v = v_\mathrm{m}$ and μ_k is the kinetic coefficient of friction at very low as well as very high sliding speeds. The dimensionless parameter h typically has a value of 0.35, whereas usual values for the friction coefficients are $\mu_\mathrm{k} = 0.6$–0.8, $\mu_\mathrm{m} = 2$–3. Figure 2 shows an example with $\mu_\mathrm{k} = 0.8$, $\mu_\mathrm{m} = 2$. Changes in temperature mainly result in a shift of v_m, leaving the other parameters invariant. Therefore, increasing the sliding velocity

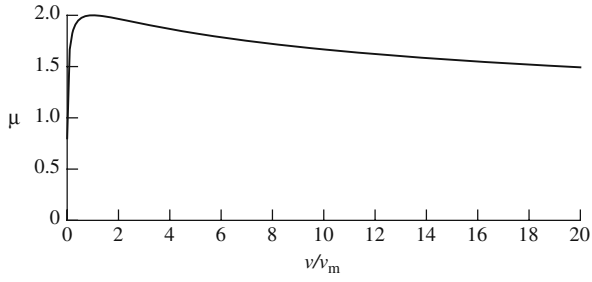

Fig. 2 Typical friction characteristic for elastomers

and decreasing the temperature have a similar effect. In particular, for low temperatures or high sliding speeds, the friction law approaches the classical Coulomb friction model with a static friction coefficient and a kinetic friction coefficient. The relation (1) represents the friction curve for stationary sliding. For cases in which the sliding speeds change rapidly, the model can be extended to a rate- and state-dependent model [8], in which the state variable is the friction coefficient that evolves according to the rate equation

$$\dot{\mu} = \left[\frac{1}{\tau_s} + \frac{|v|}{d_k}\right][\mu_{ss}(|v|) - \mu], \tag{2}$$

where τ_s is a characteristic time for sticking and d_k a relaxation length for sliding.

2.3 Normal Force Distribution

The normal force model has the radial deflection, ε_n, as an input and the contact length a, the effective rolling radius, R_{eff}, and the normal pressure distribution as outputs. From Fig. 1 it is seen that the prescribed normal displacement of the tread elements in the contact patch is approximately

$$w_t = \varepsilon_n - \frac{x^2}{2R_b}. \; (-a \le x \le a) \tag{3}$$

The differential equations for the belt deflection are

$$\begin{aligned} EIw'''' - k_P w'' + k_W w &= 0 \; (x > a \text{ or } x < -a) \\ EIw'''' - k_P w'' + (k_W + k_{tz})w &= k_{tz} w_t \; (-a \le x \le a) \end{aligned} \tag{4}$$

The solution is symmetric in x, so only $x \ge 0$ need be considered. If the belt radius is much larger than any characteristic length scale associated with the solution, the boundary conditions at $x = \pi R_b$ can be replaced by the condition that the solutions at infinity should be bounded. This leads to the solution outside the contact patch

$$w = C_1 \; \exp[-\lambda_1(x-a)] + C_2 \; \exp[-\lambda_2(x-a)], \; (x \ge a), \tag{5}$$

where C_1, C_2, are constants and

$$\lambda_{1,2} = \sqrt{\frac{k_P \pm \sqrt{k_P^2 - 4EIk_W}}{2EI}}. \tag{6}$$

The exponents are real for realistic values of the parameters, so these solutions steadily decay for increasing values of x. The condition of bounded solutions for increasing values of x can be transformed to boundary conditions at $x = a$ as

$$w'' + (\lambda_1 + \lambda_2)w' + \lambda_1\lambda_2 w = 0, \quad w''' + (\lambda_1 + \lambda_2)w'' + \lambda_1\lambda_2 w' = 0. \tag{7}$$

These conditions can be found from the general solutions outside the contact region and the continuity conditions for the displacement and its first three derivatives by equating the coefficients of the exponentially increasing terms to zero. The symmetric solution within the contact region is

$$\begin{aligned} w = {} & C_{z1}\cosh(\sigma x)\cos(\omega x) + C_{z2}\sinh(\sigma x)\sin(\omega x) \\ & +(1 - q_z)\left[\varepsilon_{\mathrm{n}} - \frac{x^2}{2R_{\mathrm{b}}} - \frac{k_{\mathrm{P}}}{(k_{\mathrm{W}} + k_{\mathrm{tz}})R_{\mathrm{b}}}\right], \end{aligned} \tag{8}$$

where $C_{z1,2}$ are constants, $q_z = k_{\mathrm{W}}/(k_{\mathrm{W}} + k_{\mathrm{tz}})$, and σ and ω are the positive real numbers defined by

$$\sigma + i\omega = \sqrt{\frac{k_{\mathrm{P}} + i\sqrt{4EI(k_{\mathrm{W}} + k_{\mathrm{tz}}) - k_{\mathrm{P}}^2}}{2EI}}. \tag{9}$$

The constants can be determined as a function of a with the two boundary conditions (7). The condition that the contact force vanishes at the edges of the contact patch gives a non-linear equation for a, which can be solved by some numerical scheme. Once w has been determined, the normal force distribution in the contact patch is given by $p_z = k_{\mathrm{tz}}(w_{\mathrm{t}} - w)$ and the normal force follows from integrating this force distribution over the contact length. For an example tyre with the parameters as given in Table 1, the normal force distribution is shown in Fig. 3 for several values of the normal deflection. It is seen that the distribution is almost parabolic for small deflections, whereas it flattens near the centre for larger deflections.

Table 1 Parameter values for an example tyre

Symbol	Value	Unit	Description
EI	2	Nm^2	Beam flexural rigidity
h	0.35	–	Friction curve parameter
k_{P}	$8 \cdot 10^3$	N	Pre-stress and foundation shear rigidity
k_{tx}	$10 \cdot 10^6$	Nm^{-2}	Longitudinal tread element stiffness
k_{tz}	$40 \cdot 10^6$	Nm^{-2}	Normal tread element stiffness
k_{W}	$200 \cdot 10^3$	Nm^{-2}	Normal foundation stiffness
R_{b}	0.28	m	Belt radius
μ_{k}	0.8	–	Kinetic friction coefficient
μ_{m}	2.0	–	Maximal friction coefficient
q_z	$4.975 \cdot 10^{-3}$	–	Stiffness ratio
λ_1	63.0	m^{-1}	
λ_2	5.02	m^{-1}	
σ	56.9	m^{-1}	
ω	35.2	m^{-1}	

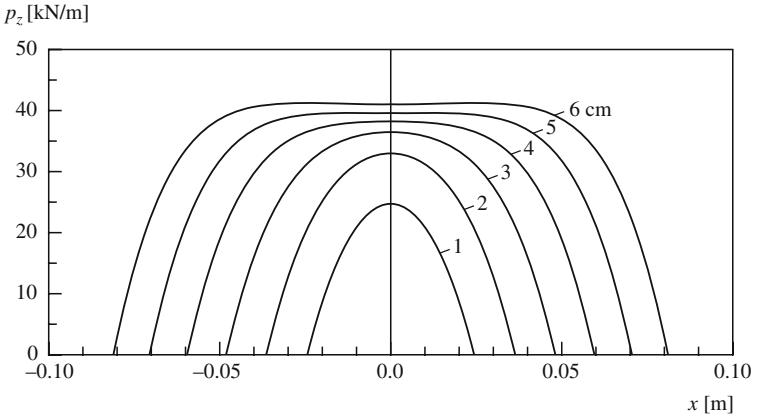

Fig. 3 Normal force distribution for a tyre with deflections of 1, 2, 3, 4, 5 and 6 cm

3 Longitudinal Force Distribution

The effective rolling radius can be obtained from the normal force distribution as

$$R_{\text{eff}} = R_{\text{b}} + l_{\text{t}} + R_{\text{b}} l_{\text{t}} w'(a)/a. \tag{10}$$

Accordingly, the longitudinal slip is defined as

$$s_x = \frac{V_x - \Omega R_{\text{eff}}}{\Omega R_{\text{b}}}, \tag{11}$$

where V_x is the forward velocity of the wheel centre and Ω its spin rate. So the longitudinal slip, and also the longitudinal force, are zero if the forward velocity satisfies $V_x = \Omega R_{\text{eff}}$. For a non-zero slip, it is generally assumed that the contact region is divided into an adhesion region near the leading edge and a sliding region near the trailing edge. The stationary longitudinal force distribution in the adhesion region is

$$p_x = k_{\text{t}x} s_x (a - x) + k_{\text{t}x} l_{\text{t}} [w'(x) - x w'(a)/a]. \tag{12}$$

For the Coulomb friction model with a static friction coefficient larger than the kinetic friction coefficient, $p_x = \mu_{\text{k}} p_z$ holds in the sliding region, with the transition at the point where $p_x = \mu_{\text{m}} p_z$. Figure 4 shows the longitudinal force–slip characteristics for several values of the normal deflection. The longitudinal force distribution, together with the normal force distribution, for a deflection of 4 cm and several values of the longitudinal slip is shown in Fig. 5. For the highest value of the slip, the adhesion region has just vanished. The characteristics show a realistic behaviour with a maximum in the longitudinal force.

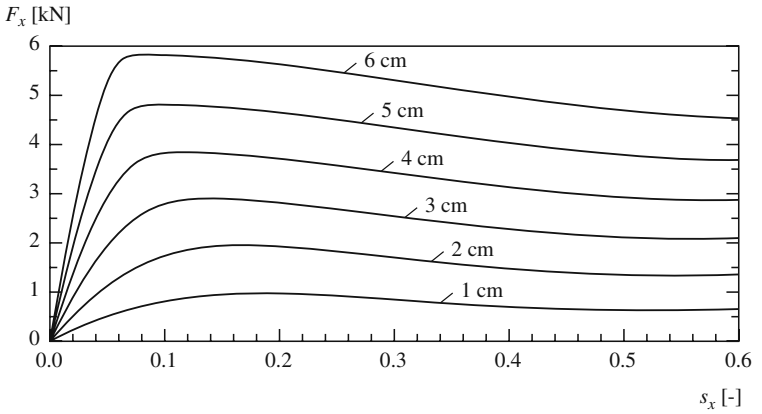

Fig. 4 Longitudinal force–slip characteristics for normal deflections of 1, 2, 3, 4, 5 and 6 cm. The corresponding normal forces are 819, 1699, 2623, 3593, 4608 and 5666 N

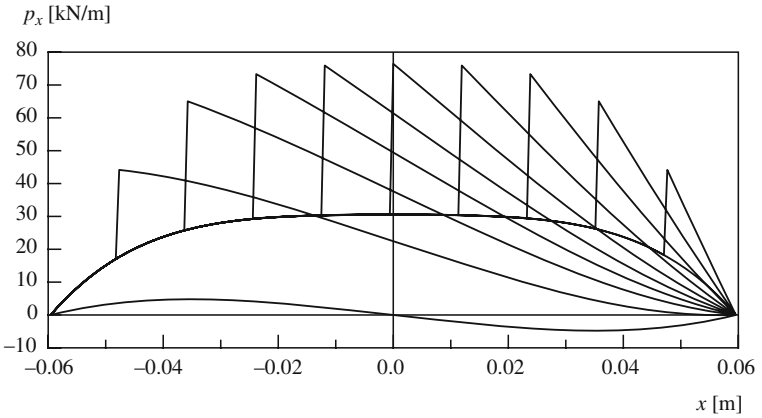

Fig. 5 Longitudinal force distribution for a normal deflection of 4 cm and longitudinal slips of 0, 0.0378, 0.0632, 0.0830, 0.1031, 0.1283, 0.1641, 0.2165, 0.2931, 0.4014 and 0.5444

For more general friction laws and non-stationary behaviour, one obtains the partial differential equation, written as ordinary differential equations on characteristics with the time as a parameter,

$$\dot{p}_x = k_{\mathrm{t}x}[\Omega R_{\mathrm{b}}(s_x + l_{\mathrm{t}} w'(a)/a - l_{\mathrm{t}} w''(x)) - v_{\mathrm{s}}], \quad \dot{x} = -\Omega R_{\mathrm{b}}, \tag{13}$$

where v_{s} is the sliding speed, which is zero in the adhesion region and follows from the friction law in the sliding region. If the friction only depends on the sliding speed, we have the relation $p_x = \mu(v_{\mathrm{s}})p_z$, which has to be solved for v_{s}, whereas for a dynamic friction law, the equation

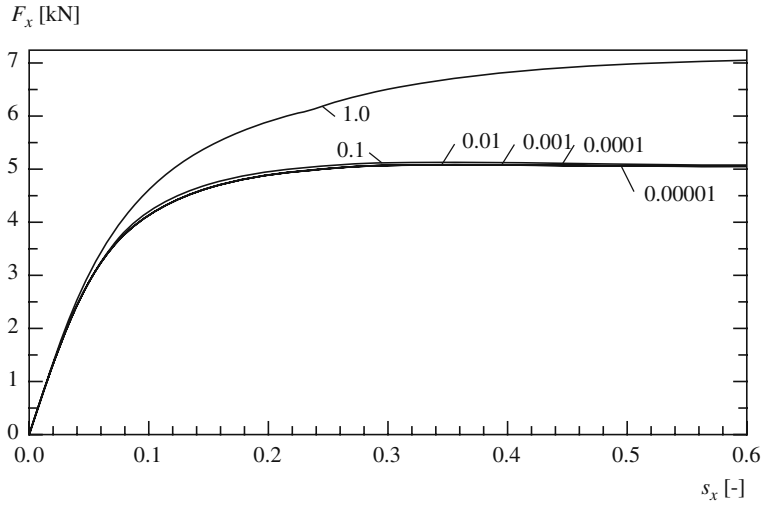

Fig. 6 Longitudinal force–slip characteristics for a normal deflection of 4 cm and several velocities: $v_m/(\Omega R_b) = 1, 0.1, 0.01, 0.001, 0.0001$ and 0.00001

$$\dot{p}_x = \dot{\mu} p_z + \mu p_z{}' \dot{x} \tag{14}$$

has to be solved for v_s. Figure 6 shows the stationary friction characteristics for the friction model (1) for a deflection of 4 cm and various values of the dimensionless parameter $v_m/(\Omega R_b)$. It can be observed that the maximal longitudinal force is larger than that for the Coulomb friction model. For the lower values of this parameter, the sliding speed is discontinuous. From the leading edge, the longitudinal force per unit of length increases until the ratio to the normal force reaches a value μ_k, after which a sliding region with small sliding speed sets in. The longitudinal force per unit of length increases further, until its ratio to the normal force becomes the maximum μ_m, after which a rapid transition with a high sliding speed sets in, until the sliding speeds return to zero. The longitudinal force per unit of length after this rapid transition does not follow directly from the model, and an additional assumption needs to be made; here it is assumed that $p_x = \mu_k p_z$. After this transition, sliding with low velocity starts anew and the force increases until the next transition occurs. Figure 7 shows the longitudinal force distribution for a typical case.

For a friction model with an internal state variable, the alternation of regions with low and high sliding speeds disappears if the evolution is sufficiently slow. For example, for the model in (2) with $\tau_s = 1$ s, $d_k = 0.01$ m, there is no alternation, but if the relaxation length is reduced to $d_k = 0.001$ m, an alternation similar to that for the model without internal state is found, where a single return to small sliding speed is present. In relation to Fig. 6, the stationary longitudinal force is generally lower, and the dependence on the slip can be discontinuous if the number of sliding speed alternations changes.

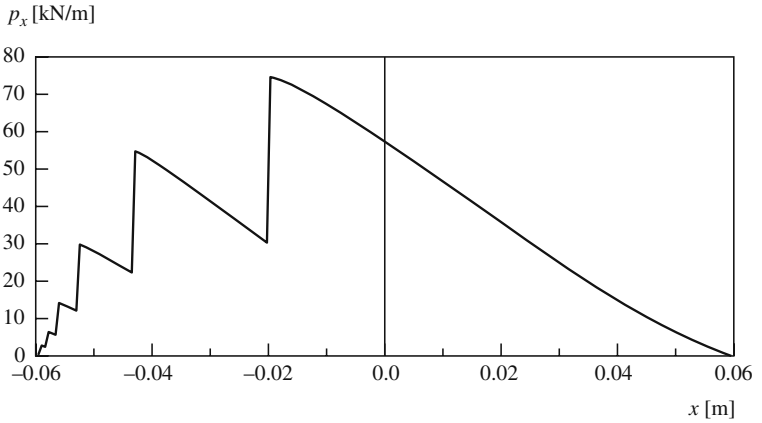

Fig. 7 Longitudinal force distribution for a normal deflection of 4 cm, dimensionless velocity parameter $v_m/(\Omega R_b) = 0.1$ and longitudinal slip $s_x = 0.1$

4 Conclusions

It has been shown that the brush model with Coulomb friction with different kinetic and static friction can explain the shape of the longitudinal force–slip characteristic of a tyre for stationary sliding. For higher temperatures or low speeds, more advanced friction models are needed. Especially the unimodal friction characteristic yields realistic results. Alternating regions of low and high sliding speed can occur. For friction models with a state variable, this phenomenon may be suppressed or the number of alternations is reduced.

References

1. Böhm, F. (ed.): Tyre Models for Vehicle Dynamics Analysis, Proceedings of the Second International Colloquium. Vehicle System Dynamics Supplement **27**, 1–345 (1997)
2. Clark, R.F. (ed.): Mechanics of Pneumatic Tires. US Department of Transportation, Washington DC (1981)
3. Gipser, M.: FTyre: A Physically Based Application-Oriented Tyre Model for Use with Detailed MBS and Finite-Element Suspension Models. Vehicle System Dynamics Supplement **43**, 76–91 (2005)
4. Lugner, P., Plöchl, (eds.): Tyre Models for Vehicle Dynamics Analysis, Proceedings of the Third International Colloquium. Vehicle System Dynamics Supplement **43**, 1–539 (2005)
5. Pacejka, H.B. (ed.): Tyre Models for Vehicle Dynamics Analysis, Proceedings of the First International Colloquium. Vehicle System Dynamics Supplement **21**, 1–192 (1993)
6. Pacejka, H.: Tyre and Vehicle Dynamics. Butterworth–Heinemann, Oxford (2002)
7. Savkoor, A.R.: Some Aspects of Friction and Wear of Tyres Arising from Deformations, Slip and Stresses at the Ground Contact. Wear **9**, 66–78 (1966)
8. Savkoor, A.R., Meijaard, J.P.: Application of bifurcation theory to the identification of the constitutive relations for sliding friction. In: Narayanan, S., Iyengar, R.N. (eds.) IUTAM

Symposium on Nonlinear and Stochastic Structural Dynamics, pp. 233–248. Kluwer, Dordrecht (2001)
9. Smiley, R.F.: Correlation, evaluation, and extension of linearized theories for tire motion and wheel shimmy. NACA Report 1299, National Advisory Committee for Aeronautics, Washington DC (1957)

Part II
Dynamics of Non-smooth Problems

Bifurcations in Non-smooth Models of Mechanical Systems

Piotr Kowalczyk and Arne Nordmark

Abstract Non-smooth models are often used for mechanical systems, for example to model contact or friction. When system parameters are varied, changes in dynamical behaviour may occur that are different from the standard bifurcations found in smooth systems. Obtaining a unified picture of such non-smooth bifurcations is difficult, because of the wide range of different types of discontinuities commonly encountered. Here we will present theorems concerning boundary induced bifurcations of equilibria and limit cycles in generic Filippov systems, and apply the theory to a model of a friction oscillator.

1 Introduction

When modeling mechanical systems, it is natural to use non-smooth models, since the character of the forces acting on the system often changes rapidly over small changes in position and/or velocity. Well-known examples are the use of simple models like Coulomb friction to model frictional contact forces, or impact laws where velocities change instantaneously to model collisions. Another example is when there are preloaded springs or dampers, which may be modeled as having zero force outside a certain region of positions.

While the resulting non-smooth models may be easy to derive, the study of such models have its own set of challenges compared to the study of smooth models. The usual results on existence and uniqueness of solutions in time does not necessary apply to non-smooth models. Even if we can define what we mean by a solution, and show that these do exist, we find that the theory of bifurcations, that is: qualitative changes in system behaviour under parameter changes, has similar problems. Which phenomena should the term bifurcation be used for? How do these phenomena unfold under parameter variations? (see [2] for a recent overview of bifurcations in non-smooth systems)

P. Kowalczyk (✉)
School of Mathematics, Alan Turing building, The University of Manchester, Oxford road, Manchester M13 9PL, UK
e-mail: piotr.kowalczyk@manchester.ac.uk

P.G. Thomsen, H. True (eds.), *Non-smooth Problems in Vehicle Systems Dynamics*,
DOI 10.1007/978-3-642-01356-0_15, © Springer-Verlag Berlin Heidelberg 2010

One major problem is that "non-smooth" can encompass such a variety of phenomena, and it seems very hard to come up with a framework that can include all or even a major subset. Thus we may try to analyse one or more "classes" of non-smooth systems, but the results obtained for one class may not carry over to another. However, we can develop techniques and tools that are applicable to several important classes of non-smooth models frequently used for mechanical systems.

We illustrate some of these techniques using a simple model of a single degree-of-freedom mechanical system, having a smooth boundary in the position/velocity space where the system changes. Our example contains a modified Coulomb friction law, and thus the system equations change at the surface of zero velocity.

The model is studied either with static loading, where the state space is two-dimensional, or using periodic loading, where the phase of the loading provides another state variable. In the case of static loading, equilibrium points are possible, and in particular we can explore the bifurcations (boundary equilibrium bifurcations) that occur as system parameters are changed from values where a boundary equilibrium exists.

In the case of periodic loading, where equilibrium points typically do not exist, the simplest bifurcations instead involves periodic orbits. In particular, we find grazing bifurcations, where parameters are changed from a situation where a periodic orbit has a quadratic tangency (grazing) to the surface where the non-smoothness occur.

2 Filippov Systems

We start by introducing simple class of non-smooth system. In a Filippov system [3], state space is divided into a finite number of non-overlapping regions S_i, each with an associated vector field F_i. On parts of the region boundaries, it may be possible to define a *sliding* vector field as a convex combination (a linear combinations with non-negative weights summing to 1) of the vector fields in the adjacent regions. In the simplest possible case, there are only 2 regions separated by a smooth boundary Σ, which may be given by the zero level set of a smooth function H.

Our system in the following is thus defined by

$$\dot{x} = \begin{cases} F_1(x) & x \in S_1 \\ F_2(x) & x \in S_2 \end{cases} \tag{1}$$

where $S_1 = \{x : H(x) > 0\}$, $S_2 = \{x : H(x) < 0\}$, with the boundary $\Sigma = \{x : H(x) = 0\}$. Although both the vector fields F_1 and F_2 have an equivalent role in our system, we will in the following regard the first vector field as being primary, and describe the second through the difference $F_d(x) = F_2(x) - F_1(x)$. We will assume that both F_1 and F_d are well defined and smooth in all of state space, and that the difference F_d is non-zero at the boundary Σ.

Let the sliding set $\hat{\Sigma}$ be the part of Σ where it is possible to define a sliding vector field F_s. Thus on $\hat{\Sigma}$ we have

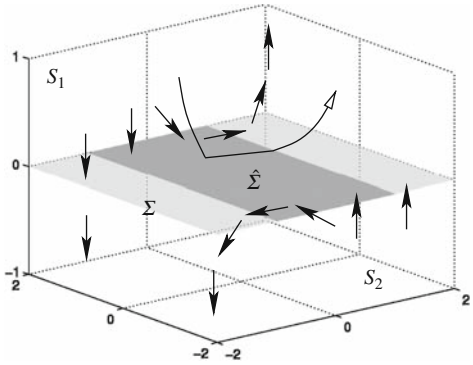

Fig. 1 Vector fields and trajectories for a Filippov system

$$\dot{x} = F_s(x) = F_1(x) + \lambda F_d(x), \quad 0 < \lambda < 1. \tag{2}$$

where λ is chosen such that F_s is tangent to Σ.

Figure 1 shows an example of a Filippov system with a trajectory starting in S_1, becoming sliding for while, and returning to S_1 after that.

3 Boundary Equilibrium Bifurcations in Filippov Systems

Let us start by examining bifurcations of equlibrium points in Filippov systems. Apart from the birfurcations that have direct counterparts in smooth systems, we also find one that is directly related to the interaction of equilibrium points with the boundary.

3.1 Equilibria in the Filippov System

In our system we can distinguish between three different kinds of equilibrium points.

A *standard equilibrium* (SE) is an equilibrium of the first[1] vector field that is located away from the boundary. Thus a standard equilibrium point x^* must satisfy

$$F_1(x^*) = 0, \quad H(x^*) > 0. \tag{3}$$

A *pseudo-equilibrium* is an equilibrium of the sliding vector field that is located away from the boundary of the sliding set. A pseudo-equilibrium point x^*, and its corresponding value of the convex combination parameter λ^*, must satisfy

$$F_1(x^*) + \lambda^* F_d(x^*) = 0, \quad H(x^*) = 0, \quad 0 < \lambda^* < 1. \tag{4}$$

[1] Although both the vector fields F_1 and F_2 have an equivalent role in our system, we will in the following only consider equilibria of the first vector field.

A *boundary equilibrium* can be viewed both as a limit of a standard equilibrium, as $H(x^*) \to 0$, and of a pseudo-equilibrium, as $\lambda^* \to 0$. It satisfies

$$F_1(x^*) = 0, \quad H(x^*) = 0. \tag{5}$$

3.2 Boundary Equilibrium Bifurcations

Now assume that the system depends on a single real parameter μ, so that all of F_1, F_2, and H depends both on x and μ. Assume (x^*, μ^*) is a boundary equilibrium point, that is

$$F_1(x^*, \mu^*) = 0, \quad H(x^*, \mu^*) = 0. \tag{6}$$

We can now investigate whether there are branches of either standard equilibria or pseudo-equilibria connecting to the boundary equilibrium when the parameter μ is varied. In the following we will use subscripts to denote partial derivatives evaluated at the boundary equilibrium point, thus F_{1x} denotes $\frac{\partial F_1}{\partial x}(x^*, \mu^*)$ and H_μ denotes $\frac{\partial H}{\partial \mu}(x^*, \mu^*)$, etc. Also F_d will denote $F_d(x^*, \mu^*)$.

A branch $x(\mu)$ of standard equilibria connecting to the boundary equilibrium must satisfy

$$F_1(x(\mu), \mu) = 0, \quad H(x(\mu), \mu) > 0, \quad x(\mu^*) = x^*. \tag{7}$$

Let us disregard the inequality for the moment. Then the implicit function theorem tells us that if F_{1x} is invertible, a branch $x(\mu)$ exists uniquely for small $\mu - \mu^*$. Further, we can evaluate the value of H on this branch:

$$H(x(\mu), \mu) = b(\mu - \mu^*) + \mathcal{O}(\mu - \mu^*)^2, \tag{8}$$

where the coefficient b is

$$b = H_\mu - H_x F_{1x}^{-1} F_\mu. \tag{9}$$

Returning to the inequality condition that the value of H on the branch must be positive, we find that if $b \neq 0$, then the branch exists only on the side where $b(\mu - \mu^*)$ is positive.

For a branch $x(\mu)$, $\lambda(\mu)$ of pseudo-equilibria, we find

$$\begin{aligned} F_1(x(\mu), \mu) + \lambda(\mu)^* F_d(x(\mu), \mu) = 0, \quad H(x(\mu), \mu) = 0, \\ 0 < \lambda(\mu) < 1, \quad x(\mu^*) = x^*, \quad \lambda(\mu^*) = 0. \end{aligned} \tag{10}$$

Again disregarding the inequality for a moment, the implicit function theorem states that if both F_{1x} is invertible and the quantity $a = H_x F_{1x}^{-1} F_d$ is non-zero, then $x(\mu)$, $\lambda(\mu)$ exists uniquely for small $\mu - \mu^*$, and

$$\lambda(\mu) = \frac{b}{a}(\mu - \mu^*) + \mathcal{O}(\mu - \mu^*)^2, \tag{11}$$

where b is the same coefficient as above. Taking the inequality (only $0 < \lambda$ is important, since we know λ is small) back, we again find that if b is non-zero, then the branch exists only on the side where $\frac{b}{a}(\mu - \mu^*)$ is positive.

In summary, we have shown [1]

Theorem 1. *If* (x^*, μ^*) *is a boundary equilibrium point, and if*

$$\det(F_{1x}) \neq 0 \tag{12}$$

$$a = H_x F_{1x}^{-1} F_d \neq 0 \tag{13}$$

$$b = H_\mu - H_x F_{1x}^{-1} F_\mu \neq 0, \tag{14}$$

then there is one unique branch of standard equilibria and one unique branch of pseudo-equilibria connecting to the boundary equilibrium. The standard equilibria branch exists when $b(\mu - \mu^*)$ *is small and positive, and the pseudo-equilibria branch exists when* $\frac{b}{a}(\mu - \mu^*)$ *is small and positive.*

Depending on the sign of a, we can make the following distinctions

Non-smooth fold	If $a > 0$, then both branches exists for one sign of $\mu - \mu^*$, and no branch for the other sign. The two branches come together at the boundary equilibrium point and annihilate. This is somewhat similar to what happens in a fold bifurcation for smooth systems.
Persistence	If $a < 0$, then one branch exists for one sign of $\mu - \mu^*$, and the other branch for the other sign. One branch is transformed into the other at the boundary equilibrium point.

3.3 Boundary Equilibrium Bifurcations in a Friction Oscillator

Consider the single degree-of-freedom friction oscillator model [6]

$$\ddot{y} + y = \alpha_1 \text{sgn}(v - \dot{y}) - \alpha_2(v - \dot{y}) + \alpha_3(v - \dot{y})^3 + \alpha_4 \tag{15}$$

where α_{1-3} are positive friction law parameters, and α_4 is a constant forcing parameter, and v is a constant driving belt velocity (Fig. 2).

This can be written as a Filippov system (using the notation $v_r = v - x_2$)

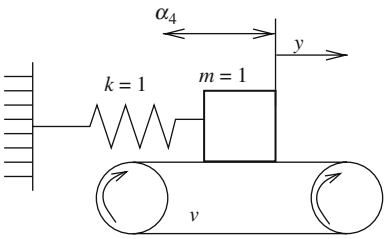

Fig. 2 The friction oscillator. The friction force is discontinuous at 0 relative velocity

$$F_1(x) = \begin{pmatrix} x_2 \\ \alpha_1 - \alpha_2 v_r + \alpha_3 v_r^3 - x_1 + \alpha_4 \end{pmatrix}, \quad F_d(x) = \begin{pmatrix} 0 \\ -2\alpha_1 \end{pmatrix} \tag{16}$$

$$H(x) = v - x_2, \tag{17}$$

$$S_1 = \{x_2 < v\}, \quad S_2 = \{x_2 > v\} \tag{18}$$

$$\Sigma = \{x_2 = v\}, \quad \hat{\Sigma} = \{x_2 = v, |\alpha_4 - x_1| < \alpha_1\} \tag{19}$$

Note that "sliding" in the Filippov sense for this system actually means sticking, that is the mass follows the belt. The set S_1 contains state points slipping left, and S_2 means slipping right.

3.3.1 Boundary Equilibrium

When the driving velocity $v = 0$, there is a boundary equilibrium at

$$x_2 = 0, \quad v = 0, \quad x_1 = \alpha_1 + \alpha_4 \tag{20}$$

We can now try to apply Theorem 1, using v as the system parameter, but when we check the conditions of the theorem we find

$$\det(F_{1x}) = 1 \quad \text{(OK)} \tag{21}$$

$$a = H_x F_{1x}^{-1} F_d = 0 \quad \text{(bad)} \tag{22}$$

$$b = H_v - H_x F_{1x}^{-1} F_\mu = 1 \quad \text{(OK)}. \tag{23}$$

Since $a = 0$ we can not guarantee the existence of a unique branch of pseudo-equilibrium points. Indeed, when $v = 0$, all points in the sliding set $\hat{\Sigma}$ are pseudo-equilibrium points, and when $v \neq 0$ there are no pseudo-equilibrium points.

3.3.2 Breaking the Degeneracy

For a single degree-of-freedom mechanical system with a forcing discontinuity, the second component of $F_{1x}^{-1} F_d$ will always be 0, and since $a = H_x F_{1x}^{-1} F_d$ we find that a is always 0 unless we introduce some position dependency into the function H, which determines whether we are slipping right or left. We can do this, for example, by letting the belt velocity v be controlled by the position. Thus we take $v = \kappa x_1$ for some constant κ, and use the constant force α_4 as our system parameter instead of v. Then we find boundary equilibria when $x_2 = 0$, $x_1 = 0$, $\alpha_4 = -\alpha_1$, and the conditions of the theorem become

$$\det(F_{1x}) = 1 + \alpha_2\kappa \tag{24}$$

$$a = H_x F_{1x}^{-1} F_d = \frac{2\alpha_1\kappa}{1 + \alpha_2\kappa} \tag{25}$$

$$b = H_{\alpha_4} - H_x F_{1x}^{-1} F_{1\alpha_4} = \frac{\kappa}{1 + \alpha_2\kappa} \tag{26}$$

which are all OK if $0 < |\kappa| < 1/\alpha_2$.

3.3.3 Numerical Results

We use the friction law parameter values $\alpha_1 = 1$, $\alpha_2 = 0.5$, $\alpha_3 = 1$. If $\kappa = 0.1$ we should have a non-smooth fold, with the two equilibrium points existing for $\alpha_4 > -\alpha_1$. If $\kappa = -0.1$ we should have a persistence, with the standard equilibrium points existing for $\alpha_4 < -\alpha_1$, and the pseudo-equlibrium for $\alpha_4 > -\alpha_1$. Figures 3 and 4 shows the phase portrait on both sides of the bifurcations. The phase portraits agree with the results for generic planar Filippov systems presented in [4].

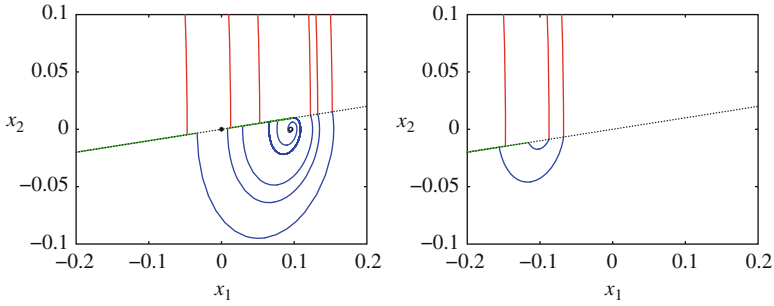

Fig. 3 Non-smooth fold for the friction oscillator, $\kappa = 0.1$: $\alpha_4 + \alpha_1 = 0.1$ (*left*) with a standard equilibrium, a pseudo-equilibrium, and a stable periodic orbit; $\alpha_4 + \alpha_1 = -0.1$ (*right*) with no local limit sets

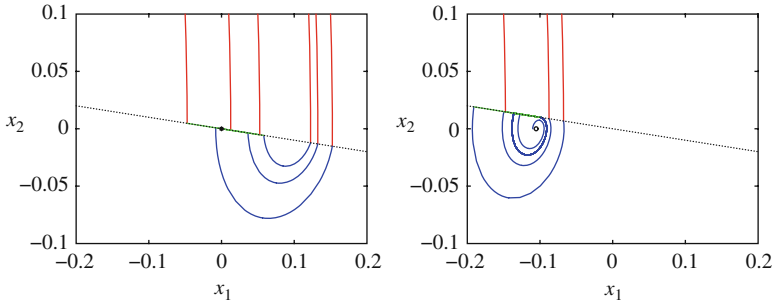

Fig. 4 Persistence for the friction oscillator, $\kappa = -0.1$: $\alpha_4 + \alpha_1 = -0.1$ (*left*) with a stable pseudo-equilibrium; $\alpha_4 + \alpha_1 = -0.1$ (*right*) with a standard equilibrium and a stable periodic orbit

4 Discontinuity Induced Bifurcations of Limit Cycles – Grazing-Sliding Bifurcations

We will now move to bifurcations that involve periodic oscillations. In particular we will focus on so-called grazing-sliding bifurcations of limit cycles. Grazing-sliding bifurcations are defined as tangential interactions between a limit cycle and the boundary of the sliding region. The grazing-sliding bifurcation, that underlies our current investigations, is schematically presented in Fig. 5. Note that, for clarity only the parts of a cycle which interact with the boundary of the sliding region are depicted. In Fig. 5, labelled by "b", we depict a segment of a cycle lying in region G_1 that grazes the boundary of the sliding region from above. Under parameter variation, we have the possibility of creating periodic orbits that either have no interaction with the sliding region (trajectory labelled "a"), have a short sliding segment (trajectory labelled "c") or combinations of "a" and "c" behaviour in an orbit of higher period. Typically only a subset of these possibilities is realised for a given parameter value. The existence of an orbit with a sliding segment born in the bifurcation under certain genericity conditions can be rigorously proven [5].

We can associate a set of analytical conditions with a grazing-sliding bifurcation. These conditions capture characteristic features of the phase space locally around the grazing point. At the grazing-sliding point $(x^*,\ \mu^*)$ we have

$$H_x \neq 0,\ H = 0, \tag{27}$$

$$H_x F_1 = 0, \tag{28}$$

$$(H_x F_1)_x F_1 > 0. \tag{29}$$

We assumed, without loss of generality $F_1(x^*,\ \mu^*) = F_s(x^*,\ \mu^*)$ (that is $\lambda^* = 0$). In the case when it is vector field F_2 that grazes at $(x^*,\ \mu^*)$ we then would expect conditions (27), (28), and (29) to hold for F_2 (with the inequality sign of (29) interchanged).

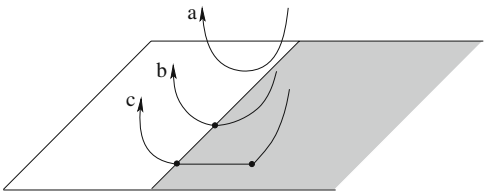

Fig. 5 Schematic illustration of one-parameter grazing-sliding bifurcation scenario

4.1 Grazing-Sliding Bifurcation in the Friction Oscillator

Let us now get back to system (15) replacing the constant force α_4 by $\alpha_4 \cos(\omega t)$. The friction model is now characterized by a periodic loading and it becomes non-autonomous. Define the variables x_1 and x_2 as in Sect. 2, and $x_3 = \omega t$. Thus, we obtain a three dimensional representation of the system. Vector fields F_1, F_d are defined as previously (16) with the third component of $F_1 = \omega$ and the third component of $F_d = 0$, and similarly $H(x)$ remains unchanged, with x being a three dimensional state vector.

Consider now a parameter region for which $\alpha_1 = \alpha_2 = 1.5$, $\alpha_3 = 0.45$ and $\alpha_4 = 0.7$. A stable orbit of period $2\pi/\omega$ exits in the system for $\omega < \omega^* = 1.2376$. This orbit undergoes a grazing-sliding bifurcations and we observe the onset of chaotic dynamics for $\omega > \omega^*$. To be able to show that it is indeed the grazing sliding bifurcation that leads to the onset of chaos we first check if the set of analytical conditions that must be satisfied at the grazing point hold. We indeed find that at $(x_1^*, x_2^*, x_3^*) = (1.291727, 1, 1.872904)$ conditions (27), (28), and (29) hold. In particular $((H_x F_1)_x F_1)(x^*) = \alpha_4 \sin(x_3^*)\omega^* = 0.827 > 0$ (Fig. 6).

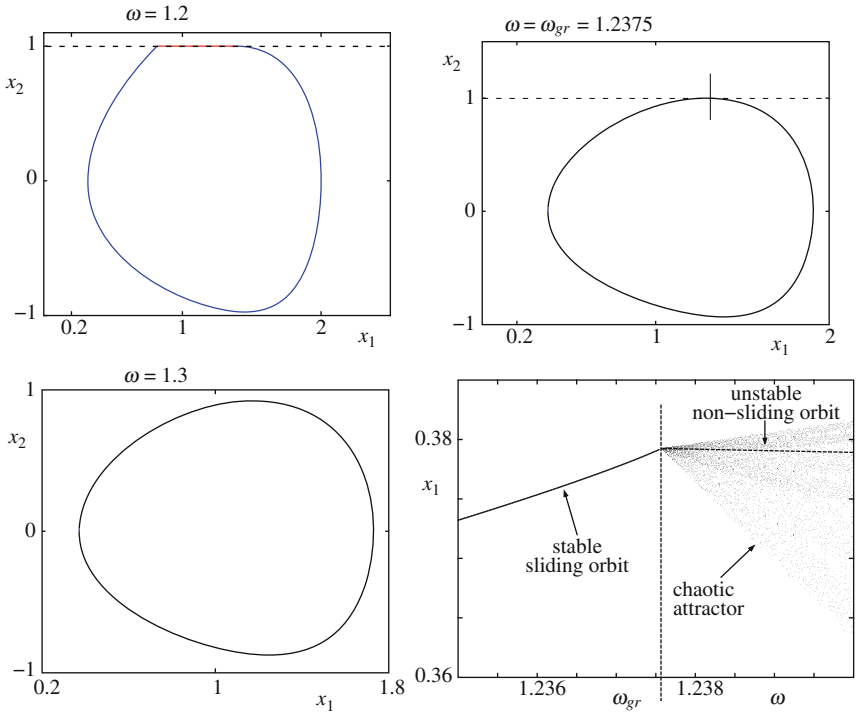

Fig. 6 Stable periodic orbit (*top left-hand corner*), grazing-sliding orbit (*top right-hand corner*), unstable non-sliding orbit (*bottom left-hand corner*) and the bifurcation diagram (*bottom right-hand corner*) of the friction system (15) with periodic loading $\alpha_4 = \alpha_4 \cos(\omega t)$

4.2 Analysis

To be able to explain the dynamics around the grazing-sliding observed in the dry-friction oscillator model we will use a stroboscopic map (a T-time map) built about a periodic point, say x_p, corresponding to periodic oscillations of the grazing orbit. Let us consider the points in some sufficiently small neighborhood of x_p on a stroboscopic section. There is a set of points that do not interact with the switching surface Σ, and a set of points that hit Σ then follow the sliding flow and leave off the switching surface Σ, and arrive to the next stroboscopic section. Let us suppose that we fix a phase at some point $x_3 = \phi_0 \in [0,\ 2\pi]$. Then let us define a two-dimensional stroboscopic section as a zero level set of $P_I(x) = t(\mathrm{mod}2\pi/\omega) - \phi_0$ with $t \in [0,\ 2\pi/\omega]$, and another stroboscopic section $P_F(x) = t(\mathrm{mod}2\pi/\omega) - \phi_0$ with $t \in [2\pi/\omega,\ 4\pi/\omega]$. Assume $x_p \in P_I$ and hence $x_p \in P_F$. We wish to find the functional expression for the map, say Π, such that $\Pi : P_I \mapsto P_F$. Note that the time which elapses for a trajectory to map points on P_I to points on P_F is $T = 2\pi/\omega$ and hence the components x_3 of the state vectors x are the same on P_I and P_F. Denote by ϕ_1 a flow generated by the vector field F_1. We can then obtain a return map from P_I to P_F about x_p as

$$P(x) = \phi_1(ZDM(\phi_1(x, t_1), y), t_2)$$

where $t_1 + t_2 = T$ and t_1 is the time of evolution from $x_p \in P_I$ to x^*, where x^* is a point on the limit cycle at which grazing with the boundary of the sliding region occurs, and t_2 is the time of evolution from x^* to $x_p \in P_F$. Finally, the function $ZDM(.\ ,\ .)$ is the mapping that captures the effect of the grazing contact. This map is piecewise affine to leading order in x, and $y = y(x)$ being some scalar variable that measures the "amount" of sliding. The key point now is to derive the expression for $ZDM(.\ ,\ .)$. Let us first define $H_{\min}(x) + y^2 = 0$; $H_{\min}(x)$ captures the minimum value of a trajectory with respect to Σ, through some point x and generated by F_1. We now proceed as follows. Consider some point $x_0 \in P_I$ sufficiently close to x_p and such that the trajectory rooted at x_0 after time $t < t_1$ crosses Σ. The evolving trajectory then switches to the sliding flow, and then again it switches to flow ϕ_1 and reaches P_F after time T, at some point, say x_0'. However, ignore the switching to the sliding flow. Hence, after time t_1 we reach some point, say x_s and such that $H_{\min}(x_s) < 0$. Similarly consider backwards evolution from x_0' for the time t_2 using ϕ_1. In this way, another point, say x_f, and such that $H_{\min}(x_f) = 0$ is reached. The map that maps x_s on x_f is $ZDM(x_s, y)$. To derive the functional expression for $ZDM(x_s,\ y)$ we can express $ZDM(x_s,\ y)$ as a composition of flows i.e.

$$ZDM(x_s, y) = \phi_1(\phi_s(\phi_1(x_s,\ t_x), t_s), -(t_x + t_s))$$

where t_x is the time (small) required to reach Σ from x_s, and t_s is the sliding time (also small). The times t_x and t_s are functions of x_s and y variables. We should note here that $ZDM(x_s, y)$ maps x_s on x_f in zero time. Then the map from x_s to x_f to leading order is given by

$$ZDM(x_s) = x_s + \begin{cases} 0, & H_{\min}(x_s) \geq 0 \\ \frac{F_d^*}{H_x^* F_d^*} y^2 & H_{\min}(x_s) < 0, \ y^2 = -H_{\min}(x_s) \end{cases}. \tag{30}$$

The "*" refers to quantities evaluated at x^*. We can now use the expression given by (30) and combine it with the solution of the variational equation corresponding to the evolution generated by vector field F_1 to obtain the leading order stroboscopic $T-$time map about the grazing point x^*. For the purpose of the analysis it is convenient to place a stroboscopic section P_I through the grazing point x^*. In that case for x on P_I, $H_{\min}(x) \approx H(x)$ and $P(x) = ZDM(\phi_1(x, T))$. We can now linearize $P(x)$ about x^* and cast this linearization in an appropriate co-ordinate set. Thus, we can obtain a piecewise affine approximation for $P(x)$. In the case of 3-dimensional vector fields the piecewise affine normal form approximation of $P(x)$, using an appropriate co-ordinate set is given by

$$\hat{P}(\tilde{x}_1, \tilde{x}_2, \mu) = \begin{cases} \begin{pmatrix} \tau_R & 1 \\ \delta_R & 0 \end{pmatrix} \begin{pmatrix} \tilde{x}_1 \\ \tilde{x}_2 \end{pmatrix} + \mu \begin{pmatrix} 1 \\ 0 \end{pmatrix} & \tilde{x}_1 \geq 0 \\ \begin{pmatrix} \tau_L & 1 \\ 0 & 0 \end{pmatrix} \begin{pmatrix} \tilde{x}_1 \\ \tilde{x}_2 \end{pmatrix} + \mu \begin{pmatrix} 1 \\ 0 \end{pmatrix} & \tilde{x}_1 < 0 \end{cases}. \tag{31}$$

Border-collision bifurcations of fixed points of (31) under the variations of μ through 0 correspond to grazing-sliding bifurcations of the associated 3-dimensional flow. To determine the parameters τ_R, τ_L, and δ_R we use the values of the nontrivial Floquet multipliers of the grazing cycle viewed as not interacting with the switching surface (allows to determine δ_R and τ_R), and as interacting with the switching surface (allows to determine τ_L). The multipliers of the grazing cycle viewed as not interacting with the switching surface are the eigenvalues of the matrix $J^* = \frac{\partial \phi_1}{\partial x}|_T$, where J is the jacobian matrix of the solution of the variation equation corresponding to the flow ϕ_1. To obtain the multipliers of the grazing cycle viewed as interacting with the switching surface we compose the jacobian matrix J^* with the jacobian matrix of the linearization of the ZDM about x^* on the sliding side. We use the fact that on the chosen stroboscopic section $H_{\min}(x) \approx H(x)$. Expanding $H(x)$ about x^* to leading order gives $H(x) \approx H(x^*) + H_x^*(x - x^*)$. Therefore, the linearization of the ZDM about x^* on the sliding side is $x - \frac{F_d^* H_x^*}{H_x^* F_d^*}(x - x^*)$ and the corresponding jacobian matrix is $I - \frac{F_d^* H_x^*}{H_x^* F_d^*}$. We can now consider the Floquet multipliers of the matrix composition $L_s = (I - \frac{F_d^* H_x^*}{H_x^* F_d^*})J^*$. One of the nontrivial Floquet multipliers is 0. Therefore, τ_L is simply equal to the second nontrivial Floquet multiplier of L_s (the third multiplier is 1). On the other hand to find τ_R and δ_R we note that τ_R is the sum and δ_R is the product of the nontrivial Floquet multipliers of J^*.

Therefore, let us use above description and determine the numerical values and hence the dynamics of the map (31) around the grazing-sliding bifurcation observed in the friction oscillator. we found that the nontrivial Floquet multipliers of J^* are

$\lambda_{1NS} = -5.732288$ and $\lambda_{2NS} = -0.016799$. The nontrivial Floquet multipliers of L_s are $\lambda_{1S} = 0$ and $\lambda_{2S} = 0.619648$. Therefore, the map $\hat{P}$ has got the form

$$\hat{P}(\tilde{x}_1, \tilde{x}_2, \mu) = \begin{cases} \begin{pmatrix} -5.7490869 & 1 \\ 0.0965801 & 0 \end{pmatrix} \begin{pmatrix} \tilde{x}_1 \\ \tilde{x}_2 \end{pmatrix} + \mu \begin{pmatrix} 1 \\ 0 \end{pmatrix} & \tilde{x}_1 \geq 0 \\ \begin{pmatrix} 0.619648 & 1 \\ 0 & 0 \end{pmatrix} \begin{pmatrix} \tilde{x}_1 \\ \tilde{x}_2 \end{pmatrix} + \mu \begin{pmatrix} 1 \\ 0 \end{pmatrix} & \tilde{x}_1 < 0 \end{cases}. \tag{32}$$

It can be shown that the above map exhibits a border-collision bifurcation under the variations of μ through 0 that leads to the onset of chaos (Fig. 7). This scenario corresponds to the dynamics around the grazing sliding bifurcations from a stable sliding cycle to chaotic dynamics observed in our friction oscillator model.

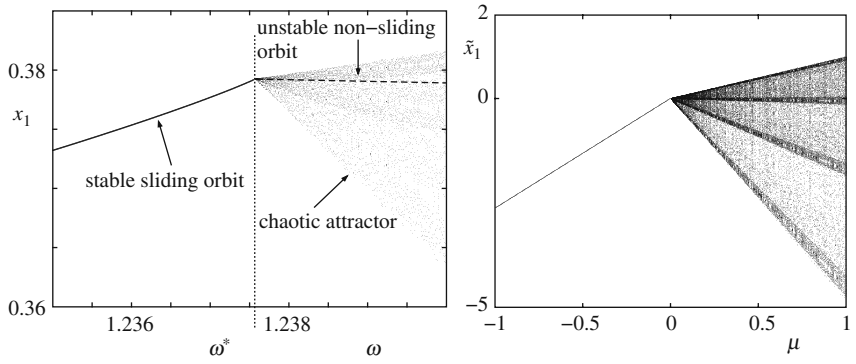

Fig. 7 Bifurcation diagram of (32) under the variation of μ through 0

5 Conclusions

Using a one degree of freedom friction oscillator model (15) under static and periodic loading we have shown the existence of bifurcations that occur due to the existence of discontinuous nonlinearities, which are termed in the literature [2] as discontinuity induced bifurcations (DIBs for short). In particular, we have shown the occurrence of DIBs that involve equilibria in the case of the friction model under static loading and periodic orbits in the case of periodic loading. In the first case the occurrence of an equivalent to a standard fold and trans-critical bifurcations have been shown. In the second case an onset of chaotic stick-slip oscillations have been explained using the theory of grazing-sliding bifurcations.

Acknowledgments Piotr Kowalczyk would like to acknowledge EPSRC grant EP/E050441/1.

References

1. di Bernardo, M., Nordmark, A.B., Olivar, G.: Discontinuity-induced bifurcations of equilibria in piecewise-smooth and impacting dynamical systems. Physica D. **237**, 119–136 (2008)
2. di Bernardo, M., Budd, C.J., Champneys, A.R., Kowalczyk, P.: Piecewise-smooth dynamical systems: theory and applications. Springer, London (2008)
3. Filippov, A.F.: Differential equations with discontinuous right-hand sides. Kluwer, Dordrecht (1988)
4. Kuznetsov, Yu.A., Rinaldi, S., Gragnani, A.: One-parameter bifurcations in planar Filippov systems. Int. J. Bif. Chaos. **13(8)**, 2157–2188 (2003)
5. Nordmark, A.B., Kowalczyk, P.: A codimension-two scenario of sliding solutions in grazing-sliding bifurcations. Nonlinearity. **19**, 1–26 (2006)
6. Yoshitake, Y., Sueoka, A.: Forced self-excited vibration with dry friction. In: Wiercigroch, M., de Kraker, B. (eds.) Applied nonlinear dynamics and chaos of mechanical systems with discontinuities, World Scientific, Series A, **28**, pp.237–260 (2000)

Vibrational Displacement Determined by Constructive and Force Asymmetry of System

Iliya I. Blekhman

Abstract The phenomenon of vibrational displacement means an occurrence of directed on average "slow" changing (particularly motion) due to undirected on average "fast" (vibration) effects.

The following phenomena are based on this effect: vibrational transportation of single bodies and granular materials in the vibrating trays and vessels; the work of the devices called vibrational transformers of motion and vibro-engines; vibrational sinking of piles, sheet piles and shells; vibrational separation of particles of the granular material according to their density, size and some other parameters; the motion of vibratiing coaches; the flight and swimming of living organisms. A harmful effect of vibration displacement can be exemplified by the occurrence of the mobility of the nominally immobile parts of machines under the action of vibration (particularly – the self-unscrewing of nuts) [1,2].

The majority of vibration displacement theory problems reduces to essentially nonlinear differential equations with time periodical and discontinuous right parts. The last one is caused by the occurrence of dry friction forces and unilateral constrains in the concerned mechanical system. Moreover, in the separate areas of phase space the motion can be described by various differential equations, particularly, by the equitation of different order. At that the main interest is motions in which the change rates of generalized coordinates have the form

$$\dot{x} = \dot{X}(t) + \dot{\psi}(t, \omega t)$$

where $\dot{X}(t)$ is a slowly changing component, $\dot{\psi}$ is a fast changing component, ω is frequency of vibration. Component $\dot{X}$ is called *vibration displacement speed*; its determination is of the greatest applied interest. Such form of solutions predetermines the practicability of using vibrational mechanics approach and method of direct separation of motions for their determination. It's important that the equations

I.I. Blekhman (✉)
Institute of Problems of Mechanical Engineering, Academy of Sciences of Russia and Mekhanobr, Tekhnika Corporation, St. Petersburg, Russia
e-mail: blekhman@vibro.ipme.ru

P.G. Thomsen, H. True (eds.), *Non-smooth Problems in Vehicle Systems Dynamics*,
DOI 10.1007/978-3-642-01356-0_16,

of slow component $\dot{X}$ turn to be smooth in spite of unsmooth character of initial system. From the physical point of view vibrational displacement is caused by system asymmetry; six types of such asymmetry can be defined [2].

The systems with vibrational displacement caused by the so-called constructive asymmetry that is asymmetry inside the system have been considered in the report; at that vibrational excitation can be symmetrical. The results belonging to the author, Jakimova K.S., Molasyan S.A., Thomsen J., Fidlin A.Ya., Zimmerman K. and his colleagues, Ghernousko F.L. and his colleagues have been briefly considered. Then the peculiarities of granular medium behaviour in vibrating communicating vessels have been considered in detail. It has been noted that in such vessels the medium behaviour in some cases is similar to the behaviour of heavy viscous fluid and in other cases it differs markedly from it. Two cases of similar paradoxical behaviour have been considered. Their physical explanation and theoretical description have been given.

Acknowledgments This work was carried out in the frame of Federal Task Program (State Contract 02.515.11.5092) and was partly supported by Russian Foundation for Basic Research (project 07-08-00241).

References

1. Blekhman I.I., Dzhanelidze G.Yu. Vibrational Displacement. Nauka, Moscow, 1964, 410 p. (in Russian).
2. Blekhman I.I. Vibrational Mechanics. Fizmatlit, Moscow, 1994, 349p. (in Russian). English translation enlarged and revised: Vibrational Mechanics. Nonlinear Dynamic Effects, General Approach, Applications. World Scientific, Singapore, 2000, 509p.

Smoothing Dry Friction by Medium Frequency Dither and Its Influence on Ride Dynamics of Freight Wagons

Jerzy Piotrowski

Abstract According to results of carried-out experiments and simulations, dry friction exposed to dither results in viscous-like, frequently linear damping. This means that dither smoothes dry friction as far as damping is concerned. One dithered system of technical importance is a railway freight wagon with friction dampers in the primary suspension developing two-dimensional dry friction. The dither exciting dampers are generated in rolling contact of wheel and rail. Employing proposed rheological model of 2D friction in simulations it has been shown that dither significantly influences ride dynamics of freight wagons.

1 Smoothing Effect of Dither

In many instances friction dampers of mechanical systems are exposed to medium frequency (M-F) dither.[1] The dither is called the medium frequency one if its dominating frequency is several times higher than the highest eigenfrequency of the system.

One dithered system of technical importance is a railway freight wagon with friction dampers developing two-dimensional friction in the primary suspension. It is mainly this technical object that motivated the present investigation. The M-F dither that excites dampers of the wagon originates from rolling contact of wheel and rail.

In this chapter some results of investigation of the influence of M-F dither on one- and two-dimensional friction are presented.

J. Piotrowski (✉)
Institute of Vehicles, Warsaw University of Technology, Narbutta 84, PL-02-524, Warsaw, Poland
e-mail: jpt@simr.pw.edu.pl

[1] "Airplane bombers used mechanical computers to perform navigation and bomb trajectory calculations. Curiously, these computers (boxes filled with hundreds of gears and cogs) performed more accurately when flying on board the aircraft, and less well on ground. Engineers realized that the vibration from the aircraft reduced the error from sticky moving parts. Instead of moving in short jerks, they moved more continuously. Small vibrating motors were built into the computers, and their vibration was called 'dither' from the Middle English verb 'didderen' meaning 'to tremble'." *-Ken Pohlmann: Principles of Digital Audio, 4th edition, page 46.*

P.G. Thomsen, H. True (eds.), *Non-smooth Problems in Vehicle Systems Dynamics*,
DOI 10.1007/978-3-642-01356-0_17,

The objective of the investigation was to explore the influence of dither qualitatively, evaluate it quantitatively and to identify properties or parameters of dither influencing dry friction damping. To this end an experimental set-up has been built that allows investigating friction damping in the presence of M-F dither.

The carried-out experiments have shown that dry friction damping in the presence of M-F dither behaves like a viscous, frequently linear damping in cases of one- and two-dimensional friction. This means that dither smoothes dry friction. Figures 1 and 2 show plots of recorded displacements of the body of the experimental set-up with and without dither in case of one-dimensional friction.

It is evident that friction has the Coulomb characteristic. This is indicated by straight-line envelopes of displacements during runs without dither. With dither on, fitted exponential envelopes show that damping behaves like the viscous linear one.

To investigate the phenomenon theoretically a rheological model of dry friction has been proposed in the form of the element of the Prandtl body composed of the friction slider with the Coulomb characteristic (the de Saint Venant element) and

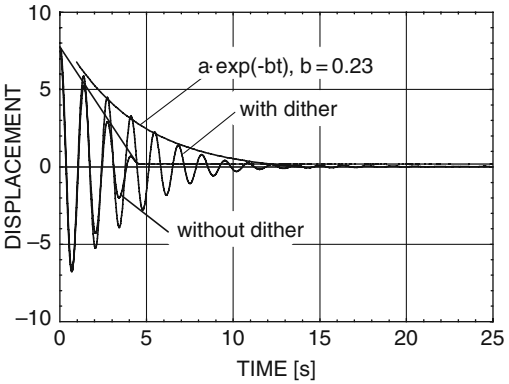

Fig. 1 Recorded displacements with and without dither. Dither perpendicular to the body velocity

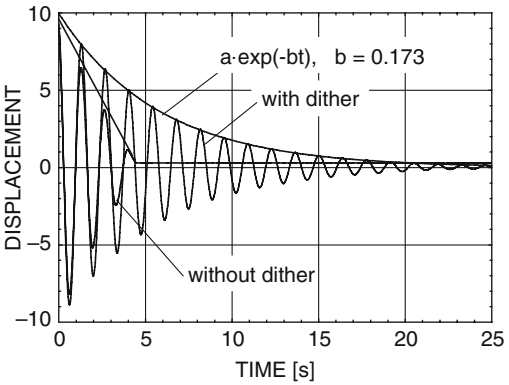

Fig. 2 Recorded displacements with and without dither. Dither and velocity of the body co-linear

the spring. The model is a non-smooth elastic element. The friction force has been described by the differential equation.

The model is applicable to one- and two-dimensional friction. In case of the two-dimensional friction the model takes into account friction anisotropy. The description involves the determination of the friction force direction angle for both the isotropic and anisotropic friction.

The model has been successfully verified experimentally in cases of one- and two-dimensional friction.

Figures 3 and 4 present measured and modeled trajectories of the body of the experimental set-up in a case of two-dimensional friction. They are similar.

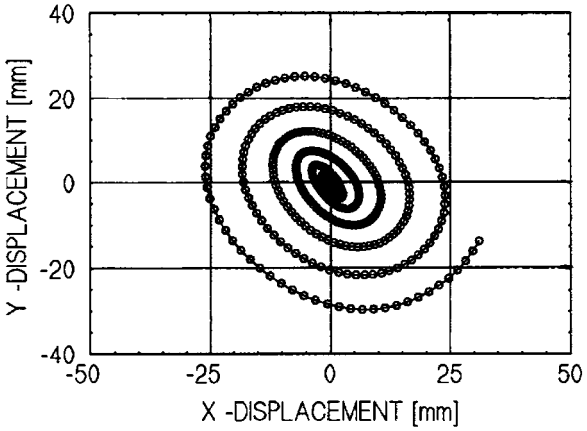

Fig. 3 Measured trajectory of the body with dither on

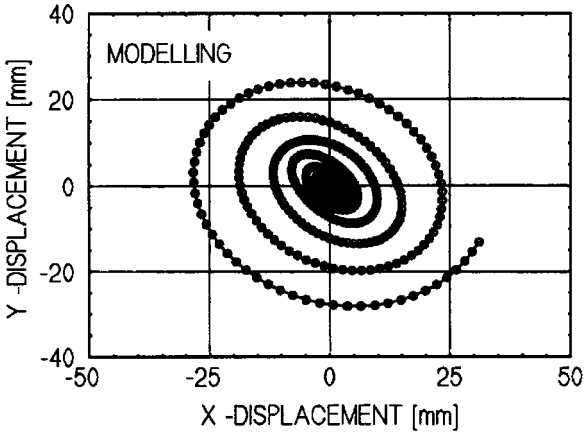

Fig. 4 Trajectory of the body with dither on obtained from modelling

Numerical simulations using the model have helped to explain the phenomenon of smoothing dry friction by dither. There are basically two mechanisms involved.

Numerical simulations have also indicated that in case of the sinusoidal dither the most important parameter influencing dry friction smoothing is the amplitude of dither velocity. With the higher amplitude the effect of smoothing is stronger in the sense that damping becomes lighter and of strictly linear characteristic.

2 Influence of M-F Dither on Dynamics of Freight Wagon

Smoothing dry friction by M-F dither influences lateral and vertical ride dynamics of freight wagons with friction dampers developing two-dimensional friction in the primary suspension.

A simulation model of a two-axle wagon with two-dimensional friction dampers in the primary suspension has been written. The model employs contemporary wheel-rail contact mechanics [1]. The description of friction damper employs the proposed model of friction mentioned in Sect. 1. The vehicle model is composed of rigid bodies and elastic elements but it takes into account M-F vertical dither generated by rolling contact. The excitation by M-F dither supplied to the model comes from measured vertical accelerations of axleboxes. The accelerations were recorded with the sampling frequency 1 kHz.

According to the results of numerical simulations of the wagon motion there may be significantly different behavior of the vehicle on theoretical, ideally smooth track (without dither) and on track with excitation by M-F dither. For example, on smooth track, speed 36 m/s and chosen parameters of the suspension the basic (rectilinear) motion is unstable and the vehicle soon reaches the limit cycle of self-excited lateral vibrations with contact angles of wheels and rails reaching 15° at extreme lateral displacements of wheelsets. Once the vehicle enters the section of track with irregularities resulting in M-F vertical dither the lateral vibrations die out, motion of the vehicle stabilizes and finally the vehicle runs with the rectilinear motion without any residual misalignments of wheelsets because sticking in dampers has been removed by dither. This is illustrated by plots in Figs. 5 and 6. The smooth section of track has the length of 140 m.

3 Conclusions

According to carried-out experiments, dry friction damping in the presence of M-F dither behaves like viscous, frequently linear damping in cases of one- and two-dimensional friction. This property has been also confirmed by numerical simulations employing proposed model of dry friction. This means that dither smoothes

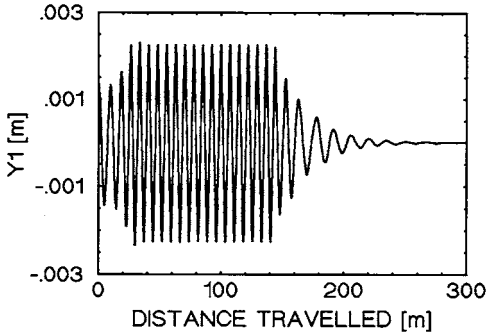

Fig. 5 Lateral displacement of leading wheelset

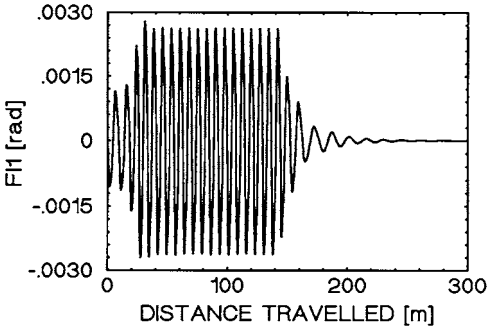

Fig. 6 Yaw angle of the leading wheelset

dry friction. In case of the sinusoidal dither the main parameter of dither that influences dry friction smoothing is the amplitude of dither velocity.

In case of rail freight wagon the dither generated by rolling contact of wheels and rails excites vertical sliding in friction dampers of the primary suspension. Smoothing dry friction by dither strongly influences ride dynamics of the wagon.

The overall conclusion referring to rail vehicles is that the influence of M-F dither should be accounted for in numerical simulations of motion of vehicles with friction dampers in the primary suspension by employing the proper model of the two-dimensional friction and application of realistic M-F dither generated by rolling contact. Otherwise some strange dynamic phenomena could occur in simulation of motion that may have little to do with reality.

As the M-F dither is available for free and has smoothing influence on friction the future work should concentrate on efficient exploitation of dither generated by rolling contact to improve ride quality and safety of rail vehicles with friction damping.

References

1. J. Piotrowski, W. Kik. A simplified model of wheel/rail contact mechanics for non-Hertzian problems and its application in rail vehicle dynamic simulations, *Vehicle System Dynamics*, 46, 1–2: 27–48, 2008.

Simulation of Gear Hammering With a Fully Elastic Model

Pascal Ziegler and Peter Eberhard

Abstract In large Diesel engines often geartrains are used to drive the camshafts. As the average transmitted load is small, dynamic loads, e.g. gas forces, are typically dominant. This can result in a rattling motion of teeth within the backlash, called gear hammering. We will show that for these impact-like contacts rigid body models are not sufficient, instead, elastic models are necessary to precisely simulate contact forces. The model proposed here is a modally reduced elastic multibody model including a contact algorithm. Due to the size of the modal transformation matrices, additional ways to reduce the computational effort are necessary, e.g. a dynamic reloading scheme. The model is robust and fast enough to allow simulations of many revolutions and many contacts. Furthermore, basic experiments have been carried out to validate the model. Experimental results are presented and agree very well with the simulations.

1 Introduction

The dynamic behaviour of geartrains in Diesel engines is very often accompanied by a rattling motion of teeth within the backlash, called gear hammering. It originates in a transmitted mean torque that is small compared to dynamic loads, for instance introduced by gas forces. Therefore, the flanks are likely to lift off and reestablish impact-like contacts on both sides of the flanks causing a hammering noise. As the main purpose of geartrains is to transmit motion rather than torque, the gears are often thin to reduce inertia and consequently the compliance of the gear bodies influences the contact behaviour significantly. In fact, detailed contact investigations of gears using transient finite element models reveal that the gear body compliance strongly influences the contact behaviour. Consequently, dynamic gear body effects may not be neglected for precise simulations of contact forces. However, it is industrial practise to use rigid body models to simulate these contacts, even though they

P. Ziegler (✉)
Institute of Engineering and Computational Mechanics, University of Stuttgart
Pfaffenwaldring 9, 70569 Stuttgart, Germany
e-mail: ziegler@itm.uni-stuttgart.de

P.G. Thomsen, H. True (eds.), *Non-smooth Problems in Vehicle Systems Dynamics*,
DOI 10.1007/978-3-642-01356-0_18,

have been developed for sliding contacts instead of impacts and for very rigid gear wheels. This is mainly due to the tremendous numerical effort needed for elastic models like finite element models.

Obviously, as rigid body models can not account for complex elastic effects on the one hand and finite element models can only be used for some few impacts on the other hand, there is a demand for a physically motivated fully elastic model with simulation times that allow simulations of many revolutions. The gear wheels are modelled as elastic bodies using a floating frame of reference. The elasticity is described using a modally reduced formulation. In combination with collision detection, this approach allows very precise investigations of contact problems. Moreover, since all necessary data are determined in preliminary analyses, the integration is numerically very efficient.

To validate this approach, basic experiments have been carried out. Test bodies of simple geometrical shape are used to impact teeth of real gears. Comparisons between experiments and simulation results uniformly show very good agreement. Therefore, this approach offers a validated and precise contact model that is numerically efficient enough to be incorporated into large overall engine models and has no need for any heuristic parameters.

2 Numerical Impact Investigations

For the numerical impact investigations, a gear pairing from a real geartrain is used to investigate several consecutive impacts. This is done using a classical rigid body model and a very detailed finite element model. The gear pair consists of a crankshaft gear and an idler gear and is mainly chosen here, because of the very compliable idler gear that has a very thin gear body with several axial holes, see Fig. 1 (left). Therefore, considerable dynamical effects can be expected. Both gears

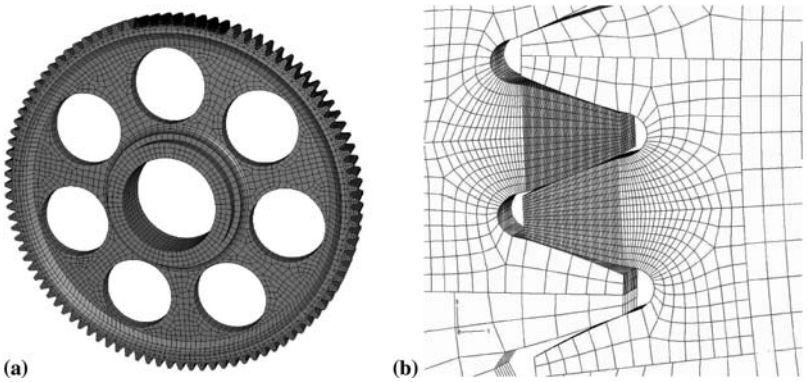

Fig. 1 Finite element mesh of the idler gear (*left*) and finer mesh in contact region with mesh transition (*right*)

have $z_c = z_i = 97$ teeth of modulus $m = 6\,\text{mm}$ and no profile shift. The face widths are $h_c = 57\,\text{mm}$ and $h_i = 50\,\text{mm}$, respectively. The gear wheels are made of steel, so a material with Young's modulus of $E = 210000\,\text{MPa}$, a density of $\rho = 7850\,\text{kg/m}^3$ and Poisson ration of $\nu = 0.3$ is used.

For the impact investigations, the gears are setup with a centre distance of $a = 582\,\text{mm}$ and supported by rotational joints with one rotational degree of freedom. The crank shaft gear is initially at rest, the idler gear is given an initial rotational velocity of $\omega_i = 100^\circ/\text{s}$. The gears are orientated in such a way that the first contact will occur in the pitch point.

Impact problems often show wave propagation phenomena with frequencies up to over 80 kHz. Therefore, the finite element model is meshed with hexahedral elements with a characteristic element length smaller than 8 mm. That allows to evaluate waves with frequencies up to about 80 kHz in the used material, see [10]. However, in the contact area, the elements are chosen much smaller. In the contact patch, which has an approximate size of 1 mm, an element size of 0.1 mm is used, see Fig. 1 (right). This results in a finite element model of about 80000 nodes and 65000 elements for each gear. For the contact formulation, the kinematic contact provided by ABAQUS is used, see [1]. The rotational joints are implemented by kinematically constraining all fit bore nodes to a reference point in the gear centre having one rotational degree of freedom. For the integration of the system an explicit integration scheme based on central differences is used, see [9].

Classical rigid body models of a gear pair typically consist of two rigid bodies with a rotational degree of freedom for each body. Both bodies are coupled by a linear spring damper combination acting on the base radii, see [3, 4]. The spring combines all elasticities in the gear pairing, the damper accounts for a possible oil film and material damping. Backlash can be accounted for by an additional backlash element. In this work the so called single stiffness c', see [8], is used for the coupling stiffness, as it is common in industrial practice. According to the German industry norm [6], method C, the single stiffness can be obtained using finite element models. For the investigated gear pair the static finite element analysis is carried out using the model described above. The single stiffness follows as $c' = 5.68\,\text{N}/\mu\text{m}/\text{mm}$, see [7]. Damping is neglected. The system is set up with the commercial multibody package SIMPACK, see [5]. For the integration a RADAU 5 scheme is used.

2.1 Simulation Results

The finite element model has been setup very carefully and the applied numerical methods have been verified to be appropriate. Therefore, the results from the finite element model can be regarded as being very precise. Consequently, they are used as a reference in the following. Figure 2 shows the contact forces, as well as the rotational velocity of the idler gear.

Obviously, the results for the contact forces differ significantly. The forces calculated with the rigid body model are generally too high which is mainly due to the elasticity of the idler gear. This can very well be seen for the first contact, where

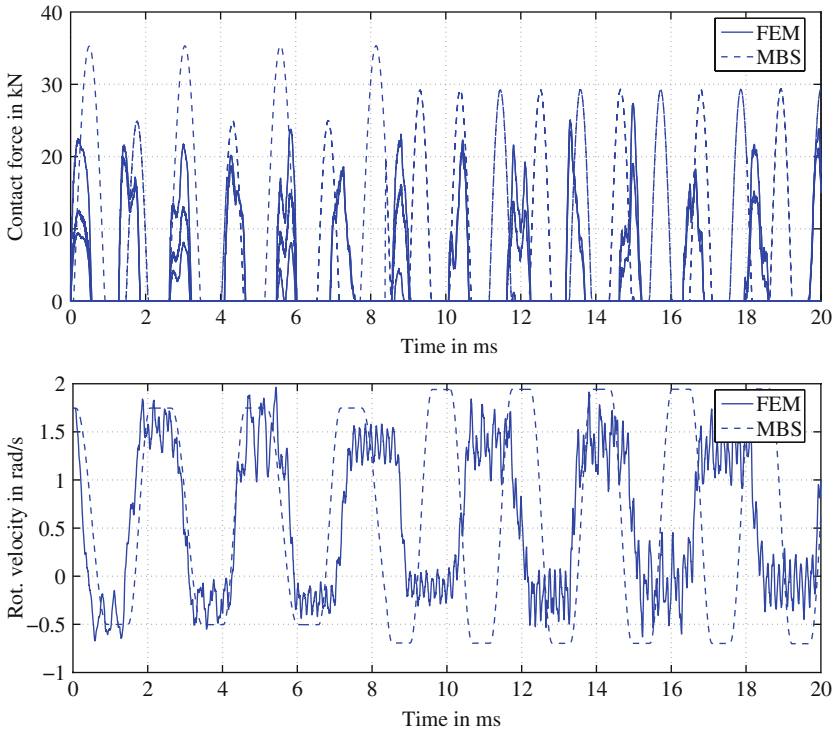

Fig. 2 Comparison of contact forces and rotational velocities of the idler gear for the finite element model and the rigid body model

the finite element solution shows three simultaneous contact forces. This means that three pairs of teeth are in contact at the same time, which cannot happen when rigid bodies are considered, hence, the rigid body model only gives one contact force. Another effect directly related to the elasticity of the gear can be observed for the third contact. Here, after an initial increase, the contact force temporarily decreases and eventually increases to its maximum. As shown in [11], this is due to a deformation of the gear body during contact. This deformation is partly radial and, therefore, the contact force decreases while energy is stored in the deformed body. When this energy is restored, an increase of the contact force is observed. The remaining deformation excites a torsional vibration of the tooth rim against the fit bore rim and can be observed from the rotational velocities, particularly in the free flight phases, where no contact occurs.

The elasticity of the gear wheel considerably influences the contact forces, but also the global motion. Apparently, the rigid body model gives bad results, even though the stiffness has been precalculated by a static finite element analysis. The simulation results show that this is primarily due to elastic effects. Therefore, in order to obtain precise results, an elastic approach is imperative. However, the simulation time for the finite element analysis presented in Fig. 2 is already about 8 days

on a Pentium 4 computer with 2Gbyte RAM. Obviously, finite element analyses are not appropriate to simulate many contacts or even several revolutions.

3 Elastic Multibody Model

One way to reduce the large system dimension of a finite element system and still use a fully elastic description is to use a modally reduced elastic multibody model. Here, a floating frame of reference formulation is used, see [12, 13], where the deformation is described with respect to a reference frame, which is allowed to undergo large rotations. Therefore, the large rotation for an appropriate operation of gear wheels can easily be described. The deformation can be considered to be small, and, therefore, allows a modal description. External driving torques can easily be applied via the reference frame. The equation of motion follows as

$$\begin{aligned} \boldsymbol{M}(\boldsymbol{y}) \cdot \ddot{\boldsymbol{y}} - \boldsymbol{h}_{\omega}(\boldsymbol{y}, \dot{\boldsymbol{y}}) - \boldsymbol{h}_{e}(\boldsymbol{y}, \dot{\boldsymbol{y}}) - \boldsymbol{h}_{c}(\boldsymbol{y}, \dot{\boldsymbol{y}}) = \\ \begin{bmatrix} \boldsymbol{M}_{tt} & & \text{sym} \\ \boldsymbol{M}_{rt} & \boldsymbol{M}_{rr} & \\ \boldsymbol{M}_{et} & \boldsymbol{M}_{er} & \boldsymbol{M}_{ee} \end{bmatrix} \cdot \begin{bmatrix} \ddot{\boldsymbol{y}}_t \\ \ddot{\boldsymbol{y}}_r \\ \ddot{\boldsymbol{y}}_e \end{bmatrix} - \begin{bmatrix} \boldsymbol{h}_{\omega t} \\ \boldsymbol{h}_{\omega r} \\ \boldsymbol{h}_{\omega e} \end{bmatrix} - \begin{bmatrix} \boldsymbol{0} \\ \boldsymbol{0} \\ \boldsymbol{h}_{e} \end{bmatrix} - \begin{bmatrix} \boldsymbol{h}_{ct} \\ \boldsymbol{h}_{cr} \\ \boldsymbol{h}_{ce} \end{bmatrix} = \boldsymbol{0}, \end{aligned} \tag{1}$$

where $\boldsymbol{M}$ is the mass matrix, $\boldsymbol{h}_{\omega}$ are the generalised inertia forces, $\boldsymbol{h}_{e}$ are the generalised internal forces, $\boldsymbol{y}_t$ and $\boldsymbol{y}_r$ are the generalised coordinates of the reference motion and $\boldsymbol{y}_e$ are the elastic coordinates. External forces and torques, including contact forces, are given by $\boldsymbol{h}_c$. For a modal model $\boldsymbol{y}_e$ are modal coordinates and $\boldsymbol{M}_{ee}$ is a diagonal matrix.

3.1 Calculation of Standard Data

To evaluate Eq. (1), several intermediate matrices, called standard data, are needed, see [13]. The standard data have to be precomputed before the simulation from the finite element system matrices and the modal matrix. For many calculations, the standard data evaluations are of type

$$\boldsymbol{A} = \boldsymbol{\Phi}^T \cdot \boldsymbol{B} \cdot \boldsymbol{\Phi}, \tag{2}$$

where $\boldsymbol{\Phi}$ is the modal matrix and $\boldsymbol{B}$ is the finite element mass or stiffness matrix. A reasonable finite element model, capable to describe all relevant mentioned effects, easily exceeds 80000 nodes per gear. Since a Guyan reduction in not appropriate, the matrices are of full size, though sparse. Moreover, as shown in [7], sufficiently precise contact forces able to represent impacts require modes with frequencies up to 80kHz. Consequently, the modal matrix is often of tremendous size and the calculation of standard data requires a huge amount of memory which makes most commercial converters fail. However, the memory request can be reduced, by an

out-of-core approach, which uses the linearity of Eq. (2) by solving it with partial modal matrices in consecutive steps and temporarily stores intermediate results on the harddisk.

3.2 Contact Algorithm

The maximum number of possible contacts for two gears with z_1 and z_2 number of teeth is $n_{c,max} = 2z_1z_2$. Since for geometrical reasons, typically only two or three pairs of teeth can come into contact at a given time, a contact algorithm that checks for all possible contacts is extremely inefficient. Therefore, the collision detection is divided in a coarse and a fine collision detection phase.

For the coarse collision detection, index points are defined on every tooth, see Fig. 3 (left). Only for those index points, a transformation from modal coordinates to nodal positions is carried out. Then, the index point nearest to the centre of the associated gear is determined. When these centre teeth are determined, z_s teeth to left and right of the centre tooth are considered as contact candidates, see Fig. 3 (right). Dependent on the geometry, typically $z_s = 1$ or $z_s = 2$ is sufficient.

For the fine collision detection and the calculation of the contact forces, a master-slave node-to-segment penalty approach is used. Therefore, the nodal coordinates of all flank nodes of the previously determined contact candidates are required. The necessary modal transformation matrices for each flank node on the contact candidates are combined in one transformation matrix. This comparably small transformation matrix can easily be kept in the computers main memory and only has to be updated when the contact situation changes. Therefore, when a change of the centre index teeth is determined, the new corresponding transformation data is dynamically updated. Keeping only this minimal transformation data in the computer's memory decreases both memory request and integration time.

Since only contacts between perfectly aligned spur gears are investigated here, the three dimensional contact situation is mapped to a two dimensional contact problem for the contact calculation. This is done by only considering the flank nodes in the mid-plane. This reduces the contact problem to a polygonal contact,

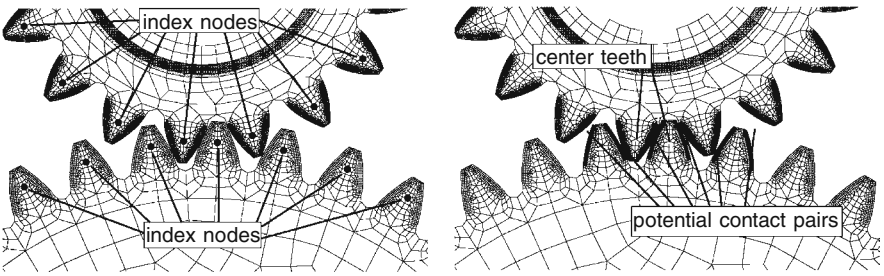

Fig. 3 Preselection of contact candidates using index nodes (*left*) on every tooth to determine potential contact pairs (*right*)

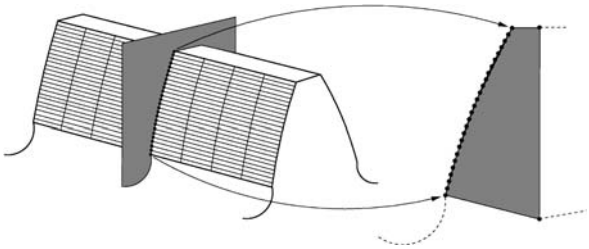

Fig. 4 Mapping the three dimensional contact problem to a two dimensional polygonal contact problem for perfectly aligned spur gears

see Fig. 4. The fine collision detection is done using the ray-crossing method, see [14]. In the case that a slave node has penetrated the master polygon, the node is projected onto the corresponding segment and the penetration depth δ is calculated. The nodal contact force immediately follows by multiplying the penetration with the penalty factor. This contact force is distributed equally to all nodes lying on the contact line intersecting this contact node.

3.3 Time Integration

For the integration of the elastic multibody system, a central differences method is used. Since the evaluation of the equation of motion (1) requires velocities in each time step, a discretization with a velocity lagging half a step is used as proposed in [15]

$$\dot{\boldsymbol{y}}_{n-1/2} = \frac{1}{\Delta t}\left(\boldsymbol{y}_n - \boldsymbol{y}_{n-1}\right), \tag{3}$$

$$\ddot{\boldsymbol{y}}_n = \frac{1}{\Delta t^2}\left(\boldsymbol{y}_{n+1} - 2\boldsymbol{y}_n + \boldsymbol{y}_{n-1}\right). \tag{4}$$

The new displacement $\boldsymbol{y}_{n+1}$ can eventually be obtained by

$$\boldsymbol{y}_{n+1} = \Delta t^2 \boldsymbol{M}^{-1} \cdot (\boldsymbol{h}_\omega + \boldsymbol{h}_e + \boldsymbol{h}_c) + 2\boldsymbol{y}_n - \boldsymbol{y}_{n-1}. \tag{5}$$

The central difference method is a conditionally stable integration scheme and the integration step size has to be smaller than a critical time step which can be calculated from the highest eigenfrequency of the system as $\Delta t_{crit} = 2/\omega_{max}$. The scheme in Eqs. (3) and (4) has linear convergence due to the discretization of the velocity lagging half a step.

In Eq. (5) the inverse of the mass matrix is needed. Since the mass matrix is state dependent, the inverse has to be calculated in every integration step. For a modal model with properly scaled eigenmodes, the sub-matrix $\boldsymbol{M}_{ee}$ in Eq. (1) is an identity matrix. This allows to use the structure of the mass matrix for an efficient calculation of the inverse, see [16],

$$\boldsymbol{M}^{-1} = \begin{bmatrix} \widetilde{\boldsymbol{M}} & \text{sym} \\ [\boldsymbol{M}_{et}\ \boldsymbol{M}_{er}] \cdot \widetilde{\boldsymbol{M}} & \boldsymbol{I} + [\boldsymbol{M}_{et}\ \boldsymbol{M}_{er}] \cdot \widetilde{\boldsymbol{M}} \cdot [\boldsymbol{M}_{et}\ \boldsymbol{M}_{er}]^T \end{bmatrix}, \tag{6}$$

with

$$\widetilde{\boldsymbol{M}} = \left(\begin{bmatrix} \boldsymbol{M}_{tt} & \boldsymbol{M}_{rt}^T \\ \boldsymbol{M}_{rt} & \boldsymbol{M}_{rr} \end{bmatrix} - \begin{bmatrix} \boldsymbol{M}_{et}\ \boldsymbol{M}_{er} \end{bmatrix}^T \cdot \begin{bmatrix} \boldsymbol{M}_{et}\ \boldsymbol{M}_{er} \end{bmatrix} \right)^{-1}. \tag{7}$$

The inverse of the mass matrix can now be calculated by only inverting the 6×6 matrix yielding $\widetilde{\boldsymbol{M}}$ and several matrix multiplications. This is not only much faster, but also much more precise than an iterative inversion of the full mass matrix.

3.4 Simulation Results

Figure 5 shows simulation results for the impact investigation presented in the beginning, using the finite element model and the elastic multibody model. The elastic multibody model is fully implemented in MATLAB, see [2], solely the fine collision

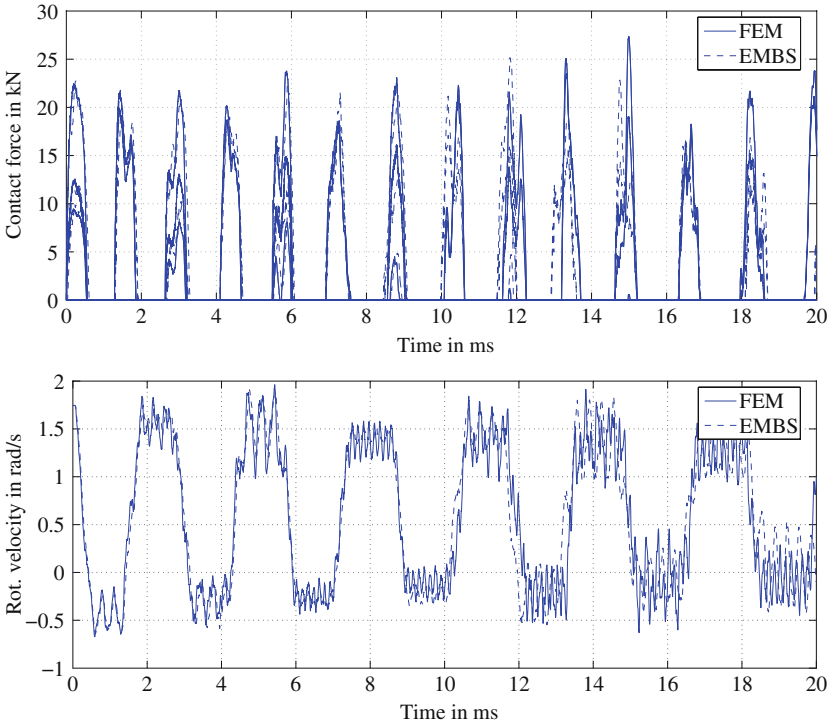

Fig. 5 Comparison of contact forces and rotational velocities of the idler gear for the finite element model, the rigid body model and the elastic multibody model

Table 1 Integration time and memory requirement for two gears and 13 impacts

Model	Pre-processing (h)	Int. time 13 impacts (s)	Disk requirement	Memory requirement
FEM	0	698400	≈ 1 GB	≈ 1 GB
MBS	0	5	$\ll 100$ MB	$\ll 100$ MB
EMBS	28	550	≈ 8 GB	≈ 500 MB

detection is implemented in C to increase performance. Apparently, the results from the elastic multibody model are very close to the finite element analysis. Unlike the rigid body model, the elastic multibody model shows very precise contact forces, both in time response and contact time. The three simultaneous contacts for the first contact agree exactly, as well as the vibration of the contact force due to the radial deformation. The results for the rotational velocity also show the torsional vibration. Clearly, the elastic model tremendously improves the accuracy of the simulation results.

To compare the numerical effort, the integration time and the memory request for the three presented models are summarised in Table 1. The rigid body model shows by far the smallest simulation times, but the simulation results differ significantly from the finite element results. The elastic multibody model is slower than the rigid model, but still about a factor of 1000 faster than the finite element model and gives very precise results, as shown above. The speed-up can mainly be explained by the pre-computed modal data. The calculation of the modal data is numerically expensive, however, it only has to be carried out once and, therefore, the elastic multibody model particularly pays off when investigating many contacts.

4 Experimental Impact Investigations

To validate the proposed elastic multibody model, basic experimental impact investigations have been carried out. For these investigations, a simple impact body with cuboid shape has been impacted on a gear. The gear used for the experimental investigations has $z = 18$ teeth of modulus $m = 4.9$ mm and a cylindrical gear body. To reduce the experimental complexity, we limited ourself to stationary gear wheels, which tremendously reduces the measurement setup, particularly the alignment of impact body and gear wheel.

To guarantee a very precise guidance of the impact cuboid, a guiding slide rail is used. To allow reproducible experimental conditions and negligible friction, the slide rail is supplied by pressured air that generates an air cushion upon which the cuboid hovers almost frictionless, see Fig. 6.

Furthermore, some air exhausts from the gap between cuboid and slide rail, producing a self-aligning effect. The slide rail is mounted on a precision rotary stage that allows to adjust the alignment angle β with a precision of less than $1/1000^\circ$. The rotary stage itself is mounted on a frame that allows to adjust the alignment angles α and γ, see Fig. 7 (left). The entire experimental setup is shown in Fig. 7 (right).

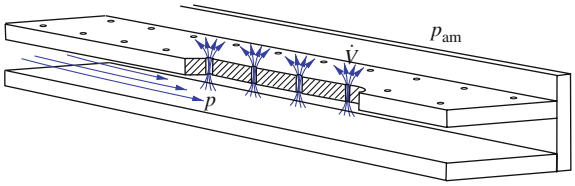

Fig. 6 Schematic drawing of the air supplied slide rail

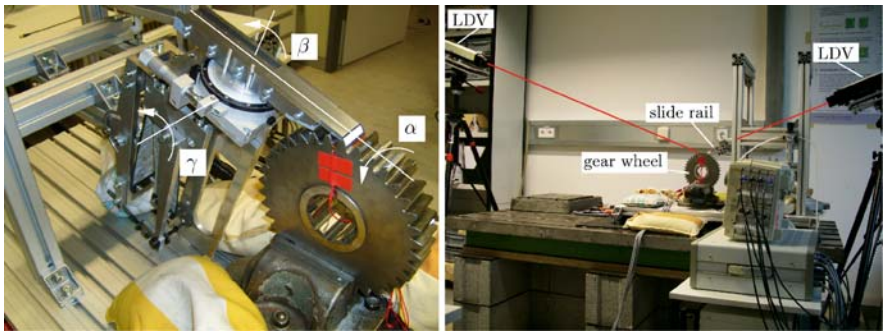

Fig. 7 Rotary stage and supporting frame for cuboid impact body (*left*) and overall experimental setup (*right*)

Generally, the direct measurement of contact forces is difficult. Therefore, flank velocities, as well as strains are measured in close vicinity to the contact area and compared to corresponding simulation results. To do so, Laser-Doppler vibrometers are used to measure the flank velocity on the back side of the impacted tooth and strain gauges are applied in the dedendum. Since the interesting frequency range is 80 kHz, DC amplifiers instead of carrier frequency amplifiers are used, to directly measure the mistune of the bridge.

Figure 8 shows the flank velocity measured in the middle of the rear flank and the cuboid velocity for one experiment together with the simulation results from

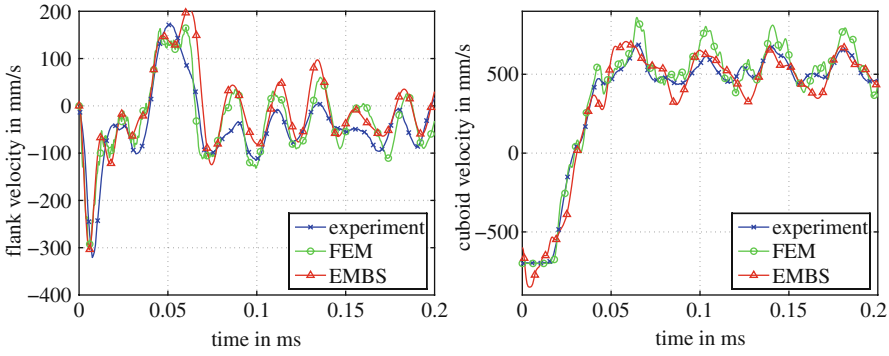

Fig. 8 Flank velocities in the middle of the rear flank (*left*) and cuboid velocity (*right*) for experiment, finite element model and elastic multibody model

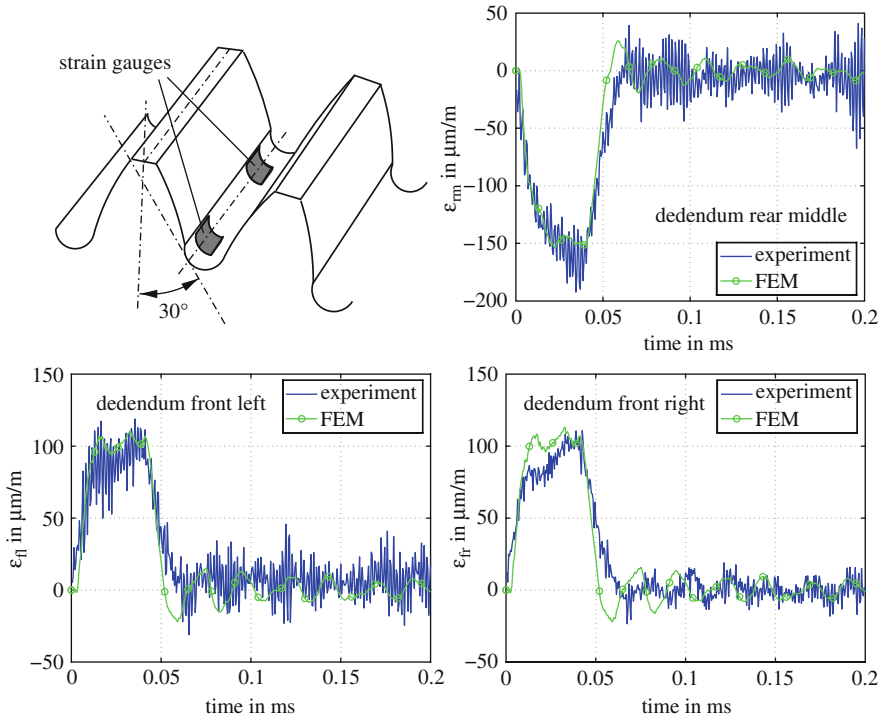

Fig. 9 Position of the strain gauges in the dedendum and strain signals for one impact for experiment and finite element model

the finite element model and the elastic multibody model. Apparently, the results agree very well.

The measured and simulated strains in the dedendum are shown in Fig. 9. The signal of the strain gauges turns out to be very noisy which is mainly due to the use of DC amplifiers. To reduce the noise ten measurements have been averaged. Here too, a good agreement between simulation and experiment can be observed.

Comparing the experimental results with simulations, apparently, the finite element model and the elastic multibody model give very good results. Both the surface velocities on different teeth, as well as strains in the dedendum can be calculated precisely and the good agreement between simulation and experiments even holds for a long time after the contact. For the basic impact conditions described above, the elastic multibody model can be regarded as validated.

5 Conclusions

Impacts between two gears of a real geartrain have been investigated using a classical rigid body model, a finite element model and an elastic multibody model. The results clearly show that for impacts on compliable bodies the elasticity has

to be considered using a fully elastic model. A rigid body model is not applicable when precise results, particularly precise contact forces, are required. To avoid the tremendous numerical effort needed to solve the full finite element model, a modally reduced elastic multibody model with contact was introduced. To reduce the memory request for storing the transformation data necessary for the contact calculation, a coarse collision detection including a dynamic reloading scheme was presented. In combination with an explicit integration scheme which exploits the structure of the mass matrix for its inversion, this elastic multibody model allows very precise simulations in very short time compared to the finite element solution. This approach can therefore be used to simulate many contacts and many rotations and is suitable for being incorporated into overall engine models. To validate the numerical models, basic experimental impact investigations have been carried out. In order to simplify the experimental setup, a stationary gear wheel was impacted with a cuboid impact body and flank velocities, and also strains in the dedendum have been measured. Comparing simulation and experiment, a very good agreement can be found.

Acknowledgments The project "Rädertriebsimulation" was supported by the Forschungsvereinigung Verbrennungskraftmaschinen (FVV) and the Forschungsvereinigung Antriebstechnik (FVA) from January 2005 until December 2008. This support is highly appreciated and further, we would like to thank all the industrial members of the "Arbeitskreis Rädertriebsimulation" for their contributions and ideas. This work has partially been presented in the final report of this project.

References

1. N.N.: SIMULA, ABAQUS v6.5, for contact information and informative literature see www.simula.com.
2. N.N.: The Mathworks, MATLAB 6.5, for contact information and informative literature see www.mathworks.com.
3. G.W. Blankenship, A. Kahraman: Steady State Forced Response of a Mechanical Oscillator with Combined Parametric Excitation and Clearance Type Non-Linearity. Journal of Sound and Vibration, Vol. 185(5), pp. 743–765, 1995.
4. F. Kücükay: Rheonichtlineare Zahnradschwingungen (in German). Journal of Applied Mathematics and Mechanics, Vol. 64, pp. T58–T61, 1984.
5. N.N.: INTEC GmbH, SIMPACK v8.8, for contact information and informative literature see www.simpack.de.
6. N.N.: DIN 3990, Tragfähigkeitsberechnung von Stirnrädern, Teil 1 (in German), Berlin: Beuth Verlag, 1987.
7. P. Ziegler, P. Eberhard, B. Schweizer: Simulation of Impacts in Geartrains Using Different Approaches, Archive of Applied Mechanics, Vol. 76 (9–10), pp. 537–548, 2006.
8. G. Niemann, H. Winter: Maschinenelemente – Band 2 (in German), Berlin: Springer Verlag, 1989.
9. K.J. Bathe: Finite Element Procedures, Upper Saddle River: Prentice Hall, 1996.
10. P. Ziegler, P. Eberhard, B. Schweizer: Impact Studies of Gears in Combustion Engines, in: P. Eberhard (Ed.), Proceedings of the IUTAM 2006-Multiscale Problems in Multibody System Contacts, Dordrecht: Springer, pp. 243–256, 2007.
11. P. Ziegler, P. Eberhard: Simulative and Experimental Investigation of Impacts on Gear Wheels. Computer Methods in Applied Mechanics and Engineering, Vol. 197 (51–52), pp. 4653–4662, 2008.

12. A. Shabana: Dynamics of Multibody Systems, Cambridge: Cambridge University Press, 2005.
13. R. Schwertassek, O. Wallrapp: Dynamik flexibler Mehrkörpersysteme (in German), Braunschweig: Vieweg, 1999.
14. J. O'Rourke: Computational Geometry in C, Cambridge: Cambridge University Press, 2nd edition, 1995.
15. R. Cook, D. Malkus, M. Plesha: Concepts and Applications of Finite Element Analysis, New York: John Wiley & Sons, 1989.
16. S. Hagg: Untersuchung von Zahnkontakten mit wanderndem Kontaktbereich (in German), STUD-266, Institute of Engineering and Computational Mechanics, University of Stuttgart, 2007.

Part III
Numerical Analysis of Non-smooth Problems

Discontinuities in ODEs: Systems with Change of State

Per Grove Thomsen

Abstract The occurrence of discontinuous right hand sides in ODE-systems often appears in technical applications. Such applications may be characterised by the cases where the system changes between several states. Each state is defined by a system of ODEs and the transition between states is defined by an algebraic condition. The numerical solution that is done in order to simulate the behaviour of the system will be possible by using standard numerical software but this approach is very ineffecient. We present an alternative approach based upon the tracking of state-changes and accurate numerical determination of transition points. Real applications from railway dynamics are used to illustrate the approach.

1 Systems with Changes of State

In many applications of numerical simulation the systems may change state. Such cases are found in the simulation of multibody dynamics and control systems, for example when a thermostat makes some part of the system cut in and off. This means in the mathematical model that the equations for the dynamic system are changing in a discontinuous way across a solution point [2].

The direct application of a numerical method for the solution of such a system will lead to unwanted growth of errors as well as a wasted extra computational effort. All in all this is an unwanted situation.

By applying modern continuous extensions in combination with the solution method we may derive a strategy for passing the discontinuity points without loss of accuracy and at a very minimal extra cost in computational effort.

P.G. Thomsen (✉)
Informatics and Mathematical Modelling, DTU, Lyngby, Denmark
e-mail: pgt@imm.dtu.dk

P.G. Thomsen, H. True (eds.), *Non-smooth Problems in Vehicle Systems Dynamics*,
DOI 10.1007/978-3-642-01356-0_19,

1.1 ODE's with Discontinuous Right Hand Sides

The dynamic system we will consider for illustration can be defined the following way

$$y' = f(t, y) \ , \ t \in [a, b] \ , \ y(a) = \eta \tag{1}$$

where the function $f(t, y)$ is given by

$$f(t, y) = \begin{cases} f_1(t, y) \text{ for } \phi(t, y) < 0 \\ f_2(t, y) \text{ for } \phi(t, y) \geq 0 \end{cases} \tag{2}$$

The functions $f_1(t, y)$ and $f_2(t, y)$ need not have the same value at the point where the solution crosses the curve $\phi(t, y) = 0$. This means that the solution will have a discontinuous derivative across this curve (see [6]). We illustrate the situation in the Fig. 1 below.

The existence and continuity of the solution is guaranteed under very modest assumptions for the differential system, we refer to [6] for the details. If we assume that $\phi(t, y)$ is analytic in t and y we will obtain that the curve $\phi(t, y)$ is differentiable with respect to both t and y and the solution to

$$y_1'(t) = f_1(t, y_1(t)) \ , \ y_1(a) = \eta \tag{3}$$

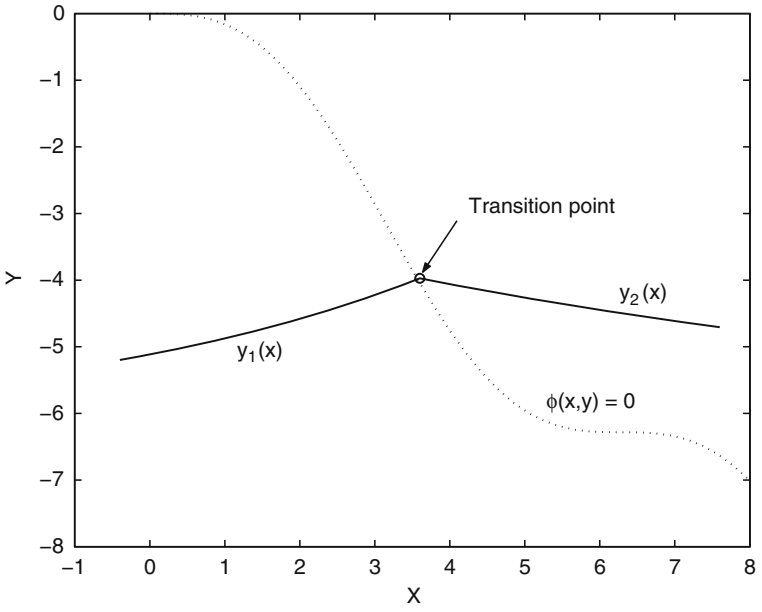

Fig. 1 Discontinuity across curve of state change

will cross the curve $\phi(t, y)$ at some point P defined by the condition

$$\phi(t_1, y_1(t_1)) = 0 \tag{4}$$

The differential equation (1) defines a new initial value problem that may be rewritten as

$$y_2'(t) = f_2(t, y_2(t)) \ , \ y_2(t_1) = y_1(t_1). \tag{5}$$

The solution to (1) can now be found as the solution to (3) in combination with the solution to (5) where the initial condition is determined by (4). The simple form of a discontinuous problem is found when we have a jump-discontinuity that satisfy the condition

$$\mid f_1(t, y) - f_2(t, y) \mid < C \tag{6}$$

We will consider in this report problems where this condition is assumed to be satisfied everywhere.

1.2 The Numerical Solution Across a Jump-Discontinuity

Following the idea from [3] we consider the problem specified in the previous section using either a one-step method like a Runge Kutta method or a multistep method. In the two domains specified by the regions where the function ϕ is either positive or negative the methods are solving IVP's in the usual manner and all we need to consider is the region close to the point where the solution crosses from one region to the other. The point P is called the transition point.

The case where multiple zeroes of the transition function inside the step may occur in practical situations but this is a special situation that must be dealt with by the actual implementation and will not be covered in this aper.

1.2.1 Multistep Methods

When solving the system (1) using a multistep method we consider for simplicity a constant stepsize defined by

$$y_n \approx y(t_n) \ , \ t_n = a + nh \ , \ h = t_{n+1} - t_n \ , \ n = 1, 2, \ldots, N. \tag{7}$$

We follow the treatise of multistep methods in [5] where the multistep method is defined as

$$\sum_{j=0}^{k} \alpha_j y_{n+j} = \sum_{j=0}^{k} \beta_j y'_{n+j} \tag{8}$$

The accuracy of the formula is found by looking at the local truncation error given by the linear difference operator

$$\mathbf{L}[y(t_n); h] = \sum_{j=0}^{k} (\alpha_j y(t_n + jh) - h\beta_j y'(t_n + jh)) \tag{9}$$

The assumption that $y(t)$ has continuous derivatives of sufficiently high order leads to the result that for a method of order p we find that

$$\mathbf{L}[y(t_n); h] = C_p h^{p+1} y^{(p+1)} + O(h^{p+2}) \tag{10}$$

This is the traditional result that leads to convergence when $p \geq 1$. Now consider the situation shown in the figure below where the step is across a transition point as illustrated in Fig. 2.

In this case we can derive the result for the truncation error by using Taylor expansions of the sum from (10) and we arrive to the result (after some derivation) using the conditions for order p that

$$\mathbf{L}[y(t_n); h] = h(1 - \delta - \beta_k)(y'(\xi^+) - y'(\xi^-)) + O(h^2) \tag{11}$$

According to the normal definition of order we conclude that in this case the order is $p = 0$ and the method is no longer convergent. We may simplify the expression for the local truncation error by using the bound from the jump-condition (6) and we obtain

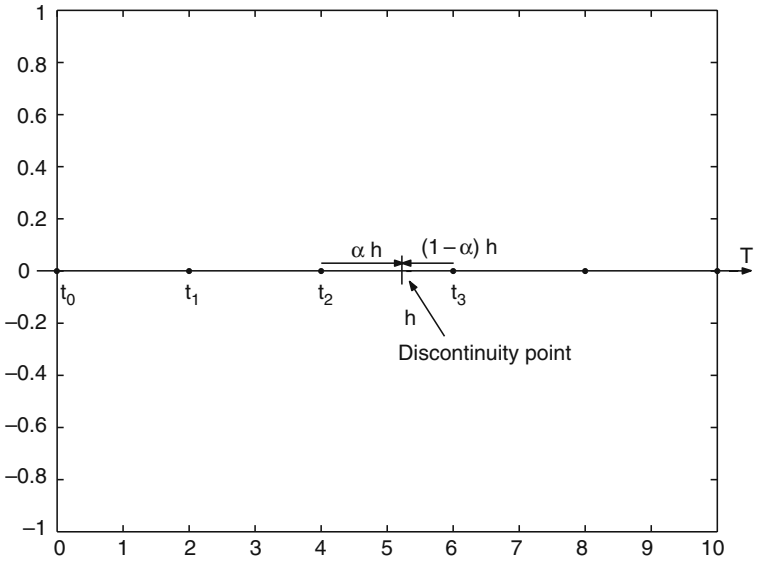

Fig. 2 Integrating across a point of state change

$$| \mathbf{L}[y(t_n); h] | \leq h \mid (1 - \delta - \beta_k) \mid C \tag{12}$$

Basically we obtain that the local truncation error is proportional to h and to the size of the jump in first derivative across the discontinuity.

For discontinuities in higher order derivatives we may use the same type of derivation to obtain the result that if the jump is in the q'th derivative and bounded like (6) we find

$$\mathbf{L}[y(t_n); h] \approx h^q \hat{C} \tag{13}$$

We see that in cases where $q < p + 1$ we may expect a decrease in the order observed. This result means that we will be able to predict the local behaviour of a given method across boundaries with discontinuities in derivatives of variable orders.

1.2.2 One-step Methods

The general form of a onestep method is the following

$$y_{n+1} = y_n + h\Phi(t_n, y_n; h) \tag{14}$$

Again assuming smoothness of all derivatives up to the order $p + 1$ will lead to a local truncation error of the form

$$T_{n+1} = \psi(t_n, y(t_n))h^{p+1} \tag{15}$$

The result of the analysis in the case with a discontinuity in the derivative will in this case lead to a similar result to the case with multistep methods and we find

$$T_{n+1} \approx \tilde{\psi}(t_n, \xi^+ - \xi^-)h \tag{16}$$

In the onestep case we find that the discontinuity may be in any of the mixed derivatives of the function $f(t, y)$ of orders lower than the order of the method. In principle though the two types of methods behave in a similar way. To get more details we refer to the reference [3].

Example 1. In order to give an example of how the behaviour of a standard solver is reflecting the results we have looked at the problem

$$y' = \begin{cases} y & for\ 0 \leq t \leq 1 \\ -y & for\ 1 < t \leq 2 \end{cases} \quad y(0) = 1\ ,\ t \in [0, 1] \tag{17}$$

The Fig. 3 shows that the automatic stepsize control will cut down the stepsize to the smallest allowable value because the error estimator becomes unreliable due to the fact that the error behaves like order zero instead of order p. If we assume the correct

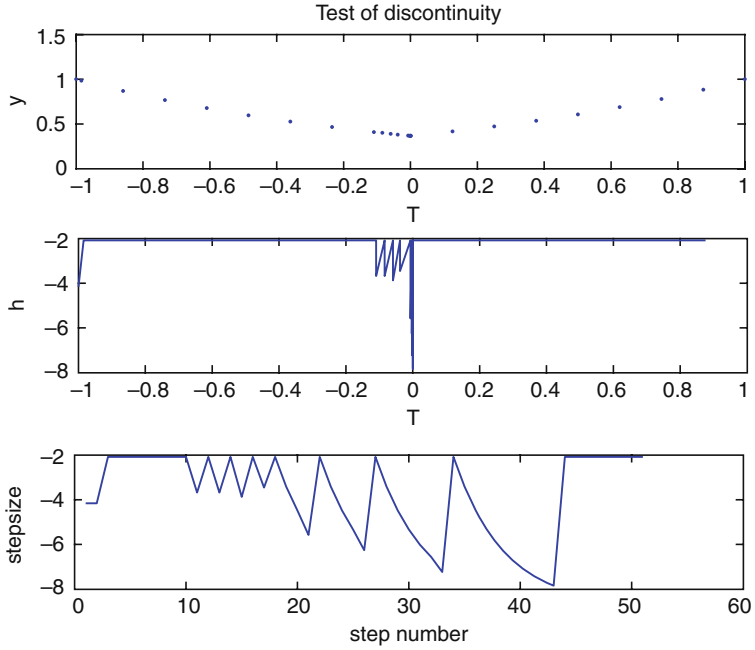

Fig. 3 Solution and stepsize history with a discontinuity

order of the method the error will be estimated to the actual stepsize times the size of the jump. For the example this would mean that the step should be of the order of 10^{-4} compared to the value 10^{-6} observed from the result. The driver wastes many unaccepted steps cutting down the stepsize before passing the transition point.

1.3 Continuous Extension

A traditional method for the solution of ODE's is basically finding the approximate solution on a discrete set of points, the discretization is defined by the stepsize control. The transition points wil however not in general be at one of these points. In order to develop a method for passing the transition point we need to be able to find an approximate solution in a continuous way. The tool for doing that is the continuous extension, developed for Runge Kutta methods ([7, 10]) and the general interpolant for multistep methods ([8]).

Example 2. **The Trapezoidal method with continuous extension.** As a simple example of an implicit method we illustrate the ideas by using the Trapezoidal method, in this case we use the GERK-formulation by giving the Butcher tableau of the method.

0	0	
1	$\frac{1}{2}$	$\frac{1}{2}$
y_{n+1}	$\frac{1}{2}$	$\frac{1}{2}$
$\tilde{y}_{n+1}(\theta)$	$\theta(1-\frac{\theta}{2})$	$\frac{\theta^2}{2}$

Coefficients for the trapezoidal-method with continued extension (Fig. 4).

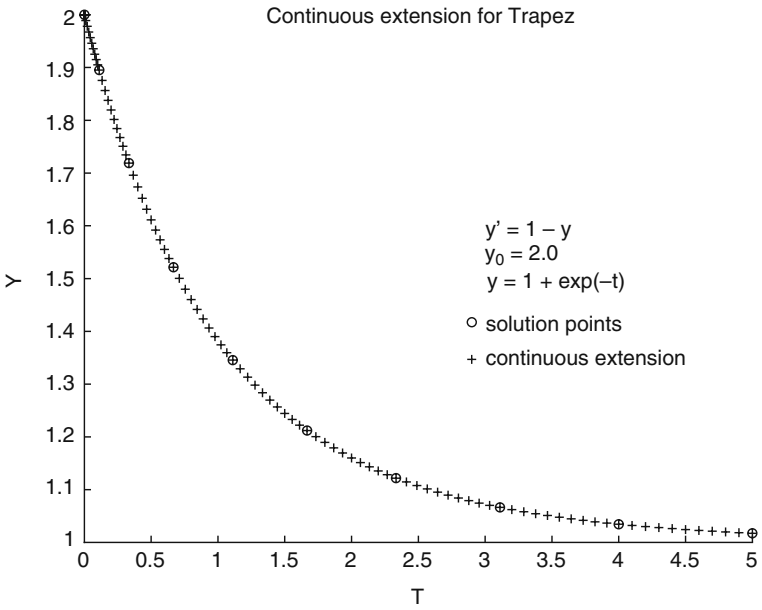

Fig. 4 Solution and continuous extension

It is customary to use θ as the parameter for defining the interpolation point. This point will in connection with the discontinuity be defined by the position of the transition point. We wish to determine this point and the condition for this is the function $\phi(t, y)$ being zero.

$$\phi(t, y(\theta)) = 0\ ,\ 0 \leq \theta \leq 1. \tag{18}$$

This equation is a normal condition for a zero of the function with θ as the variable. Any convenient zero-finding method may be used for determining the solution, if $\phi(t, y)$ is a smooth function the most efficient method will be based on a Newton-Raphson method. This assumes that derivatives of the functions are available. In the

following example we treat a system which passes a level, like in an application where a thermostat reaches a set-point. The system is the following.

$$y' = 1 - y,\ \ y(0) = 2,\ \ y(t) = 1 + \exp(-t) \tag{19}$$

The set-point is defined by the condition,

$$\phi(t, y) = y - 1.5 = 0. \tag{20}$$

The solution is shown in the Fig. 5 and the transition point is marked. We have applied a constant stepsize to get to the setpoint and then the value θ is found from the equation that is derived from (4) leading to the equation.

$$y_n - 1.5 - h\left(\frac{\theta^2}{2}(f_{n+1} - f_n) + \theta f_n\right) \quad = \quad 0$$
$$\theta = 0.084\ t = 0.6931\ .$$

The stepsize strategy here is very different from the one leading to the results in Fig. (5) and no steps are wasted for the approach to the transition point. The solution may be restarted using the transition point as the initial value for a solution in the new state.

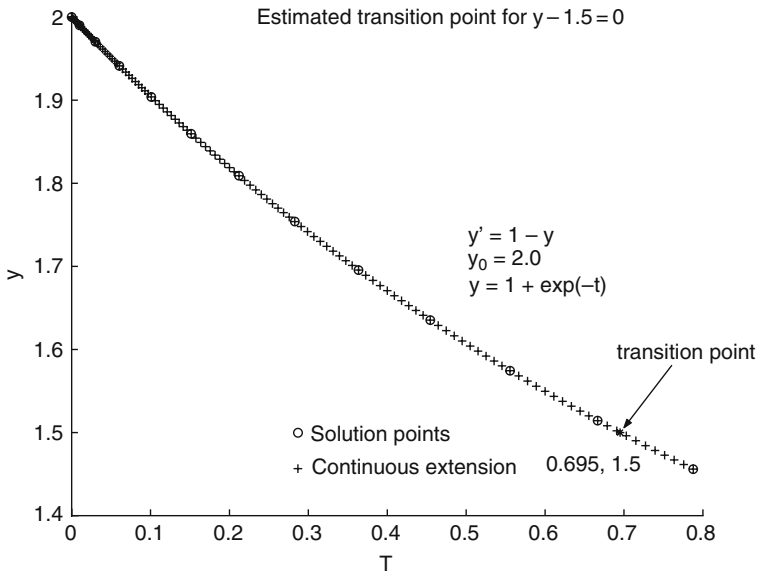

Fig. 5 Solution and determination of a transition point

1.4 Implementations

The example in the previous section has shown that a quite general strategy may be applied to change from state to state if we apply the conditions (18) in connection with the continuous extension a discussion is found in [9]. This is straightforward in the scalar case with only one active condition as in the example. In the general case where we may have a system of ODE's and where change of state may happen between several states and guided by a number of conditions, the implementation must be done very carefully to give satisfactory performance.

In the DALI [1] a matrix of conditions are kept, rows representing the active states and columns containing the conditions for passing to another state. Thus $\phi_{i,j}(t, y)$ changing sign will mean that the system in state i will change to state j. Not all states are reachable from all other states and we define a state-transition matrix containing "ones" where a change is possible and "zeros" where there is no possible state transition. The Fig. 6 shows the situation for a system illustrated by a state diagram and the corresponding state transition matrix. The example is from a simulation of a glider in the starting process over a free flight to landing, the transition is one-way following the numbering of the states assuming that the landing leads back to the original state of start.

$$\begin{pmatrix} 0\,1\,0\,0\,0 \\ 0\,0\,1\,0\,0 \\ 0\,0\,0\,1\,0 \\ 0\,0\,0\,1\,0 \\ 1\,0\,0\,0\,0 \end{pmatrix} \tag{21}$$

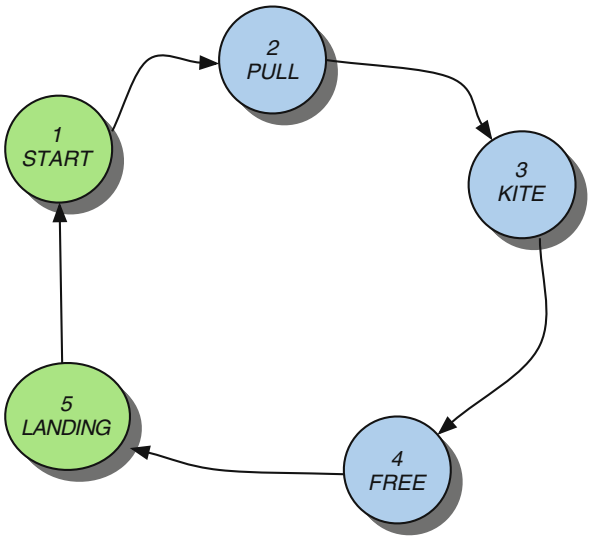

Fig. 6 State transition diagram and matrix

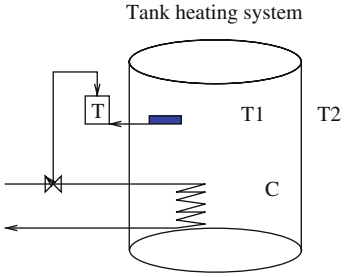

Fig. 7 The tank with heater and thermostat

Example 3. **Tank-heater example.** We consider the simulation of a tank heated to a given temperature and controlled by thermostats to keep its temperature between given bounds. The system is shown in the Fig. 7 below. The states of the system can be identified quite easily and the state diagram is shown in Fig. (8). When carrying out the simulation the model will change state using the continuous extension for determining the transitions between states and the solution will look like shown here (Fig. 9).

Example 4. **Dynamics of a wheelset.** We illustrate the dynamics of a wheel-axle system used on a train wagon. The system is shown in the Fig. 10 below where the wheel axle set is travelling along a set of tracks.

The nonlinear equations of motion for the lateral displacement and the yaw angle are as follows

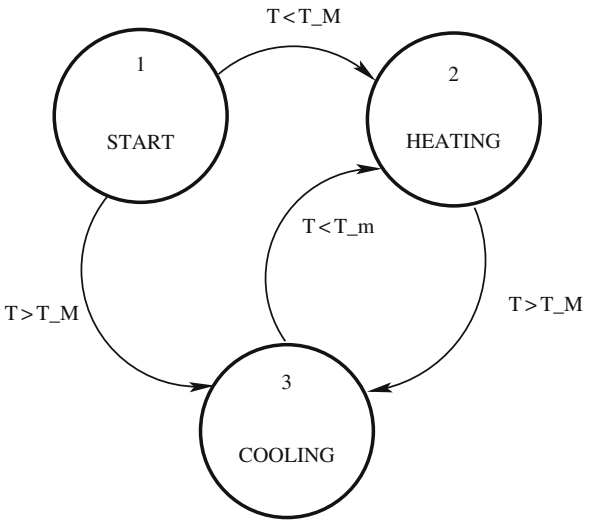

Fig. 8 State diagram for the tank-heater

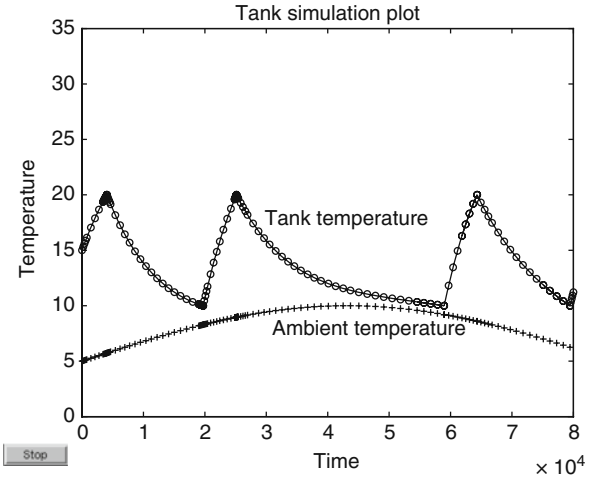

Fig. 9 Simulation of the tank-heater

$$m\ddot{y} + \frac{2f_{11}}{V}(\dot{y} - V\psi) + \frac{2f_{12}}{V}\dot{\psi} - \frac{2f_{12}}{r_o}\Delta_2(y) + W_A\Delta_L(y) + k_y y + c_y\dot{y} = F_y(t)$$

$$I_\omega\ddot{\psi} + \frac{2a^2}{V}f_{33}\dot{\psi} + \frac{2af_{33}}{r_o}(\frac{r_L - r_R}{2}) + \frac{2f_{22}}{V}\dot{\psi} - \frac{2f_{12}}{V}(\dot{y} - V\psi)$$
$$-\frac{2f_{22}}{r_o}\Delta_1(y) - a\psi W_A\delta_o + k_\psi\psi + c_\psi\dot{\psi} = F_\psi(t)$$

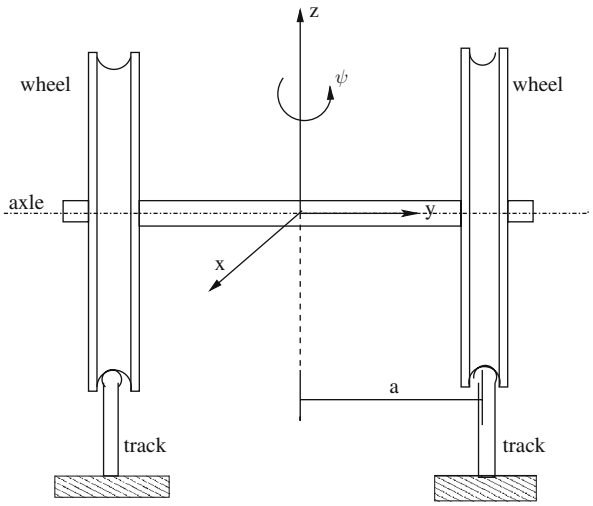

Fig. 10 The wheel axle arrangement

Table 1 Physical parameter values

Name	Value	Physical meaning	Unit
m	30	Mass of wheel-axle set	$lbsec^2/in$
I_ω	16500	Yaw moment of inertia	$lbinsec^2$
a	30	Half distance between contact points on two rails	in
r_o	20	Wheel radius	in
f_{11}	3.6e6	Longitudinal creep coefficient	lb
f_{12}	0.46e6	Lateral/spin creep coefficient	$inlb$
f_{22}	66000	Spin creep coefficient	lb
f_{33}	3.9e6	Lateral creep coefficient	lb
W_A	66000	Axle load	lb
k_y	5000	Lateral stiffness	lb/in
c_y	100	Lateral damping	$lbsec/in$
k_ψ	187200000	Yaw stiffness	$lbinsec/rad$
c_ψ	31200	Yaw damping	$lbinsec/rad$
V	15056	Axle speed	in/sec
δ_o	0.05	Initial taper angle	$\circ$
$F_y(t)$	see fig	Lateral input force	lb
$F_\psi(t)$	0	Yaw input moment	

The values of the different physical parameters are as shown in the Table 1 above. The variation with lateral displacement of the difference in the rolling radii of the wheel-axle set is shown below (Fig. 11 and Table 2).

For different entries we have the following values of the constants c_1 and c_2.

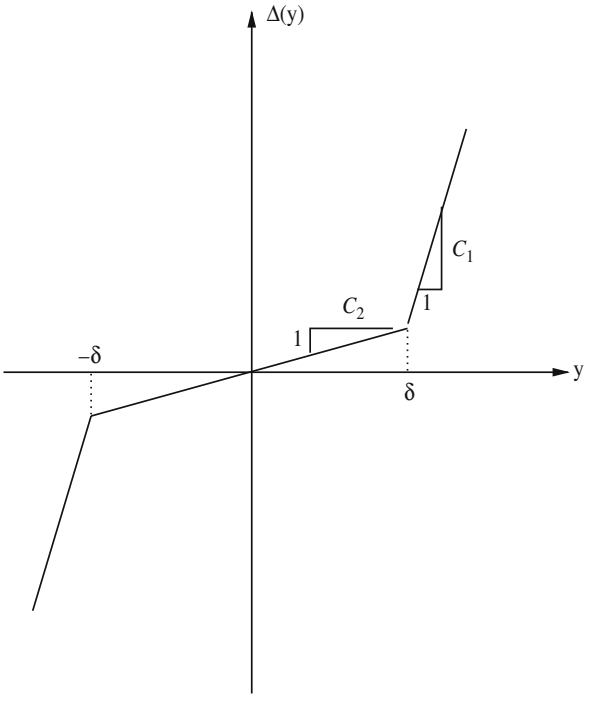

Fig. 11 The variation of different variables with lateral displacements

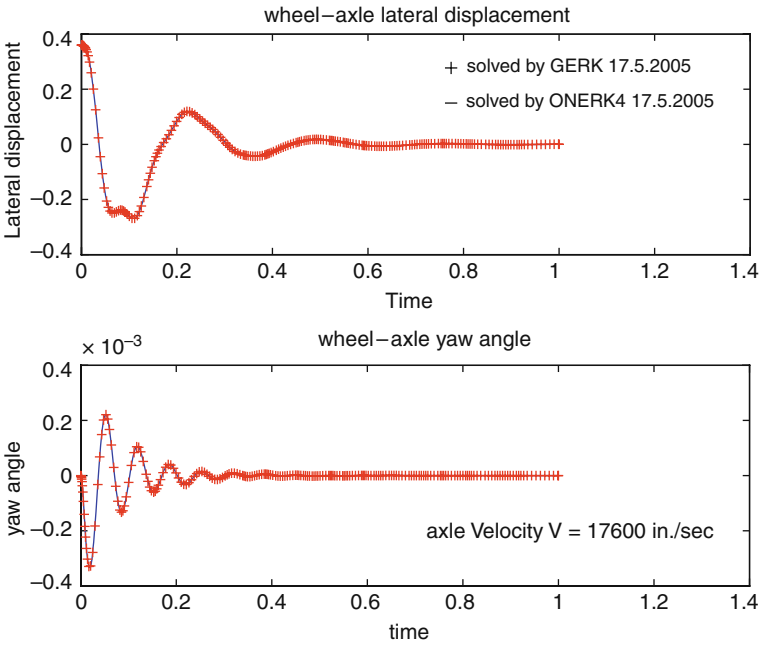

Fig. 12 Wheel-axle dynamics solution for V = 100 mph

In order to illustrate the importance of the determination of the discontinuities accurately we carry out the solution first by a constant but relatively small stepsize and then by a variable stepsize implementation where the discontinuities are determined. The two solutions are then compared (Fig. 12).

Solving the problem for an initial lateral displacement $y = 0.36$ with a velocity of 100 miles/h leads to the solution above where the damping is strong and only one passage of the discontinuity occurs. Here the solution with constant stepsize is called ONERK4 and the solution that tracks down the discontinuity called GERK are very close. Increasing the velocity to near instability where more passages of discontinuities occur show very different solutions and the constant stepsize solution is much less accurate than the one where the discontinuities are tracked as seen from Fig. 13. This leads to very different interpretations of the dynamic properties. Of cause this is critical since this case is near the point where instability is occurring. From the example with the wheel-axle system we see, that in regions where the damping is small the determination of transition points is very important in order

Table 2 Lateral discontinuities

var	c_1	c_2
Δ_1	0	18
Δ_2	0	18
Δ_L	0.15	22
$\frac{r_L - r_R}{2}$	0.005	10

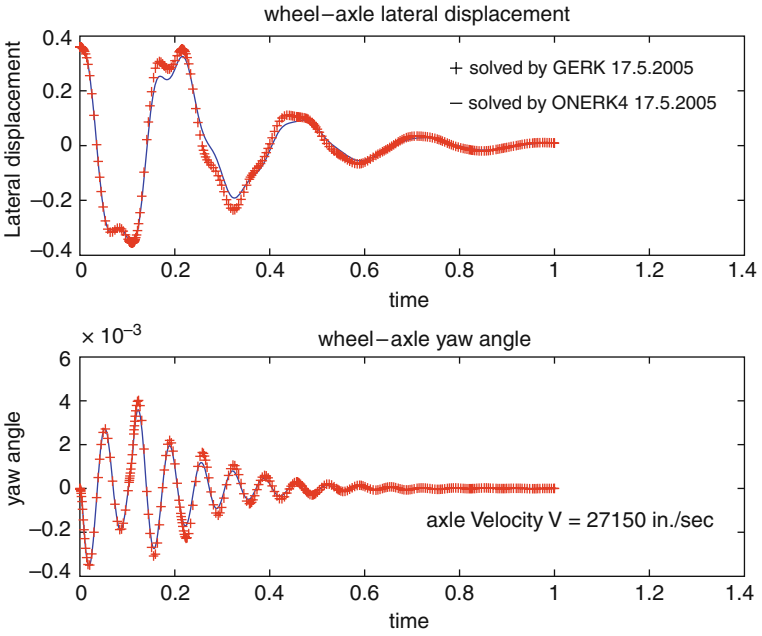

Fig. 13 Wheel-axle solution for V = 154 mph

for the solution to reflect the true dynamic properties of the system. If not treated properly the interpretation of the dynamic properties from the numerical results may be very different from the true system properties. Applying the continuous extension is an efficient way of determining the transition points and the technique may be implemented at almost no extra computational cost.

For further examples of applying the strategies is found in [4] where a full investigation of the dynamic properties of a two-axle freight wagon has been carried out.

2 Conclusion

In the application of numerical methods for the integration of dynamic systems from practical applications the presence of discontinuities are shown to give rise to large local errors across discontinuity points. This may lead to inefficient solution processes when stepsize control is based upon estimation of the local error. Implementing a state – space model will be a good tool to make sure the accuracy of the solution is sufficient and at the same time improving the efficiency of the computational process.

The examples used for illustration have verified that in critical areas of the solution the use of a continuous extension to the numerical integration method will be robust and give reliable solutions. Careful analysis of dynamic systems are

dependent on accurate numerical results to be reliable and great care should be given to the choice of method and implementation when carrying out this kind of work.

References

1. K.F. Askjær. Dali, en differential-algebraisk ligningsløser. thesis, 1986.
2. C. Bendtsen and P. G. Thomsen. Numerical solution of differential algebraic equations. 1998.
3. C.W. Gear and O. Østerby. Solving ordinary differential equations with discontinuities. *ACM Trans. Math. Softw.*, 10(1):23–44, 1984.
4. M. Hoffmann. *Dynamics of European two-axle freight wagons.* PhD thesis, Danish Technical University, Informatics and Mathematical Modelling., 2006.
5. J.D. Lambert. *Computational Methods in Ordinary Differential Equations*. J. Wiley & sons, 1972.
6. R. Mannshardt. One step methods of any order for ode's with discontinuous right hand sides. *Numerische Mathematik*, 31(1), 1978.
7. S.P. Nørsett and P.G. Thomsen. Imbedded sdirk-methods of basic order three. *BIT*, 24:634–646, 1984.
8. S.P. Nørsett, W.A. Enright, K.R. Jackson and P.G. Thomsen. Interpolants for Runge-Kutta formulas. *ACM TOMS*, 12(3):193–218, 1986.
9. S.P. Nørsett, W.A. Enright, K.R. Jackson and P.G. Thomsen. Effective solution of discontinuous ivp's using a runge kutta formula pair with interpolants. *Appl. Math. Comput*., 27: 313–335, 1988.
10. B. Owren and M. Zennaro. Derivation of efficient continuous explicit runge-kutta methods. *SIAM J. Sci. Stat. Comput.*, 13: 1488–1501, 1992.

Towards Improved Error Estimates for Higher Order Time Integration of ODEs with Non-Smooth Right Hand Side

Martin Arnold

Abstract The classical convergence analysis of higher order ODE time integration methods is based on rather strong smoothness assumptions on the right hand side that are typically not satisfied in technical applications since spline approximations of input functions and look-up tables result in frequent discontinuities in derivatives of the right hand side. Practical experience shows, however, that nevertheless the resulting non-smooth model equations may often be solved efficiently by higher order ODE time integration methods. For one typical problem class, the present paper gives a theoretical explanation of this behaviour. The results of the theoretical analysis are illustrated by a series of numerical tests for the simplified model of an agricultural device that moves along a track being defined by the spline approximation of a periodic smooth input function.

1 Introduction

In nonlinear system dynamics, the mathematical-physical modelling results typically in a nonlinear ordinary differential equation (ODE)

$$\dot{\boldsymbol{x}}(t) = \boldsymbol{f}(\boldsymbol{x}(t), \boldsymbol{u}(t)), \quad (t \in [t_0, t_e]), \quad \boldsymbol{x}(t_0) = \boldsymbol{x}_0 \tag{1}$$

with a right hand side $\boldsymbol{f}$ that may be strongly influenced by system inputs $\boldsymbol{u}(t)$.

The efficient and numerically stable time integration of initial value problems (1) is a classical topic of numerical mathematics. Several well developed classes of time integration methods for ODEs (1) are available [1–3]. They typically proceed in time steps $t_n \to t_{n+1} = t_n + h_n$ of stepsize h_n from the initial state $\boldsymbol{x}_0$ at $t = t_0$ to the end time t_e.

M. Arnold (✉)
NWF III – Institute of Mathematics, Martin Luther University Halle-Wittenberg, D-06099 Halle (Saale), Germany
e-mail: martin.arnold@mathematik.uni-halle.de

P.G. Thomsen, H. True (eds.), *Non-smooth Problems in Vehicle Systems Dynamics*,
DOI 10.1007/978-3-642-01356-0_20,

For ODEs (1) with smooth right hand side $\boldsymbol{f}$, higher order time integration methods like explicit Runge-Kutta methods or BDF offer an optimal compromise between numerical effort per time step and accuracy of simulation results [1, 3]. They compute a numerical solution $(\boldsymbol{x}_n)_{n=1}^N$ with $\boldsymbol{x}_n \approx \boldsymbol{x}(t_n)$, $(n = 1, \ldots, N)$ and $t_N = t_\mathrm{e}$ that has a *global error*

$$\epsilon := \max_{1 \le n \le N} \|\boldsymbol{x}_n - \boldsymbol{x}(t_n)\| = \mathcal{O}(h^p) \quad \text{with} \quad h := \max_{1 \le n \le N} h_n \tag{2}$$

and $p \ge 1$ denoting the *order* of the method. The classical convergence analysis of p-th order ODE time integration methods supposes that the right hand side $\boldsymbol{f}$ and the input functions $\boldsymbol{u}$ in (1) are (at least) p times continuously differentiable on $[t_0, t_\mathrm{e}]$, see [1, 2]. If this strong smoothness assumption is violated and $\boldsymbol{f}$ and $\boldsymbol{u}$ are only $r < p$ times continuously differentiable, the standard error estimates give only a bound

$$\epsilon := \max_{1 \le n \le N} \|\boldsymbol{x}_n - \boldsymbol{x}(t_n)\| = \mathcal{O}(h^r) \tag{3}$$

for the global error ϵ that is substantially larger than (2) if linear ($r = 0$) or cubic ($r = 2$) spline interpolation of input functions $\boldsymbol{u}$ is used in (1) and the (classical) order of the method is $p > 2$.

Practical experience suggests that error bound (3) is too pessimistic if the discontinuities in derivatives of the right hand side result from linear or cubic spline interpolation of smooth input data $\boldsymbol{u}(t)$. In the present paper, this practical observation is examined in detail combining an improved theoretical convergence analysis (Sect. 2) and numerical tests for a benchmark problem from vehicle system dynamics (Sect. 3).

2 Improved Error Estimates

Spline approximation of smooth system inputs. Throughout the present paper we consider the approximation of a scalar smooth system input $u(t) \in C^\infty[t_0, t_\mathrm{e}]$ in (1) by spline functions $s_\Delta(t)$ that interpolate $u(t)$ at the spline grid

$$\{\, \tau_i \,:\, \tau_i = t_0 + i\,\Delta,\ (i = 0, 1, \ldots, N_\Delta)\,\}$$

of mesh width $\Delta := (t_\mathrm{e} - t_0)/N_\Delta$:

$$s_\Delta(\tau_i) = u(\tau_i)\,, \quad (i = 0, 1, \ldots, N_\Delta)\,.$$

To simplify notation, we restrict ourselves to equidistant spline grids but the analysis may be carried over straightforwardly to the non-equidistant case.

From the practical viewpoint, linear and cubic splines $s_\Delta(t)$ are the most important ones resulting in $s_\Delta \in C^r[t_0, t_\mathrm{e}]$ with $r = 0$ in the linear case and $r = 2$ for cubic splines and

$$s_\Delta\big|_{[\tau_i,\tau_{i+1}]} \in C^\infty[\tau_i, \tau_{i+1}], \quad (i = 0, 1, \ldots, N_\Delta - 1).$$

Substituting the scalar system input $u(t)$ in (1) by the interpolating spline $s_\Delta(t)$, we end up with an ODE initial value problem

$$\dot{\boldsymbol{x}}(t) = \boldsymbol{f}(\boldsymbol{x}(t), s_\Delta(t)), \quad (t \in [t_0, t_e]), \quad \boldsymbol{x}(t_0) = \boldsymbol{x}_0 \tag{4}$$

that has a right hand side that is (at most) r times continuously differentiable w.r.t. $\boldsymbol{x}$ and t.

Restricted number of time steps that are affected by the discontinuities. The first important observation is that the number of discontinuities in (t_0, t_e) is bounded by the number $N_\Delta - 1$ of internal grid points in the spline grid. Since N_Δ is independent of the stepsizes h_n in time integration, the asymptotic error analysis for $h = \max_n h_n \to 0$ may be splitted into $N_\Delta - 1$ time steps that may contain a discontinuity and the remaining $N - (N_\Delta - 1)$ time steps that are not affected by the discontinuities of s_Δ at $\{\tau_i : i = 0, 1, \ldots, N_\Delta\}$. A similar observation is known from the convergence analysis of time integration methods for delay differential equations [4].

Extending the classical analysis of error propagation in ODE time integration [1, 2], the improved global error bound

$$\epsilon := \max_{1 \le n \le N} \|\boldsymbol{x}_n - \boldsymbol{x}(t_n)\| \le C(h^p + N_\Delta h^{r+1}), \quad (h \to 0)$$

with a constant $C > 0$ being independent of h is proved straightforwardly, see also (2) and (3).

Piecewise linear interpolating splines. To keep notation compact, we restrict ourselves in the following to fixed stepsize one-step methods

$$\boldsymbol{x}_{n+1} = \boldsymbol{x}_n + h\boldsymbol{\Phi}(t_n, \boldsymbol{x}_n; h, \boldsymbol{f}, s_\Delta), \quad (n = 0, 1, \ldots, \ldots, N - 1) \tag{5}$$

and suppose furthermore $h < \Delta$. The increment function $\boldsymbol{\Phi}$ in (5) may represent (explicit or implicit) Runge-Kutta methods as well as linearly implicit and other methods [2]. The most simple example of (5) is the explicit Euler method

$$\boldsymbol{x}_{n+1} = \boldsymbol{x}_n + h\boldsymbol{f}(\boldsymbol{x}_n, s_\Delta(t_n))$$

with $\boldsymbol{\Phi}(t_n, \boldsymbol{x}_n; h, \boldsymbol{f}, s_\Delta) := \boldsymbol{f}(\boldsymbol{x}_n, s_\Delta(t_n))$.

In a critical time step $t_n \to t_{n+1} = t_n + h$ with $t_n < \tau_i < t_{n+1}$ for some τ_i with $i \in \{1, \ldots, N_\Delta - 1\}$, the right hand side of (4) is only r times continuously differentiable w.r.t. t and the local error of a p-th order method is not bounded by $\mathcal{O}(h^{p+1})$ like in the classical theory [1, 2] but only by $\mathcal{O}(h^{\tilde{p}+1})$ with $\tilde{p} := \min\{p, r\}$.

Let us study the local error in more detail for a piecewise linear interpolation $s_\Delta \in C[t_0, t_e]$ of a smooth scalar system input $u(t)$. Because of $h < \Delta$ and $\tau_i \in (t_n, t_{n+1})$, we have for $t \in [t_n, t_{n+1}]$

$$s_\Delta(t) := \begin{cases} s_\Delta^{(-)}(t) \text{ if } t \le \tau_i \,, \\ s_\Delta^{(+)}(t) \text{ if } t \ge \tau_i \end{cases}$$

with smooth functions

$$s_\Delta^{(-)}(t) := u(\tau_i) + \frac{t-\tau_i}{\Delta}(u(\tau_i) - u(\tau_{i-1}))\,, \tag{6a}$$

$$s_\Delta^{(+)}(t) := u(\tau_i) + \frac{t-\tau_i}{\Delta}(u(\tau_{i+1}) - u(\tau_i)) \tag{6b}$$

interpolating $u(t)$ at $t = \tau_{i-1}$, $t = \tau_i$ and at $t = \tau_i$, $t = \tau_{i+1}$, respectively. With Taylor expansion of $u(\tau_{i-1})$ and $u(\tau_{i+1})$ at $t = \tau_i$, we get from (6)

$$s_\Delta^{(-)}(t) = u(\tau_i) + \dot{u}(\tau_i)(t-\tau_i) - \frac{\Delta}{2}\ddot{u}(\tau_i - \vartheta^{(-)}\Delta)(t-\tau_i)\,, \tag{7a}$$

$$s_\Delta^{(+)}(t) = u(\tau_i) + \dot{u}(\tau_i)(t-\tau_i) + \frac{\Delta}{2}\ddot{u}(\tau_i + \vartheta^{(+)}\Delta)(t-\tau_i) \tag{7b}$$

with some $\vartheta^{(-)}, \vartheta^{(+)} \in (0, 1)$. Therefore, both $s_\Delta^{(-)}$ and $s_\Delta^{(+)}$ are in a tube of radius $\mathcal{O}(\Delta h)$ around s_Δ for all $t \in [t_n, t_{n+1}]$. Because of this property, we consider in $[t_n, t_{n+1}]$ the formal substitution of the piecewise linear function $s_\Delta \in C^0[t_0, t_e]$ by a smooth transition from $s_\Delta^{(-)}$ to $s_\Delta^{(+)}$:

$$\tilde{s}_\Delta^{(n)}(t) := \frac{t-t_n}{h}s_\Delta^{(+)}(t) + \frac{t_{n+1}-t}{h}s_\Delta^{(-)}(t) \;\in C^\infty[t_n, t_{n+1}]\,.$$

From

$$\tilde{s}_\Delta^{(n)}(t) - s_\Delta(t) = \frac{t-t_n}{h}(s_\Delta^{(+)}(t) - s_\Delta(t)) + \frac{t_{n+1}-t}{h}(s_\Delta^{(-)}(t) - s_\Delta(t))$$

and (7) we get

$$\begin{aligned} &\max_{t\in[t_n,t_{n+1}]} |\tilde{s}_\Delta^{(n)}(t) - s_\Delta(t)| \le \\ &\qquad \le \max_{t\in[t_n,t_{n+1}]} |s_\Delta^{(+)}(t) - s_\Delta(t)| + \max_{t\in[t_n,t_{n+1}]} |s_\Delta^{(-)}(t) - s_\Delta(t)| \le C^{(n)}\Delta h \end{aligned} \tag{8}$$

with some constant $C^{(n)} \ge 0$ being independent of Δ and h.

Local error analysis based on a locally defined smoothed problem. For the analysis of the local error in time step $t_n \to t_{n+1} = t_n + h$ we introduce a locally defined smoothed initial value problem

$$\dot{\tilde{\boldsymbol{x}}}^{(n)}(t) = \boldsymbol{f}(\tilde{\boldsymbol{x}}^{(n)}(t), \tilde{s}_{\Delta}^{(n)}(t)), \quad (t \in [t_n, t_{n+1}]), \quad \tilde{\boldsymbol{x}}^{(n)}(t_n) = \boldsymbol{x}(t_n), \tag{9}$$

that has a solution $\tilde{\boldsymbol{x}}^{(n)}(t)$ close to $\boldsymbol{x}(t)$ provided that $\Delta \ll 1$ and $\boldsymbol{f}$ is Lipschitz continuous w.r.t. $\boldsymbol{x}$ and s_{Δ}, see, e.g., [5]:

$$\begin{aligned}\tilde{\boldsymbol{x}}^{(n)}(t) - \boldsymbol{x}(t) &\le \tilde{C}_1 \mathrm{e}^{\tilde{L}(t-t_n)} \max_{t\in[t_n,t_{n+1}]} |\tilde{s}_{\Delta}^{(n)}(t) - s_{\Delta}(t)| \\ &\le \tilde{C}_2 (t - t_n) \cdot C^{(n)} \Delta h \le \tilde{C}^{(n)} \Delta h^2, \quad (t \in [t_n, t_{n+1}])\end{aligned} \tag{10}$$

with constants $\tilde{C}^{(n)}$, $\tilde{C}_1$, $\tilde{C}_2$, $\tilde{L}$ being independent of Δ and h.

In contrast to the original ODE (4), the locally defined smoothed ODE (9) is not affected by any discontinuities in $[t_n, t_{n+1}]$ and the formal application of one step method (5) with stepsize h to (9) is not affected by any order reduction. With

$$\tilde{\boldsymbol{x}}_{n+1} = \boldsymbol{x}_n + h\boldsymbol{\Phi}(t_n, \boldsymbol{x}_n; h, \boldsymbol{f}, \tilde{s}_{\Delta}^{(n)}), \tag{11}$$

the local error of time step $t_n \to t_{n+1}$ satisfies the classical error estimate

$$\tilde{\boldsymbol{x}}^{(n)}(t_n) + h\boldsymbol{\Phi}(t_n, \tilde{\boldsymbol{x}}^{(n)}(t_n); h, \boldsymbol{f}, \tilde{s}_{\Delta}^{(n)}) - \tilde{\boldsymbol{x}}^{(n)}(t_{n+1}) = \mathcal{O}(h^{p+1}), \tag{12}$$

see [1, 2]. With (10), (12), $\tilde{\boldsymbol{x}}^{(n)}(t_n) = \boldsymbol{x}(t_n)$ and a Lipschitz condition for the increment function $\boldsymbol{\Phi}$:

$$\begin{aligned}\|\boldsymbol{\Phi}(t_n, \boldsymbol{x}(t_n); h, \boldsymbol{f}, \tilde{s}_{\Delta}^{(n)}) - \boldsymbol{\Phi}(t_n, \boldsymbol{x}(t_n); h, \boldsymbol{f}, s_{\Delta})\| &\le L_{\Phi} \max_{t\in[t_n,t_{n+1}]} |\tilde{s}_{\Delta}^{(n)}(t) - s_{\Delta}(t)| \\ &\le L_{\Phi} C^{(n)} \Delta h,\end{aligned}$$

the local error

$$\boldsymbol{x}(t_n) + h\boldsymbol{\Phi}(t_n, \boldsymbol{x}(t_n); h, \boldsymbol{f}, s_{\Delta}) - \boldsymbol{x}(t_{n+1})$$

of one step method (5) applied to the original problem (4) is bounded by

$$\begin{aligned}&\|\boldsymbol{x}(t_n) + h\boldsymbol{\Phi}(t_n, \boldsymbol{x}(t_n); h, \boldsymbol{f}, s_{\Delta}) - \boldsymbol{x}(t_{n+1})\| \le \\ &\quad \le \|\tilde{\boldsymbol{x}}^{(n)}(t_n) + h\boldsymbol{\Phi}(t_n, \tilde{\boldsymbol{x}}^{(n)}(t_n); h, \boldsymbol{f}, \tilde{s}_{\Delta}^{(n)}) - \tilde{\boldsymbol{x}}^{(n)}(t_{n+1})\| + \\ &\quad + h\|\boldsymbol{\Phi}(t_n, \boldsymbol{x}(t_n); h, \boldsymbol{f}, s_{\Delta}) - \boldsymbol{\Phi}(t_n, \boldsymbol{x}(t_n); h, \boldsymbol{f}, \tilde{s}_{\Delta}^{(n)})\| + \\ &\quad + \|\tilde{\boldsymbol{x}}^{(n)}(t_{n+1}) - \boldsymbol{x}(t_{n+1})\| \\ &\quad \le \mathcal{O}(h^{p+1}) + L_{\Phi} C^{(n)} \Delta h^2 + \tilde{C}^{(n)} \Delta h^2 = \mathcal{O}(h^{p+1}) + \mathcal{O}(\Delta h^2).\end{aligned} \tag{13}$$

Note, that the additional error term $\mathcal{O}(\Delta h^2)$ results from the missing differentiability of s_{Δ} at $\tau_i \in (t_n, t_{n+1})$. In all time steps $t_n \to t_{n+1} = t_n + h$ with $[t_n, t_{n+1}] \subseteq [\tau_i, \tau_{i+1}]$ for some $i \in \{0, 1, \ldots, N_{\Delta} - 1\}$ the spline input function s_{Δ} is smooth and the classical bound for the local error is obtained instead of (13):

$$\|\boldsymbol{x}(t_n) + h\boldsymbol{\Phi}(t_n, \boldsymbol{x}(t_n); h, \boldsymbol{f}, s_{\Delta}) - \boldsymbol{x}(t_{n+1})\| = \mathcal{O}(h^{p+1}). \tag{14}$$

Error propagation and bounds for the global error. Summarizing the error bound (13) for at most $N_\Delta - 1$ time steps $t_n \to t_{n+1}$ and the error bound (14) for the remaining $\leq N$ time steps $t_n \to t_{n+1}$, the bound

$$\epsilon = \max_{1 \leq n \leq N} \|\boldsymbol{x}_n - \boldsymbol{x}(t_n)\| \leq C(h^p + N_\Delta \cdot \Delta h^2) \tag{15}$$

with some constant $C \geq 0$ being independent of Δ and h is proved following line by line the classical error propagation analysis for one step methods, see, e.g., Sect. II.3 of [2].

Since $\Delta = (t_\mathrm{e} - t_0)/N_\Delta$, error bound (15) may be simplified to

$$\epsilon = \max_{1 \leq n \leq N} \|\boldsymbol{x}_n - \boldsymbol{x}(t_n)\| \leq \mathcal{O}(h^p) + \mathcal{O}(h^2) = \mathcal{O}(h^{\tilde{p}}) \tag{16}$$

with $\tilde{p} := \min\{p, 2\} = \min\{p, r+2\}$.

By the refined error analysis, the bound for the global error ϵ was improved by a factor of h^2, see (3). The same improvement is possible in the case of cubic splines s_Δ since s_Δ and its derivatives converge for $\Delta \to 0$ uniformly to u and its derivatives if $u \in C^4[t_0, t_\mathrm{e}]$, see, e.g., [6]. In the case of interpolating cubic splines s_Δ, the global error is bounded by $\epsilon = \mathcal{O}(h^{\tilde{p}})$ with $\tilde{p} := \min\{p, r+2\} = \min\{p, 4\}$ instead of the classical result $\tilde{p} := \min\{p, r\} = \min\{p, 2\}$ from (3).

3 Numerical tests

In the present section, the results of the theoretical analysis of Sect. 2 are verified by numerical tests for the equations of motion of a two mass system that models essential dynamic effects of an agricultural device [7]. A similar model was used in a recent applied project to test control strategies and to calibrate controller parameters for a device that moves along a rough track and should keep at the same time a long horizontal bar as close as possible to its optimal horizontal position, see Fig. 1.

The device is excited by two tyre forces acting at the lower left corner ($f_{\mathrm{T},l}$) and at the lower right corner ($f_{\mathrm{T},r}$) of the central body in Fig. 1. The tyres are modelled by linear spring-damper elements connecting central body and track.

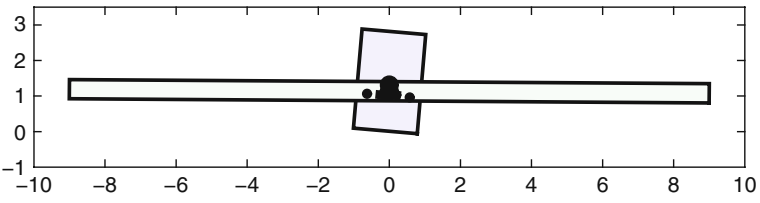

Fig. 1 Two mass model of an agricultural device [7]

In the applied project, they follow a track that is defined pointwise by measured data [8].

For the numerical tests, a smooth track without irregularities is used resulting in an ODE model (1) with smooth inputs $\boldsymbol{u}(t) = (\, u_l(t), u_r(t)\,)^\top \in \mathbb{R}^2$ for undamped tyre forces and $\boldsymbol{u}(t) = (\, u_l(t), \dot{u}_l(t), u_r(t), \dot{u}_r(t)\,)^\top \in \mathbb{R}^4$ in the damped case. Figure 2 shows a typical solution of (1) for harmonic inputs

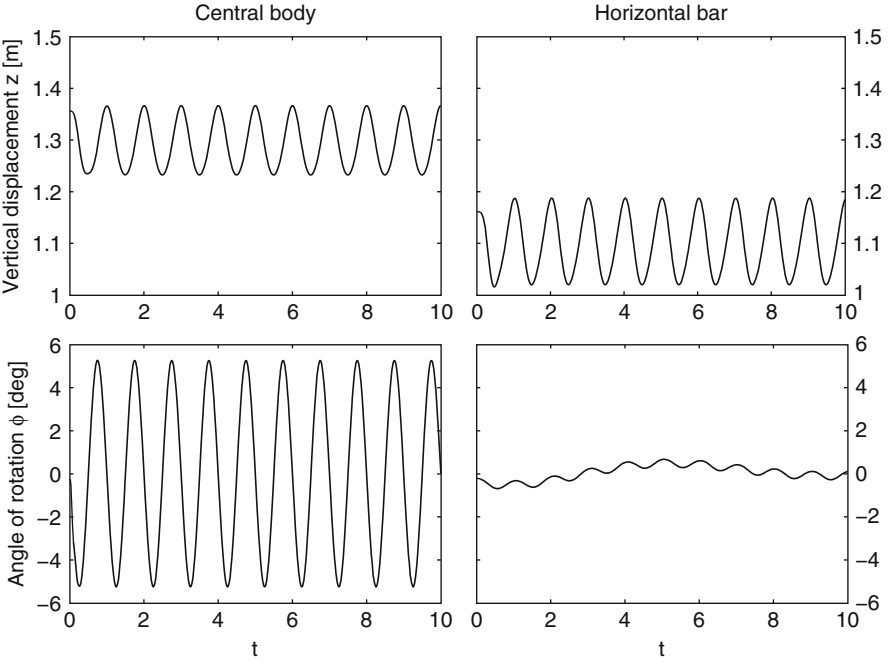

Fig. 2 Two mass model: Solution for a harmonic excitation with $\omega = 2\pi f$ and $f = 1.0\,\mathrm{Hz}$

$$u_{l,r}(t) = u_{\max} \sin(\omega t + \varphi_{l,r})$$

with

$$u_{\max} = 0.1\,\mathrm{m},\ \omega = 2\pi f,\ \ f = 1.0\,\mathrm{Hz},\ \varphi_l = 0.4,\ \varphi_r = 0.1.$$

With this fairly simple test problem, the influence of spline approximations and look-up tables on the convergence behaviour of higher order time integration methods may nicely be illustrated. Substituting $u_l(t)$, $u_r(t)$ by splines $s_{\Delta,l}(t)$, $s_{\Delta,r}(t)$, four test scenarios may be studied combining undamped tyre forces $(s_{\Delta,l}, s_{\Delta,r})$ and damped tyre forces $(s_{\Delta,l}, \dot{s}_{\Delta,l}, s_{\Delta,r}, \dot{s}_{\Delta,r})$ for cubic and for linear interpolating splines $s_{\Delta,l}(t)$, $s_{\Delta,r}(t)$, respectively. Classical and improved error estimates are summarized in Table 1.

In the first four numerical tests, the 5th order explicit Runge-Kutta method of Dormand and Prince [9] is applied with fixed time stepsize h to ODEs (4). If the tyre force model includes damping, the right hand side of (4) does not only depend

Table 1 Simulation scenarios in the numerical tests of Figs. 3 – 6.

Scenario	Spline s_Δ	Damping	Smoothness	Error bound (3)	Error bound (16)
1	cubic	no	$r = 2$	$\mathcal{O}(h^2)$	$\mathcal{O}(h^p) + \mathcal{O}(h^4)$
2	cubic	yes	$r = 1$	$\mathcal{O}(h)$	$\mathcal{O}(h^p) + \mathcal{O}(h^3)$
3	linear	no	$r = 0$	?	$\mathcal{O}(h^p) + \mathcal{O}(h^2)$
4	linear	yes	$r = -1$	?	$\mathcal{O}(h^p) + \mathcal{O}(h)$

on the interpolating spline s_Δ itself but also on its derivative $\dot{s}_\Delta$ with $\dot{s}_\Delta \in C[t_0, t_e]$ for cubic splines s_Δ and piecewise constant $\dot{s}_\Delta$ in the case of linear splines.

The diagrams of Figs. 3 – 6 show in double logarithmic scale global error ϵ vs. time stepsize h for a spline grid of mesh width $\Delta = 0.01$ (dashed line) and $\Delta = 0.005$ (dotted line). In all four figures, the global error ϵ of the explicit Runge–Kutta method applied to (4) does not increase for decreasing Δ. This observation is in perfect agreement with the improved error bound (16) that is independent of the number N_Δ of grid points τ_i.

For small time stepsizes h, the additional error term $\mathcal{O}(h^{r+2})$ that results from the discontinuities in derivatives of the spline functions s_Δ dominates the global error ϵ. In Figs. 3 – 6, this error term is indicated by straight lines of slope $r + 2$. For linear splines s_Δ, this error term dominates over the whole stepsize range of interest. For cubic splines s_Δ, the classical global error term $\mathcal{O}(h^5)$ of the 5th order method is dominant for stepsizes $h \geq 1.0\,\text{ms}$. In the undamped case, the additional lower order error term $\mathcal{O}(h^{r+2}) = \mathcal{O}(h^4)$ is even completely negligible, see Fig. 3.

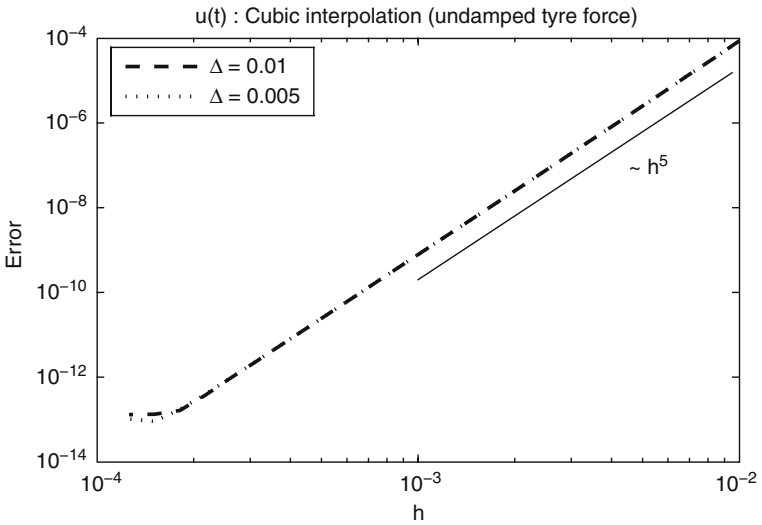

Fig. 3 Global error of 5th order method of Dormand and Prince applied to (4), cubic splines s_Δ, no damping, $r = 2$. Improved error bound (16): $\epsilon = \mathcal{O}(h^5) + \mathcal{O}(h^4)$

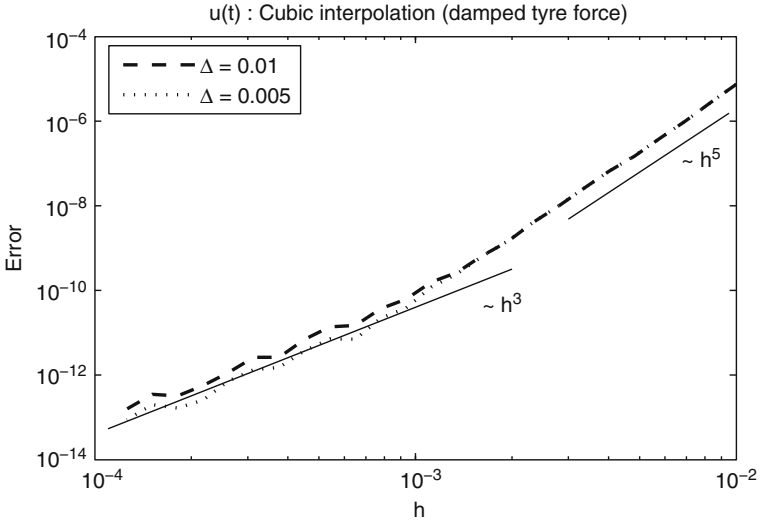

Fig. 4 Global error of 5th order method of Dormand and Prince applied to (4), cubic splines s_Δ, with damping, $r = 1$. Improved error bound (16): $\epsilon = \mathcal{O}(h^5) + \mathcal{O}(h^3)$

The numerical tests illustrate the well known practical observation that higher order ODE time integration methods may also be successfully applied if the right hand side of ODE (4) does not satisfy the strong smoothness assumptions of the classical convergence analysis. For Scenario 3 with linear splines $s_\Delta \in C^0[t_0, t_e]$ that

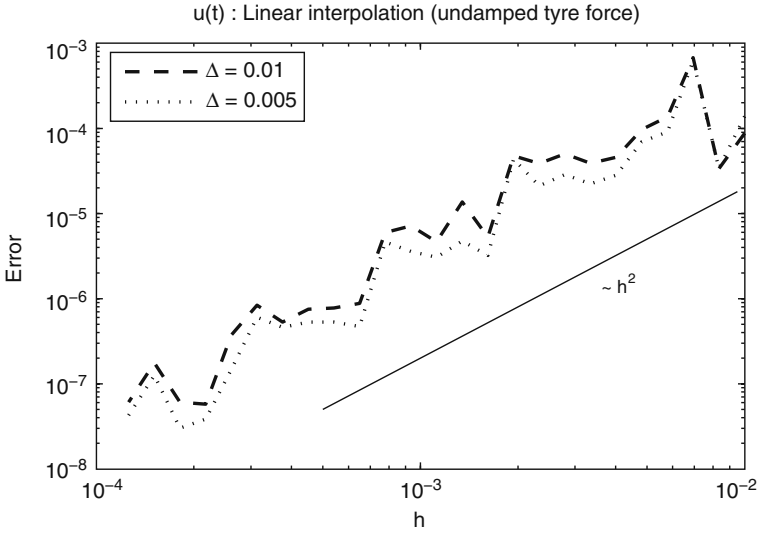

Fig. 5 Global error of 5th order method of Dormand and Prince applied to (4), linear splines s_Δ, no damping, $r = 0$. Improved error bound (16): $\epsilon = \mathcal{O}(h^5) + \mathcal{O}(h^2)$

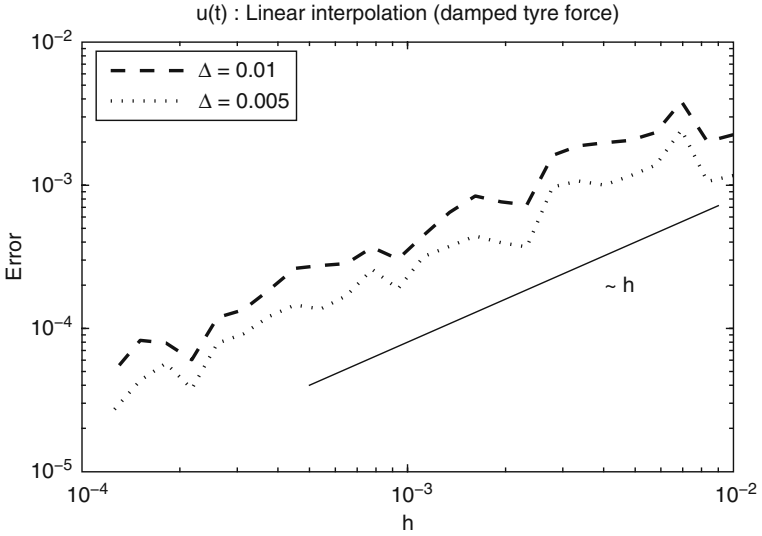

Fig. 6 Global error of 5th order method of Dormand and Prince applied to (4), linear splines s_Δ, with damping, $r = -1$. Improved error bound (16): $\epsilon = \mathcal{O}(h^5) + \mathcal{O}(h)$

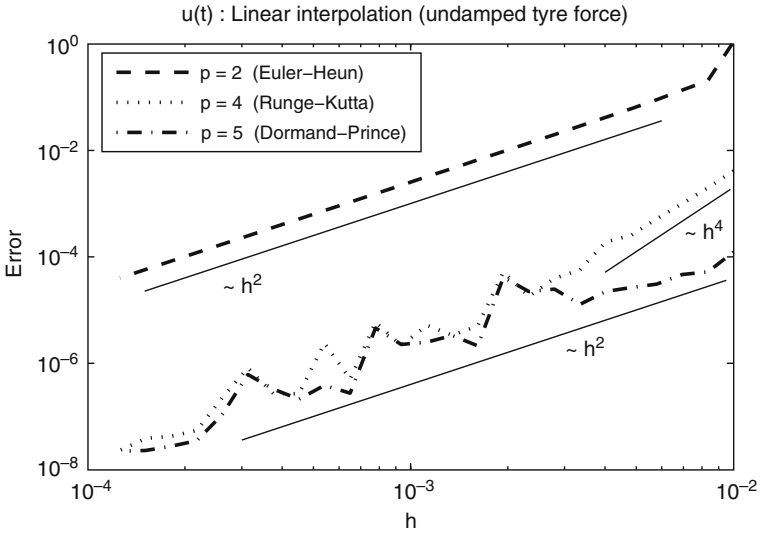

Fig. 7 Global error of explicit Runge-Kutta methods applied to (4) with linear splines s_Δ, no damping, $r = 0$. Improved bound (16) for global error: $\epsilon = \mathcal{O}(h^p) + \mathcal{O}(h^2)$

result in an error bound $\epsilon = \mathcal{O}(h^p) + \mathcal{O}(h^2)$, Fig. 7 compares explicit Runge-Kutta methods of different (classical) order p. In the whole stepsize range of interest, higher order methods like the classical 4th order method of Runge and Kutta or the 5th order method of Dormand and Prince have a substantially smaller global error ϵ than lower order methods like the second order Euler-Heun method.

4 Summary and Outlook

For a special problem class, improved error bounds for higher order time integration methods applied to ODEs with non-smooth right hand side are derived. The convergence analysis gives some additional theoretical justification for the application of higher order methods to systems with discontinuities in derivatives of the right hand side. The results are verified by numerical tests for a two mass system with harmonic excitations that are approximated by linear or cubic splines.

It should be stated explicitly that the convergence analysis of Sect. 2 does not consider practical aspects like stepsize control for systems with non-smooth right hand side.

The extension of the convergence analysis for systems with non-smooth right hand side to ODEs and to DAEs with state dependent spline functions $s_\Delta = s_\Delta(t, \boldsymbol{x})$ will be the logical next step to a better understanding of higher order time integration methods applied to non-smooth systems.

References

1. Ascher, U., Petzold, L.: Computer Methods for Ordinary Differential Equations and Differential–Algebraic Equations. SIAM, Philadelphia (1998)
2. Hairer, E., Nørsett, S., Wanner, G.: Solving Ordinary Differential Equations. I. Nonstiff Problems. 2nd edn. Springer–Verlag, Berlin Heidelberg New York (1993)
3. Moler, C.: Numerical Computing with MATLAB. SIAM, Philadelphia (2004)
4. Bellen, A., Zennaro, M.: Numerical Methods for Delay Differential Equations. Oxford University Press, Oxford, UK (2003)
5. Walter, W.: Ordinary Differential Equations. Number 182 in Graduate Texts in Mathematics. Springer (1998)
6. Freund, R., Hoppe, R.: Stoer/Bulirsch: Numerische Mathematik 1. 10th edn. Springer–Verlag, Berlin, Heidelberg (2007)
7. Hertig, T.: Splineinterpolation bei der numerischen Lösung von gewöhnlichen Differentialgleichungen mit Hilfe expliziter Runge-Kutta-Verfahren. Diploma Thesis, Martin Luther University Halle-Wittenberg (Germany), Department of Mathematics and Computer Science (2005)
8. Pickel, P.: Simulation fahrdynamischer Eigenschaften von Traktoren. Fortschritt-Berichte VDI Reihe 14, Nr. 65. VDI–Verlag, Düsseldorf (1993)
9. Dormand, J., Prince, P.: A family of embedded Runge–Kutta formulae. J. Comp. Appl. Math. **6** (1980) 19–26

Sensitivity Analysis of Discontinuous Multidisciplinary Models: Two Examples

Andreas Pfeiffer and Martin Arnold

Abstract Discontinuous system modeling is a present topic when working with practical models of technical systems. Numerical algorithms can only handle models with a given structure of the discontinuity effects. In the paper we show some examples that motivate the investigation of extended problem classes. The sensitivity analysis of all the systems gives important information about the dependency of the model solution on model parameters like controller parameters. We discuss models with nonsmooth switching functions and models with several switching functions influencing the model dynamics at the same time.

1 Introduction

The complexity of system models in engineering processes is growing more and more. Beyond the increasing complexity the models also have to assemble different physical disciplines, e.g., mechanics, electrics, hydraulics or thermodynamics into *multidisciplinary* models. Several software systems support the modeling and simulation of such applied problems. One of the standard tools is Modelica [1] that is especially tailored to discontinuous and hybrid discrete/continuous systems. Discontinuities often arise when simplifying physical laws or effects with the goal to harmonize the internal levels of detail for multidisciplinary models. One challenge for a robust and efficient numerical integration of automatically generated model code is the correct detection and handling of different classes of discontinuous phenomena.

The paper contributes to the theoretical analysis for extended problem classes of discontinuous models by detailed investigations of practical examples. This analysis includes the sensitivity analysis with respect to model parameters. Gradient based optimization algorithms need the sensitivity information for a reliable convergence to optimal parameter values. The algorithmic optimization of dynamical models is a widely used technique to improve the model quality in technical applications.

A. Pfeiffer (✉)
DLR Oberpfaffenhofen, Institute of Robotics and Mechatronics, D-82230 Wessling, Germany
e-mail: Andreas.Pfeiffer@dlr.de

P.G. Thomsen, H. True (eds.), *Non-smooth Problems in Vehicle Systems Dynamics*,
DOI 10.1007/978-3-642-01356-0_21,

After this introduction the paper has two main sections. In Sect. 2 we formulate the standard structure and a solution procedure of dynamical systems with discontinuous right hand sides before we introduce the generalized solution according to Filippov [2]. A mechanical example shows a simple system that does not fulfill the standard assumption used so far. We construct the solution of this example in detail.

Section 3 recalls the sensitivity analysis for smooth systems and discontinuous systems with traditional requirements. We analyze the type of systems from Sect. 2 and prove for an example from electrical circuit analysis, that several active switching functions can lead to problems since the existence of sensitivities is not longer guaranteed. The paper closes with a short summary.

2 Discontinuous Models

We consider initial value problems

$$\dot{x} = f(x, t), \qquad x(t^0) = A \tag{1}$$

with a state vector $x \in \mathbb{R}^{n_x}$, a right hand side $f : \mathbb{R}^{n_x+1} \to \mathbb{R}^{n_x}$ and initial values $A \in \mathbb{R}^{n_x}$ at the time $t^0 \in \mathbb{R}$. It is a classical result in analysis [3] that for a sufficiently smooth function f a unique local solution $x(t)$, $t \in [t^0, t^\infty]$ with $t^\infty > t^0$ exists. If we enlarge the problem class by accepting *discontinuous* functions f for the right hand side of the dynamical system (1), then the classical solution theory for ordinary differential equations is not applicable. The consideration of differential inclusions $\dot{x} \in F(x, t)$ and set valued right hand sides F may solve this problem [4, 2]. Based on this very general theory, we concentrate on problems that are relevant for a large class of technical systems and for which algorithms exist to compute numerical solutions.

The standard approach [5] in numerical analysis relies on *switching* functions $q : \mathbb{R}^{n_x+1} \to \mathbb{R}$. Their signs define the right hand side:

$$\dot{x} = f(x, t) := \begin{cases} f^+(x, t), & \text{if } q(x, t) > 0, \\ f^-(x, t), & \text{if } q(x, t) < 0. \end{cases} \tag{2}$$

The two vectors f^+, f^- denote smooth functions that are active on disjunct sets in the phase space $\mathbb{R}^{n_x+1}$. Modeling environments like Modelica automatically generate this kind of equations for the numerical integration algorithms.

In the following we will explicitly describe the solution theory for problem (2). For a time t^* and the value $x^* := x(t^*)$ we assume $q(x^*, t^*) = 0$. The configuration (x^*, t^*) is called an *event*. In the case $q(x^*, t^*) \neq 0$ a unique right hand side f^+ or f^- is defined in (2) and the classical theory holds as long in time as $q(x(t), t)$ does not change its sign. To decide how the solution can be extended after an event for $t > t^*$, it is advantageous [6, 7] to consider for a smooth switching function q the directional derivatives

$$D^+q := q_x f^+ + q_t, \qquad D^-q := q_x f^- + q_t.$$

We use the notation $q_x := \partial q/\partial x$. The signs of D^+q, D^-q show the qualitative behavior of the switching function q in the direction of possible velocities $\dot{x}$.

In the case of equal signs of $D^+q(x^*, t^*)$ and $D^-q(x^*, t^*)$, it is obvious how to define f locally for $t \geq t^*$:

$$f(x,t) = \begin{cases} f^+(x,t), & \text{if } D^+q(x^*,t^*),\ D^-q(x^*,t^*) > 0, \\ f^-(x,t), & \text{if } D^+q(x^*,t^*),\ D^-q(x^*,t^*) < 0. \end{cases}$$

In the case $D^+q(x^*, t^*) > 0$, $D^-q(x^*, t^*) < 0$ no unique solution exist. Because the possible solutions are unstable with respect to the initial values [2], we do not consider them in the following. We also do not consider cases with $D^+q(x^*, t^*) = 0$ or $D^-q(x^*, t^*) = 0$. For more information about these cases we refer to [8].

The last case $D^+q(x^*, t^*) < 0$, $D^-q(x^*, t^*) > 0$ describes a situation where no classical solution can be defined, because both velocity vectors $(f^+, 1)$, $(f^-, 1)$ are directed into the switching surface $\Sigma := \{(x, t) : q(x, t) = 0\}$. Therefore, Filippov [2] supposes $q(x(t), t) = 0$ locally for $t \geq t^*$ and suggests to generalize the solution concept, where the right hand side is selected from the convex hull $F := \text{conv}\{f^+, f^-\}$. This definition is in line with physical observations on important phenomena like dry friction in one dimension [2].

By the use of $\lambda \in [0, 1]$ we obtain

$$\dot{x} = \lambda f^+(x,t) + (1-\lambda) f^-(x,t), \quad x(t^*) = x^*, \quad q(x(t),t) = 0.$$

Differentiation of $q(x(t), t) = 0$ and elimination of λ results in

$$\dot{x} = f^*(x,t) := \frac{D^+q f^- - D^-q f^+}{D^+q - D^-q}(x,t), \quad x(t^*) = x^*. \tag{3}$$

The system (3) of differential equations is valid until one of the directional derivatives $D^+q(x(t), t)$ or $D^-q(x(t), t)$ changes its sign. Then the solution can leave the switching surface Σ and one of the vectors f^+ or f^- may serve as right hand side again.

Example 1 (Lossy gear model)

We investigate a Modelica model [9] which describes a mechanical transmission gear in a simple manner. The rotating gear wheels are modeled by mechanical inertias which are coupled by an efficiency torque load and an ideal gear without losses, see Fig. 1. Depending on the direction of the power flow, the efficiency `eta` is a factor in the left or right hand side of the torque equation of the model `Efficiency`. It has the following Modelica-Code:

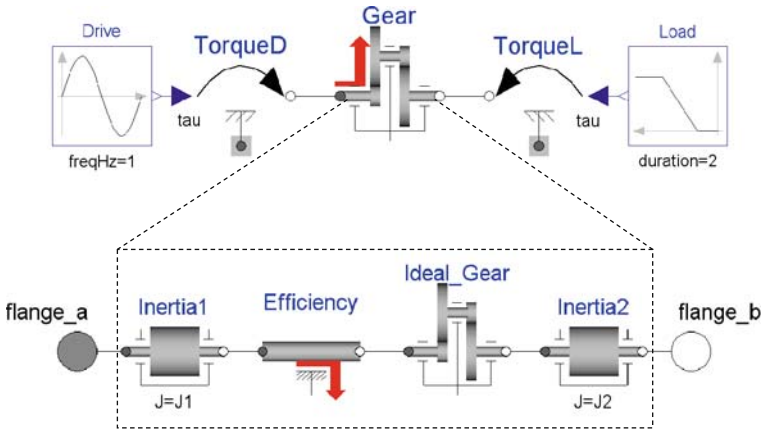

Fig. 1 Modelica model for a mechanical gear inside a test environment with torque inputs

```
model Efficiency
 extends TwoFlanges;
 parameter Real eta = 0.5;
 SIunits.Angle phi;
 SIunits.Power power_a;
equation
 phi = flange_a.phi;
 phi = flange_b.phi;
           ...
```

```
                ...
 power_a = flange_a.tau*der(phi);
 if power_a >= 0 then
 flange_b.tau = -eta*flange_a.tau;
 else
 eta*flange_b.tau = -flange_a.tau;
 end if;
end Efficiency;
```

Some more detailed gear models can be found in [9]. Fig. 1 shows a model that can be simulated to test the gear model's properties. Both mechanical flanges of the gear are fed by time dependent torques to analyze the behavior for different load and drive torques. All the significant parameters and variables are listed in Table 1. The total model can be formulated as follows:

$$\dot{x} = \begin{cases} f^+(t), & \text{if } q(x,t) > 0, \\ f^-(t), & \text{if } q(x,t) < 0, \end{cases} \qquad x(0) = 0$$

Table 1 Parameters und variables for the lossy gear model

Name	Modelica variable	Description	Value	Unit
J_1	`Gear.J1`	Inertia, left gear wheel	1	kg m^2
J_2	`Gear.J2`	Inertia, right gear wheel	1.5	kg m^2
r	`Gear.r`	Transmission ratio	2	1
η	`Gear.eta`	Efficiency	0.5	1
τ_D	`TorqueD.tau`	Torque at left flange	$10\sin(2\pi t)$	Nm
τ_L	`TorqueL.tau`	Torque at right flange	$-10 + 2.5t$	Nm
ω_1	`Gear.w1`	Rotation speed, left wheel	$x(t)$	rad/s
ω_2	`Gear.w2`	Rotation speed, right wheel	$\omega_2(t)$	rad/s

with

$$f^+(t) := \frac{\eta r^2 \tau_D(t) + r\tau_L(t)}{\eta r^2 J_1 + J_2}, \quad f^-(t) := \frac{\frac{1}{\eta} r^2 \tau_D(t) + r\tau_L(t)}{\frac{1}{\eta} r^2 J_1 + J_2},$$

$$q(x,t) = x\big(\tau_D(t) - J_1 \dot{x}\big) = \begin{cases} x\big(\tau_D(t) - J_1 f^+(t)\big) =: q^+(x,t), & \text{if } q > 0, \\ x\big(\tau_D(t) - J_1 f^-(t)\big) =: q^-(x,t), & \text{if } q < 0. \end{cases}$$

Here, we find a switching function q that depends on $\dot{x}$ and results in two cases for the switching function:

$$q^+(x,t) = x\frac{J_2\tau_D(t) - rJ_1\tau_L(t)}{\eta r^2 J_1 + J_2}, \quad q^-(x,t) = x\frac{J_2\tau_D(t) - rJ_1\tau_L(t)}{\frac{1}{\eta} r^2 J_1 + J_2}.$$

It follows $\operatorname{sgn} q^+ = \operatorname{sgn} q^-$, because the conditions $\eta r^2 J_1 + J_2$, $r^2/\eta J_1 + J_2 > 0$ are satisfied. As a consequence the equations $q^+ = 0$ and $q^- = 0$ hold on the same set and so Σ is well defined. In Fig. 2 the function $q(x,t)$ is displayed in different grayscales for the areas $q > 0$, $q < 0$ and $q = 0$. Because of $\operatorname{sgn} q^+ = \operatorname{sgn} q^-$ the function q is continuous but not necessarily differentiable. If we consider the derivatives

$$q_x^+(x,t) = \frac{J_2\tau_D(t) - rJ_1\tau_L(t)}{\eta r^2 J_1 + J_2}, \qquad q_x^-(x,t) = \frac{J_2\tau_D(t) - rJ_1\tau_L(t)}{\frac{1}{\eta} r^2 J_1 + J_2},$$

$$q_t^+(x,t) = x\frac{J_2\dot{\tau}_D(t) - rJ_1\dot{\tau}_L(t)}{\eta r^2 J_1 + J_2}, \qquad q_t^-(x,t) = x\frac{J_2\dot{\tau}_D(t) - rJ_1\dot{\tau}_L(t)}{\frac{1}{\eta} r^2 J_1 + J_2},$$

then it becomes clear, that for $\eta \neq 1$ we have in general $q_x^+ \neq q_x^-$ *and* $q_t^+ \neq q_t^-$.

In [8] a solution theory, which is based on the theory above, is developed for systems with discontinuous right hand sides and nonsmooth switching functions. We apply this theory to the current example. We get the identities $q^+(0,0) = q^-(0,0) = 0$ and

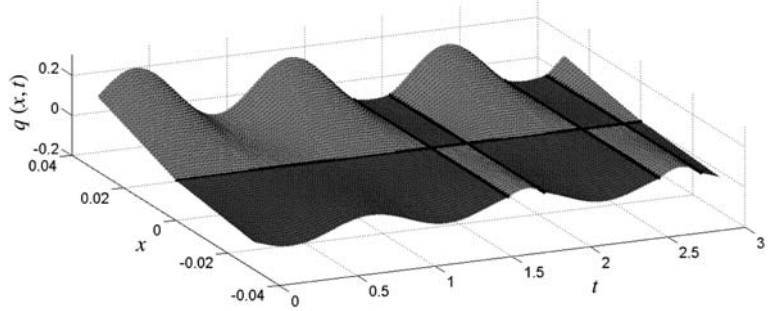

Fig. 2 Nonsmooth switching function $q(x,t)$ for Example 1

$$q_x^+(0,0) = \frac{40}{7}, \quad q_t^+(0,0) = 0, \qquad f^+(0) = -\frac{40}{7}, \quad f^-(0) = -\frac{40}{19}.$$

It follows: $D^+q^+(0,0) = -1600/49 < 0$ and $D^-q^+(0,0) = -1600/133 < 0$. Hence, the solution is locally for $t > 0$ generated by

$$f^-(t) = \frac{160\sin 2\pi t - 40 + 10t}{19}.$$

The corresponding switching function

$$q^-(x,t) = x\frac{30\sin 2\pi t + 40 - 10t}{19}$$

has a zero crossing for $t \in (0, 1.5)$ if and only if x vanishes. The solution

$$x(t) = \frac{-\frac{80}{\pi}(\cos 2\pi t - 1) - 40t + 5t^2}{19}$$

becomes equal to zero the first time for $t^* = 0.080477$. This yields $q^-(0,t^*) = 0$, $q_x^-(0,t^*) = 2.8277$ and $q_t^-(0,t^*) = 0$. We can follow [8] from the directional derivatives $D^+q^-(0,t^*) = -8.0065 < 0$ and $D^-q^-(0,t^*) = 5.70087 > 0$ that there exists a Filippov solution with $f^* = 0$ and $x(t) = 0$ locally for $t > t^*$. To detect when the solution leaves the switching surface the directional derivatives D^+q^- and D^-q^- are analyzed: The first zero crossing for D^+q^- or D^-q^- is at $t^{**} = 0.1995$ for D^+q^-. The solution can then be continued by $f = f^+$ locally for $t > t^{**}$:

$$x(t) = \frac{\frac{-20}{\pi}(\cos 2\pi t - \cos 2\pi t^{**}) - 40(t - t^{**}) + 5(t^2 - t^{**2})}{7}.$$

The next zero crossing of q^+ is at $t^{***} = 0.3713$. The solution stays again a period of time in the switching surface before it leaves this region. Figure 3 shows the constructed solution $x(t)$. Solution details are illustrated by numerical simulations of the gear model in [8].

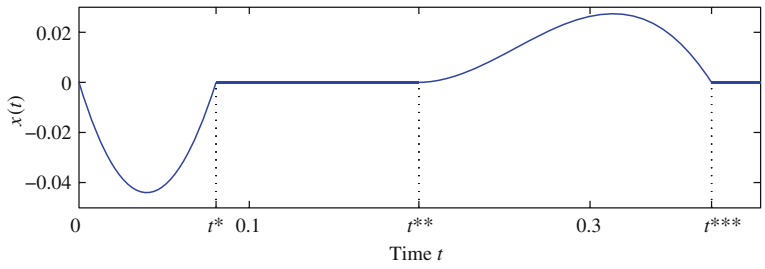

Fig. 3 Constructed solution $x(t)$ for the lossy gear model. The constant phases result from generalized solutions of Filippov.

The physical interpretation of these simulation results is as follows: The connection flanges of the gear do not rotate at the time $t \in [t^*, t^{**}]$, although the fed torques are changed. Mechanical losses in the gear prevent a motion in both directions as long as the torque at one of the flanges is not sufficiently large to drive the other flange including the internal losses.

3 Sensitivity Analysis

Practical models mostly contain a lot of parameters to calibrate the model behavior in comparison to measurements on a test bench. In addition to the solution of the corresponding dynamical system also the sensitivity of the solution with respect to small variations of model parameters is of interest. From an analytical point of view the sensitivities are derivatives of a parameter depending solution $x = x(p, t)$ with respect to the model parameters $p \in \mathbb{R}^{n_p}$. Based on the sensitivity analysis for systems with smooth right hand sides we investigate the existence of sensitivities for discontinuous systems with structures that are typical of models in practical applications.

For a parameter dependent initial value problem

$$\dot{x} = f(x, p, t), \qquad x(p, t^0) = A(p) \tag{4}$$

with smooth functions $f : \mathbb{R}^{n_x+n_p+1} \to \mathbb{R}^{n_x}$ and $A : \mathbb{R}^{n_p} \to \mathbb{R}^{n_x}$ there exists a neighborhood of $p = p^*$ and an interval around t^0, such that the solution $x = x(p, t)$ is defined on the product of the sets [3]. We assume, that the interval contains a given interval $[t^0, t^\infty]$. The sensitivities x_p locally exist, if f and A are sufficiently smooth functions. Then the sensitivity equations are fulfilled:

$$\dot{x}_p = f_x x_p + f_p, \qquad x_p(p, t^0) = A_p(p). \tag{5}$$

This system of linear ordinary differential equations is the basis of numerical methods to compute the sensitivities. For example, the system (5) is numerically integrated together with the original system (4) by the BDF-Code DASPK3.1, see [10].

An important application of the sensitivity analysis is the gradient based optimization of technical models. Unknown model parameters can often only be identified by efficient optimization algorithms that need the sensitivities of the model response w.r.t. the model parameters. In all these applications we have to assume, that sufficiently smooth model functions are available. Otherwise, serious numerical problems can occur and the algorithms may fail.

Many practical models consist of submodels that introduce discontinuous or non-smooth behavior. Modelica explicitly supports discontinuous and discrete model elements [11]. It is desirable to apply a sensitivity analysis to these models. Therefore, we investigate different classes of discontinuous models in this direction:

In a first step, we consider a classical solution of a parameter dependent discontinuous system

$$\dot{x} = \begin{cases} f^+(x, p, t), & \text{if } q(x, p, t) > 0, \\ f^-(x, p, t), & \text{if } q(x, p, t) < 0, \end{cases} \qquad x(p, t^0) = A(p). \tag{6}$$

We assume $q(A(p^*), p^*, t^0) > 0$ and $q(x^*, p^*, t^*) = 0$ for a fixed parameter p^* and a time $t^* > t^0$. We also use the abbreviation $x^* := x(p^*, t^*)$. If $D^{\pm}q(x^*, p^*, t^*) < 0$ holds, then we get the solution $x(p^*, t)$ with

$$\dot{x} = f(x, p^*, t) = \begin{cases} f^+(x, p^*, t), & \text{if } t \in [t^0, t^*), \\ f^-(x, p^*, t), & \text{if } t \in (t^*, t^\infty]. \end{cases}$$

We want to study how the solution depends on the parameter p. The time t^* for the event is in general not constant but depends on p. We denote this time by $t^1(p)$ which is implicitly defined by $q(x(p, t^1), p, t^1) = 0$. In consequence we have $t^1(p^*) = t^*$. To distinguish the solutions at the switching surface Σ, we introduce the following notation:

$$\begin{aligned} \dot{x}^0 &= f^0(x^0, p, t) := f^+(x^0, p, t) \quad \text{for } t \in [t^0, t^1(p)], \\ \dot{x}^1 &= f^1(x^1, p, t) := f^-(x^1, p, t) \quad \text{for } t \in [t^1(p), t^\infty]. \end{aligned}$$

Hence, we get

$$x(p, t) = \begin{cases} x^0(p, t) & \text{if } t \in [t^0, t^1(p)), \\ x^1(p, t), & \text{if } t \in (t^1(p), t^\infty]. \end{cases}$$

Outside the switching surface it is obvious, that the following sensitivity equations hold:

$$\begin{aligned} \dot{x}^0_p &= f^0_x x^0_p + f^0_p, \quad \text{if } t \in [t^0, t^1(p)], \\ \dot{x}^1_p &= f^1_x x^1_p + f^1_p, \quad \text{if } t \in [t^1(p), t^\infty]. \end{aligned}$$

Rozenvasser [12] found the following jump conditions for the sensitivities at the event t^*:

$$x^1_p(p^*, t^*) = x^0_p(p^*, t^*) + \left(f^0(x^*, p^*, t^*) - f^1(x^*, p^*, t^*)\right) \cdot t^*_p \tag{7}$$

with

$$t^*_p := t^1_p(p^*) = -\frac{q_x(x^*, p^*, t^*)x^0_p(p^*, t^*) + q_p(x^*, p^*, t^*)}{q_x(x^*, p^*, t^*)f^0(x^*, p^*, t^*) + q_t(x^*, p^*, t^*)}.$$

The formulas result from the implicit function theorem. Equation (7) shows, that the sensitivities are in general not continuous at an event point. Therefore, numerical methods have to compute the jump condition at $t = t^*$ in order to get the correct initial values $x^1(p^*, t^*)$ for the further integration ($t > t^*$).

In a second step we show, that the theory can also be applied to the generalized solution according to Filippov including nonsmooth switching functions like the ones in Example 1. The analysis is based on the following system with two smooth switching functions q^+, q^- that define a unique switching surface Σ:

$$\dot{x} = \begin{cases} f^+(x, p, t), & \text{if } q^+(x, p, t) > 0, \\ f^-(x, p, t), & \text{if } q^-(x, p, t) < 0, \end{cases} \qquad x(p, t^0) = A(p).$$

We assume the relation $q^+\left(A(p^*), p^*, t^0\right) > 0$. Then the first part of the solution can be formulated as

$$\dot{x}^0 = f^+(x^0, p^*, t) \text{ for } t \in [t^0, t^1]$$

with $q^+\left(x^0(p^*, t^1), p^*, t^1\right) = 0$. Under the assumptions

$$D^+q^+\left(x^0(p^*, t^1), p^*, t^1\right) < 0 \text{ and } D^-q^+\left(x^0(p^*, t^1), p^*, t^1\right) > 0$$

there is a phase of the generalized solution after $t = t^1 = t^1(p^*)$:

$$\dot{x}^1 = f^*(x^1, p^*, t) = \left[\frac{D^+q^+f^- - D^-q^+f^+}{D^+q^+ - D^-q^+}\right](x^1, p^*, t) \text{ for } t \in [t^1, t^2]. \qquad (8)$$

The event at $t = t^2$ shall be defined by the equation $D^-q^+\left(x^1(p^*, t^2), p^*, t^2\right) = 0$, that implies:

$$\dot{x}^2 = f^-(x^2, p^*, t) \text{ for } t \in [t^2, t^\infty].$$

The sensitivities fulfill the following sensitivity equations:

$$\begin{aligned} \dot{x}_p^0 &= f_x^+(x^0, p^*, t)x_p^0 + f_p^+(x^0, p^*, t), && t \in [t^0, t^1], \\ \dot{x}_p^1 &= f_x^*(x^1, p^*, t)x_p^1 + f_p^*(x^1, p^*, t), && t \in [t^1, t^2], \\ \dot{x}_p^2 &= f_x^-(x^2, p^*, t)x_p^2 + f_p^-(x^2, p^*, t), && t \in [t^2, t^\infty] \end{aligned}$$

with the initial values

$$\begin{aligned} x_p^0(p^*, t^0) &= A_p(p^*), \\ x_p^1(p^*, t^1) &= x_p^0(p^*, t^1) + \left[\frac{(f^+ - f^-)\left(q_x^+x_p^0(p^*, t^1) + q_p^+\right)}{q_x^+(f^- - f^+)}\right]\left(x^0(p^*, t^1), p^*, t^1\right), \\ x_p^2(p^*, t^2) &= x_p^1(p^*, t^2). \end{aligned}$$

For transitions from a generalized solution to a classical one the identity $f^* = f^-$ is satisfied at the event point. This fact can easily be verified by inserting $D^-q^+ = 0$ into (8). This is also the reason for the smooth transition from the sensitivities x_p^1

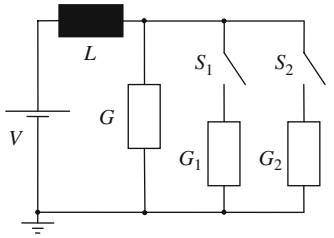

Name	Description	Value	Unit
G	Conductance, basic load	$1 \cdot 10^{-2}$	S
G_1	Conductance, first load	$2 \cdot 10^{-2}$	S
G_2	Conductance, second load	$5 \cdot 10^{-2}$	S
V	Supply voltage	12	V
L	Inductance	1	H
p	Switching time for S_2	p	s
i	Current through inductor	$i(t)$	A

Fig. 4 Electrical circuit for parallel switching of loads. Table with variables and parameters

to x_p^2 at $t = t^2$. For these classes of discontinuous models it was possible to prove the existence of the sensitivities and extend the sensitivity analysis from smoother problems. In the following we introduce a new problem class by an example. It turns out, that the sensitivity analysis fails for this practical example. The new structural property of the system is the existence of two switching functions being active at the same time. The consideration can be extended to several active switching functions [8]. Previous work [6, 13, 14] assumes exactly one active switching function per event.

Example 2 (Simultaneous switching of electrical loads)

The electrical circuit in Fig. 4 describes switchable loads G_1 and G_2 that are connected by switches S_1, S_2 in parallel to a basic load G. The loads are supplied by a voltage source V with a linear inductor L. All the loads are given by their linear conductances. Initially, both switches are open. The switch S_1 closes after $\frac{1}{2}$ second and increases the total load. The moment when switch S_2 closes shall be variable and is defined by a parameter p. The dynamics of the current i through the inductor is modeled by the linear ordinary differential equation

$$\frac{di}{dt} = \frac{1}{L}\left(V - \frac{1}{G + G_1^* + G_2^*} i\right) \tag{9}$$

with

$$G_1^* := \begin{cases} 0, & \text{if } t - \frac{1}{2} < 0, \\ G_1, & \text{if } t - \frac{1}{2} > 0, \end{cases} \qquad G_2^* := \begin{cases} 0, & \text{if } t - p < 0, \\ G_2, & \text{if } t - p > 0 \end{cases}$$

and the initial value $i(0) = 0$.

The system (9) has a discontinuous right hand side with several switches. For the parameter value $p^* = \frac{1}{2}$ both switching functions $t - \frac{1}{2}$ and $t - p$ have their zero crossing at $t^* = \frac{1}{2}$. Therefore, the problem is not of the form (6) which we know how to handle. The solution of system (9) can be calculated by hand and splits up in the following solution parts:

$0 < p \leq \frac{1}{2}$:	$\frac{1}{2} < p$:
$i(p,t) = \begin{cases} i^0(p,t), & \text{if } 0 \leq t < p, \\ i^{1-}(p,t), & \text{if } p \leq t < \frac{1}{2}, \\ i^{2-}(p,t), & \text{if } \frac{1}{2} \leq t, \end{cases}$	$i(p,t) = \begin{cases} i^0(p,t), & \text{if } 0 \leq t < \frac{1}{2}, \\ i^{1+}(p,t), & \text{if } \frac{1}{2} \leq t < p, \\ i^{2+}(p,t), & \text{if } p \leq t \end{cases}$

with $G_S := G + G_1 + G_2$,

$$
\begin{aligned}
i^0(p,t) &= VG\left(1 - e^{-\frac{t}{LG}}\right), \\
i^{1-}(p,t) &= V\left(G + G_2 - \left(G_2 + Ge^{-\frac{p}{LG}}\right)e^{-\frac{t-p}{L(G+G_2)}}\right), \\
i^{2-}(p,t) &= V\left(G + G_1 + G_2 - \left(G_1 + \left(G_2 + Ge^{-\frac{p}{LG}}\right)e^{-\frac{\frac{1}{2}-p}{L(G+G_2)}}\right)e^{-\frac{t-\frac{1}{2}}{LG_S}}\right), \\
i^{1+}(p,t) &= V\left(G + G_1 - \left(G_1 + Ge^{-\frac{1}{2LG}}\right)e^{-\frac{t-\frac{1}{2}}{L(G+G_1)}}\right), \\
i^{2+}(p,t) &= V\left(G + G_1 + G_2 - \left(G_2 + \left(G_1 + Ge^{-\frac{1}{2LG}}\right)e^{-\frac{p-\frac{1}{2}}{L(G+G_1)}}\right)e^{-\frac{t-p}{LG_S}}\right).
\end{aligned}
$$

From this solution we can also calculate the sensitivities by differentiation w.r.t. the parameter p:

$$
\begin{aligned}
i_p^0(p,t) &= 0, \\
i_p^{1-}(p,t) &= \frac{VG_2}{L(G+G_2)}\left(e^{-\frac{p}{LG}} - 1\right)e^{-\frac{t-p}{L(G+G_2)}}, \\
i_p^{2-}(p,t) &= \frac{VG_2}{L(G+G_2)}\left(e^{-\frac{p}{LG}} - 1\right)e^{-\frac{\frac{1}{2}-p}{L(G+G_2)} - \frac{t-\frac{1}{2}}{LG_S}}, \\
i_p^{1+}(p,t) &= 0, \\
i_p^{2+}(p,t) &= \frac{VG_2}{LG_S}\left(\frac{1}{G+G_1}\left(G_1 + Ge^{-\frac{1}{2LG}}\right)e^{-\frac{p-\frac{1}{2}}{L(G+G_1)}} - 1\right)e^{-\frac{t-p}{LG_S}}.
\end{aligned}
$$

Especially, the following equations hold:

$$
\begin{aligned}
i_p^{2-}(p^*,t^*) &= \frac{VG_2}{L(G+G_2)}\left(e^{-\frac{1}{2LG}} - 1\right) \approx -10.0, \\
i_p^{2+}(p^*,t^*) &= \frac{VGG_2}{L(G+G_1+G_2)(G+G_1)}\left(e^{-\frac{1}{2LG}} - 1\right) \approx -2.5.
\end{aligned}
$$

In Fig. 5, the time and parameter dependent solution and the sensitivity are illustrated in the neigborhood of (p^*, t^*). The grayscale figure for the sensitivities shows that the solution $i(p,t)$ is not differentiable w.r.t. the parameter p on the

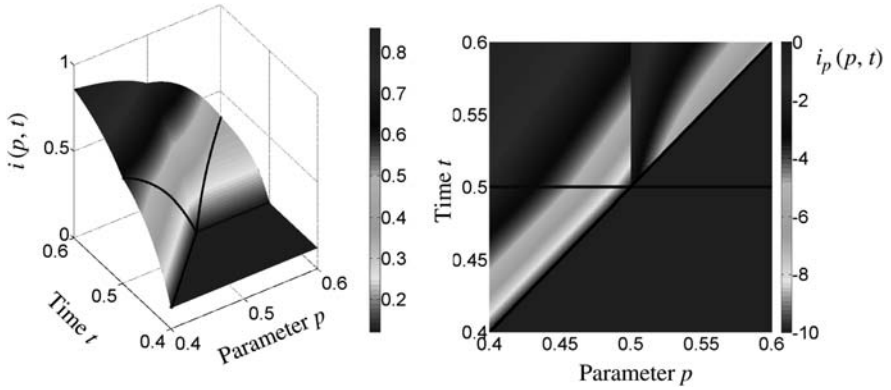

Fig. 5 Solution $i(p,t)$ (*left*) and sensitivity $i_p(p,t)$ (*right*) for Example 2. The switching times $t^1(p) = \frac{1}{2}$ and $t^2(p) = p$ are plotted in the solution surface

set $\{(p^*, t) : \ t > t^*\}$. For the differential quotients, the limits from the right and from the left do not coincide.

4 Summary

It is well known that the numerical simulation of nonsmooth models demands special care. We show on the basis of a lossy gear model that practical models may have nonsmooth switching functions not being considered in the literature so far. The construction of both a unique solution and parameter sensitivities is anyway possible. The second example of switched electrical consumers illustrates the limits of the sensitivity analysis. Two switching functions that are getting zero at the same time prevent the existence of the sensitivities after the switching time. In summary, we demonstrated additional theoretical problems and solution approaches for models with discontinuities that do not fit into the the common problem classes, but arise in practical applications.

References

1. Otter, M., Elmqvist, H., Mattsson, S.E.: Multidomain Modeling with Modelica. In Fishwick, P., ed.: CRC Handbook of Dynamic System Modeling. CRC Press (2007) 36.1–36.27
2. Filippov, A.F.: Differential Equations with Discontinuous Righthand Sides. Kluwer Academics Publishers (1988)
3. Königsberger, K.: Analysis 2. 2. edn. Springer-Verlag (1997)
4. Aubin, J.P., Cellina, A.: Differential Inclusions. A Series of Comprehensive Studies in Mathematics. Springer-Verlag (1984)
5. Hiebert, K.L., Shampine, L.F.: Implicitly defined output points for solutions of ode's. Sandia Report SAND80-0180, USA (February 1980)

6. Bock, H.G.: Randwertproblemmethoden zur Parameteridentifizierung in Systemen nichtlinearer Differentialgleichungen. PhD thesis, Bonner Mathematische Schriften Nr. 183, Bonn (1987)
7. Eich-Soellner, E., Führer, C.: Numerical Methods in Multibody Dynamics. B. G. Teubner, Stuttgart, Corrected reprint (2002)
8. Pfeiffer, A.: Numerische Sensitivitätsanalyse unstetiger multidisziplinärer Modelle mit Anwendungen in der gradientenbasierten Optimierung. Fortschrittberichte VDI, Reihe 20, Nr. 417, VDI Verlag (2008)
9. Pelchen, C., Schweiger, C., Otter, M.: Modeling and simulating the efficiency of gearboxes and of planetary gearboxes. In: Proceedings of 2nd International Modelica Conference, Oberpfaffenhofen (March 2002) 257–266
10. Li, S., Petzold, L.R.: Design of New DASPK for Sensitivity Analysis. Technical report, Department of Computer Science, University of California Santa Barbara, USA (May 1999)
11. Fritzson, P.: Principles of object-oriented modeling and simulation with Modelica 2.1. IEEE Press, Wiley-Interscience (2004)
12. Rozenvasser, E.N.: General sensitivity equations of discontinuous systems. Automat. Remote Control (1967) 400–404
13. Callies, R.: Entwurfsoptimierung und optimale Steuerung. Differential-algebraische Systeme, Mehrgitter-Mehrzielansätze und numerische Realisierung. Habilitationsschrift, Centre for Mathematics, Technical University Munich (July 2000)
14. Galán, S., Feehery, W.F., Barton, P.I.: Parametric sensitivity functions for hybrid discrete/continuous systems. Applied Numerical Mathematics **31**(1) (1999) 17–47

Smoothing Discontinuities in the Jacobian Matrix by Global Derivatives

Georg Rill

Abstract Hardware-In-the-Loop (HIL) test rigs are more and more used to develop and/or improve modern control units. Due to the increasing complexity of these systems detailed vehicle models running in real-time are required. The main task in real time applications is to achieve a stable but still sufficiently accurate numerical solution under all operating conditions. Complex vehicles modeled by multi body systems result in stiff differential equations. In particular, taking into account the effects of dry friction requires sophisticated modeling techniques and simple but robust numerical solvers.

1 Introduction

Vehicle modeling is usually done by multi body systems, [4]. As real vehicles incorporate many complex dynamic systems, such as the drive train, the steering system and the wheel/axle suspension, modern vehicle models will consist of different subsystems, [7]. However, real time performance for complex vehicle systems can only be achieved by a sophisticated modeling technique and a tailored integration algorithm, [10]. Besides the steering system [9] and complex axle suspension systems including compliances [6] tires and wheels are critical model parts too [8]. This paper will focus on dry friction which is present in many parts of a vehicle and influences the dynamics of steering and suspension systems.

2 Vehicle Modeling

Different vehicles like agricultural tractors, passenger cars, buses and trucks can be handled by one generic vehicle model, Fig . 1. Depending on the complexity of the vehicle the overall number of ordinary differential equations (ODEs) describing a vehicle depends on the model complexity and is usually in the range from

G. Rill (✉)
University of Applied Sciences Regensburg, Galgenbergstr. 30, D-93053 Regensburg, Germany
e-mail: georg.rill@maschinenbau.fh-regensburg.de

P.G. Thomsen, H. True (eds.), *Non-smooth Problems in Vehicle Systems Dynamics*,
DOI 10.1007/978-3-642-01356-0_22,

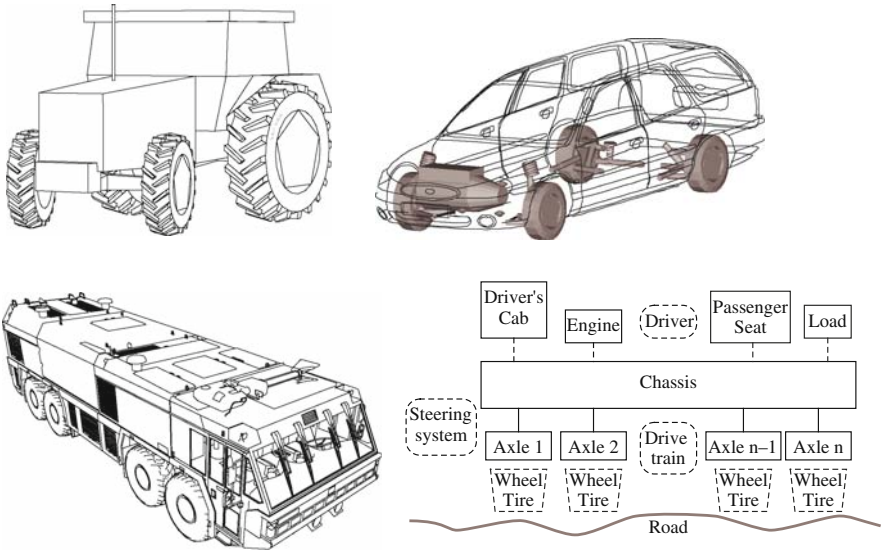

Fig. 1 Different types of vehicles and generic model structure

$n_{eq} = 20$ to $n_{eq} = 100$. The generic model structure covers nearly all different types of single vehicles including semitrailers and trailers. By interpreting tractor and trailer as single vehicle 1 and single vehicle 2 the generic model approach can still be used, Fig. 2. Coupling both vehicles via constraint equations however results in differential algebraic equations (DAEs) but will still make possible the real time simulation of large vehicle combinations, [3].

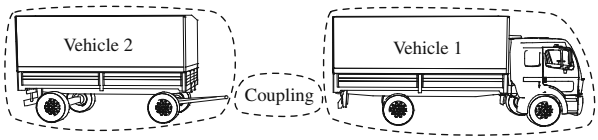

Fig. 2 Model approach to a tractor trailer combination

3 Dry Friction Modeling

Dry friction forces may be approximated by a quite simple Coloumb model

$$F_F = F_F^M \, sign(v) \tag{1}$$

where v denotes the sliding velocity and F_F^M represents the maximum friction force, Fig. 3. Due to the discontinuity at vanishing sliding velocities this approach will

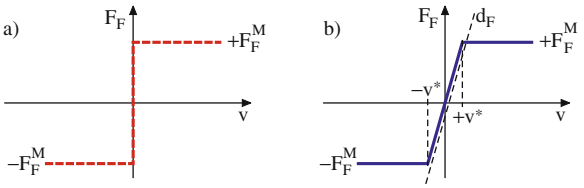

Fig. 3 Dry friction: (**a**) simple Coloumb model, (**b**) continuous approximation

cause severe problems in the numerical solution. Applying a simple regularization results in

$$F_F = \begin{cases} -F_F^M & v < -v^* \\ d_F\, v & -v^* \le v \le +v^* \\ +F_F^M & v > +v^* \end{cases} \quad \text{where} \quad v^* = \frac{F_F^M}{d_F} \tag{2}$$

where the fictitious damping coefficient d_F have to be chosen properly. On one hand as large as possible to come close to the sign-function in (1) on the other hand to be small enough to make a numerical integration possible in real time. However, large values for d_F result in a stiff system performance and will therefore require implicit integration algorithms.

4 Equations of Motion

By applying the principle of virtual power (Jordain's principle) the dynamics of the vehicle framework including at least the chassis and the axles can be described by a set of two first order differential equations

$$\begin{aligned} K_V(y_V)\ \dot{y}_V &= z_V\ , \\ M_V(y_V)\ \dot{z}_V &= q_V(y_V,\ z_V,\ y_S,\ z_S,\ s_F) \end{aligned} \tag{3}$$

where the vector y_V contains the generalized coordinates of the vehicle framework, the kinematic matrix K_V defines the generalized velocities which are arranged in the vector z_V, M_V names the mass matrix and q_V is the vector of generalized forces and torques applied to the vehicle framework. This vector depends also on the states of the subsystems y_S, z_S and the internal states s_F of dynamic force elements. Similar to the vehicle framework, mechanical subsystems like the steering systems and the drive train are described by further sets of first order differential equations

$$K_S(y_S)\ \dot{y}_S = z_S\ , \quad \text{and} \quad M_S(y_S)\ \dot{z}_S = q_S(y_S,\ z_S,\ y_V,\ z_V,\ s_F) \tag{4}$$

where K_S and M_S are the kinematic and the mass matrix of a subsystem. The dynamics of dynamic force elements like tires, dampers, hydro or rubber mounts can be described by an additional set of first order differential equations

$$\dot{s}_F \;=\; f_F(s_F,\; y_V,\; z_V,\; y_S,\; z_S) \tag{5}$$

The basic ideas of a modeling technique tailored to the simulation of vehicles in real time can be found in [5], detailed information on vehicle modeling by subsystems are presented in [7]. Combining generic vehicle models to tractor semi-trailer or tractor trailer combinations finally will result in differential algebraic equations, [3].

5 Numerical Solution

For real time simulations of complex multibody system models including strong nonlinearities low order fixed step size methods are used in practice. According to [2] these methods produce surprisingly good results compared to sophisticated step size controlled high order methods. As shown in [10] the implicit Euler formalism can be adapted to the specific structure of the equations of motion describing complex vehicle models. Applying the implicit Euler formalism to the equations of motion for the vehicle framework (3) at first results in

$$y_V^{k+1} = y_V^k \;+\; h\, K_V \left(y_V^{k+1}\right)^{-1} z_V^{k+1} \tag{6}$$

$$z_V^{k+1} = z_V^k \;+\; h\, M_V \left(y_V^{k+1}\right)^{-1} q_V \left(y_V^{k+1}, z_V^{k+1}, y_S^{k+1}, z_S^{k+1}, s_F^{k+1}\right) \tag{7}$$

where h denotes the integration step size and the superscripts ^{k} and $^{k+1}$ indicate the known states at time t and the unknown ones at $t + h$. In order to minimize the computation effort the following assumptions which will hold very well for vehicles are made now

1. all subsystem and dynamic forces will have a faster dynamics then the vehicle framework
2. the dependency of the kinematic matrix K_V and the mass matrix M_V on the generalized coordinates is weekly nonlinear

In consequence

1. the new states of the subsystems and the force elements y_S^{k+1}, z_S^{k+1} and s_F^{k+1} can be calculated with a semi-implicit Euler step using the known states of the framework y_V^k and z_V^k instead of the implicit and unknown ones.
2. the implicit states of the kinematic and the mass matrix can be approximated by their explicit ones $K_V \left(y_V^{k+1}\right) \approx K_V \left(y_V^k\right)$ and $M_V \left(y_V^{k+1}\right) \approx M_V \left(y_V^k\right)$

Then, the vector of generalized forces is expanded into a Taylor series

$$
\begin{aligned}
q_V\left(y_V^{k+1}, z_V^{k+1}, y_S^{k+1}, z_S^{k+1}, s_F^{k+1}\right) \approx\; & q\left(y_V^k + h\, z_V^k, z_V^k, y_S^{k+1}, z_S^{k+1}, s_F^{k+1}\right) \\
& + \frac{\partial q_V}{\partial z_V}\left(z_V^{k+1} - z_V^k\right) \\
& + \frac{\partial q_V}{\partial y_V}\Big(\underbrace{y_V^{k+1} - y_V^k}_{h\, K_V\left(K_V^k\right)^{-1} z_V^{k+1}} - h\, z_V^k\Big) \;+\; h.o.t.
\end{aligned}
\tag{8}
$$

where higher order terms (h.o.t.) are neglected and the difference in the position vectors $y_V^{k+1} - y_V^k$ is related via (7) to the new state of the corresponding generalized velocity z_V^{k+1}. Equation (7) can be transformed to the linearly implicit step now

$$
z_V^{k+1} = z_V^k + h\left(M_V(y_V) - h\,\frac{\partial q_V}{\partial z_V} - h^2\,\frac{\partial q_V}{\partial y_V}\right)^{-1} q\left(y_V^k + h\, z_V^k, z_V^k, y_S^{k+1}, z_S^{k+1}, s_F^{k+1}\right) \tag{9}
$$

which as shown in [1] is still sufficiently stable and will only require the solution of a system of linear equations at each step. The integration step for the vehicle framework is completed by (7) which is a full implicit step now because the vector of the implicit generalized velocities z_V^{k+1} is given by (9). As (9) is the result of a first order approach the calculation of the Jacobians $\partial q_V / \partial y_V$ and $\partial q_V \partial z_V$ may be performed at the same approximation level. At first the vector of generalized forces is separated into two parts

$$
q_V \;=\; q_V^i \;+\; q_V^a \tag{10}
$$

where q_V^i collects the inertia forces and moments and q_V^a contains the contribution of all applied forces and moments. Similar to the kinematic and the mass matrix the vector of the generalized inertia forces for the vehicle framework is weekly nonlinear. Hence, the partial derivatives $\partial q_V^i / \partial y_V$ and $\partial q_V^i \partial z_V$ can be neglected. Within the principle of virtual power the vector of the generalized applied forces is generated by

$$
q_V^a \;=\; \sum_{i=1}^{n_F}\left(\frac{\partial v_i}{\partial z_V}\right)^T F_i \;+\; \sum_{j=1}^{n_M}\left(\frac{\partial \omega_j}{\partial z_V}\right)^T M_j \tag{11}
$$

where it was assumed that n_F forces F_i, $i = 1(1)n_F$ and n_M moments M_i, $i = 1(1)n_M$ are applied to the vehicle framework. The partial velocities $\partial v_i \partial z_V$, $\partial \omega_j \partial z_V$ are part of the principle of the virtual power algorithm and need not to be calculated additionally. The applied forces and moments are described by potentially nonlinear characteristics

$$
F_i = F_i(u_i, \dot{u}_i) \quad \text{and} \quad M_j = M_j(u_j, \dot{u}_j) \tag{12}
$$

where the element displacements u_i, u_j and their time derivatives can be expressed by the generalized coordinates y_V and the generalized velocities z_V

$$u_i = u_i(y_V),\ u_j = u_j(y_V) \quad \text{and} \quad \dot{u}_i = \dot{u}_i(y_V, z_V),\ \dot{u}_j = \dot{u}_j(y_V, z_V) \tag{13}$$

Hence, the partial derivatives of the vector of the generalized forces with respect to the generalized coordinates y_V and the generalized velocities z_V may be approximated by

$$\frac{\partial q_V}{\partial y_V} \approx \frac{\partial q_V^a}{\partial y_V} \approx \sum_{i=1}^{n_F} \left(\frac{\partial v_i}{\partial z_V}\right)^T \frac{\partial F_i}{\partial u_i} \frac{\partial u_i}{\partial y_V} + \sum_{j=1}^{n_T} \left(\frac{\partial \omega_j}{\partial z_V}\right)^T \frac{\partial M_j}{\partial u_j} \frac{\partial u_j}{\partial y_V} \tag{14}$$

and

$$\frac{\partial q_V}{\partial z_V} \approx \frac{\partial q_V^a}{\partial z_V} \approx \sum_{i=1}^{n_F} \left(\frac{\partial v_i}{\partial z_V}\right)^T \frac{\partial F_i}{\partial \dot{u}_i} \frac{\partial \dot{u}_i}{\partial z_V} + \sum_{j=1}^{n_T} \left(\frac{\partial \omega_j}{\partial z_V}\right)^T \frac{\partial M_j}{\partial \dot{u}_j} \frac{\partial \dot{u}_j}{\partial y_V} \tag{15}$$

where dominating terms were taken into account only. The calculation of the partial derivatives $\partial F_i/\partial u_i$, $\partial F_i/\partial \dot{u}_i$, $\partial M_j/\partial u_j$, $\partial M_j/\partial \dot{u}_j$ and $\partial u_i/\partial y_V$, $\partial \dot{u}_i \partial z_V$ $\partial u_j/\partial y_V$, $\partial \dot{u}_j \partial y_V$ can be done with a small additional calculation effort. Hence, the modified implicit Euler formalism consisting of a series of a linearly implicit step (9) followed by a full implicit one (7) requires not much more computation effort than an explicit Euler step but usually increases the range of stability significantly.

6 Local and Global Derivatives

In vehicle dynamics the derivatives of most spring and damper characteristics are rather smooth. In contrast the derivative dF_F/dv of the friction force $F_F = F_F(v)$ given by (2) results in a jump from zero to the fictitious damping coefficient d_F at small velocities, Fig. 4. This discontinuity in the derivative and hence in the Jacobian $\partial q_V/\partial z_V$ can be avoided by replacing the discontinuous local by a continuous global derivative

$$\frac{d\,F_F}{d\,v} = \begin{cases} d_F & -v^* \le v \le +v^* \\ F/v & else \end{cases} \quad \text{where} \quad v^* = \frac{F_F^M}{d_F} \tag{16}$$

Using this global derivative means that the Newton step performed in (9) to approximate the implicit solution will be substituted by a secant step.

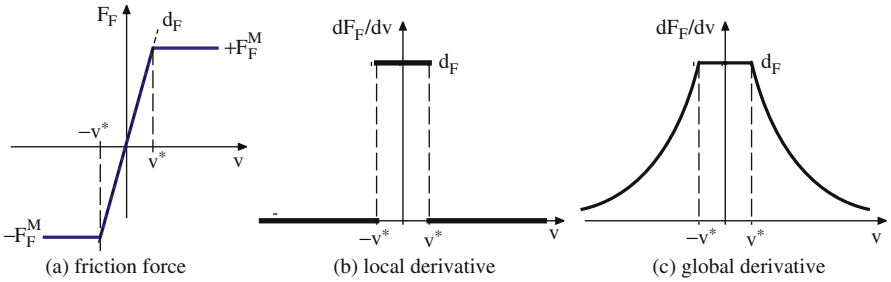

Fig. 4 Friction forces with local and global derivative

7 Example

A simple quarter car model representing a heavy truck suspension is used to show the advantages of the presented method. The maximum friction force F_F^M in the leaf spring amounts to 10% of the spring force magnitude $|F_S|$. The fictitious damping coefficient d_F is adjusted to the suspension damping d_S. The vehicle runs with a constant travel velocity of $v_T = 60\,\text{km/h}$ across a cosine-shaped bump of the height $H = 0.1\,\text{m}$ and a length of $L = 5.0\,\text{m}$. Figure 5 shows all relevant vehicle data and

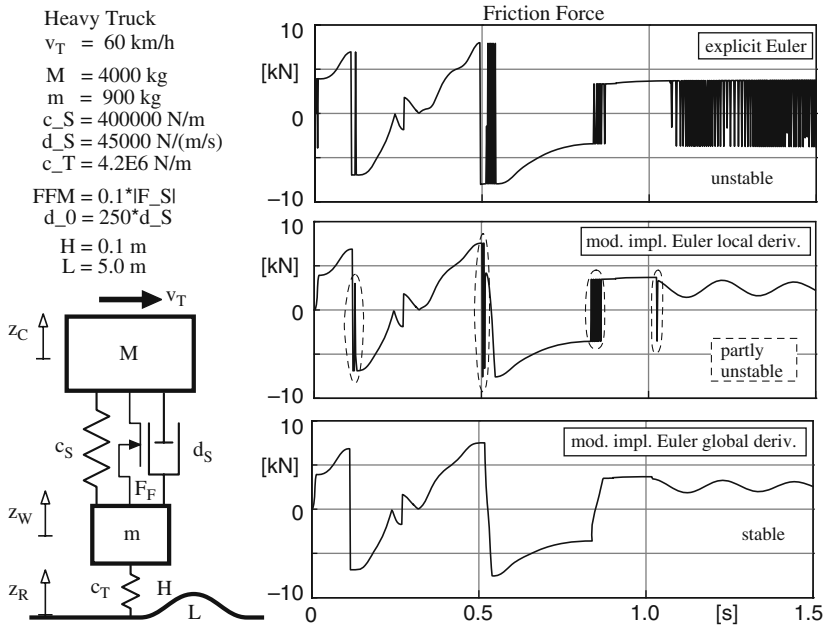

Fig. 5 Friction forces with different Euler algorithms with a step size of $h = 2\,\text{ms}$

the time history of the friction force. The explicit Euler solution becomes unstable when the suspension travel velocity $v = \dot{z}_C - \dot{z}_W$ approaches zero. Here, the friction force changes from the constant sliding value $F_F = \pm F_F^M$ to the continuous approximation for adhesion $F_F = d_F v$. In order to come very close to the Coloumb model shown in Fig. 3 the fictitious damping was chosen quite large. At any time, when the branch $F_F = d_F v$ of the friction law (2) is active the equations of motion for the quarter car model become stiff. Here, the explicit Euler solution with a integration step size of $h = 2\,\text{ms}$ becomes unstable because the friction force will jump from $+F_F^M$ to $-F_F^M$ at each integration step. Using the modified implicit Euler integration as defined in Sect. 5 in a straight forward manner causes stability problems too. The reason is quite obvious. As long as the friction law (2) is in sliding regions the local derivative of the friction force is zero. Then, the corresponding Jacobian $\partial q_V / \partial z_V$ will vanish too and the first linearly implicit step (9) degenerates to a simple explicit one. The stabilizing effect of the second fully implicit step (7) is too weak to achieve an overall stable solution with an integration step size of $h = 2\,\text{ms}$ but results at least in a stable transition to the steady state position at the end of the simulation ($t > 1.2\,\text{s}$). The modified implicit Euler integration given in Sect. 5 together with the global derivative of the friction force defined by (16) does a perfect job. The numerical solution with an integration step size of $h = 2\,\text{ms}$ is now perfectly stable and still sufficiently accurate, Fig. 6. Besides in deviations in the peak values of the chassis acceleration and the wheel load the numerical damping of the modified implicit Euler solution is very well noticeable in the time history of the friction force while approaching steady state.

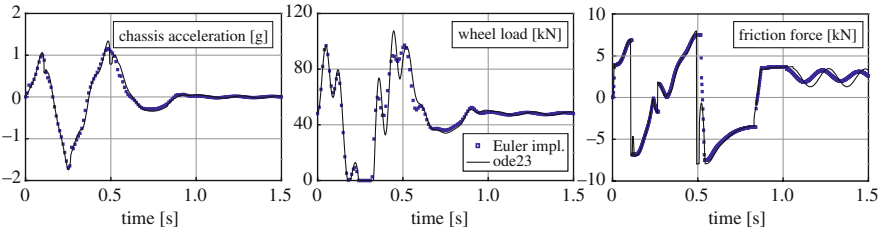

Fig. 6 Modified implicit Euler solution with global derivatives compared to Matlab-solver ode23

8 Conclusion

The modified implicit Euler solution combined with global derivatives to avoid discontinuities in the Jacobians is very well suited for real time simulations in the field of vehicle dynamics. This solver is simple, fast, stable and sufficiently accurate.

References

1. Arnold, M.; Burgermeister, B.; Eichberger, A.: Linearly implicit time integration methods in real-time applications: DAEs and stiff ODEs. Multibody System Dynamics 17 pp. 99–117 (2007)
2. Arnold, M.; Weidemann, Ch.; Mauer, L.: Stepsize control versus fixed stepsize time integration: Theory and practical experience. In: Conference Proc. of Multibody Dynamics 2007, (ECCOMAS Thematic Conference) Politecnico di Milano, Italy (2007)
3. Esterl, B.; Butz, T.; Simeon, B.; Burgermeister, B.: Real-time integration and vehicle trailer-coupling by algorithms for differential-algebraic equations. Vehicle System Dynamics, Vol. 45, No. 9, pp. 819–834 (2007)
4. Rauh, J.: Virtual Development of Ride and Handling Characteristics for Advanced Passenger Cars. Vehicle System Dynamics, Vol. 40, Nos. 1–3, pp. 135–155 (2003)
5. Rill, G.: Simulation von Kraftfahrzeugen. Vieweg-Verlag, Braunschweig/Wiesbaden (1994) reprint at: http://homepages.fh-regensburg.de/~rig39165
6. Rill, G.; Kessing, N.; Lange, O.; Meier, J.: Leaf Spring Modeling for Real Time Applications. In: The Dynamics of Vehicles on Road and on Tracks – Extensive Summaries, IAVSD 03, Atsugi, Kanagawa, Japan (2003)
7. Rill, G.: Vehicle Modeling by Subsystems. Journal of the Brazilan Society of Mechanical Sciences and Engineering, ABCM, Vol. XXVIII, No. 4, pp. 431–443 (2006)
8. Rill, G.: Wheel Dynamics, In: Conference Proc. of the XII International Symposium on Dynamic Problems of Mechanics (DINAME), ABCM, Brasil (2007)
9. Rill, G.; Chucholowski, C.: Modeling Concepts for Modern Steering Systems. In: Conference Proc. of Multibody Dynamics 2005, ECCOMAS Thematic Conference, Universidad Politecnica de Madrid, Spain (2005)
10. Rill, G.; Chucholowski, C.: Real Time Simulation of Large Vehicle Systems. In: Conference Proc. of Multibody Dynamics 2007, (ECCOMAS Thematic Conference) Politecnico di Milano, Italy (2007)

Index

A

Acoustic optimization of wheel sets, 67–71
  examples, 69–71
    BA 004, 69–70
  modal behaviour of wheel set, 68–69
    axle vibration mode, 68
    blower oscillations, 68–69
    eigenmodes, 68–69
    umbrella oscillations, 68
  optimization method, 68
  stages in, 68
    force excitation in the rolling contact, 68
    sound radiation, 68
    wheel structure-borne sound, due to force excitation, 68
AK-Master test, 107
American 3-piece-freight truck, 7, 9, 10

B

Bifurcation analysis of system vehicle/track, 18–24
  in nonlinear stability assessment, 25
  nonlinearities of vehicle model, 23–24
  numerical simulation method, 21
  of oscillation behaviour, 25
  PATH software tool, 20
  of safety, 25
  SIMPACK software package, 20
  wheel-rail contact nonlinearity, 21–23
  See also Hopf bifurcation
Bifurcations
  in non-smooth models of mechanical systems, 173–184
    Filippov systems, 174–179, *see also individual entry*
    See also Grazing-sliding bifurcations
Bogies, for pasenger car, 3–4
Bolster, railway passenger car, 3–4
Boundary equilibrium bifurcations
  in a friction oscillator, 177–179
    boundary equilibrium, 178
    breaking the degeneracy, 178–179
  in Filippov systems, 176–177
Brake pad structure, 102
Brake systems, vibrations in, 101–111
  See also Tangential friction induced vibrations in brake systems
Bumpstop instabilities suppression in a quarter-car model, 137–146
  dynamical instabilities, 141–143
    compositions, 143
    discontinuity maps, 141–142
  feedback-control strategy, 138
  feedback stabilization, 143–144
    control algorithm, 143–144
  high-velocity impacts, 137
  impact velocity
    with and without control, 144–145
  low-velocity impacts, 137
  See also Discontinuity map approach, in bumpstop instabilities suppression; Quarter-car model

C

Chamber equations, 128–129
Closed-form analysis, 29–39
  of handling performance, 29–39
  passive methods
    See also individual entry
  semiactive methods, 29–39
    See also individual entry
  of vehicle suspension ride, 29–39
  See also Quarter-car model
Constructive asymmetry, 187–188
Contact geometry functions, in wheel/rail contact nonlinearity assessment, 21–23

P.G. Thomsen, H. True (eds.), *Non-smooth Problems in Vehicle Systems Dynamics*,
DOI 10.1007/978-3-642-01356-0, © Springer-Verlag Berlin Heidelberg 2010

Contact model, in hunting instability investigation, 58
Contacts in vehicle systems, 5–6
  contact angle, 5–6
  contact point, 5
  contact surface, 5
  creep, 6
  creep force, 6
  rail/wheel contact, 5–6
    geometry, 5
  shear force relation between, 6
Continuous extension
  in numerical solution across a jump-discontinuity, 216–218
  trapezoidal method with, 216–217
Coulomb model, for longitudinal tyre behaviour, 161
Critical speed, numerical evaluation, 45–47
  'elastic contact' simplifying assumptions, 47
  multi-body model of railway vehicle, 46
  multi-Hertzian contact model, 47
  normal measuring method, 45–46
  simplified measuring method, 45–46
  wheel rail contact model, 47
Curve squealing of trains, 73–84
  measurements, 74–75
    elastic FE model of wheel, 75–77
    frequency spectrum of noise, 75
    noise recording, 74
    phases in, 74
  modelling, 73–84
  multibody simulation of stationary run, 77–79
  numerical simulation of self-excitation, 82–84
    of friction-induced self-excited oscillations, 83
  simulation, 73–84
  squeal model, design, 79–81
    elastic wheel, 80
    rigid rail, 80
  stability analysis of stationary run, 81–82
Curved track, rail vehicles in, 87–98
  kinematics, as non-smooth functions cause, 96–98
    imaginary forces, 96–97
    measures, types, 96
    torques, 96–97
  non-linear dynamics of, 87–98
    bifurcation plots, 91–92
    model's structure, 88
    non-smooth properties, 91–94
    objects of the analyses and their models, 88
    two-point contact modelling, 88–90
    See also Two-point contact modelling, of rail vehicles in curved track
  non-linear features, 94–96
    See also under Transition curves, non-linear features in
  stability maps, 92–93
    for unworn wheel/rail pair S1002/UIC60 and 1:20 rail inclination, 93
    for unworn S1002/UIC60 wheel/rail pair and 1:40 rail inclination, 92
    vehicle lateral dynamics, 90
    for worn s1002/UIC60 wheel/rail pair and 1:40 rail inclination, 93

D

Damper modelling in railway simulation program, 123–134
  chamber equations, 128–129
    auxiliary chamber, 129
    compression chamber, 128
    rebound chamber, 128
  check valves, 126–128
    FE model of, 127
    opening and closing of, pressure evolution during, 132
    opening of, stops in, 126–127
    valve opening versus pressure difference, 128
  damping valve, 125–126
  main components modelling, 125–128
  mathematical model, 129
  railway damper, description, 124–125
    chambers, 124
    compression stroke, 124
    operation, 125
    rebound stroke, 124–125
    structure, 124
  simplified model, 130–134
    auxiliary chamber, 132–133
    compression stroke, 133
    rebound stroke, 134
Damping effect, closed-form analysis
  on suspension deflection response, 36
  on tire deflection response, 37
  on vertical acceleration response, 35
Discontinuities in ODEs, 211–225
  numerical solution, 211, 213–216
    across a jump-discontinuity, 213–216
    continuous extension, 216–218

integrating across a point of state change, 214
multistep methods, 213–215
one-step methods, 215–216
systems with changes of state, 211–224
discontinuity across curve of, 212
dynamics of a wheelset, 220–223
implementations, 219–224
ODE's with discontinuous right hand sides, 212–213
tank-heater example, 220–221
transition point, solution and determination of, 218
Discontinuity induced bifurcations of limit cycles, 180–184
See also Grazing-sliding bifurcations
Discontinuity map approach, in bumpstop instabilities suppression, 138, 141–142
Discontinuous models
multidisciplinary models, sensitivity analysis, 239–250
sensitivity analysis, 240–245
See also Modelica model
Dither, 189–193
smoothing effect of, 189–192
influence on freight wagon dynamics, 192
numerical simulations, 192
Dry friction elements, modelling, 113–122, 254–255
continuous approximation, 255
integration method, modification, 116–118
drawback in, 117
infinite loop situation in, 118
switching algorithm, 117–118
integration method, modification application
connection elements model, 119
coupler crash elements, 118
forces in coupler with crash elements, 119–120
forces in tambours, 119–121
longitudinal force determination, 119
to train bumping into an obstacle problem, 118–121
mechanical model of, 113–116
compression force, 113–115
constant contact side bearing, 114
Coulomb friction element, 113–114
force-displacement history of elastic-plastic deformation, 114
mathematical description, 115
numerical integration methods, 113–122
simple Coloumb model, 254–255
Dry friction smoothing by medium frequency dither, 189–193
influence on ride dynamics of freight wagons, 189–193
See also Dither
Dynamic model, for longitudinal tyre behaviour, 161
Dynamical instabilities suppression
in a quarter-car model, 141–143
compositions, 143
discontinuity maps, 141–142

E

Elastic model
gear hammering simulation with, 195–206
See also individual entry
Elastic multibody model, 199–203
contact algorithm, 200–201
index point, 200
simulation results, 202–203
standard data, calculation, 199–200
time integration, 201–202
Elements, non-smooth, in vehicle systems, 3–13
motorized vehicles, 13
general vehicle model, 3–5
See also Railway passenger car
rail/wheel contact, 5–6
See also Contacts in vehicle systems
See also Suspension elements, non-smooth
Equations of motion, 255–256
Equivalent conicity, 15, 23, 42–44
harmonic quasi-linearization method, 44
hunting instability and, 56–57
as a mean to relate hunting motion and wheel rail profiles, 47–51
conicity diagrams, 49–50
empiric limit curve, 48
filing conic diagrams, 49
limitations, 48
trapezoidal integration method, 43–44
UIC 519 method, 43–44
Error estimation for higher order time integration of ODEs, 227–237
improved error estimates, 228–232
error propagation and bounds for the global error, 232
local error analysis based on a locally defined smoothed problem, 230
piecewise linear interpolating splines, 229

restricted number of time steps that are affected by the discontinuities, 229
spline approximation of smooth system inputs, 228–229
numerical tests, 232–236
Euler-Heun method, 236
global error of 5th order method, 234–236
simulation scenarios in, 234
two mass model, 232–233
with non-smooth right hand side, 227–237
Error propagation and bounds for the global error, 232
Euler formalism, 256, 259–260
Euler-Heun method, 236

F
FE-analysis of elastic wheel, 75–77
mesh, designing, 76
validation, 76
Feedback-control strategy, in bumpstop instabilities suppression, 138
Feedback stabilization, in a quarter-car model, 143–144
control algorithm, 143–144
Filippov systems, 174–175
boundary equilibrium bifurcations in, 175–179
boundary equilibrium, 176–177
pseudo-equilibrium, 175
standard equilibrium (SE), 175
Floquet multipliers, 183–184
Force asymmetry, 187–188
Freight wagons
dry friction smoothing by M-F dither in, 189–193
See also Dither
Friction in brake systems, 101–111
See also Tangential friction induced vibrations in brake systems
Friction models, in longitudinal tyre behaviour, 163–164
Friction oscillator
boundary equilibrium bifurcations in, 177–179
grazing-sliding bifurcation in, 181

G
Gear hammering simulation with a fully elastic model, 195–206
experimental impact investigations, 203–205
contact forces measurement, 204
impact investigations, 196–199
See also Elastic multibody model
General vehicle model, 3–5
Grazing-sliding bifurcations, 180–184
analysis, 182–184
in the friction oscillator, 181

H
Hardware-In-the-Loop (HIL) test, 253
Harmonic quasi-linearization method, 4
Heat causing friction in brake system, 105–108
See also Tangential friction induced vibrations in brake systems
Hopf bifurcation, 18, 23
continuation-based, 20
subcritical, 20, 25–26
supercritical, 20, 25–26
Hunting instability, avoiding, 53–65
in Milan's metro line, 53
cause of instability, 54
experimental assessment, 54–57
See also Low-cost maintenance operation for avoiding hunting instability; Wheel limit profile for hunting instability
Hunting motion and wheel rail profiles
equivalent conicity as a mean to relate, 47–51
limitations, 48
Hydraulic dampers, 6

I
Impact investigations, in gear hammering simulation, 196–199
Index point, 200
Integration method, in dry friction elements, modelling, 116–118
See also under Dry friction elements, modelling

J
Jacobian matrix, smoothing discontinuities in, 253–260
dry friction modelling, 254–255
equations of motion, 255–256
local and global derivatives, 258–259
numerical solution, 256–258
vehicle modelling, 253–254
Jump-discontinuity, numerical solution across, 213–216

K
Klingel's formula, 43

L
Lenoir dampers, 7–8
Limit profile for hunting instability, *see* Wheel limit profile for hunting instability
Local error analysis based on locally defined smoothed problem, 230
Longitudinal tyre behaviour, 161–169
  Coulomb model, 161
  dynamic model, 161
  factors influencing force generation, 162
  longitudinal force distribution, 166–169
    effective rolling radius, 166
    longitudinal slip, 166
    stationary, 166
  modelling, 161–169
    See also Tyre force model
  simulation, 161–169
  speed-dependent friction model, 161
Lossy gear model, 241–242
  constructed solution for, 244
  parameters for, 242
  variables for, 242
  See also Modelica model
Low-cost maintenance operation for avoiding hunting instability, 53–65
  axlebox for instability detection, 55
  equivalent conicity, 56–57
  instability indicators, 55
  instrumented bogie for instability detection, 55
  low-cost solution, 62–64
  numerical investigation, 57–62, *see* Vehicle numerical model
  UIC 519 method, 56
  See also under Hunting instability, avoiding

M
Mechanical model
  of friction element, 113–116
    See also under Dry friction elements, modelling
  in longitudinal tyre behaviour, 162–163
Medium frequency (M-F) dither, 189–192
Modelica model, 241–244
  solution theory, 243
  switching function, 243
  See also Lossy gear model
Motorized vehicles, 13
Multi-body model of railway vehicle, 46
Multibody simulation of stationary run, 77–79
Multistep methods, in numerical solution across a jump-discontinuity, 213–215

N
Newton-Raphson method, 217
Nonlinear stability analysis, *see* Stability analysis in railway vehicle industry
Nonlinearities of vehicle model, 23–24
  yaw dampers influence, 24
Normal force distribution, in longitudinal tyre behaviour, 164–166
Normal measuring method, in critical speed evaluation, 45–46
Numerical simulation method, in bifurcation analysis, 21
Numerical tests
  in error estimation for higher order time integration of ODEs, 232–236
    simulation scenarios in, 234
    two mass model, 232–233

O
One-step methods, in numerical solution across a jump-discontinuity, 215–216
Optimization method, 68
Ordinary differential equation (ODE)-systems, 211–225
  See also Discontinuities in ODEs; Error estimation for higher order time integration of ODEs

P
Passive methods, in closed-form analysis, 29–39
Patches in brake systems, 102–104
  contact patches, 104
    contact zone of type I, 104
    contact zone of type II, 104
  See also Tangential friction induced vibrations in brake systems
PATH software tool, 20
Piecewise linear interpolating splines, 229
Pseudo-equilibrium bifurcations in Filippov systems, 175

Q
Quarter-car model, 139–141
  condition of contact, 139
  condition of free flight, 139
  condition of quasi-contact, 139
  transitions, 140–141
  two-degree-of-freedom mechanical model, 139
  vector fields, 140

Quarter-car model, closed-form analysis, 29–30
damping effect on suspension deflection response, 36
groundhook, 36
hybrid, 36
passive, 36
skyhook, 36
damping effect on tire deflection response, 37
groundhook, 37
hybrid, 37
passive, 37
skyhook, 37
damping effect on vertical acceleration response, 35
groundhook, 35
hybrid, 35
passive, 35
skyhook, 35
dimensionless parameters, 34
mass ratio, 34
natural frequency of unsprung mass, 34
off-state damping ratio of sprung mass, 34
on-state damping ratio of sprung mass, 34
stiffness ratio, 34
model formulation, 30–35
suspension system, 30
passive configuration, 30
semiactive configuration, 30
transfer functions, 31–32
of sprung mass vertical acceleration, 32
of suspension deflection, 33
of tire deflection, 33
vibration level measurement, 31

R

Railway passenger car
4-axle, 3–4
bogies, 3–4
bolster, 4
dampers, 4
lower part, 4
springs, 4
upper part, 4
secondary suspension, 4
primary suspension, 4
Runge-Kutta methods, 229, 236
Running stability assessment in railway industry, 16–18
based on simulations of vehicle acceptance tests, 19
criteria used, 17
forces between wheelset and track, 17
lateral acceleration on bogie frame, 17
linearized, 16
methods used, 17–18
nonlinear, using computer simulations, 16
classification based on assessment criteria, 16
classification based on track alignment, 16
in rolling stock industry, 25

S

Self-excitation, numerical simulation, 82–84
Semiactive methods, in closed-form analysis, 29–39
groundhook, 29–30
hybrid control, 29–30
skyhook, 29–30
Sensitivity analysis of discontinuous multidisciplinary models, 239–250
classical solution of a parameter dependent discontinuous system, 245
switching functions, solutions, 247
simultaneous switching of electrical loads, 248
See also Discontinuous models
Shimmy phenomenon, *see* Towed elastic tyres during rolling, experimental modal analysis
SIMPACK software package, 20–21
Simplified measuring method, in critical speed evaluation, 45–46
Smoothing discontinuities in Jacobian matrix, 253–260
See also Jacobian matrix, smoothing discontinuities in
Smoothing effect of dither, 189–192
Sound level of wheel sets, *see* Acoustic optimization of wheel sets
Speed-dependent friction model, for longitudinal tyre behaviour, 161
Spline approximation of smooth system inputs, 228–229
Squealing, 73–84
See also Curve squealing of trains
Stability analysis in railway vehicle industry, 15–27
based on limit cycle occurrence and safety limits assessment, comparison, 20
based on simulations of vehicle acceptance tests, 19
necessity of, 16

See also Bifurcation analysis of system vehicle/track; Running stability assessment in railway industry
Standard equilibrium (SE) bifurcations in Filippov systems, 175
State change, systems with, 211–224
discontinuity across curve of, 212
numerical solution
integrating across, 214
See also under Discontinuities in ODEs
Stationary run, stability analysis, 81–82
Suspension elements, non-smooth
adapters and side frames, dry friction contact between, 10
American 3-piece-freight truck, 7, 9, 10
car body and bolster, connection between, 9
coil springs, 6–7
freight wagon bogies, 6
hydraulic dampers, 6
Lenoir dampers, 7–8
in railway passenger vehicles, 4
two-axle freight wagon, 11
UIC standard suspension of, 11
UIC double link suspension, 11–12
wedges and bolster and side frame
vertical and lateral dry friction damping between, 10
Switching algorithm, in dry friction elements modelling, 117–118
Switching functions, sensitivity analysis, 245–250
simultaneous switching of electrical loads, 248

T

Tangential friction induced vibrations in brake systems, 108–111
contact patches, 102–104
as stick-slip oscillators, 109–110
contact zone of type I, 104
contact zone of type II, 104
lateral patch vibrations, 109
phasing of, 109
as dynamic equilibrium of processes, 104
heat and wear causing, 105–108
AK-Master test, 107
friction coefficient μ, 106
measurement, 106–107
polymeric matrix causing, 102–103
Timescale, 101
Towed elastic tyres during rolling, experimental modal analysis, 149–158
linear stability chart of, 153
mechanical model, 150–151
modal analysis, 156–158
parameter identification, 154–155
damping, 154–155
linear stability boundary, validation, 155–156
stiffness, 154–155
tyre relaxation parameters, 154
stability analysis, 152–153
travelling wave-like solution, 151–152
Track model, in hunting instability investigation, 58
Train-track interaction, simulation, in hunting instability investigation, 58–62
Transition curves, non-linear features in, 94–96
CC, 94
ST, 94
See also under Curved track, rail vehicles in
Transitions, quarter-car model, 140–141
Trapezoidal integration method, 43–44
Two-point contact modelling, of rail vehicles in curved track, 88–90
methods in, 89
first (original) method, 89
second (modified) method, 89
Tyre force model, 162–166
friction models, 163–164
mechanical model, 162–163
normal force distribution, 164–166

U

UIC 519 method, 43

V

Vector fields, quarter-car model, 140
Vehicle modelling, 253–254
in hunting instability investigation, 57–62
contact model, 58
equivalent conicity, 60–61
measured bogie lateral acceleration, 59, 63–64
simulated bogie lateral acceleration, 59, 61–62
track model, 58
train-track interaction, simulation, 58–62
vehicle model, 57
Vehicle numerical model, 58–59
Vibrational displacement determination
by constructive and force asymmetry of system, 187–188

Vibrations in brake systems, 101–111
See also Tangential friction induced vibrations in brake systems

W
Wear in brake system, 102–103
polymeric matrix causing, 102–103
See also Tangential friction induced vibrations in brake systems
Wheel limit profile for hunting instability, 41–52
critical speed, numerical evaluation, 45–47
wheel rail contact model, 47
See also Equivalent conicity
Wheel-rail contact nonlinearity, 21–23
influence of, 21–22
contact geometry functions used in assessing, 21, 23
on railway vehicle behaviour, 22

Y
Yaw dampers, 24